Lehigh University
Lehigh Preserve

Theses and Dissertations

2015

Flow Structure on a Rotating Wing: Effect of Radius of Gyration

Maxwell Marshall Wolfinger
Lehigh University

Follow this and additional works at: http://preserve.lehigh.edu/etd

 Part of the Mechanical Engineering Commons

Recommended Citation
Wolfinger, Maxwell Marshall, "Flow Structure on a Rotating Wing: Effect of Radius of Gyration" (2015). *Theses and Dissertations.* Paper 1673.

This Dissertation is brought to you for free and open access by Lehigh Preserve. It has been accepted for inclusion in Theses and Dissertations by an authorized administrator of Lehigh Preserve. For more information, please contact preserve@lehigh.edu.

FLOW STRUCTURE ON A ROTATING WING: EFFECT OF RADIUS OF GYRATION

by

Maxwell Wolfinger

Presented to the Graduate Research Committee

Of Lehigh University

In Candidacy for the Degree of

Doctor of Philosophy

in

Mechanical Engineering

Lehigh University

January, 2015

Approved and recommended for acceptance as a dissertation in partial fulfillment of the requirements for the degree of Doctor of Philosophy.

_____

Date

_____

Donald Rockwell

Dissertation Advisor

_____

Accepted Date

Committee Members:

_____

Professor Donald Rockwell

_____

Professor Yaling Liu

_____

Professor Alparslan Oztekin

_____

Professor John Spletzer

To Kate

ACKNOWLEDGEMENTS

I would like to thank a number of people at Lehigh for helping bring this research together. First, I would like to extend my greatest appreciation to Professor Donald Rockwell, for his guidance and commitment to this research project. Professor Rockwell's collaborative efforts as my advisor were invaluable, and his attention to detail and thoroughness have helped this project immeasurably.

In addition to Professor Rockwell, I would like to thank my committee members, Professor Alparslan Oztekin, Professor Yaling Liu, and Professor John Spletzer for their guidance and suggestions throughout the PhD process.

I would also like to offer my gratitude to several fellow graduate students, particularly Matthew Bross and Daniel Tudball-Smith, for their collaborative efforts. Our parallel projects all benefited from mutual support that expedited the research process, and allowed us the chance to help each other with countless issues.

This experimental research would not have been possible without technical support from a number of excellent Lehigh community members. For that reason, I would like to acknowledge the work of Richard Towne, Eli Towne, and James Bunderla, who constructed the experimental systems used for this research project. I would also like to thank Naazer Ashraf, for his work maintaining our computing systems. The

administrative staff of the Mechanical Engineering and Mechanics department, JoAnn Casciano in particular, was also immensely helpful, and for that, I am thankful.

My family was integral in keeping me motivated throughout my time in graduate school and pushing me to finish my PhD. They inspired me to pursue graduate research, and supported me in countless ways.

Finally and most importantly, I would like to thank my wife, Kate. She was with me throughout this process, helping with editing and listening to countless presentations, for which I am eternally grateful.

TABLE OF CONTENTS

Page

LIST OF FIGURES

Page

NOMENCLATURE

AR	Aspect ratio
a	Smoothing parameter
b	Wingspan
C	Chord length
CCD	Charge-coupled device
d_a	Point source image size
d_s	Diffraction limited spot diameter
d_τ	Particle image size
d_p	Particle size
FFT	Fast-fourier-transform
$f^\#$	Lens f-number
h	Helical density
LEV	Leading-edge vortex
MAV	Micro air vehicle
M_o	Image magnification
O	Of the order
PIV	Particle image velocimetry
Q	Second invariant of the velocity gradient tensor
r	radial distance
Re	Reynolds number
r_g	Radius of gyration
Ro	Rossby number
RV	Root vortex

SPIV	Stereoscopic particle image velocimetry
$\|\|\boldsymbol{S}\|\|$	Magnitude of rate-of-strain tensor
TV	Tip vortex
tw	Wing thickness
t	Time Variable
Δt	Time delay
u_{rms}	Root-mean-square velocity fluctuation
$\boldsymbol{V}$	Velocity vector
Vrg	Velocity at the radius of gyration
x	Coordinate tangential to wing motion
y	Coordinate orthogonal to wing motion and wing span
z	Coordinate parallel to wing span
Δz	Volumetric reconstruction plane spacing

Greek Symbols

α	Angle of attack
λ	Wavelength of light
ζ	Coordinate parallel to wing span
η	Coordinate normal to wing surface
θ	Azimuthal coordinate
ν	Kinematic viscosity
σ	Gaussian smoothing kernel
	Random velocity error
Φ	Rotation angle
χ	Coordinate orthogonal to wing-normal and wing span
Ω	Angular velocity

$||\boldsymbol{\Omega}||$ Magnitude of vorticity tensor

$\boldsymbol{\omega}$ Vorticity vector

ABSTRACT

The flow structure on a rotating wing (flat plate) is characterized over a range of Rossby number $Ro = r_g/C$, in which r_g and C are the radius of gyration and chord of the wing, as well as travel distance $r_g\Phi/C$, where Φ is the angle of rotation. Wings having low aspect ratio $AR = 1$, and moderate aspect ratio $AR = 2$ are considered. Stereoscopic particle image velocimetry (SPIV) is employed to determine the flow patterns on defined planes and, by means of reconstruction, throughout entire volumes. Images including Q-criterion, spanwise vorticity, spanwise velocity, downwash velocity, tangential velocity, vorticity flux and helical density are employed to represent the flow structure. These quantities are represented both with iso-surfaces, and on sectional slices along the span.

The flow structure on a low aspect ratio wing is characterized for a range of radius of gyration r_g/C, at a travel distance well after the onset of motion. When the radius of gyration is small, the leading-edge, tip and root vortices are highly coherent, with large dimensionless values of Q in the interior regions of all vortices, and large downwash between these components of the vortex system. For increasing radius of gyration, however, the vortex system rapidly degrades, accompanied by loss of large Q within its interior, and downstream displacement of the region of large downwash. These trends are accompanied by increased deflection of the leading-edge vorticity layer away from the surface of the wing, and decreased spanwise velocity and vorticity flux in the

trailing region of the wing, which are associated with the degree of deflection of the tip vortex across the wake region. Radius of gyration also affects development of the sectional flow structure determined at the midspan of the wing. Combinations of large radius of gyration r_g/C and travel distance $r_g\Phi/C$ lead to separated flow patterns, similar to those observed on rectilinear translating wings at high angle of attack. In the extreme case, where the wing travels a distance corresponding to a number of revolutions, the highly coherent flow structure is generally preserved if the radius of gyration is small; it degrades substantially, however, at larger radius of gyration.

The three-dimensional flow structure is also characterized on a moderate aspect ratio wing, at low and moderate radii of gyration, for a range of travel distance. Increase of the radius of gyration reduces the influence of rotation on the flow structure. At small radius of gyration, a coherent leading-edge vortex develops rapidly, then persists over a range of travel distance. At moderate radius of gyration, this leading-edge vortex is replaced by an arch vortex, which develops over a larger travel distance than the leading-edge vortex; it is eventually swept into the wake of the wing. The subsequent vortical structures on the wing are much less coherent, and these structures resemble a separated shear layer typical on a translating wing at high angle of attack α. The foregoing classes of vortical structures are associated with distinctive patterns of helical density, downwash, and tangential velocity.

Taken together, the above results demonstrate the critical influence of radius of gyration on flow structure coherence for a range of wing aspect ratio. When the parameter r_g is small, a coherent vortex system forms rapidly on a rotating wing, and this

vortex system persists as the wing continues to rotate at constant angular velocity. When the parameter r_g is increased to a moderate value, the flow structure development is not as rapid, and coherent vortical structures do not persist as the wing rotates at constant angular velocity.

CHAPTER 1

INTRODUCTION

The study of bio-inspired flight, particularly that of insects, has become a prevalent area of research in recent years. Much of this research has been driven by interest in the development of micro air vehicles (MAVs), and the desire to emulate the performance of biological flyers in the design of these vehicles. Comprehensive reviews of bio-inspired research are given by Sane (2003), Wang (2005), and Shyy *et al.* (2010). In addition, Pines and Bohorquez (2006) relate our understanding of insect flight to practical issues of micro air vehicles. This chapter is divided into sub-sections that respectively: (i) describe the motivation behind recent research of bio-inspired flight; (ii) summarize the results of those studies that are most relevant to the current investigation; (iii) identify issues related to bio-inspired flight that have not been resolved; and (iv) propose objectives for this investigation to address these issues.

1.1 MOTIVATION FOR BIO-INSPIRED RESEARCH

One of the primary motivations behind recent research of bio-inspired flight has been a desire to gain an understanding of the mechanisms that allow flapping animals, particularly animals such as insects and hummingbirds that are capable of steady hover flight, to be such outstanding flyers. Insects have been of particular interest, due to their small size. These flapping animals take flight using unsteady wing kinematics that are much different from the wing motion employed in conventional, fixed-wing aircraft, rotorcraft, and even the kinematics of larger biological flyers. Identification of the aerodynamic mechanisms that result from these kinematics has been a major goal of much of the research into bio-inspired flight. This goal has been augmented recently by efforts to develop micro air vehicles that exploit the same mechanisms used by biological flyers.

Ellington (1984) provided an excellent, all-encompassing investigation of insect flight. This investigation characterized many of the differences between insect flight and the flight of conventional, fixed-wing aircraft and rotorcraft. The morphological parameters and kinematics of wing motion employed by several biological flyers were identified. Insects generally employ flexible, low aspect-ratio wings ($AR < 5$) that flap periodically. In comparison, fixed-wing aircraft and rotorcraft typically employ higher aspect ratio wings or rotors that respectively undergo constant translation and constant rotation; these conventional airfoils do not oscillate. During the wing beat of an insect, the angle of attack α is typically not static; it dynamically changes throughout the motion. This variation of α is facilitated passively, through wing flexibility, as well as actively,

through control by the insect. In contrast, aircraft wings are rigid, and do not typically rely on unsteady variation of α. Another characteristic difference is the oscillatory nature of insect wing motion, compared with the unidirectional nature of conventional wing motion. Finally, insect wings operate at low Reynolds number in the range $10 < Re < 10^4$, which is lower than the range $Re > 10^5$ for conventional, fixed-wing aircraft.

The morphological and kinematic differences between the flight of insects and the flight of conventional aircraft and rotorcraft result in significantly larger aerodynamic forces on insect wings. That is, the lift forces generated per square inch of lifting surface of a periodically-flapping insect wing are greater than the lift forces generated per square inch of a conventional aircraft wing. Several investigators, including Ellington (1984), have used conventional aerodynamic principles to predict performance of insect wings, based on their morphological parameters, and found that the results underestimated the actual lift and drag. Since insect flight is different from conventional flight in numerous ways, it has been difficult for researchers to identify what parametric or kinematic mechanisms account for the most significant differences of lift force. Several flow mechanisms have been proposed to account for this difference, but the contributions of each of these mechanisms to the lift forces on insect wings are heretofore unclarified.

1.1.1 MAV design

In addition to the interest of biological researchers in understanding insect flight, a desire for small micro air vehicles (MAVs) has emerged in recent years, which has

increased the interest of engineers in bio-inspired research. This interest for MAVs is widespread, with applications ranging from military reconnaissance to parcel delivery. The characteristics proposed for a MAV, as identified by Pines and Bohorquez (2006), include: no length scale greater than 6 inches, gross weights of 200 grams or less, and flight time greater than 60 minutes.

The earliest MAV prototypes were miniaturized conventional aircraft that employed the same flight characteristics as these much larger vehicles. Figure 1.1, from Pines and Bohorquez (2006), shows photographs of some early MAV designs, and a plot that compares the flight time of each MAV to the weight of that aircraft. Most of the MAVs included in this figure employ fixed wings and conventionally operated propellers or rotors. The aircraft shown are also quite large, and the performance of these vehicles did not meet the design benchmarks necessary for their intended use.

The lack of comprehensive understanding of bio-inspired flight has not stopped several aircraft designers from using bio-mimetic design. Several recent MAV designs have employed bio-mimicry, in an attempt to generate lift and drag similar to insects, *i.e.*, MAV designers have imitated wing geometries and wing kinematics found in biological flight, in the hope that these mimetic designs will offer similar performance to their natural counterparts. An example of a bio-mimetic MAV, which was created in the likeness of a hummingbird, is shown in figure 1.2. This vehicle employs electric motors to generate oscillatory wing motion, similar to a typical flapping flyer. Moreover, the leading-edge of each wing is rigid, and a flexible membrane serves as the wing in order to imitate the wing flexibility seen in biological flyers. This resulted in close mimicry of

the oscillatory wing motion employed by an actual hummingbird, and it offered substantial improvement over the miniaturized aircraft discussed in the previous paragraph (Keennon *et al.* 2012). However, this design, and other bio-mimetic MAVs, still have not achieve all of the desired goals identified by Pines and Bohorquez (2006). In addition, MAVs that employ such intricate bio-mimetic wing kinematics are much more difficult to design and produce, due to the complexity of wing motion.

The incomplete understanding of flow physics in the parametric space where insects operate has challenged potential MAV designers, since they do not have an accurate representation of the aerodynamic mechanisms used by the flapping animals that they are trying to mimic. A greater understanding of the flow physics responsible for the performance advantages of bio-inspired flight would enable MAV designers to simplify designs and improve performance. Specifically, it would be useful to characterize the flow physics on bio-inspired wings. In turn, such knowledge of the physics can lead to parameters and design considerations for MAVs that perform as well as biological flyers. Significant research efforts have been pursued in recent years. Recent investigations are briefly reviewed in section 1.2.

1.2 REVIEW OF BIO-INSPIRED RESEARCH

Research into the flight characteristics and aerodynamic mechanisms employed by insects has been conducted in several ways. Experimental studies have been presented that: (i) recorded the wing motion/kinematics employed by live insects; (ii) determined

the lift and drag forces on live insects and model insect wings, and (iii) visualized the flow around live or model insect wings. Flow visualization has been conducted either qualitatively, using smoke or dye injection, or quantitatively, using particle image velocimetry. Computational studies that computed the flow velocities and forces on insect wings have also been presented.

1.2.1 Flow structure on wings in flapping motion

Investigation of the flow physics and aerodynamic performance of flapping flight at the scale of insects has been conducted using several approaches. Ellington (1984), and Wilmott and Ellington (1997a & b) related insect wing kinematics to aerodynamic force production. Ellington *et al.* (1996) and Bomphrey *et al.* (2006) employed respectively qualitative and quantitative flow visualization to characterize the flow structure along the wings of live insects. The flow structures visualized in these respective studies are shown in figure 1.3. Ellington *et al.* (1996), and Lentink and Dickinson (2009*b*) determined the forces and qualitative flow structure on mechanical models of flapping-wings, which were scaled to match insects. Further investigations employed force measurement (Dickinson *et al.* 1999; Birch and Dickinson, 2001; Poelma *et al.* 2006) and quantitative flow visualization (Birch and Dickinson, 2001; Poelma *et al.* 2006; Lu and Shen, 2008). The computations of Liu *et al.* (1998), Sun and Tang (2001), Aono *et al.* (2007), Kweon and Choi (2010), and Jardin *et al.* (2012) provided insight into the flow structure, largely in concert with the experimental studies described in the foregoing summary. The three

dimensional flow structure on a flapping insect, computed by Aono *et al.* (2007), is shown in figure 1.4.

Ellington (1984) and Dickinson *et al.* (1999), among others, identified several aspects of the flow structure in relation to the wing kinematics of insects; this flow structure has been linked, in turn, to the production of lift. These flow features include: (i) maintenance of flow attachment during wing rotation at high angle of attack α; (ii) additional circulation due to wing pronation and supination; and (iii) capture of shed vorticity during stroke reversal. The latter two mechanisms require respectively angle of attack variation and stroke reversal, and are therefore exclusive to the periodic (flapping) wing motion that occurs in natural fliers. The maintenance of flow attachment during wing rotation, however, has been observed during the portion of the oscillation (flapping) cycle where pure rotation of the wing occurs at high angle of attack α. This motion makes up a significant portion of the flapping cycle of certain insects (Ellington, 1984; Wilmott and Ellington, 1997*a*). This flow attachment improves lift production through an increase in circulation around the wing.

1.2.2 Flow structure on wings in pure rotation

Pure rotation involves rotation of a wing about a fixed axis at constant angular velocity Ω and constant angle of attack α, following acceleration from rest. Dickinson *et al.* (1999) recorded the time history of force production on a finite aspect-ratio wing undergoing pure rotation and compared it to the force production on a two-dimensional

model wing undergoing rectilinear translation (Dickinson and Götz, 1992). They observed peak values of lift and drag coefficients shortly after the onset of motion for both translation and rotation. These peaks were followed by relatively constant lift while the wing moved at constant angular or translational velocity. An excerpt from that investigation is shown in figure 1.5. The time history of force production on a rotating wing is shown in the upper-left of figure 1.5. The early force peak, seen in the figure at approximately t = 0.25 s, has been associated with non-circulatory forces and a phenomenon known as delayed stall by several investigators (Ellington 1984; Dickinson *et al.* 1999; Sane and Dickinson 2001; Hubel and Tropea 2009). After the initial force peak, Dickinson *et al.* (1999) found that the rotating wing produced significantly larger lift and drag coefficients than the two-dimensional, translating wing. Lift and drag polar plots of the rotating (labeled as 3-D steady) and translating (labelled as 2-D steady) wing are shown in the lower-right corner of figure 1.5. This portion of the figure clearly shows significantly larger sustained lift and drag forces on the rotating wing. Usherwood and Ellington (2002*a*), Birch *et al.* (2004), Luo and Sun (2005), Garmann *et al.* (2013), and Harbig *et al.* (2013) also described time histories of aerodynamic force production on wings undergoing pure rotation. They reported results that were similar to Dickinson *et al.* (1999) across a broad range of wing planforms and Reynolds number, although the early force peak was not evident in all investigations (Garmann *et al.* 2013). Lentink and Dickinson (2009*b*) and Garmann *et al.* (2013) compared lift and drag on finite aspect-ratio wings undergoing pure rotation and rectilinear translation. These studies revealed that significantly larger lift and drag were produced when the wing was undergoing pure rotation. While the variation of these forces with time has a generally similar form over

the range of Reynolds number in these investigations, larger magnitude lift and drag coefficients have been associated with larger values of Reynolds number (Birch *et al.* 2004; Lentink and Dickinson, 2009*b*; Garmann *et al.* 2013; Harbig *et al.* 2013).

A number of studies have addressed the flow structure associated with increased lift and drag on rotating wings. Many investigators have documented the existence of a stable leading-edge vortex along a wing undergoing pure rotation, well after the wing reached constant velocity (*e.g.*, Birch *et al.* 2004; Luo and Sun, 2005; Poelma *et al.* 2006; Ansari *et al.* 2009; Lentink and Dickinson, 2009*b*; Kim and Gharib, 2010; Ozen and Rockwell, 2011, Harbig *et al.* 2013, Garmann *et al.* 2013; Carr *et al.* 2013). Figure 1.6 shows results from the quantitative flow imaging of Ozen and Rockwell (2011). In this figure, the components of velocity are represented with color contours, as is the vorticity $\omega C/V_{rg}$, which is a parameter that indicates vortical structures. This figure shows the flow structures on rotating and rectilinearly translating wings well after the onset of wing motion. The horizontal rows at the top of figure 1.6 show the flow structure at the mid span of a rotating wing (top row) and a translating wing (second row). An attached leading-edge vortex is clearly visible on the rotating wing, as seen by the (red) positive vorticity in the upper-right contour plot. In contrast, the vorticity contours on the translating wing (immediately below the rotating wing) show the separated shear layer originating from the leading-edge (red) and trailing-edge (blue) of that wing. At the bottom of figure 1.6, contours of vorticity taken at several spanwise locations are stacked on top of each other, and small magnitude contours are removed. This representation clearly shows that the leading-edge vortex remains close to the wing surface across the

wingspan for the rotating wing (left), and, in contrast, the flow is dominated by separated shear layers across the span of a translating wing. The leading-edge vortex on a rotating wing, which arose from separation at the leading-edge, remained close, or 'attached', to the leading-edge of the wing in all of the foregoing studies. In these studies, this stable leading-edge vortex existed across a broad range of wing planforms and Reynolds number. Similar vortical structures have been observed on models of flapping wings (Ellington *et al.* 1996; Birch and Dickinson, 2001; Jardin *et al.* 2012) and live insects (Ellington *et al.* 1996; Bomphrey *et al.* 2006). In addition to the aforementioned findings, Lentink and Dickinson (2009*a*), Kim and Gharib (2010), Ozen and Rockwell (2011), and Garmann *et al.* (2013) determined the difference between the stable leading-edge vortex on a wing undergoing pure rotation and the flow structure on the same wing undergoing rectilinear translation. As shown in figure 1.6, Ozen and Rockwell (2011) found that the fully-evolved flow structure on a translating wing was dominated by separated shear layers on the leading- and trailing-edges of the wing. Garmann *et al.* (2013) found rectilinear translation resulted in detachment or shedding of the leading-edge vortex shortly after the onset of motion.

Other features of the flow structure on a rotating wing have been identified during steady rotation, well after the onset of wing motion. Near the tip of the wing, the leading-edge vortex connects to the tip vortex that extends into the wake (Poelma *et al.* 2006; Ansari *et al.* 2009; Kim and Gharib, 2010; Ozen and Rockwell, 2012; Garmann *et al.* 2013; Carr *et al.* 2013; Harbig *et al.* 2013). A figure from Kim and Gharib (2010) is reproduced in figure 1.7. In this figure, the (transparent green) spanwise vorticity ω_z iso-

surface highlights the leading-edge vortex, and the (opaque blue) streamwise vorticity ω_x iso-surface highlights the coherent tip vortex. Ozen and Rockwell (2012) and Garmann *et al.* (2013) also observed well-defined vortices near the root of a rotating wing that extended into the wake. The vortical structure in the tip region was less organized or, in some studies, not stably attached (Ansari *et al.* 2009; Lentink and Dickinson, 2009*b*; Jones and Babinsky, 2011; Ozen and Rockwell, 2012; Carr *et al.* 2013). This phenomenon has been linked to larger values of Reynolds number (Lentink and Dickinson, 2009*b*; Garmann *et al.* 2013; Harbig *et al.* 2013) and aspect-ratio $AR = b/C$, where b is the span of the wing and C is the average chord (Carr *et al.* 2013; Harbig *et al.* 2013, Garmann and Visbal, 2014). The studies of Birch *et al.* (2004), Poelma *et al.* (2006), Ansari *et al.* (2009), Kim and Gharib (2010), Ozen and Rockwell (2012), Carr *et al.* (2013), Garmann *et al.* (2013), Harbig *et al.* (2013) found significant spanwise flow and vorticity flux from the root of the wing to its tip. Birch *et al.* (2004) found that the distribution of this spanwise flow was dependent on Reynolds number. Ozen and Rockwell (2012) observed significant downward-oriented flow (downwash) associated with the attached leading-edge vortex and the coherent tip and root vortices.

1.2.3 Time-resolved, volumetric flow structure on wings in pure rotation and rectilinear translation

In addition to the flow structure that occurs during steady rotation well after the onset of wing motion, several investigations have described different stages of the

transient, volumetric flow structure. That is, the three-dimensional flow structure near a rotating wing, as a function of time.

Ozen and Rockwell (2012) observed a stable leading-edge vortex (LEV) at two stages of the flow structure development on an impulsively started rotating wing. Poelma *et al.* (2006), Kim and Gharib (2010), Harbig *et al.* (2013), Carr *et al.* (2013), Garmann *et al.* (2013) and Garmann and Visbal (2014) characterized the temporal development of this leading-edge vortex on an impulsively started rotating wing. A coherent tip vortex was often observed adjacent to the leading-edge vortex. The leading-edge vortex quickly develops to a stable state, *i.e.*, the vortex rapidly attains a size and shape that persists as the wing continues to rotate. The results of Carr *et al.* (2013), which characterized the leading-edge vortex with particle image velocimetry, are shown in figure 1.8. Iso-surfaces of Q-criterion colored with contours of helicity are shown for the flow structure development on an $AR = 2$ wing (first and third horizontal row), and on an $AR = 4$ (second and forth horizontal row) wing. The Q-criterion indicates regions dominated by rotation, and is therefore used to identify vortical structures. A conical leading-edge vortex is evident on both wings, and this vortex persists at all rotation angles Φ. Both Poelma *et al.* (2006) and Jardin *et al.* (2012) observed similar leading-edge vortices on rotating wings undergoing periodic, reciprocatory motion similar to a hovering insect.

Lentink and Dickinson (2009*a* & *b*) related the stability of the leading-edge vortex on a wing in pure rotation to centripetal and Coriolis accelerations. Their conceptual framework indicated that these accelerations enhanced the stable state of the leading-edge vortex. Garmann *et al.* (2013) assessed these accelerations and the spanwise

pressure gradient through computations. Garmann and Visbal (2014) subsequently showed that elimination of the centrifugal force substantially altered development of the flow structure, and decreased the coherence of the leading-edge vortex.

The three-dimensional vortex system arising from a rectilinearly translating wing is markedly different from that on a rotating wing. Garmann *et al.* (2013) characterized the development of an arch-like vortex on an impulsively started, rectilinearly translating wing. The development of this arch vortex can be seen in the second horizontal row of figure 1.9. Garmann and Visbal (2013) also observed an arch vortex on a wing undergoing periodic hover motion. Various forms of arch vortex structures are indicated in the images of impulsively started, rectilinearly translating wings by Taira and Colonius (2009), and Kim and Gharib (2010), and on a rectilinearly translating wing undergoing periodic motion by Jardin *et al.* (2012). The fundamental physics of the arch vortex was first computed and assessed in detail by Visbal (2011), for the case of a heaving wing in the presence of inflow, and was confirmed experimentally on a heaving wing by Visbal *et al.* (2013). Yilmaz and Rockwell (2011) experimentally characterized the structure of the arch vortex on a pitching wing with inflow.

Direct comparisons of the development of the volumetric flow structure on both a rotating wing $r_g = O(1)$ and on a translating wing $r_g = \infty$ are given by Kim and Gharib (2010), Jardin *et al.* (2012), Garmann *et al.* (2013), and Garmann and Visbal (2013). These studies demonstrated that the attached leading-edge vortex and the arch vortex occur respectively on rotating and rectilinearly translating wings. Moreover, the development of the leading-edge vortex was more rapid than the arch vortex. Garmann *et*

al. (2013) found fundamentally different surface pressure distributions on rotating and translating wings. Both results are shown in figure 1.9. In the top two horizontal rows of figure 1.9, iso-surfaces of constant total pressure that resulted from both wing motions are presented. A leading-edge vortex is evident on the rotating wing, and an arch vortex is evident on the translating wing. In the bottom two horizontal rows, the surface pressure on each wing is shown for several travel distances. The magnitudes of pressure coefficient are significantly greater on the rotating wing than on the translating wing. This negative pressure difference accompanied greater lift and drag forces on the rotating wing. For both types of vortical structure, the maximum negative (suction) pressure occurred at the location where each respective vortical structure was closest to the wing. However, significantly larger negative pressure was associated with the leading-edge vortex than with the arch vortex. This distinction of the magnitude of negative pressure is associated with larger lift and drag forces on the rotating wing. In addition, Garmann and Visbal (2013) computed surface pressure distributions and force trends on rotating and rectilinearly translating wings in simulated hover motion; they are similar to those described in the foregoing.

1.2.4 Effect of large travel distance on flow structure

Experimental and computational investigation of the flow structure on a rotating wing has generally been limited to angles of rotation well within its first full revolution, that is, $\Phi < 360°$ where Φ is the angle of rotation measured from the onset of motion. When the wing rotates beyond one full revolution $\Phi > 360°$, it interacts with previously

generated vorticity in its wake while the flow structure continues to relax. Usherwood and Ellington (2002*a*) found, however, that the magnitudes of horizontal and vertical forces generated by a rotating wing did not significantly change from Φ = 180° to Φ = 1,260° (3.5 revolutions). Mayo and Jones (2013) compared sectional patterns of the instantaneous flow structure at angles of rotation Φ = 180° and 540° corresponding to 0.5 and 1.5 revolutions of the flat plate. They observed a minor reduction in the scale of the leading-edge vortex near the root of the wing. At the midspan, an elongated concentration of vorticity adjacent to the leading-edge was present at both 0.5 and 1.5 revolutions of the wing, but it was located closer to the wing at 1.5 revolutions.

1.2.5 Scaling of effects of rotation on flow structure

Identification of the flow mechanisms responsible for a stable leading-edge vortex on rotating wings, a condition associated with enhanced lift, has motivated much of the research in this field. Lentink and Dickinson (2009*a*) defined the mechanisms of stability of the leading-edge vortex in relation to the aerodynamic forces via an analytical framework. Their framework indicates that the force components due to centripetal and Coriolis accelerations in a non-inertial frame of reference fixed to a rotating wing stabilize the flow structure. Garmann and Visbal (2014) found, via high fidelity computations of the flow along a rotating wing, that Coriolis effects do not contribute to an attached, stable leading-edge vortex. Moreover, introduction of a term that cancelled centripetal forces significantly altered the flow structure, thereby causing the leading-edge vortex to break down while the wing rotated at constant angular velocity. The flow

structure development without the centripetal force is shown in figure 1.10. Wojcik and Buchholz (2014) evaluated vorticity transport in the leading-edge vortex and found that annihilation of vorticity was an important factor in leading-edge vortex stability.

The dimensionless magnitudes of the rotational accelerations proposed by Lentink and Dickinson (2009*a*) can be related to the dimensionless Rossby number $Ro = r/C$ where r is a characteristic radial dimension of the wing. Variation of this parameter has been investigated using the following approaches. The first defines the Rossby number as the ratio of the span b of the wing to its chord C, *i.e.*, $Ro = b/C = AR$, and the value of the aspect ratio AR is varied. The second approach defines the Rossby number as the ratio of the radius of gyration r_g of the wing to the chord C of the wing, *i.e.*, $Ro = r_g/C$, and the radius of gyration r_g is varied while the wing aspect ratio AR is held constant. The effect of varying the Rossby number via r_g is shown in figure 1.11. As r_g is increased, the radius of the circle circumscribed by the wingtip is also increased, and the influence of rotation on the flow structure is diminished.

Investigations that describe the effects of aspect ratio AR on the flow structure and forces on a wing undergoing pure rotation include the experiments of Usherwood and Ellington (2002*b*) and Carr *et al.* (2013), and the computations of Luo and Sun (2005), Harbig *et al.* (2013), and Garmann and Visbal (2014). Collectively, these studies have found that at locations beyond the midspan of a rotating wing, where local Rossby number $Ro_{local} = r_{local}/C$ is largest, the leading-edge vortex lifts off the surface of the wing and becomes less coherent. This breakdown is more pronounced on higher aspect-

ratio wings, perhaps due to decreased spanwise vorticity flux on those wings (Carr *et al.* 2013), and is consistent with the vortex separation and shedding found on the outer half-span of rotating wings by Ansari *et al.* (2009) as well as Jones and Babinsky (2011). Harbig *et al.* computed the structure on several aspect ratio wings with bio-inspired planforms. The results of this investigation at three aspect ratios AR = 2.91, 5.10, and 7.28 are shown in figure 1.12. In this figure, the flow structure is visualized with Q-criterion and colored with spanwise vorticity. The lowest aspect ratio wing, shown in the top of figure 1.12, is associated with the most coherent vortical structures. As the aspect ratio is increased, the vortical structures become less coherent. Harbig *et al.* (2013) showed that, for a wing rotating about its root, definition of the Reynolds number based on the tip radius reduced the differences in the flow structure, due to variation of aspect ratio and Reynolds number, to a single scaling parameter $Re_R = v_{tip}R/\nu$, where v_{tip} is the tip velocity of the wing and R is the span of the wing. The effect of variation of the aspect ratio on the aerodynamic forces observed by Usherwood and Ellington (2002*b*), Luo and Sun (2005), and Garmann *et al.* (2013) was small compared to the difference in forces observed between rotating and translating wings by Usherwood and Ellington (2002*b*), Lentink and Dickinson (2009*b*), and Garmann *et al.* (2013). Luo and Sun (2005) observed that, as the aspect ratio of the wing increased, the decrease in lift due to breakdown of the leading-edge vortex balanced an increase in lift due to reduced three-dimensional effects.

Investigation of the effect of Rossby number via variation of the radius of gyration of a fixed wing-planform has been less extensive. Lentink and Dickinson

(2009*b*) showed that increasing the Rossby number led to a decrease in lift and drag coefficients over four values of Rossby number: $Ro = r_{tip}/C = 2.9$, 3.6, 4.4, and ∞ (purely translating wing). Lift-drag polar plots, provided by Lentink and Dickinson (2009*b*), for these different wing configurations are reproduced in figure 1.13. An arrow indicates the decrease in lift and drag forces, as the Rossby number of the wing is increased. The wing at lowest Rossby number produced the largest magnitude aerodynamic forces (largest radius 'circle' on figure 1.13), while the rectilinearly translating wing produced the smallest magnitude aerodynamic forces (smallest radius 'circle' on figure 1.13). Schlueter *et al.* (2014) also found that as the radius of gyration of a rotating wing was increased, the lift and drag approached values corresponding to a translating wing. Increase of the Rossby number by variation of the radius of gyration r_g has an important limit: when the radius of gyration becomes infinitely large, *i.e.*, $r_g/C = Ro = \infty$, the motion of the finite aspect ratio wing approaches rectilinear translation. In other words, a translating wing is equivalent to a rotating wing with infinite radius of gyration, $r_g/C = Ro = \infty$. The aforementioned qualitative and quantitative flow visualization of Lentink and Dickinson (2009*b*), Kim and Gharib (2010), Ozen and Rockwell (2011), and Garmann *et al.* (2013) describes the difference in flow structure at $Ro = O(1)$ (rotating wing) and $Ro = \infty$ (rectilinearly-translating wing).

1.3 UNRESOLVED ISSUES

When considered collectively, the research studies presented above have offered significant insight into bio-inspired flight. However, they have not adequately addressed the following issues.

Flow structure at different radii of gyration of a wing. A number of studies have identified the flow structure on two classes of wings: (i) rotating wings where $r_g = O(1)$; and (ii) translating wings where $r_g = \infty$. In addition, when the lift and drag forces on wings at different radii of gyration were characterized, increasing the radius of gyration was found to decrease the lift and drag forces on a rotating wing. Currently, no studies have addressed the quantitative characterization of the flow structure on wings at different, finite radii of gyration. Quantitative determination of the flow near a rotating wing will allow for identification of the different flow structures responsible for the decrease in lift and drag forces, and should offer insight into the parameters responsible for any change in flow physics as a function of radius of gyration.

Structure of leading-edge vortex at large travel distance. Recent investigations have identified the existence of a stable leading-edge vortex on a purely rotating wing. This vortex remained attached to the wing through a range of rotation angles $\Phi < 360°$. In addition, the lift and drag on rotating wings remain nearly constant from $\Phi = 180°$ to $\Phi =$ 1,260°. Conversely, the lift on a translating wing is known to attenuate rapidly after an impulsive start, a phenomenon known as delayed stall. Currently, no studies have confirmed the continued existence of the leading-edge vortex on a rotating wing as the

wing continues to rotate through large rotation angles and the flow structure continues to relax, or the transformation of vortical structures on a wing at different radii of gyration.

Flow physics associated with leading-edge vortex stability. The leading-edge vortex on rotating wings has been associated with spanwise flow and spanwise vorticity flux. However, other quantities such as downwash and enhanced helicity may contribute to leading-edge vortex stability. The physics behind stability of the flow structure on rotating wings, in particular the retention of a leading-edge vortical structure, is not adequately understood.

Temporal development of the flow structure with moderate rotational effects. The flow structure development on both rotating and translating wings has been characterized using time resolved results with fine temporal resolution. On these wings, markedly different flow structures were observed: a stable leading-edge vortex was observed on a rotating wing, and an arch vortex was observed on a translating wing. The transformation of development of the flow structure between these extremes, due to reduced rotational effects at larger, finite values of radius of gyration, has not been characterized. This characterization would provide a better understanding of the flow physics that causes such different flow structures and lift forces.

1.4 RESEARCH OBJECTIVES

The objective of the present investigation is to characterize, experimentally, the three-dimensional flow structure on rotating wings at different radii of gyration. The flow

will be quantitatively determined at several stages of development of the flow structure, and the results will be interpreted in terms of vorticity, *Q*-criterion, components of velocity (*u, v,* and *w),* vorticity flux, helicity and streamlines. Both iso-surfaces and sectional slices will be used to represent the flow structure.

More specifically, the current investigation aims to:

- Develop and implement an experimental system to determine the flow structure on a rotating wing. Stereoscopic particle image velocimetry (SPIV) will be employed, with volumetric reconstruction, to determine this flow structure quantitatively.
- Characterize the flow on a rotating wing at multiple radii of gyration to identify the role of rotation on the flow structure near this wing.
- Determine the time-resolved flow structure on a rotating wing using temporal reconstruction, *i.e.*, quantify the volumetric flow structure at several stages of flow development, to characterize the effect of radius of gyration on this development.
- Determine the flow structure on a rotating wing after the wing has rotated through an extremely large rotation angle Φ, when the flow structure has had significant time to relax to a final state.
- Identify flow characteristics such as helicity and downwash velocity that are associated with leading-edge vortex stability on rotating wings.

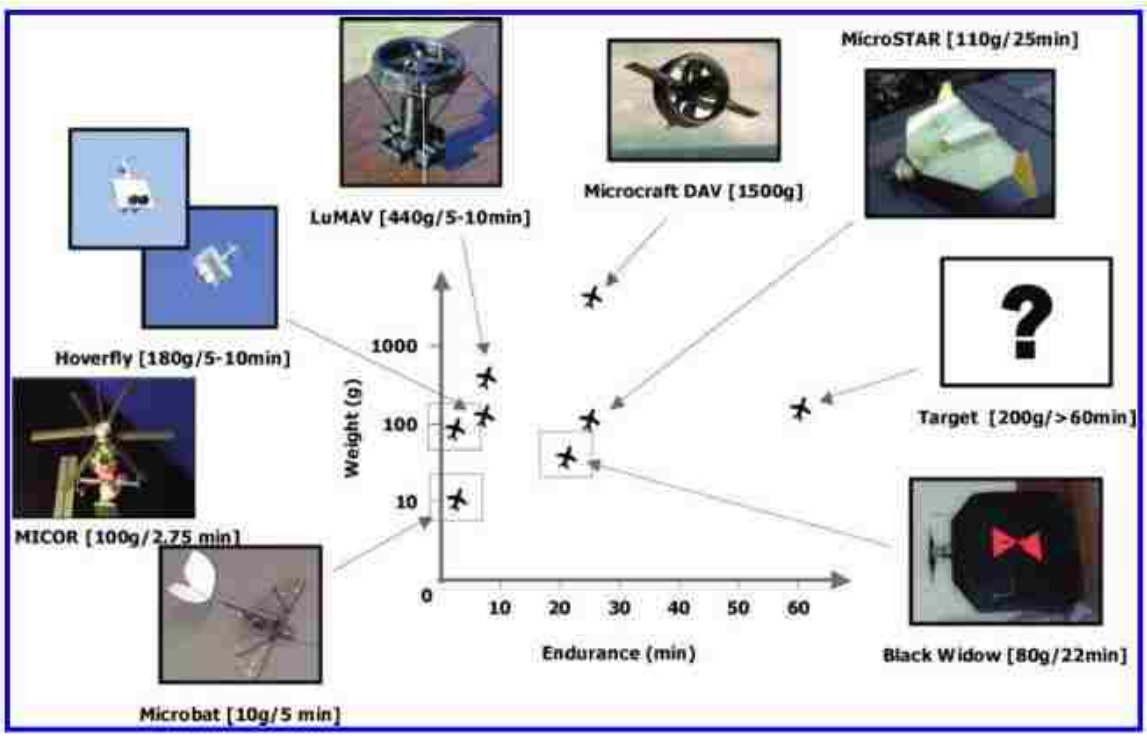

Figure 1.1. Photographs of several early micro air vehicles (MAVs), and performance characteristics of each. (Pines and Bohorquez, 2006).

Figure 1.2. Photograph of DARPA hummingbird MAV. (AeroVironment, 2014).

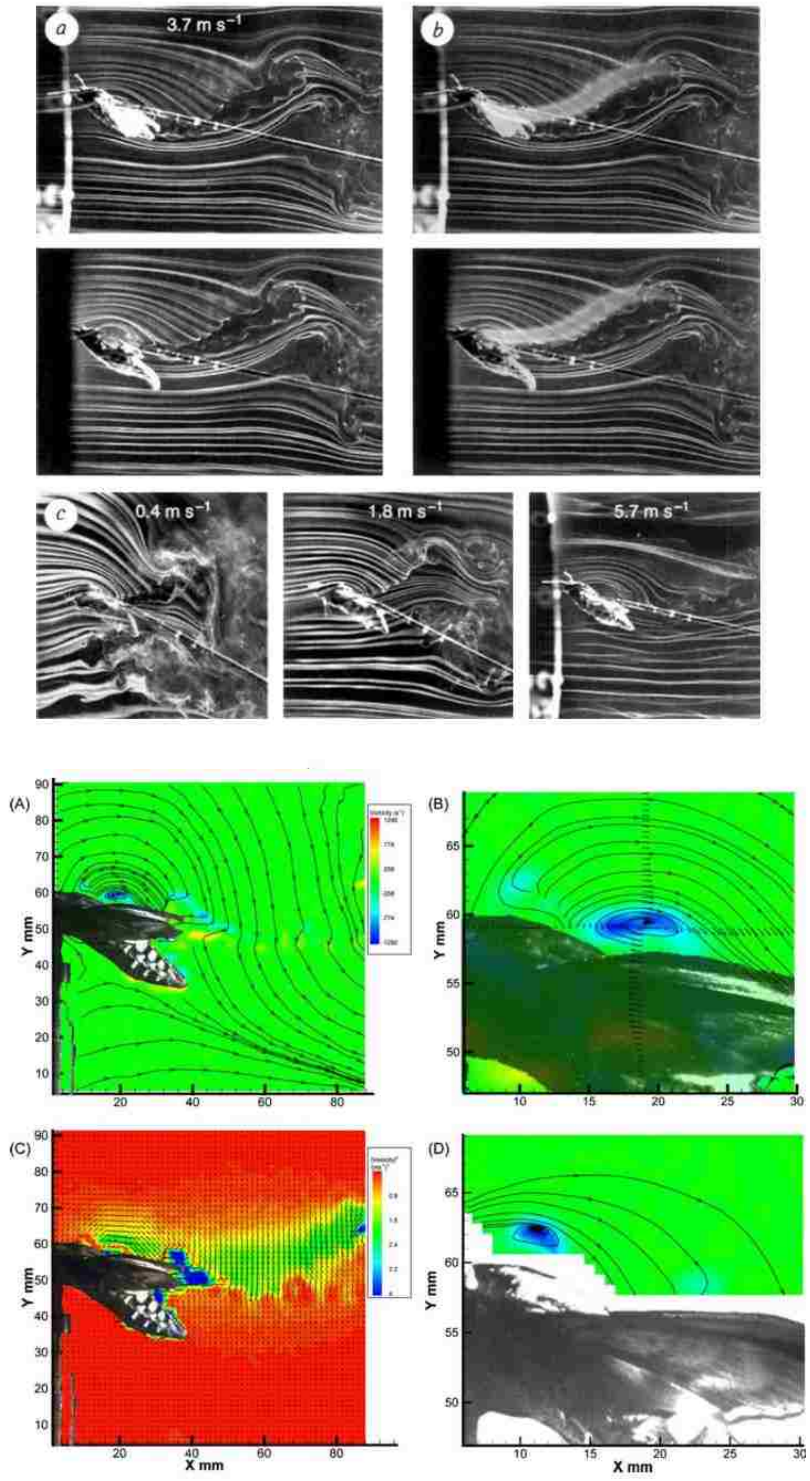

Figure 1.3. Flow structure on live insects. Qualitative visualization of Ellington *et al.* (1996) (top three rows), and quantitative visualization of Bomphrey *et al.* (2006) (bottom two rows).

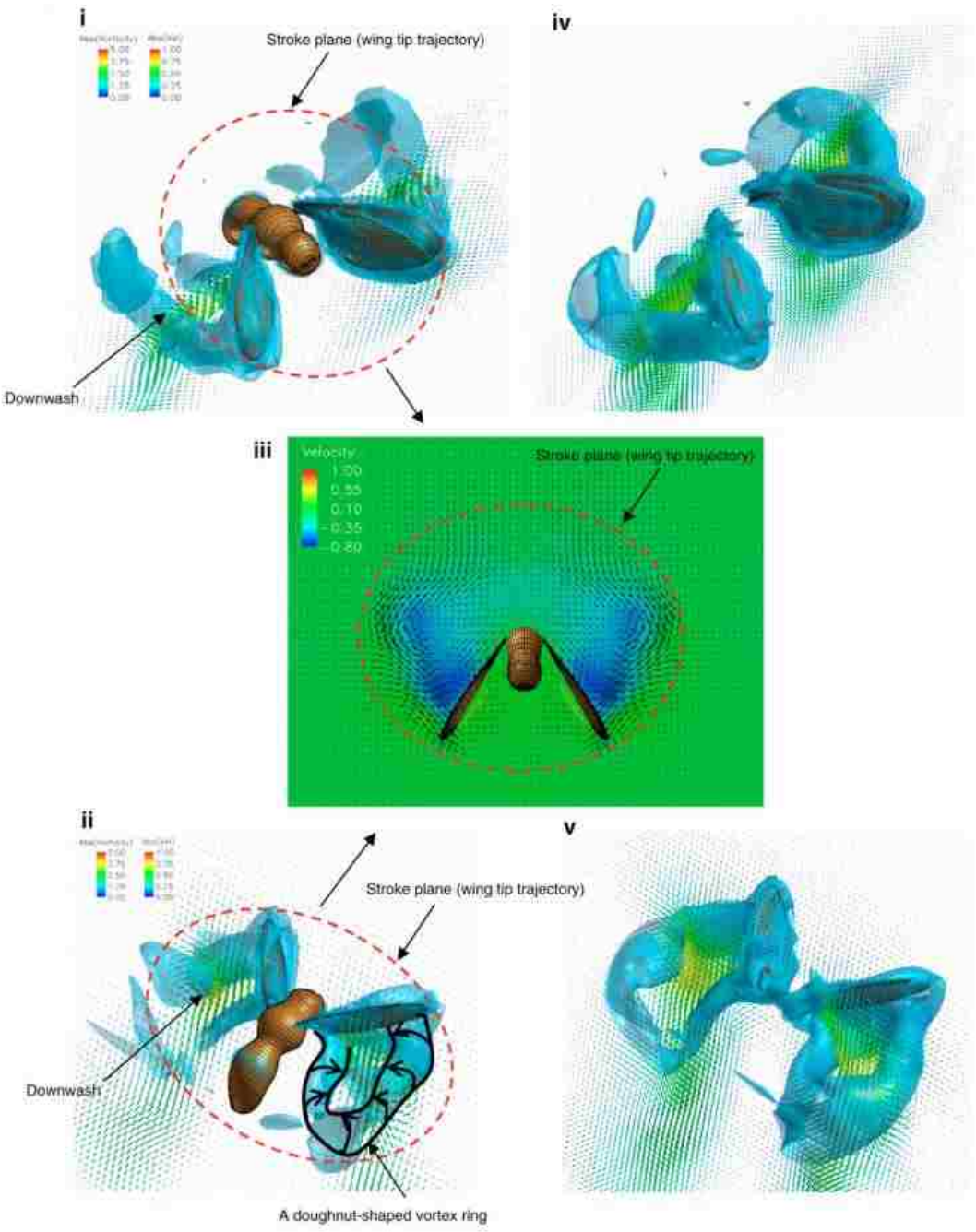

Figure 1.4. Flow structure computed on a flapping insect (Aono *et al.* 2007).

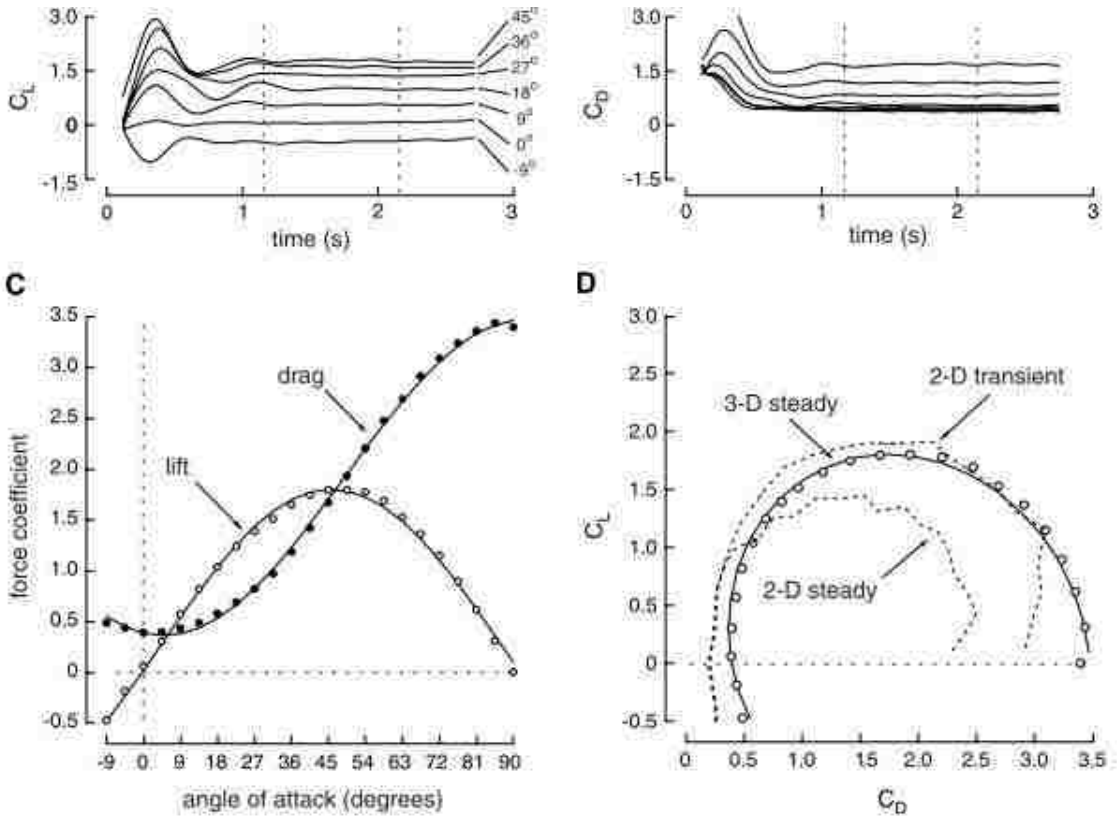

Figure 1.5. Lift and drag forces on purely rotating (3-D) and translating (2-D) wing. (Top-left) time-history of lift on a rotating wing at several angles of attack α. (Bottom-right) Comparison of the lift and drag forces on a rotating wing (3-D steady) to the peak (2-D transient), and sustained (2-D steady) forces on a 2-D translating wing (Dickinson *et al.* 1999).

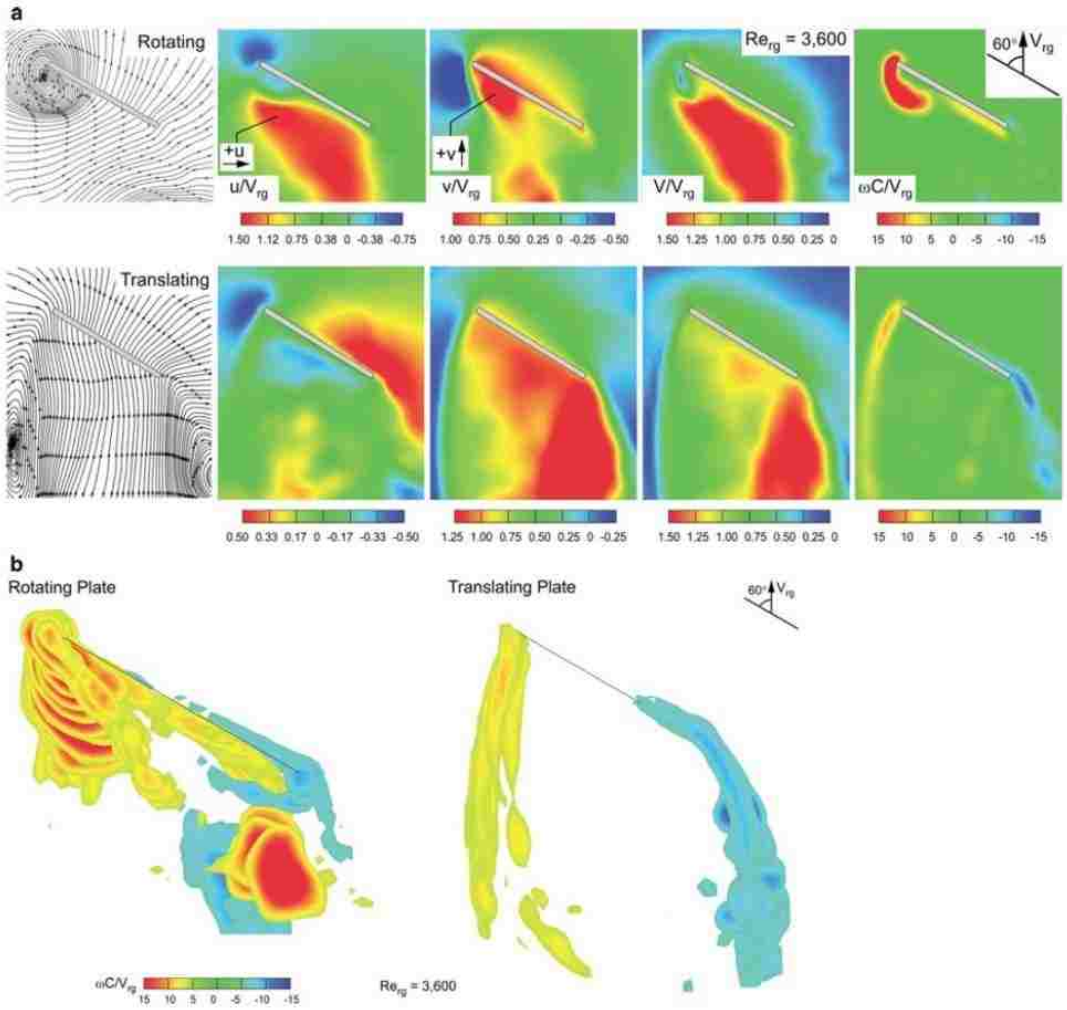

Figure 1.6. Flow structure on rotating and translating wing. (*a*) Streamlines, contours of components of velocity and contours of vorticity at the midspan. (*b*) Stacked contours of vorticity across the span (Ozen and Rockwell, 2011).

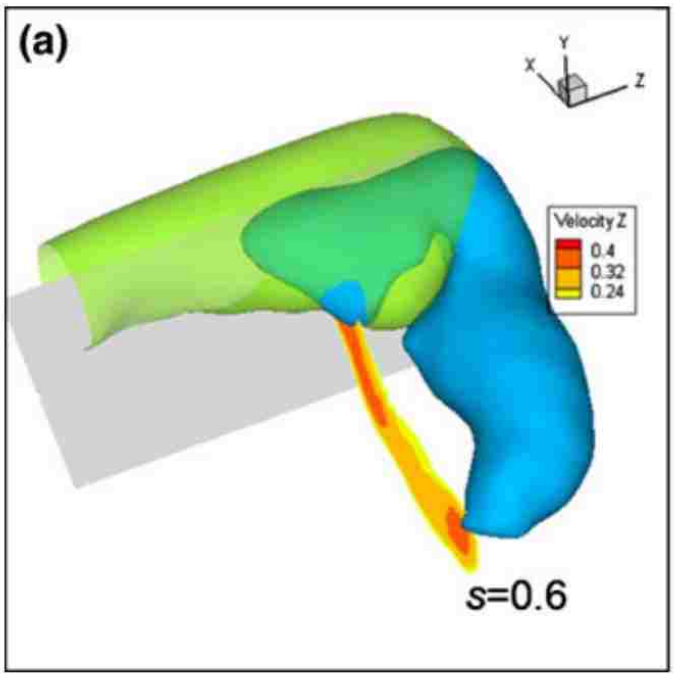

Figure 1.7. Iso-surfaces of spanwise vorticity ω_z (green), and streamwise vorticity ω_x (blue) on a rotating wing (Kim and Gharib, 2010).

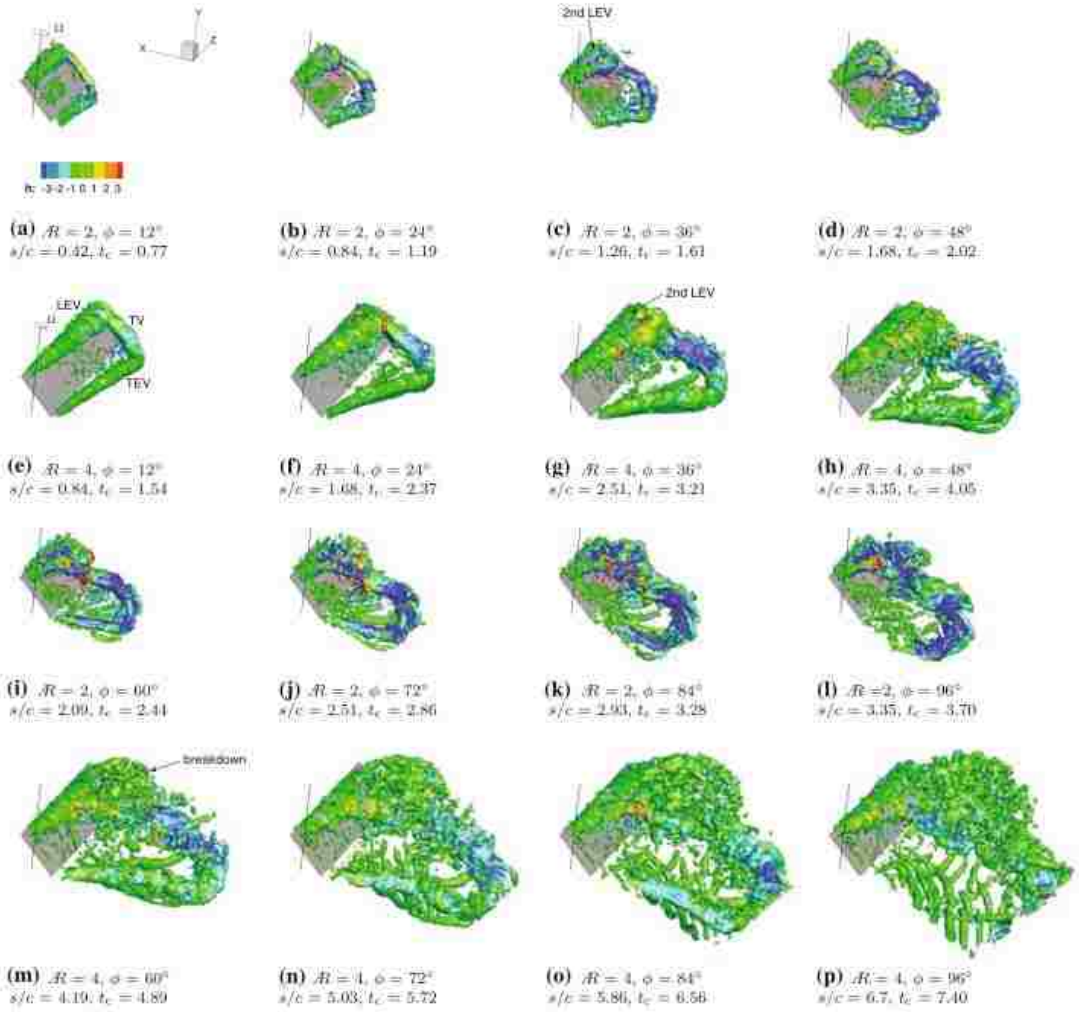

Figure 1.8. Flow structure visualized with iso-surfaces of *Q*-criterion, on *AR* = 2 and *AR* = 4 rotating wings, at several rotation angles *Φ* (Carr *et al.* 2013).

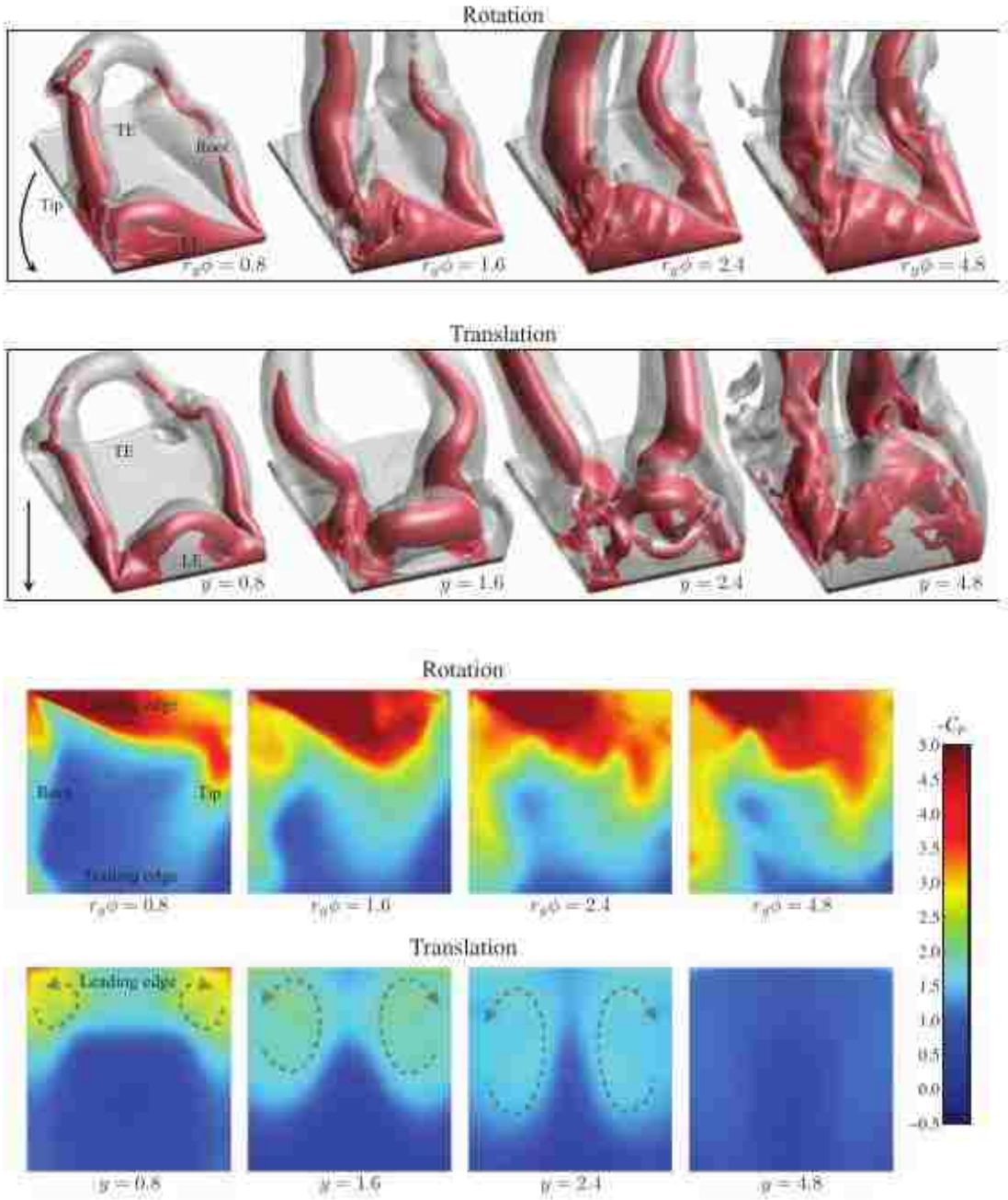

Figure 1.9. (Top two rows) Flow structure development on rotating and translating wing visualized with iso-surfaces of total pressure. (Bottom two rows) Pressure coefficient development on the leeward surface of rotating and translating wings (Garmann *et al.* 2013).

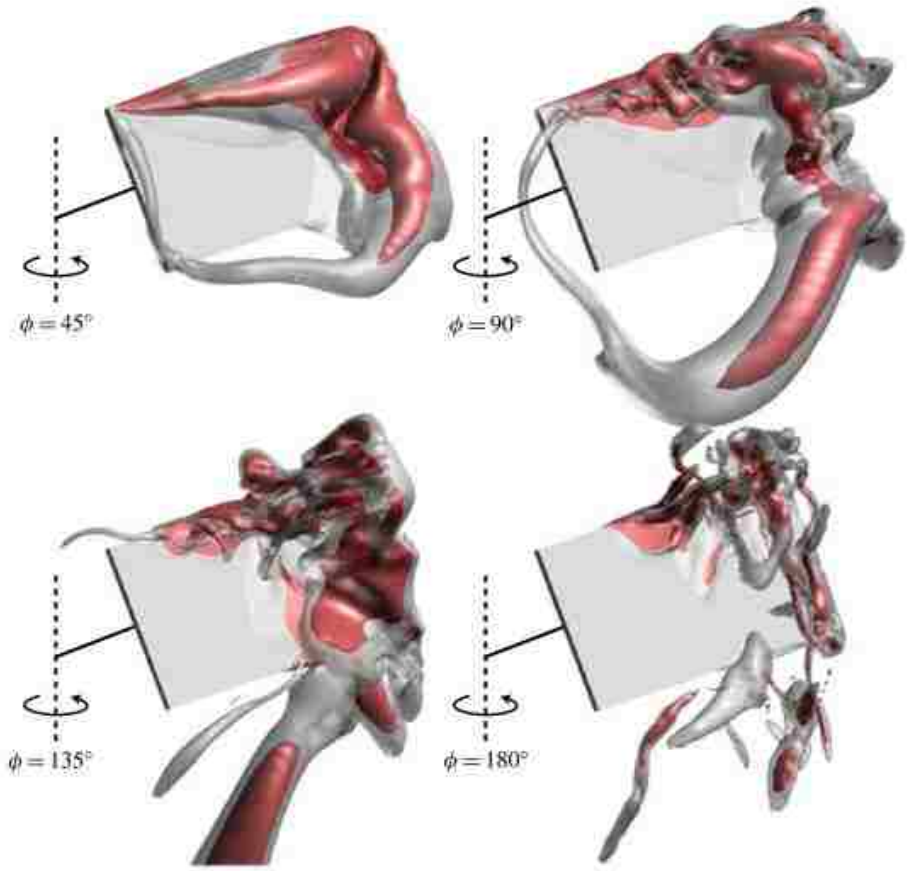

Figure 1.10. Flow structure development on a rotating wing visualized with iso-surfaces of total pressure without centrifugal force (Garmann and Visbal, 2014).

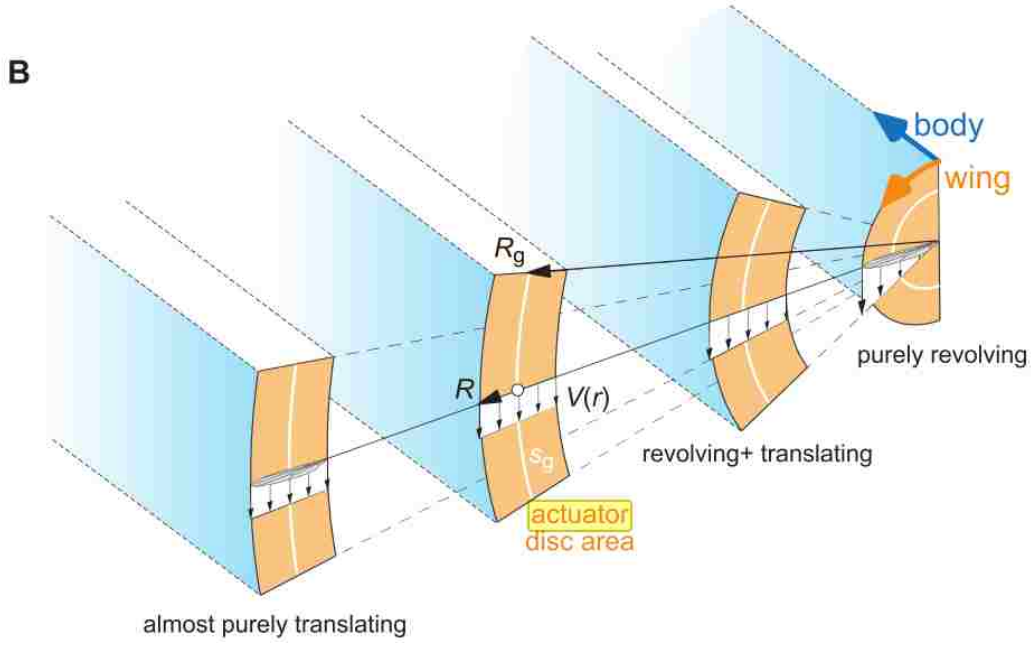

Figure 1.11: Diagram showing the path of a rotating wing at four radii of gyration R_g (Lentink and Dickinson, 2009*a*).

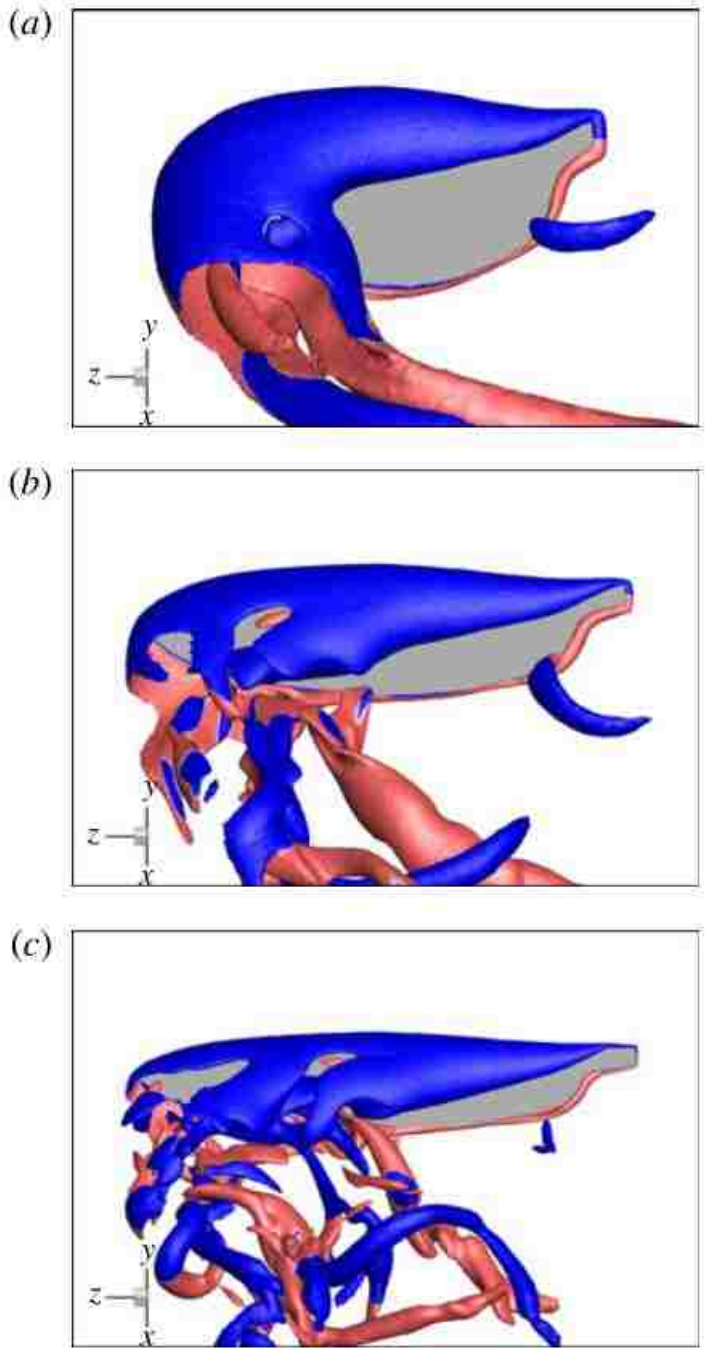

Figure 1.12. Transformation of the flow surface with increasing aspect-ratio. Flow structure visualized with iso-surfaces of *Q*-criterion (Harbig *et al.* 2013).

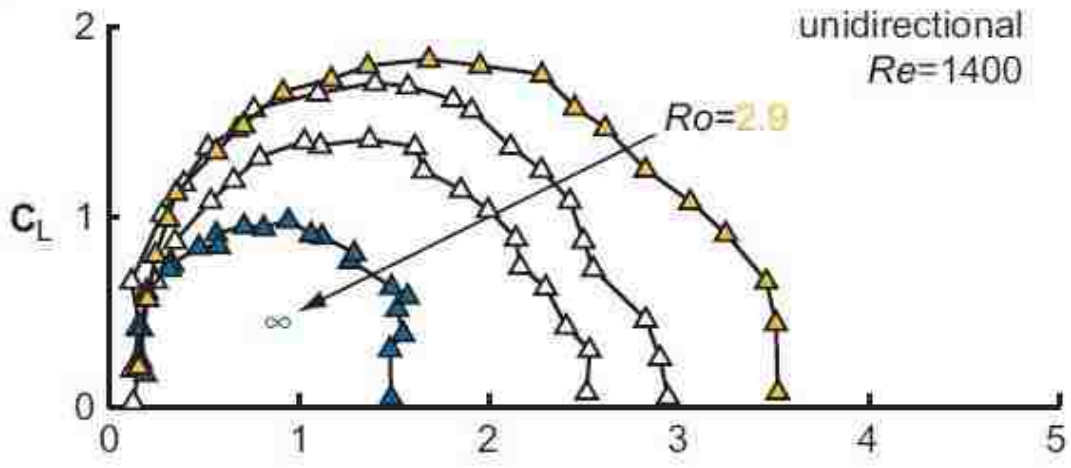

Figure 1.13. Lift and drag forces on a rotating wing at four radii of gyration (Lentink and Dickinson, 2009*b*).

CHAPTER 2

EXPERIMENTAL SYSTEMS AND TECHNIQUES

Experiments were conducted in a large-scale, free surface water channel in the Fluids Lab at Lehigh University. Figure 2.1 shows a photograph of the test facility and experimental system. The investigations discussed herein considered a bio-inspired, low aspect ratio wing undergoing pure rotation. An experimental apparatus was constructed to simulate this motion. Stereoscopic particle image velocimetry (SPIV) was employed to determine the fluid motion generated by the rotating wing. This chapter is divided into sub-sections that respectively describe: (i) the water channel; (ii) the wing parameters, kinematics, and motion control; (iii) the quantitative flow-imaging technique used to determine flow patterns; and (iv) the uncertainty associated with the quantitative imaging technique.

2.1 WATER CHANNEL

The channel consisted of transparent, Plexiglass walls that allowed for visualization of the flow through these walls. The test section had dimensions of 5,435 mm length, 613 mm width, and 594 mm height. This section was filled with water, filtered with four 5 μm filters, and the water temperature was maintained at 24°C. The channel was filled to a depth of 508 mm for experiments. A large recirculation pump in the test facility was capable of producing inflow, but no inflow velocity was employed in the experiments presented herein, *i.e.*, all experimental results presented in this investigation were performed in initially quiescent water. Since no inflow velocity was employed, removable Plexiglass panels, which served to block fluid movement in-to and out-of of the test section, were installed at the upstream and downstream ends of the test section. These panels helped maintain seeding-particle density during flow visualization experiments by limiting the exchange of fluid between the test section and the large reservoirs seen in figure 2.1.

2.2 WING PARAMETERS AND MOTION

An experimental apparatus was constructed to control the wing kinematics and positioning during experiments. The system consisted of: (i) a traverse system with three degrees of freedom that allowed precise control of wing motion during experiments; (ii) several wing geometries, with various means of attaching them to the rotating shaft, which enabled variation of specific parameters relevant to the investigations presented in

this report; and (iii) a digital motion control system, with three computer-controlled motors, that allowed for precise control of wing positioning and motion.

2.2.1 Motion axes

Figure 2.2 shows an isometric view of the three-axis traverse system that was constructed for this research. A wing was mounted to the vertically-oriented brass rod. The cylindrical, vertical rod had a diameter of 12.7 mm and a length of 622 mm. The traverse system was capable of moving the rod in three ways: (i) linear motion in the vertical direction; (ii) linear motion in one horizontal direction; and (iii) rotation about the center of the rod. A Daedal 310062AT two-dimensional translation stage provided the linear modes of motion. Two bearings located the brass rod and allowed for the rotational mode of motion. These components are also indicated in figure 2.2.

2.2.2 Motion control

Dual-rod stepper motors were used to drive the wing motion along the axes described above. These motors are shown in figure 2.2. The linear axes were employed to vary the static location of the rotating rod, *i.e.*, the stepper motors powering these axes varied the static position of the brass rod relative to the water channel and flow imaging system. Compumotor model AX-57/102 stepper motors with a resolution of 25,000 steps per revolution were used to control linear motion. When combined with the translation stage, the resolution of linear motion was 1969 steps per millimeter for both axes. A third

Compumotor model AX-57/102 stepper motor with a resolution of 25,000 steps per revolution was connected to the vertical rod through a series of three rubber timing belts, resulting in an overall drive-ratio of stepper motor rotation to vertical rod rotation of 18:1. This corresponded to 450,000 steps per revolution of the brass rod. The timing belt system served to damp any vibrations induced by the incremental nature of stepper motor rotation.

All three stepper motors were controlled by Compumotor micro-stepper drives connected to a National Instruments UMI-7764 control box. An ACCU-CODER 755A encoder was installed on the stepper motor that drove rotational motion. Using the encoder, the control box was able to monitor the accuracy of motion execution during wing rotation in a closed loop. Wing motion was executed within 100 steps (0.1° of vertical rod rotation) of the prescribed motion. A desktop PC using National Instruments software generated and executed wing motion through control of the stepper motors. This PC also generated a 5V triggering signal that was sent to the particle image velocimetry (PIV) system via a National Instruments BNC-2110 BNC connector array. Triggering was used to synchronize flow visualization with wing motion.

2.2.3 Wing parameters

As shown in figure 2.2, a smaller brass rod connected the vertical rod to the midchord of the wing. This connecting rod had a diameter 2.3 mm. All wings had a constant thickness of 2.3 mm and were not cambered. These wings were machined from a

clear sheet of acrylic. All of the wings employed had a rectangular planform with sharp edges. After machining, the machined sides of the wing were sanded to remove burrs, and polished so that the sides of the wing were clear. Wings had a chord C = 25.4 mm and spans b = 28.6 mm, 50.8, 127.0 mm yielding respective aspect ratios $AR = b/C$ = 1.1, 2.0, and 5.0. The thickness to chord ratio of all wings was t_w/C = .09.

Several wing configurations were investigated. Figure 2.3 shows a plan view schematic of the rotating rod and each of these wing configurations. Chapters 3 and Chapter 4 focus on the investigation of wings at different radii of gyration r_g. The radius of gyration was calculated with the following equation (Ellington, 1984; Lentink and Dickinson, 2009*b*):

$$r_g = \sqrt{\frac{1}{S}\int_0^R r^2\, c(r)\, dr} \qquad (2.1)$$

In equation 2.1, S is the planform area of the wing, R is the distance from the center of rotation to the wing tip, $c(r)$ is the chord of the wing as a function of distance from the center of rotation (constant in this investigation), and r is distance from the center of the wing to any location along the span, which is the integrating variable dr. The value of r_g was varied for each wing by adding extension rods to the support rod that connected the wing to the vertical rod. Extension rods all had a diameter of 6.4 mm. As shown in figure 2.3, four radii of gyration were investigated with the aspect ratio AR = 1.1 wing, and two radii of gyration were investigated with the aspect ratio AR = 2.0 wing. The angle of

attack of the wing was set to α = 45° for all experiments; the angle of attack was static, *i.e.*, it did not change during wing motion.

2.2.4 Wing kinematics

The flow structure was investigated after acceleration of the wing from rest in quiescent water. After the initial acceleration, the wing rotated at constant velocity to a specified rotation angle, at which time it decelerated to a resting (non-moving) state. These periods of acceleration and deceleration were made as short as possible without inducing vibration in the motion control components. Therefore, the motion simulated an impulsive start and stop of the wing. Figure 2.4 shows a line plot of wing rotation $r_g\Phi/C$ as a function of time. Here, Φ is the angle between the initial and current location of the wing; Φ is given in radians. The motion profile employed was previously implemented by Ozen (2013), and Yilmaz (2012), who adapted it from Eldredge *et al.* (2009). It is described by the function:

$$\Phi(t) = \Phi_{max} \frac{\ln[\cosh(a(t-t_1))\cosh(a(t-t_4))\mathrm{sech}(a(t-t_2))\mathrm{sech}(a(t-t_3)]}{\max(\ln[\cosh(a(t-t_1))\cosh(a(t-t_4))\mathrm{sech}(a(t-t_2))\mathrm{sech}(a(t-t_3)])} \quad (2.2)$$

The parameter a is a smoothing parameter. An increase in the value of a increased the rates of acceleration and deceleration of the wing. Parameters t_1, t_2, t_3, and t_4 adjust the timing of the acceleration and deceleration of the motion.

Development of the flow around the rotating wing was characterized as a function of the length of the arc representing the path of the radius of gyration; it is defined as the travel distance $r_g\Phi/C$. Lentink and Dickinson (2009*a* & *b*) describe advantages of using this parameter. When $r_g\Phi/C$ is used, instead of, for example, Φ, to characterize the flow structure, the actuator disc area swept by the wing is constant for all radii of gyration. Lentink and Dickinson (2009*a*) provide a diagram that illustrates the actuator disc area at different radii of gyration, which is reproduced in figure 2.5. In this figure, a wing at four radii of gyration is shown. The orange area, which is the area swept by the rotating wing, is constant. If the rotation angle Φ were used instead of $r_g\Phi/C$, a wing at a large radius of gyration would travel through a larger arc, and therefore sweep a larger actuator disk than a wing at a smaller radius of gyration, resulting in a different stage of development of the flow structure.

This investigation was not focused on identifying the effects of different acceleration and deceleration profiles on the flow structure. Therefore, the parameters of the function above were adjusted such that the smoothed acceleration and deceleration periods, at the radius of gyration r_g, were identical for all radii of gyration investigated, *i.e.*, the distance travelled along the arc described in the foregoing as a function of time $r_g\Phi/C = f(t)$ was identical for all experiments.

2.3 QUANTITATIVE FLOW IMAGING

Stereoscopic particle-image velocimetry (PIV) was employed to characterize the flow along the rotating wing described in section 2.2. Traditional, monoscopic PIV determines the velocity of fluid in a plane. In PIV, tracer particles seeded in a fluid are illuminated with a laser sheet and photographed at two instants in time. The images are divided into interrogation windows, according to a rectangular grid, and a frame-to-frame cross correlation algorithm is used to determine the average particle displacement in each interrogation window between the two images. The average fluid velocity in each of these windows is then estimated from the average displacement and the difference in time between image acquisitions, according to the following equation (Adrian and Westerweel, 2011):

$$\left(v_{px}, v_{py}\right) \approx \frac{\left(\Delta x_p, \ \Delta y_p\right)}{\Delta t} \qquad (2.3)$$

In equation 2.3, Δx_p and Δy_p are displacements of a particle in the x and y directions, and v_{px} and v_{py} are the respective velocity components of the particle. Monoscopic PIV analysis therefore results in a two-dimensional grid or field of velocity vectors, or vector-field, one from each interrogation window. In stereoscopic PIV, the same analysis is conducted, except that two cameras photograph the illuminated particles from different perspectives. The vector-fields generated by each camera are then mapped onto the laser plane, which, along with knowledge of the orientations of the cameras relative to the laser plane, allows determination of all three components of velocity.

Both monoscopic and stereoscopic PIV have been used to evaluate a wide range of flows, since the introduction of the technique by Adrian (1984). Adrian and Westerweel (2011) provide the most recent, thorough description of PIV analysis. Their review includes practical considerations for the design and implementation of a PIV system. Stereoscopic particle image velocimetry was employed for all experiments in this investigation.

2.3.1 PIV system components

Figure 2.6 shows a schematic of the PIV system used to conduct the present experiments. A New Wave Solo III laser generated light pulses to illuminate particles. The laser employed a dual-pulsed Nd:YAG crystal to generate cylindrical laser pulses, with maximum output energy of 120 mJ at a wavelength of 532 nm (green light). The output pulses generated by the laser passed through two lenses: (i) a cylindrical lens with a focal length of -50 mm; and (ii) a spherical lens with a focal length of 1000 mm. The lens arrangement converted the output pulses into a laser sheet with a beam waist, *i.e.*, minimum laser-sheet thickness, that was approximately level with the vertical position of the wing. At the beam waist, the laser sheet had a thickness of between 0.8 and 1.2 mm. The laser sheet was oriented vertically and aligned parallel to the walls of the water channel. The error in vertical alignment of the laser sheet was less than 0.2°, and the error in alignment of the laser sheet parallel to the walls of the water channel was less than 0.8°. Laser pulses were generated in pairs for PIV at a rate of 15 Hz, *i.e.*, 30 pulses were generated per second, and each pair of pulses was used to generate one set of PIV images

to create one three-component vector-field. The exposure time delay Δt, defined as the difference in time between the first and second laser pulse in a pair, was set between 2 and 5 milliseconds, to satisfy the criterion that no particle travel more than ¼ of an interrogation window (Adrian and Westerweel, 2011). The laser light illuminated metallic-coated, hollow, plastic particles that had been seeded in the water channel. Particles were added to the water until the criterion requiring 10-15 particle images per PIV interrogation window was satisfied (Adrian and Westerweel, 2011).

Images of the illuminated particles were captured using two TSI PoweviewPlus 2MP cameras. The cameras captured pairs of images at a rate of 15 Hz, *i.e.*, 30 total images were captured per camera, per second. Images were recorded to a desktop computer using Insight 3G software. These cameras employed charge-coupled-device (CCD) sensor arrays with resolutions of 1600 x 1200 pixels. Nikon lenses, with a focal length of 28 mm, were employed, giving a magnification of between M_O = 0.06 and 0.09, which yielded respective resolutions of particles in the laser sheet of between 7.1 and 12.3 pixels/mm. An asymmetric camera configuration was used, as indicated in the plan view of figure 2.6. One camera viewed the laser sheet ‘straight-on’; the second viewed the laser sheet at an offset angle, *i.e.*, the angle between the vector normal to the light sheet and the vector normal to the lens plane of each camera was 0° (straight-on) and 45° (offset). This asymmetric arrangement was necessitated by the configuration of the motion system. If the cameras were arranged in a symmetric configuration, the motion control system, specifically the vertical rod, would have blocked the area of interest in the flow field. The Scheimpflug condition, described by Prasad (2000), states that if lines

tangent to the image-, lens-, and object-planes meet at a single point, the entire object plane will be in focus. This condition was satisfied by rotating the CCD sensor of the offset camera relative to the lens plane, as shown in figure 2.7.

2.3.2 PIV image processing

Captured images sets from each camera were processed with Insight 3G software. The steps involved in PIV processing are shown in figure 2.8. Initially, each image was divided into 32 pixel x 32 pixel interrogation windows with 50% overlap. The employed interrogation technique resulted in 7,227 vectors for each two-dimensional vector field. Average particle displacements were estimated using cross-correlation: the interrogation windows in the image of the first laser pulse were correlated with the corresponding interrogation windows in the image of the second laser pulse, Δt seconds after the first laser pulse. The Hart correlation algorithm, developed by Hart (1998*a* & *b*), was employed for particle displacement estimation. This algorithm offered faster processing speeds and better sub-pixel estimates of particle displacement than the more traditional Fast Fourier Transform (FFT) correlation method. The increase in processing speed is partially achieved by suppressing background noise below a threshold percentage of the maximum image intensity. The threshold was set to 80% of the maximum intensity. The Hart correlation algorithm required the use of bilinear peak finding. Once average particle displacements were estimated in each interrogation window, first order differencing was used to derive the average velocity in each interrogation window, as described in equation 2.3.

After vector-fields were determined, each vector was then compared with the local median in a 9-vector neighborhood, to remove spurious vectors that resulted from errant particle images or reflections in some interrogation windows. If the two values differed beyond a certain tolerance, the initial vector was removed and replaced with the median. Less than 1% of vectors, generally those very near to the wing, failed the median test. After the neighborhood test, a low-pass filter using a Gaussian weighting function was used with 24 neighbors to smooth each vector. The smoothing kernel σ was set to σ = 0.8.

The final step in processing each image set, which represented the flow field in the laser sheet at a given instant in time, was to map the 2-D vector-fields, generated from the image of each camera, onto the laser plane, to determine all three components of velocity. Prior to experiments, images were taken of a 3-D calibration target, produced by TSI for use with Insight 3G. These images allowed generation of a mapping function for each camera that mapped locations in each digital image to physical locations in the laser plane. Using these mapping functions, all three components of velocity were determined on an evenly spaced grid in the laser plane. Stereo-automapping was also employed to correct for any misalignments during calibration. The resolution of the final two-dimensional grids ranged from approximately 6,000 to 10,000 vectors, depending on the image magnification and stereoscopic calibration.

2.3.3 Volumetric and temporal reconstruction

Images of the particles illuminated by the laser sheet were acquired sequentially, as the wing followed motion prescribed by the kinematics described in section 2.2. Image capture was initiated by a precisely timed trigger signal, generated by the motion control system. The wing-motion/image-capture process was repeated several times under identical, controllable conditions; therefore, several sequences of the flow field development around the rotating wing were recorded. The triggering process ensured that the wing position for each sequence matched the wing position in all other sequences. Accuracy of the image timing was confirmed by checking the wing position between image sequences. The maximum variation in wing tip position was less than 1 mm.

After image capture and PIV processing, vector fields associated with corresponding images in each sequence were averaged to determine the mean flow velocity at each grid location. This process is known as phase-averaging. An averaged vector-field, which is the result of averaging instantaneous vector-fields, is referred to as a phase-averaged vector-field in this report. The first two horizontal rows of figure 2.9 show the steps of the phase-averaging process. Instantaneous vector fields at the midspan of a rotating wing are shown in the first row of this figure. The velocity fields were then averaged at each grid location to generate the phase-averaged vector-field. Phase-averaged vectors-fields are shown in the second row of figure 2.9.

The flow field was visualized using a sectional approach and a volumetric approach. In the first approach, the flow field was determined when wing rotation brought the chord-line of the wing parallel to the laser plane. In this approach, 6 images

were averaged for each set of experimental parameters. The spanwise location of the laser sheet coincided with the midspan of the wing. Since only 6 image sequences were required for a given set of experimental parameters, the sectional approach allowed for rapid consideration of a number of parameters.

In the second approach, flow velocities were reconstructed into a volume of fluid around the rotating wing. To determine volumetric information, phase-averaged, sectional flow fields were determined with the motion control system in different locations relative to the laser plane; this positioning was controlled by the horizontal, linear axis discussed in section 2.2. A set of 9 image sequences was acquired per sectional location. Between sets of image sequence acquisition, the motion system was translated horizontally using the stepper motor, to change the location of the rotating wing relative to the laser sheet precisely. The sectional flow fields at each horizontal location were averaged, as described in the above paragraph, and then reconstructed into a volume. The bottom two horizontal rows of figure 2.9 show this reconstruction process. In the third row of figure 2.9, averaged sectional slices are arranged with the known location of these results. Then, the data is combined into a single volumetric result, shown in the final row of figure 2.9. Volumetric data was determined for most of this investigation, since the flow structures investigated were highly three-dimensional. After volumetric reconstruction, one-dimensional spatial smoothing was applied between these sectional slices. The smoothing function was similar to that used to smooth the data in-plane, which was described in section 2.3.2. Therefore, the volumetric results have been smoothed once in each spatial dimension.

For some experiments, volume data was generated in a sequence to resolve temporal changes in the flow field. Temporal resolution of the sequence was dictated by the 15 Hz imaging rate of the PIV system. The final step in temporal reconstruction was to rotate and interpolate the sequence of volumes, such that the wing location was the same between volumes. Figure 2.10 shows the steps of this rotation process. The top row of figure 2.10 shows the data acquisition as the wing rotates. The volumes in a sequence of image acquisition were separated in time by the imaging rate $\Delta t_{volumes}$ = 0.067 s. Velocity vectors were rotated about the center of the vertical rod, as shown in the second row of figure 2.10. The data were then linearly interpolated onto a fixed grid aligned with the chord and span of the wing, which is shown in the final row of figure 2.10. In the temporally reconstructed experiments, the velocity data was also transformed into a wing-fixed frame of reference, by subtracting the wing velocity from the velocity at each location.

2.3.4 Post processing

All spatial dimensions were normalized with the chord of the wing *C*, and all velocities were normalized with the velocity V_{rg} at the radius of gyration of the wing. Several derived quantities were also used to visualize the fluid movement associated with wing motion. When necessary, first order differencing was used to estimate the first derivatives of flow velocity in each spatial dimension. Derivatives higher than first-order

were not considered. The equations for each of the quantities considered, as well as a brief description, are provided below.

1. **Vorticity.** Vorticity is defined as the curl of the velocity field $\boldsymbol{\omega} = \nabla \times \mathbf{V}$. It represents the rotational or swirling motion of the fluid. The first-order differencing equations for calculating vorticity from velocity are listed below.

$$\omega_x = \frac{\partial w}{\partial y} - \frac{\partial v}{\partial z} = \frac{w(i,j+1,k)-w(i,j-1,k)}{y(i,j+1,k)-y(i,j-1,k)} - \frac{v(i,j,k+1)-v(i,j,k-1)}{z(i,j,k+1)-z(i,j,k-1)} \qquad (2.4)$$

$$\omega_y = \frac{\partial u}{\partial z} - \frac{\partial w}{\partial x} = \frac{u(i,j,k+1)-u(i,j,k-1)}{z(i,j,k+1)-z(i,j,k-1)} - \frac{w(i+1,j,k)-w(i-1,j,k)}{x(i+1,j,k)-x(i-1,j,k)} \qquad (2.5)$$

$$\omega_z = \frac{\partial v}{\partial x} - \frac{\partial u}{\partial y} = \frac{v(i+1,j,k)-v(i-1,j,k)}{x(i-1,j,k)-x(i-1,j,k)} - \frac{u(i,j+1,k)-u(i,j-1,k)}{y(i,j+1,k)-y(i,j-1,k)} \qquad (2.6)$$

2. **Helicity.** Helicity *h* is a scalar, defined as the dot product of the velocity and vorticity vectors.

$$h = \boldsymbol{\omega} \cdot \mathbf{V} = u\omega_x + v\omega_y + w\omega_z \qquad (2.7)$$

Large helicity magnitude indicates regions where large flow velocity ***V*** is aligned with large ***ω***, *i.e.*, the regions of highest magnitude helicity will occur where strong swirling, indicated by ***ω***, is coincident with significant flow velocity.

3. ***Q*-criterion.** The *Q*-criterion represents the contributions of the antisymmetric and symmetric components of the velocity gradient tensor, such that a positive value of the *Q*-criterion indicates regions dominated by rotation.

$$Q = 0.5\left[\Omega_{ij}\Omega_{ij} - S_{ij}S_{ij}\right] = 0.5\left[||\Omega||^2 - ||S||^2\right] \qquad (2.8)$$

2.4 MEASUREMENT UNCERTAINTY

The aim of the PIV technique, described in section 2.3, is to represent the flow structure on a rotating wing accurately. Since the flow on a rotating wing at high angle of attack is highly unsteady, there is significant variability between instantaneous results under identical conditions. In addition, the PIV method itself has inherent uncertainty. Therefore, two forms of uncertainty arise in PIV that must be considered: (i) experimental error in the determination of instantaneous velocity from each set of PIV images; and (ii) variability of the flow field under identical experimental conditions, *i.e.*, run-to-run changes in the velocity field. In the following, the first section estimates the theoretical uncertainty of each PIV vector-field, according to the analysis of Adrian and Westerweel (2011). In the second section, the convergence of PIV is considered using qualitative and quantitative representations of the experimental results.

2.4.1 Theoretical PIV uncertainty

Adrian and Westerweel (2011) assessed the sources of uncertainty inherent to PIV. Their analysis focused on the limit in estimating particle displacements due to the finite nature of digital imaging, *i.e.*, the fact that determination of a particle image location can be no more accurate than the size of a pixel in the camera sensor. The following equation, for the physical size of a particle image on the camera sensor d_τ, was central to their investigation:

$$d_\tau \approx \left(M_o^2 d_p^2 + d_s^2 + d_a^2\right)^{1/2} \qquad (2.9)$$

The image size d_τ is affected by the particle size d_p, the magnification of the system M_o, the finite diameter of a point-source image due to lens aberrations d_a, and the diffraction-limited spot diameter d_s given by:

$$d_s = 2.44(1+M_o)f^{\#}\lambda \qquad (2.10)$$

Here, $f^{\#}$ is the f-number of the lens and λ is the wavelength of the laser light. For these experiments, the smallest particle-image size was d_τ = 11.0 μm. The size of each pixel in the TSI Powerview 2MP cameras was d_r = 7.4 μm, giving a particle image to pixel ratio of d_τ/d_r = 1.5. Adrian and Westerweel (2011) simulated the effect of this quantity in determining the error in PIV analysis. Figure 2.11 shows the results of these simulations.

This figure indicates that the error associated with d_τ/d_r = 1.5 is less than 0.15 pixels. This corresponds to σ_v = 4 mm/s, where σ_v is the single-run, random error of the PIV measurement. In non-dimensional terms, the random error is 8.7% of the velocity at the radius of gyration V_{rg}. Since this figure is the random error of an instantaneous measurement, it decreases with phase-averaging. The random error with 9 phase-averaged vector-fields is $\sigma_{v,9\text{-}avg} = .03V_{rg}$. According to Lawson and Wu (1997), the ratio of out-of-plane velocity error to in-plane velocity error, for the stereo half angle used in this investigation (22.5°), is σ_w/σ_v = 2.41. Therefore the maximum out of plane velocity error due to particle image size is $\sigma_{w,9\text{-}avg} = .07V_{rg}$.

2.4.2 Flow field convergence

In addition to the theoretical uncertainty analysis, the convergence of PIV results was considered. Two hundred sets of PIV images were taken, under identical experimental conditions, to evaluate the change in results, both qualitatively and quantitatively, when the number of averaged vector-fields increases. The images were acquired with the laser sheet at the midspan of an aspect ratio AR = 2 wing at an angle of attack α = 45°, a rotation angle of Φ = 57°, a radius of gyration of r_g = 4.7, and a Reynolds number Re_{rg} = 1400.

Planar, vector fields of velocity and spanwise vorticity were generated for 2 through 200 phase-averages. Figure 2.12 shows contour plots for four cases, an

instantaneous image and images corresponding to 3, 6, and 9 phase-averaged vector fields. These cases are separated into horizontal rows. The vertical columns of figure 2.12 show color contour plots of velocity components *u*, *v*, and *w*, as well as the spanwise vorticity ω_z. A schematic showing the orientation of the coordinate system is also shown; the tangential velocity of the wing is in the positive *x* direction. The instantaneous *u*- and *v*-velocity contour plots are very similar to the plots of those velocity components after 200 phase-averaged vector-fields. More low-level variations are present in the instantaneous contour plots of spanwise velocity *w*. However, the contour plots of *w* for 3, 9, and 200 averages are all very similar. The spanwise vorticity ω_z contours are also similar for the 3, 9, and 200 phase-averaged results, while the instantaneous contours are noticeably different. Overall, the contours of *u*, *v*, *w*, and ω_z are similar across 3, 9, and 200 phase-averaged vector-fields. This indicates that 9 phase-averaged images are adequate for representations of the flow structure.

Convergence of the velocity and vorticity was also evaluated quantitatively. The root-mean-squared (rms) error for the phase-averaged tangential velocity *u* is defined by the equation:

$$u_{rms}(i) = \sqrt{\frac{\sum_1^N (u(i)-u(200))^2}{N}} \qquad (2.11)$$

In equation 2.11, *N* is the number of grid locations in the vector-field, *u(i)* is the *x* component of velocity for *i* phase-averaged vector-fields, and *u(200)* is the u component

of velocity for 200 phase-averaged vector-fields. u_{rms} represents the root-mean-square difference between the u velocity field using i phase-averaged vector-fields and the u velocity field using 200 phase-averaged vector-fields, calculated across the two-dimensional vector grid. The result for u_{rms} therefore contained 200 values, one for each number of phase-averages from 1 (instantaneous data) to 200. Similar equations were used to calculate v_{rms}, w_{rms}, and ω_{zrms}.

Root-mean-square values determined from equation 2.11 are plotted against the number of phase-averaged vector-fields in figure 2.13. The velocity components are normalized by velocity at the radius of gyration $V_{rg.}$ Spanwise vorticity is normalized by $10V_{rg}/C$, which is a typically significant value. All four quantities are initially less than 0.1, *i.e.*, the rms error between an instantaneous vector-field and the vector-field generated with 200 phase-averaged vector-fields is less than 10%. With 9 phase-averages, the rms error in determining u, w, and ω_z is less than 4%; it is approximately 6.5% for v. The additional error in v is likely a result of the shed vortex, because the x location of this vortex is highly variable from run-to-run.

To ensure that the error quantities determined from equation 2.11 are consistent, the 200 instantaneous vector-fields were divided into 21 sets of 9 instantaneous vector-fields. These sets of 9 were averaged and compared with the 200-average field, using the rms formulation of equation 2.11. The results of this analysis are plotted in figure 2.14. The horizontal axis represents the n^{th} set of 9 averages, from 1 through 21. The error in

velocity and vorticity fluctuates between approximately 2% and 7%. The maximum rms error occurs at n = 1 (for v velocity) and n = 14 (for w velocity). It is approximately 7% of the radius of gyration velocity V_{rg} for both cases. Therefore, the upper-limit of possible error in a 9 phase-averaged vector-field, due to both flow variability and random PIV uncertainty, is approximately 7% of the radius of gyration velocity.

The qualitative change of the flow structure due to phase-averaging was also extended to three dimensions, as shown in figure 2.15. The volumes shown therein were imaged using an aspect ratio AR = 2 wing at α = 45° and a value of Reynolds number Re_{rg} = 1400. Transparent iso-surfaces of the Q-criterion Q = 2, 7, and 15 are represented by progressively darker colors. This sequence of colors indicates regions with increasing dominance of rotation $\|\Omega\|^2$ over irrotational strain $\|S\|^2$, and is used in chapters 3 and 4 to identify vortical structures in the flow. Four different cases are shown: an instantaneous image, and images corresponding to 3, 6, and 9 phase-averages. The volumetric results constructed from the instantaneous, planar data are noisy and less organized, which is expected given the high degree of run-to-run variability. However, the averages of 3, 6, and 9 images are very similar. 9 phase-averaged velocity-fields appear to adequately represent the three dimensional volume, *i.e.*, as of 9 phase-averages, the flow structure does not change with additional averaging.

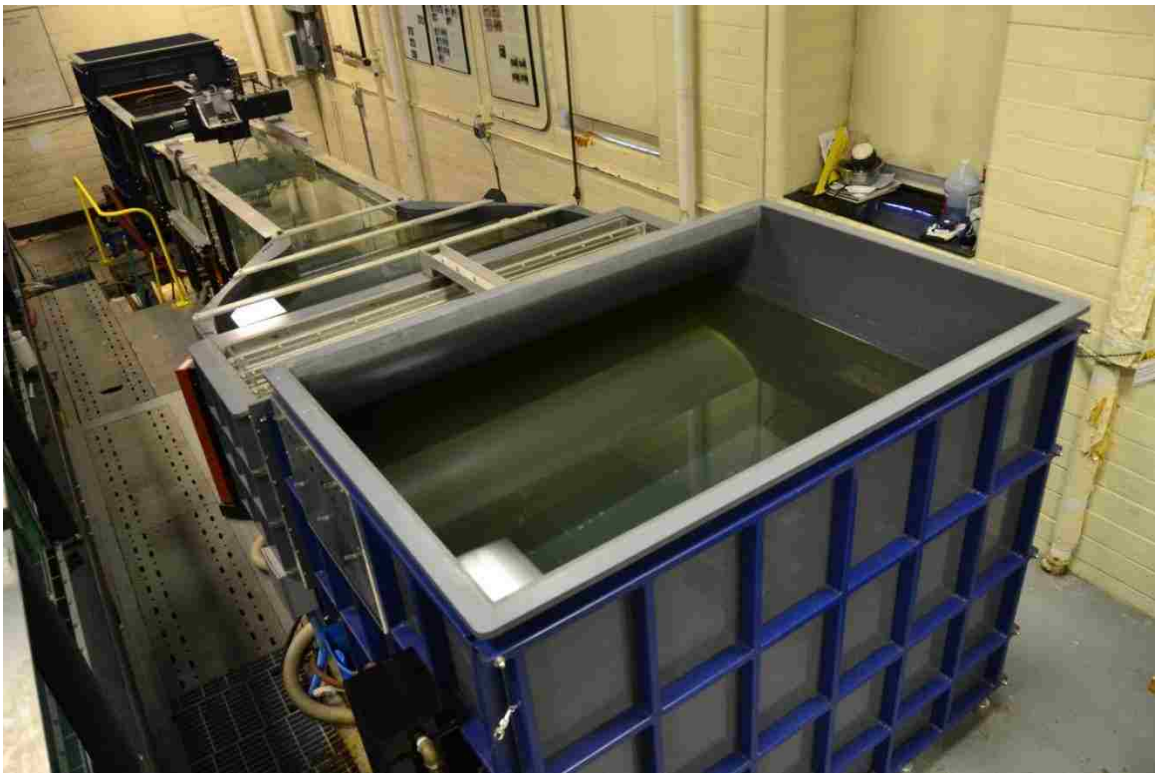

Figure 2.1: Photograph of experimental facility.

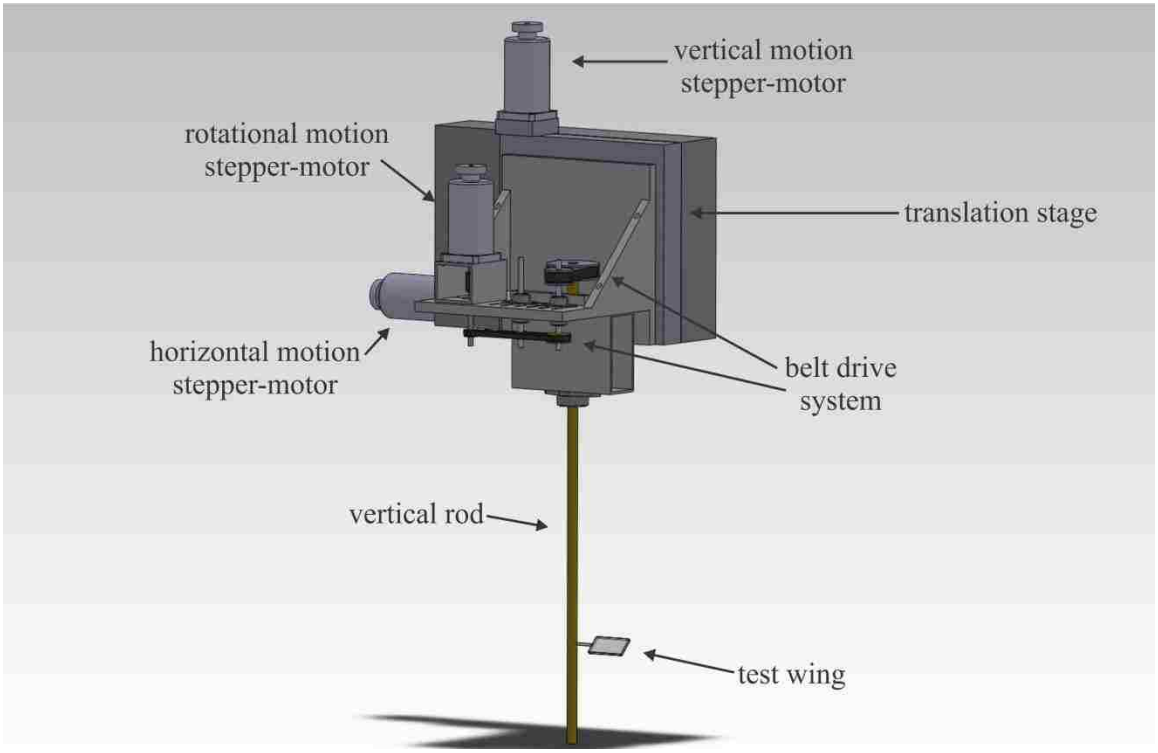

Figure 2.2: Trimetric diagram of motion control system.

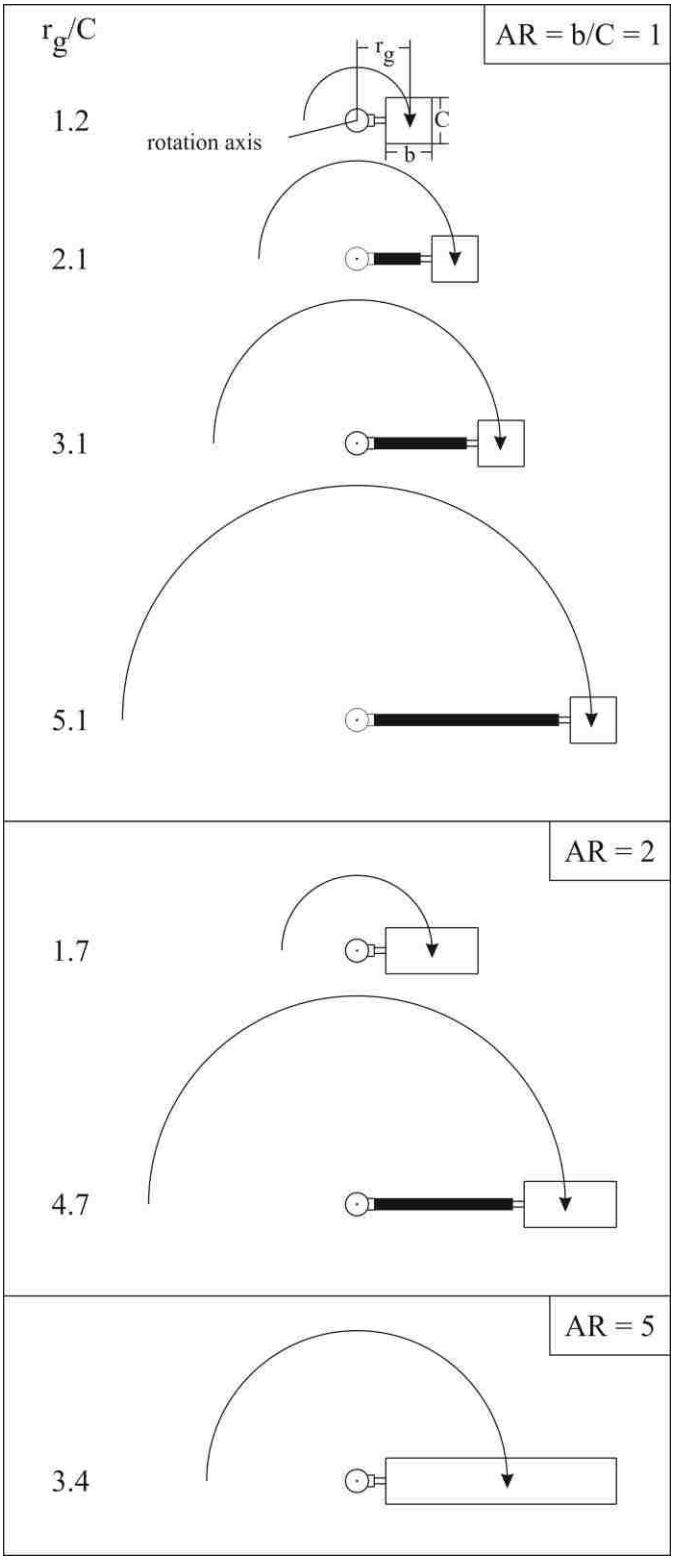

Figure 2.3: Plan view schematic of wing configurations. Arcs indicate path of the radius of gyration.

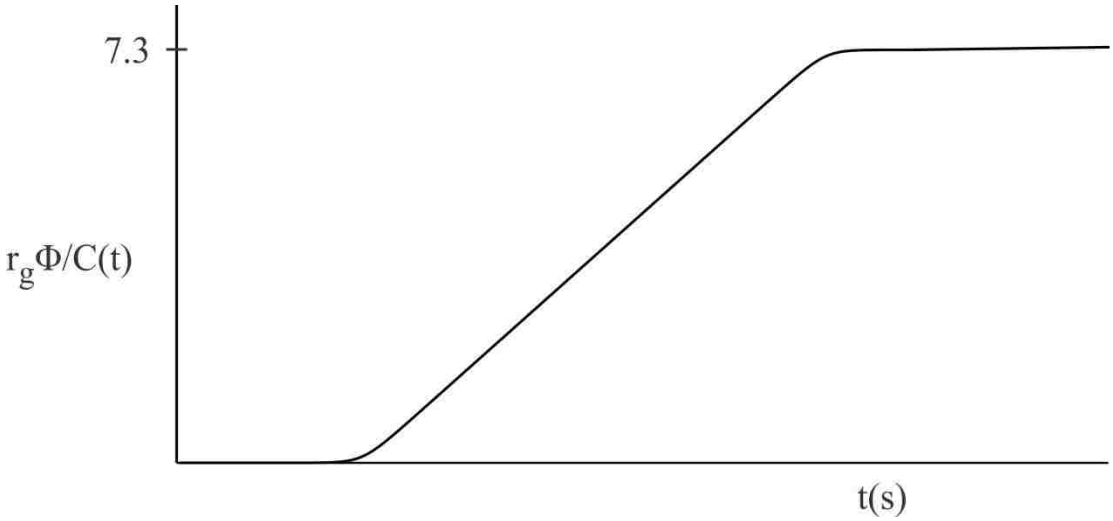

Figure 2.4: Motion profile showing the distance travelled at the radius of gyration as a function of time.

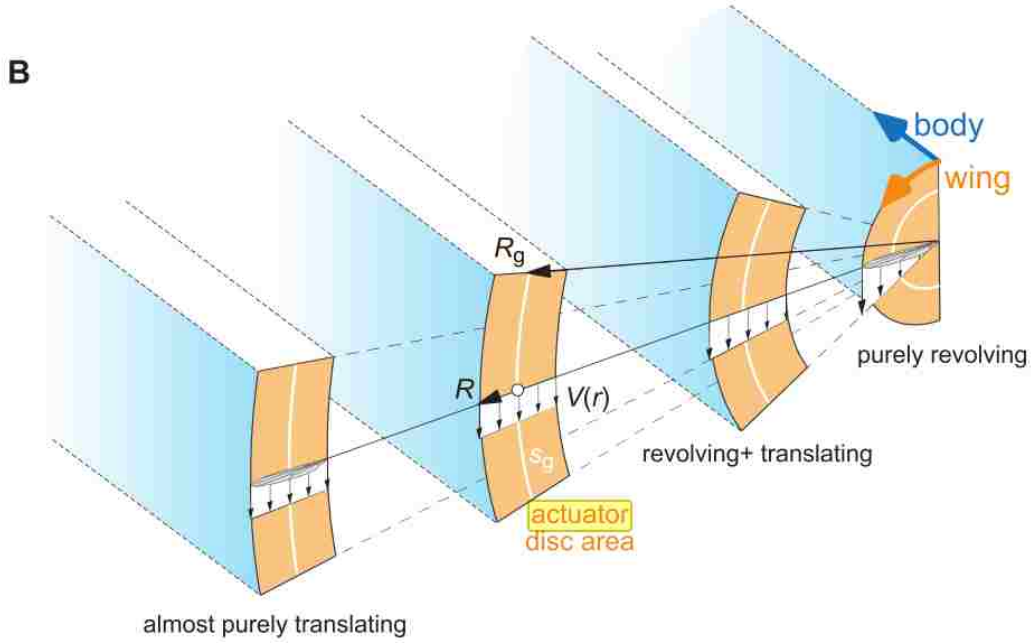

Figure 2.5: Explanation of actuator disk area for different radii of gyration. The area of the orange region is constant when $r_g\Phi/C$ is constant. (Lentink and Dickinson, 2009*a*)

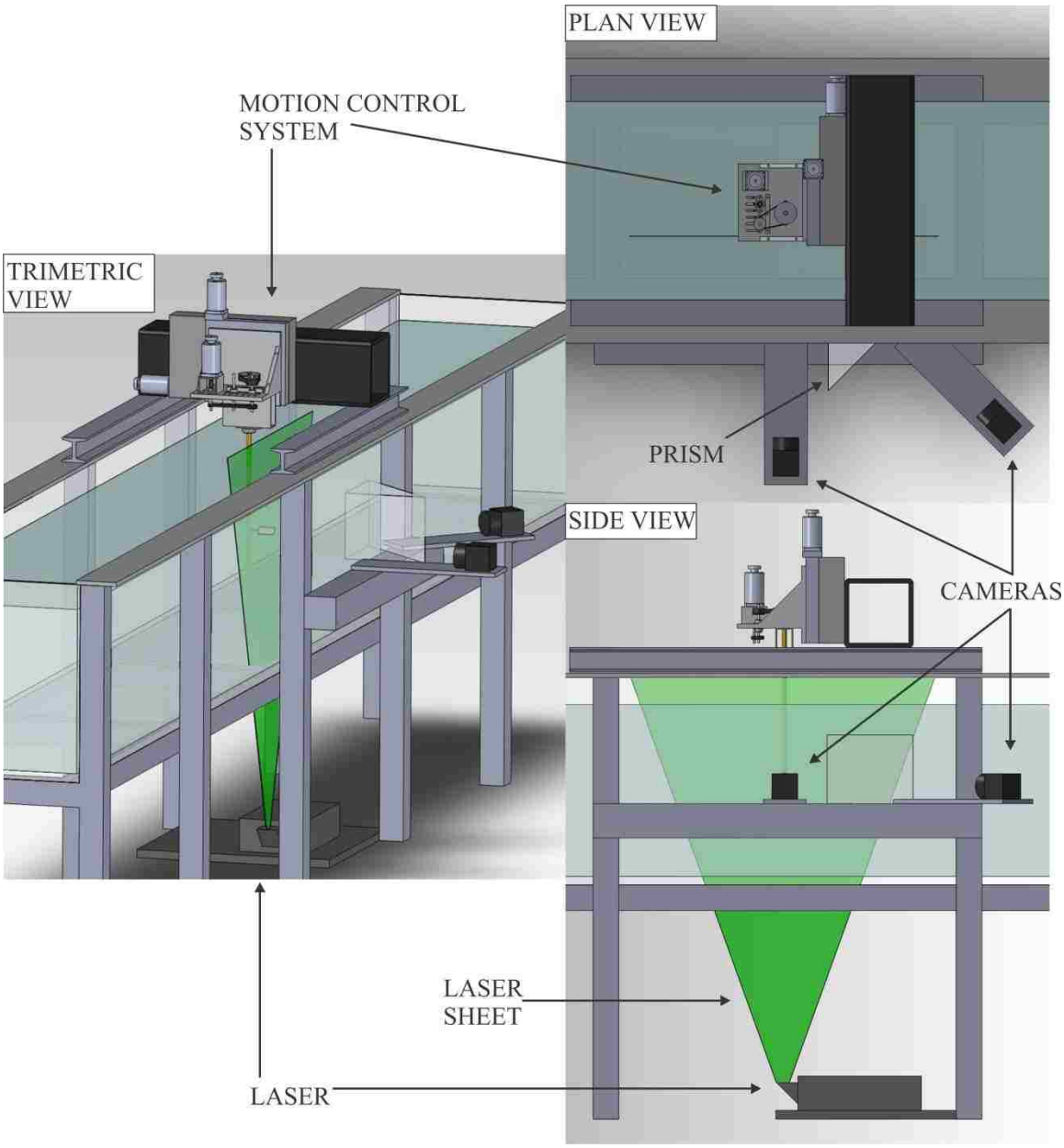

Figure 2.6: Overview of experimental apparatus, including the water channel, the motion control system and the quantitative flow imaging system.

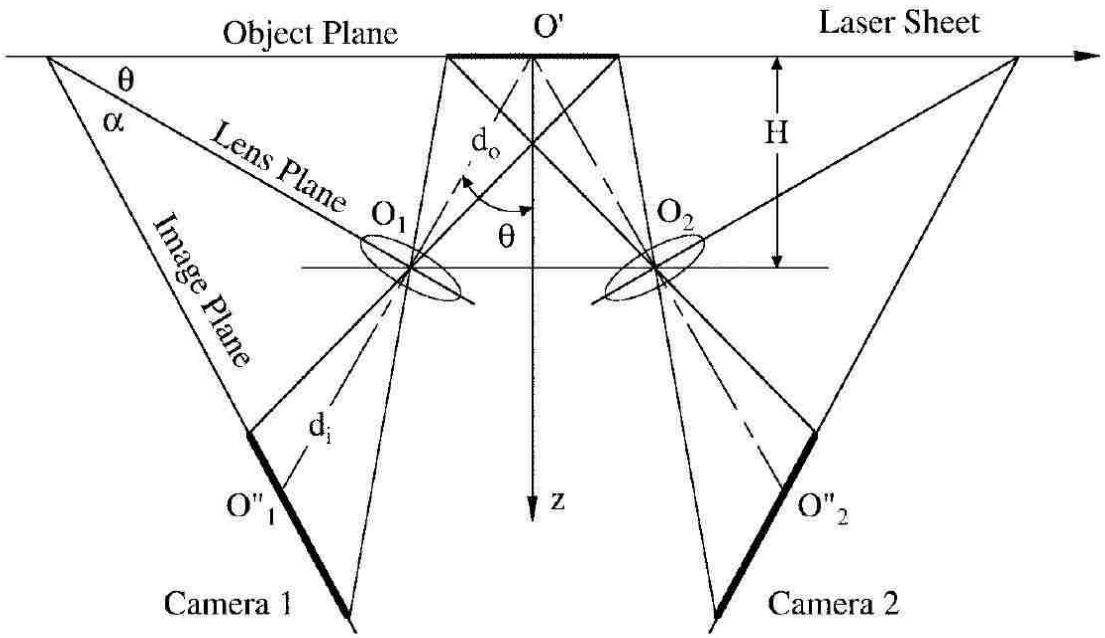

(b) Angular displacement system

Figure 2.7: Plan view schematic showing rotated camera image planes that satisfy the Scheimpflug condition (Prasad, 2000).

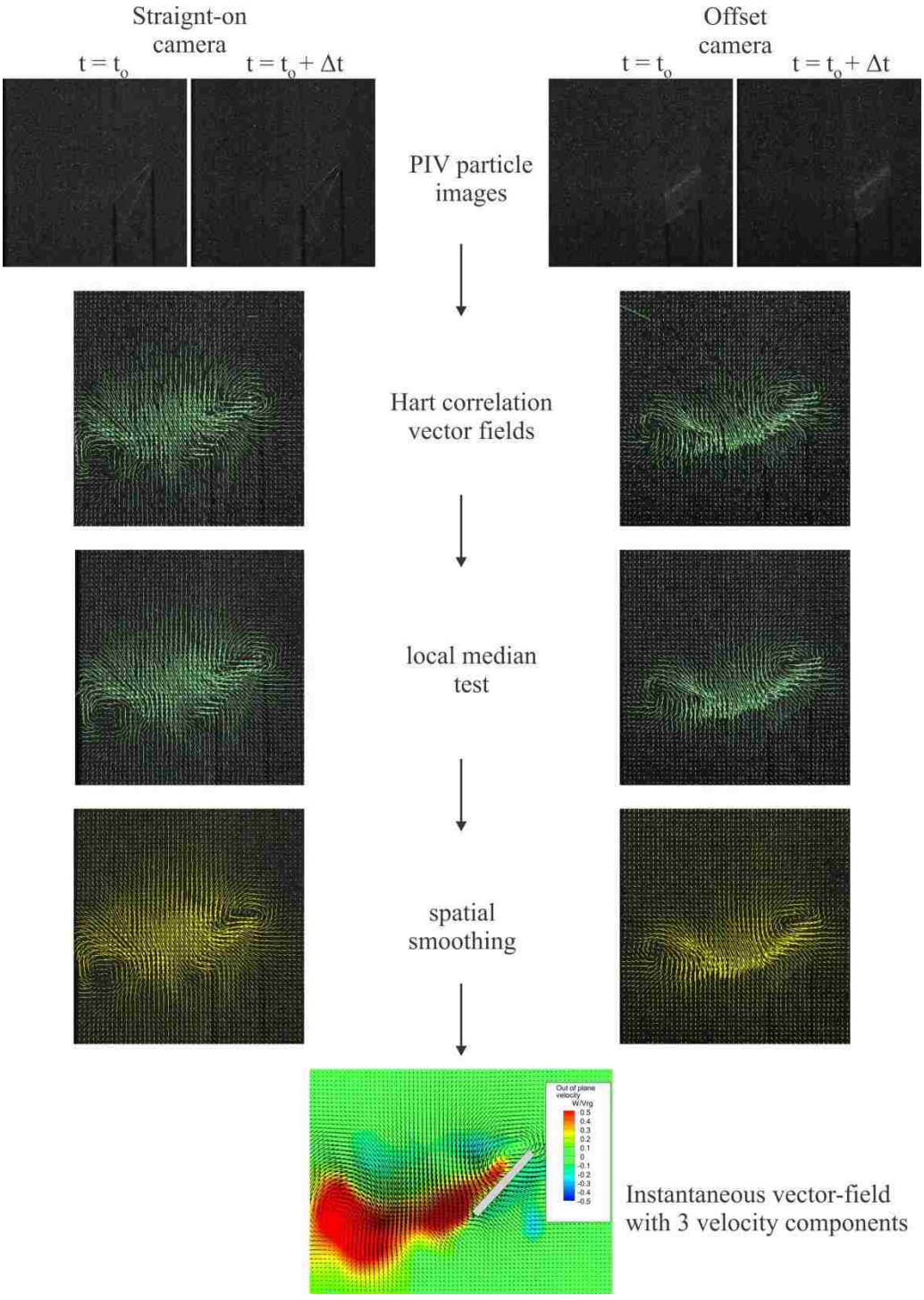

Figure 2.8: Processing pipeline for generation of instantaneous vector-fields with three components of velocity.

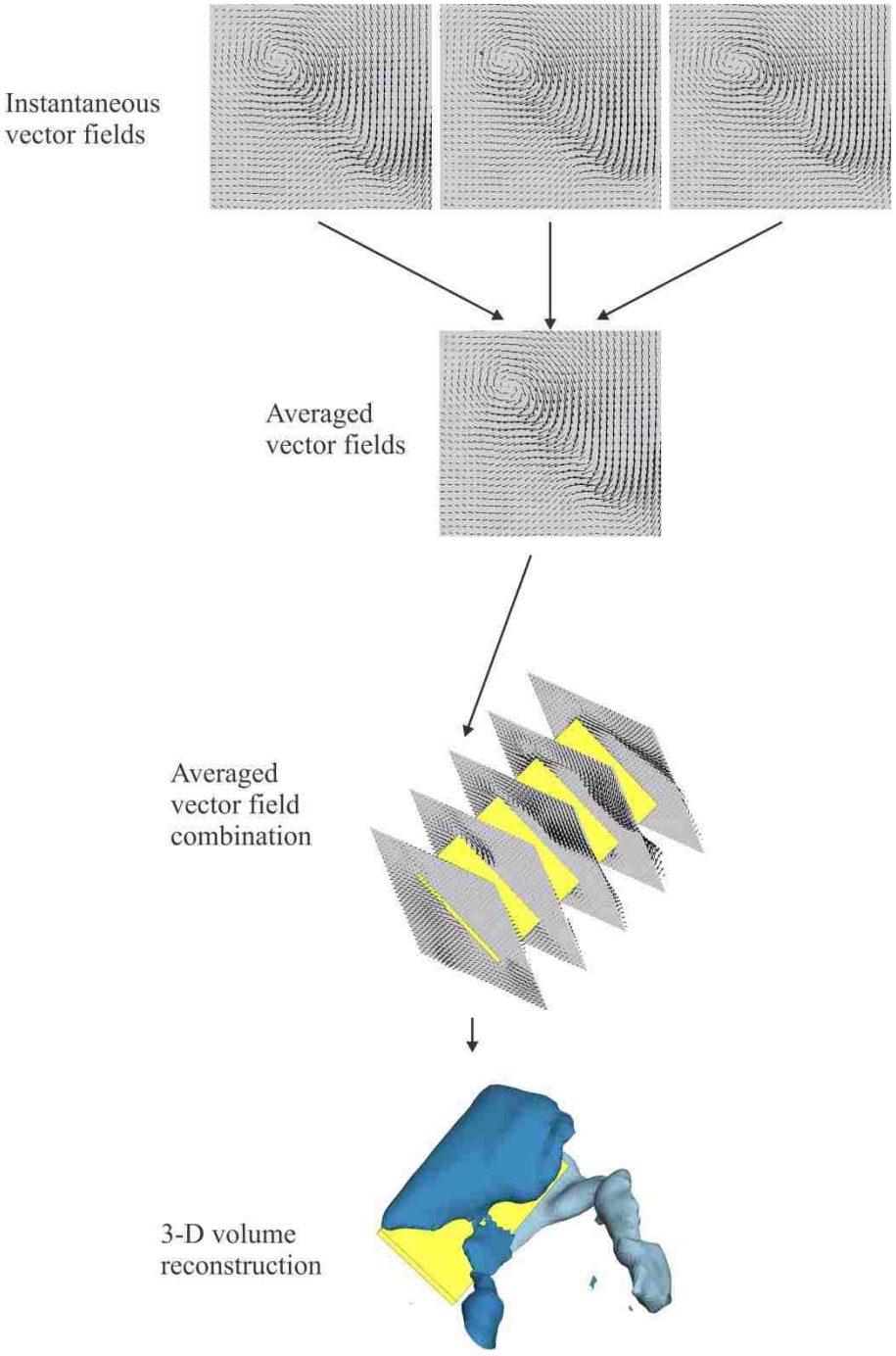

Figure 2.9: Post-processing pipeline for phase-averaging and volumetric reconstruction, using sectional results from different spanwise locations. Volumetric iso-surfaces of spanwise vorticity ω_z.

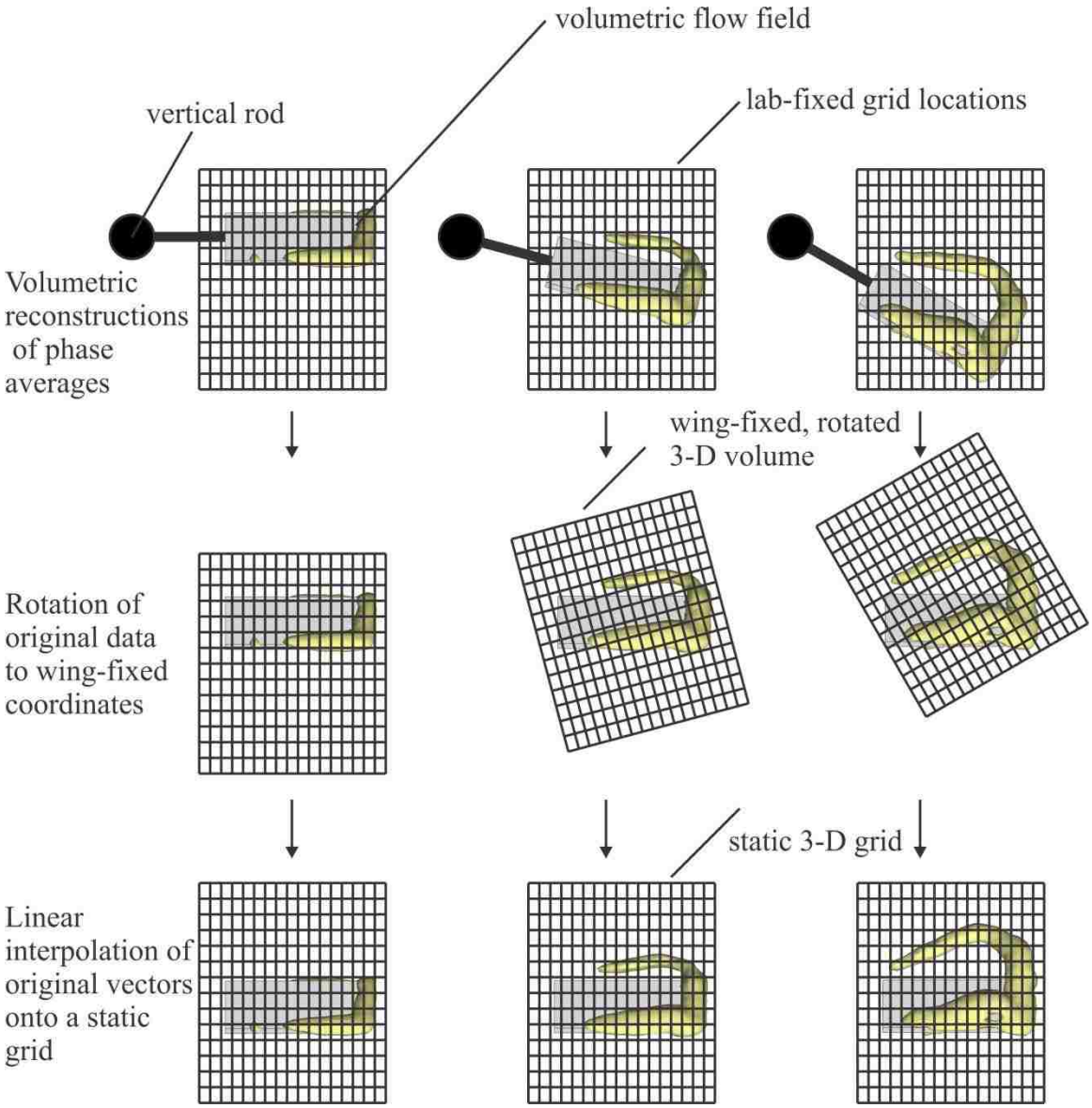

Figure 2.10: Post-processing pipeline for time-resolved flow structure development.

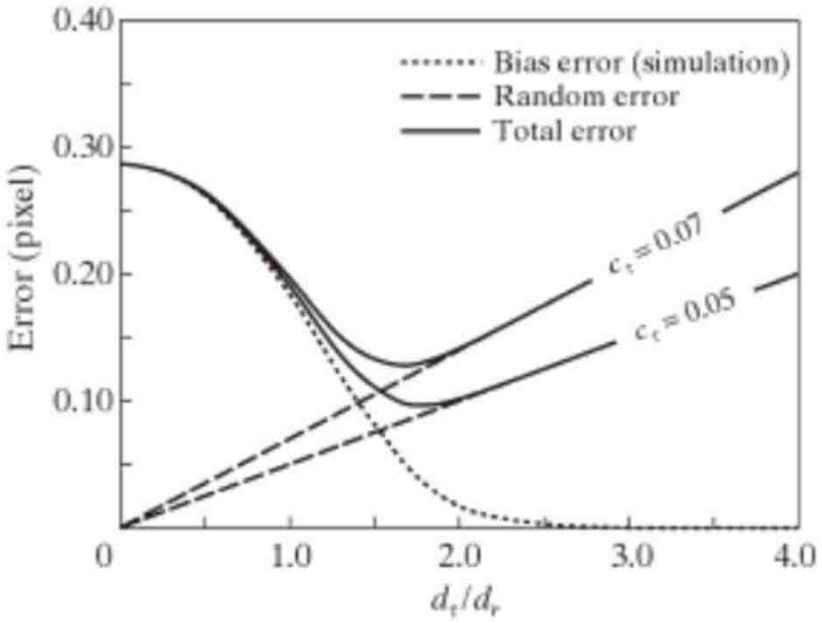

Figure 2.11: Uncertainty in determining correct particle displacements in an interrogation window (Adrian and Westerweel, 2011).

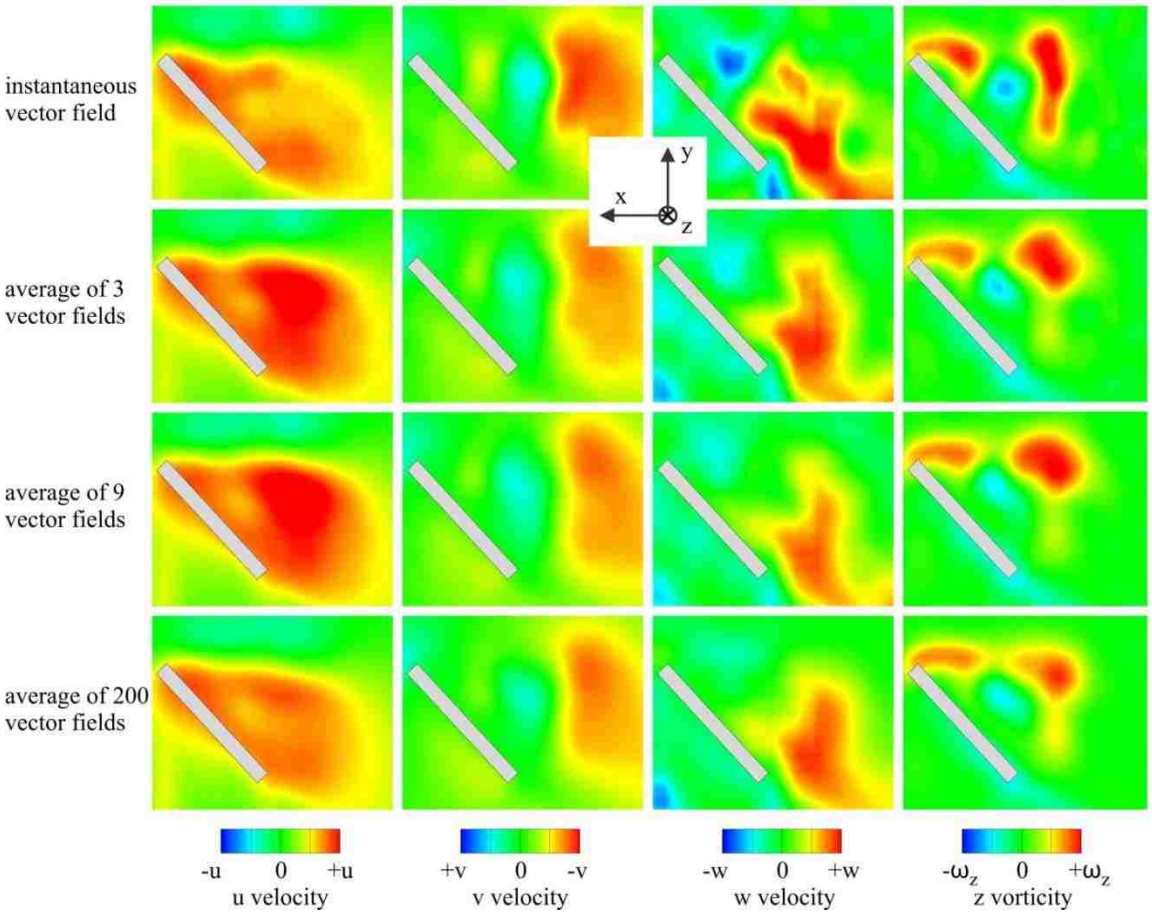

Figure 2.12: Color contours of velocity and vorticity for different phase-averaged velocity fields.

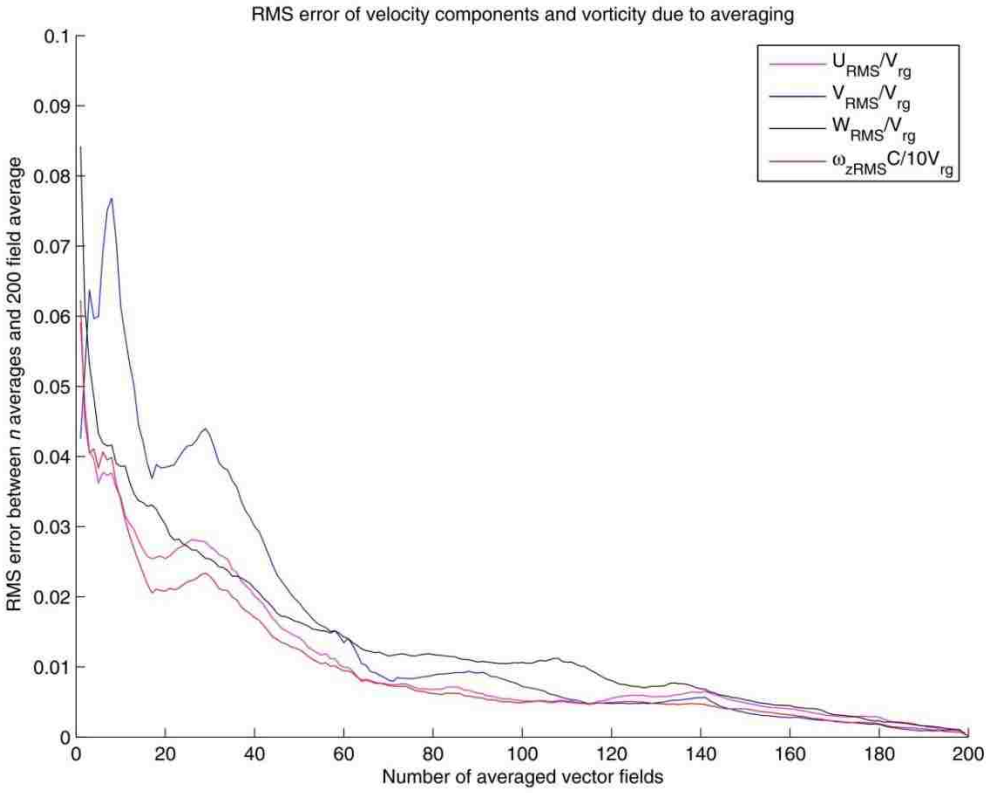

Figure 2.13: Convergence of rms error of velocity and vorticity with increasing number of phase-averaged velocity fields.

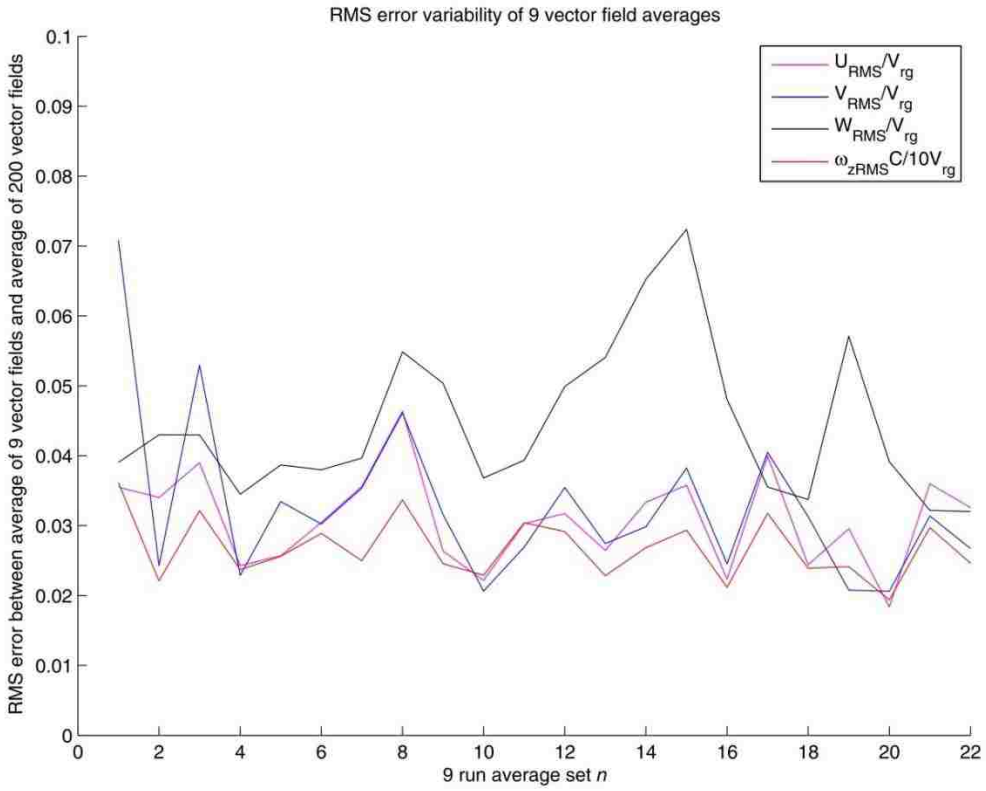

Figure 2.14: Variability of rms error of velocity and vorticity across twenty one sets of 9 phase-averaged velocity fields.

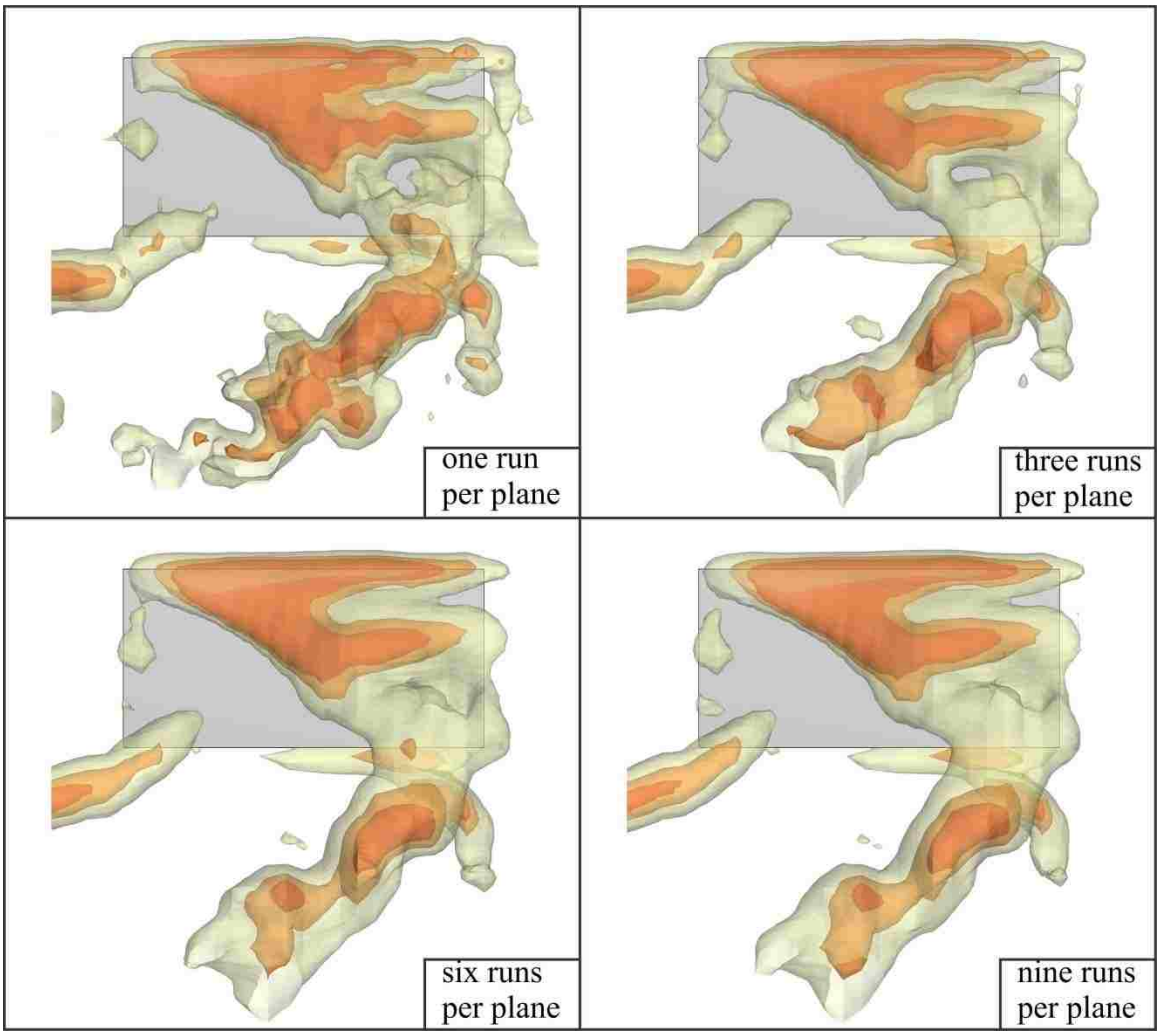

Figure 2.15: Transparent iso-surfaces of Q-criterion for different phase-averages. Q = 2 (grey-yellow), 7 (brown-orange), and 15 (orange)

CHAPTER 3

FLOW STRUCTURE ON A WING OF LOW ASPECT RATIO

In this chapter, the flow structure along a wing having low aspect ratio ($AR = 1$) is characterized at several radii of gyration via particle image velocimetry. The volumetric flow structure is determined at a travel distance of $r_g\Phi/C = 5.5$, which is well after the onset of motion. In addition, the flow structure at the midspan of the wing is assessed at four values of radius of gyration. Finally, the flow structure is characterized at a very large value of travel distance $rg\Phi/C = 78.4$, which, for the smallest radius of gyration r_g/C, corresponds to 10.75 complete rotations of the wing. The flow patterns are quantitatively represented in terms of: vorticity, components of velocity, vorticity flux, and Q-criterion. This chapter is divided into subsections that provide an introduction to this part of the investigation, a description of the experimental systems specific to this study, an assessment of quantitative visualization, and concluding remarks.

3.1 BACKGROUND

Recently, substantial efforts have focused on characterization of the flow structure on model wings simulating the flight of insects. Many studies have reduced the intricate flapping patterns employed by insects to a wing undergoing pure rotation, *i.e.*, a wing undergoing pure rotation, at constant angular velocity, after an initial acceleration from rest. This simplification of the motion has allowed researchers to identify the flow physics that arise from pure rotation of a wing at high angle of attack. Specifically, the flow structure on a purely rotating, aspect ratio $AR = 1$ rectangular wing has been characterized by Ozen and Rockwell (2011), Garmann *et al.* (2013), and Carr *et al.* (2013). Each of those investigations found an attached leading-edge vortex on a rotating wing at very low radius of gyration ($r_g/C < 2$).

In addition to determining the flow structure on a rotating wing, Garmann *et al.* (2013) determined the flow structure on a rectilinearly translating wing, and compared the flow structures and lift forces that resulted from those different motions. The flow structures that resulted from those two motions were markedly different. On the rotating wing, a leading-edge vortex formed rapidly, and this vortex remained in position throughout the wing motion. In contrast, on the translating wing, an arch vortex formed, and was eventually shed. Taira and Colonius (2009) determined the flow structure on a rectilinearly translating wing of aspect ratio $AR = 1$, well after the onset of motion. They found that the developed flow structure was steady, but it did not include a coherent leading-edge vortex.

Lentink and Dickinson (2009*b*) found, using qualitative bubble visualization, that an increase of the radius of gyration r_g/C significantly reduced the lift forces on a rotating wing, and substantially altered the flow structure observed on those wings. They proposed a framework that identified centripetal and Coriolis accelerations as the mechanisms responsible for the stability of vortical structures, namely the leading edge vortex, on rotating wings. Their framework indicated that stability of the leading-edge vortex should be unaffected by continued rotation through large travel distances. This agrees with the force measurements of Usherwood and Ellington (2002*a*), where the horizontal and vertical forces on a rotating wing did not change from a rotation angle Φ = 180° to Φ = 540°.

Alterations of the quantitative flow on an AR = 1 wing, due to changes of radius of gyration and large travel distances, have not been addressed. In particular, alterations of the degree of coherence and the interior structure of the three-dimensional vortex system, that is, the root, leading-edge, and tip vortices, have remained unclarified over a range of radius of gyration. The possibility of attaining a preserved state of the three-dimensional vortex system at very large travel distance, corresponding to large rotation angle of the wing, has not been addressed in relation to the magnitude of the radius of gyration. This chapter of the present investigation addresses these issues via quantitative imaging, and aims to interpret the flow physics in terms of multiple (nested) transparent iso-surfaces of Q-criterion, as well as surfaces of downwash and corresponding sectional patterns of spanwise vorticity, velocity and vorticity flux.

3.2 EXPERIMENTAL SYSTEMS AND TECHNIQUES

Experiments were performed in the water channel described in section 2.1. A rectangular, flat plate with sharp edges was used as a model wing. An isometric diagram of the wing system is shown in figure 3.1. The wing had a span b = 28.6 mm and a chord C = 25.4 mm, and thereby an aspect ratio AR = 1.13. Its thickness was t_w = 2.3 mm, corresponding to a thickness to chord ratio of t_w/C = 0.09. A connecting rod of diameter 3.2 mm supported the wing at its midchord. This rod was connected to a vertical shaft of diameter 12.7 mm, which served as the rotation axis. The wing was located approximately at the mid-depth of the water channel.

The wing was rotated about a vertical axis as shown in figure 3.1. This rotation consisted of rapid acceleration from rest to constant angular velocity by a computer-controlled stepper motor. The rotational motion was smoothed according to the function described by Eldredge *et al.* (2009) and was adjusted such that 90% of the maximum velocity was attained in the first 0.6 chord-lengths of travel at the radius of gyration $r_g\Phi/C$ of the wing. The angle of attack α was maintained at α = 45° for all experiments in this investigation. The maximum velocity at the radius of gyration of the wing during constant rotation was V_{rg} = 49 mm/s. This velocity corresponded to a Reynolds number based on the radius of gyration velocity and wing chord of $Re_{rg} = V_{rg}C/\nu$ = 1,400. Initial experiments were conducted to determine the Reynolds number sensitivity in the range

$1{,}400 < Re_{rg} < 5{,}000$. No significant change to the phase-averaged representations of the overall flow structure or peak magnitudes of vorticity was found in this range.

The distance between the root of the wing and the axis of rotation, defined as r_o, was varied to investigate the effect of Rossby number r_g/C on the flow structure. This distance was set to values of r_o = 16, 41, 67, 118 mm corresponding to Rossby numbers r_g/C = 1.2, 2.1, 3.1, 5.1. The angular velocity of the wing was adjusted such that the tangential velocity at the radius of gyration V_{rg}, and consequently the Reynolds number Re_{rg}, remained constant for all values of Rossby number.

Stereoscopic particle image velocimetry (SPIV) was employed to determine the quantitative flow structure along the rotating wing. The (green) plane in figure 3.1 shows the orientation of the laser sheet for determination of the velocity field at the midspan. The water was seeded with 12 μm metallic-coated, hollow, plastic spheres to facilitate particle image velocimetry. These spheres were illuminated with a dual-pulsed Nd:YAG laser system having a maximum output of 120 mJ. A camera arrangement employing an angular displacement configuration was used to image the seeding particles. This imaging system is similar to those described by Ozen and Rockwell (2012) and Bross *et al.* (2013). It consisted of two identical cameras employing charge-coupled device (CCD) sensors, both with resolutions of 1,600 pixels x 1,200 pixels. The cameras were oriented asymmetrically with respect to the light sheet: one camera viewed the light sheet 'straight-on' and the second camera viewed the light sheet at an offset angle, *i.e.*, the

angle between the normal to the light sheet and the normal to the lens plane of the camera was 0°(straight-on) and 45°(offset). Due to this orientation, it was necessary to locate a prism between the latter (offset) camera and the vertical wall of the water channel. Camera mounting systems that allowed rotation of the image plane relative to the lens plane were employed to satisfy the Scheimpflug condition (Prasad, 2000).

Captured image pairs from each camera were evaluated using a cross correlation technique with 32 x 32 pixel interrogation windows. A 50% overlap of adjacent interrogation windows was employed. The velocity vectors produced by this correlation were validated against a local average and replaced with this average if they were found to be spurious. The total number of spurious results for this evaluation technique was less than 1% of all vectors. The vector grids determined from image pairs on each camera were then combined to determine the out of plane velocity at each point on the sectional plane. This combination resulted in a sectional plane of the velocity field that was 4.98*C* X 3.18*C,* in the *x* and *y* directions, respectively, in which *C* is the wing chord. This represents an effective magnification of 12.3 pixels/mm, and an in-plane vector spacing of .05*C,* corresponding to 6,174 vectors in each plane.

This investigation considered two methods of flow field representation using these sectional planes of the quantitatively determined flow velocity: (i) sectional slices of the flow-field at the midspan of the wing, and (ii) volumetric reconstructions of the flow field using sectional slices determined at multiple locations. Sectional slices at the midspan were determined in the following way. First, sets of instantaneous images were acquired precisely when the midspan of the wing was aligned with the laser sheet. Six of

these image sets were acquired for each case. These images were processed to produce three-dimensional vector fields as described above; they were then averaged to yield the results presented in section 3.3. Sectional slices at the midspan were generated for rotation angles of Φ = 36°, 90°, 270° at the lowest Rossby number r_g/C = 1.2. These rotation angles corresponded to travel distances at the radius of gyration $r_g\Phi/C$ = 0.7, 1.8, 5.5 respectively. These same travel distances were then investigated for other values of the Rossby number r_g/C.

Volumetric reconstruction of the flow structure was conducted at two values of travel distance $r_g\Phi/C$ = 5.5 and 78.4 for selected Rossby numbers. This reconstruction was accomplished through acquisition of particle images at 16 evenly spaced locations along the span of the wing, *i.e.*, the rotation axis of the wing was translated to 16 evenly spaced locations in the *z* direction indicated in figure 3.1. The distance between these planes was $\Delta z/C$ = 0.1. Nine image sequences were acquired at each spanwise location, therefore each volumetric reconstruction consisted of 144 individual image set acquisitions. The vector fields from each of the nine sequences at each location were averaged together, and these averaged planes were combined into a three-dimensional volume.

The error of each instantaneous vector-field determination was estimated according to Adrian and Westerweel (2011). The RMS random error of in-plane velocity σ_u was approximately 4% to 6% of the maximum velocity. The ratio of the out-of-plane

RMS error to in-plane RMS error was calculated according to Lawson and Wu (1997). This error ratio was $\sigma_w/\sigma_u = 2.41$. In order to determine the uncertainty of the volumetric reconstruction process in determining flow properties, the theoretical Hill's spherical vortex (1894) was scaled to a size similar to the vortical structures observed in this study. The RMS error in calculating total vorticity using first-order differencing was 2.7% of the maximum vorticity for a Hill's spherical vortex with a radius of $0.25C$.

3.3 THREE-DIMENSIONAL IMAGES OF FLOW STRUCTURE

3.3.1 Volume images of flow structure

Iso-surfaces of the *Q*-criterion are shown in figures 3.3 through 3.4. The Rossby number varies from $r_g/C = 1.2$ to 5.1 and, for all images, the travel distance of the wing is $r_g\Phi/C = 5.5$. The *Q*-criterion represents the contributions of the antisymmetric and symmetric components of the velocity gradient tensor such that a positive value of the *Q*-criterion indicates regions dominated by rotation.

$$QC^2/V_{rg}^2 = 0.5[\ \Omega_{ij}\Omega_{ij} - S_{ij}S_{ij}\ ] = 0.5[\ \|\Omega\|^2 - \|S\|^2\ ]$$

Hunt *et al.* (1988) formulated the *Q*-criterion to identify eddy zones as strong swirling zones with vorticity. According to their interpretation, regions of large, positive *Q* indicate where irrotational straining is small compared with the vorticity.

Figure 3.2 shows representative images corresponding to a low value of Rossby number r_g/C = 1.2. The left image indicates three nested, transparent iso-surfaces of $QC^2/V_{rg}{}^2$ = 3, 8, and 13, which are represented respectively by the grey-yellow, brown-orange, and orange colors. This sequence of colors thereby indicates regions with increasing dominance of rotation $\|\Omega\|^2$ over irrotational strain $\|S\|^2$. As a comparison, the right image shows transparent iso-surfaces of total vorticity scaled to match the *Q*-criterion. Values of $||\omega||^2C^2/4V_{rg}{}^2$ = 3, 8, and 13 correspond to grey-yellow, brown-orange, and orange colors. The difference between these iso-surfaces is therefore the contribution of irrotational strain $\|S\|^2$. The iso-surfaces of $QC^2/V_{rg}{}^2$ and $||\omega||^2C^2/4V_{rg}{}^2$ representing the root vortex and tip vortex are very similar, indicating that the contribution of irrotational strain $\|S\|^2$ in these regions is small. In contrast, the iso-surfaces in the leading-edge region are noticeably different, indicating significant irrotational strain in that region.

The images of figure 3.3 show the effects of Rossby number r_g/C on the nested, transparent iso-surfaces of $QC^2/V_{rg}{}^2$. Considering the image of figure 3.3 at a value of Rossby r_g/C = 1.2, the iso-surfaces of $QC^2/V_{rg}{}^2$ indicate a well-defined leading-edge vortex. This vortex has a conical form, that is, an increasing scale with increasing radial distance from the axis of rotation. Moreover, the highest (orange) level $QC^2/V_{rg}{}^2$ = 13 in the innermost region of the leading-edge vortex persists along most of the span of the

wing. This leading-edge vortex forms a loop with the coherent root and tip vortices, which have high levels of QC^2/V_{rg}^2 along their entire extent, and are severely deflected towards the center of rotation.

The image at r_g/C = 2.1 in figure 3.3 indicates that the highest (orange) level of QC^2/V_{rg}^2 = 13 no longer exists within the innermost region of the leading-edge vortex, and the next lower level of (brown-orange) QC^2/V_{rg}^2 = 8 has been displaced towards the aft portion of the leading-edge vortex. That is, the highly concentrated structure of the leading-edge vortex that exists at r_g/C = 1.2 degrades to a less concentrated form at r_g/C = 2.1. Regarding the root and tip vortices at r_g/C = 2.1, their deflection towards the axis of rotation is milder than at r_g/C = 1.2, and, furthermore, the highest (orange) level of QC^2/V_{rg}^2 = *13* in the innermost region of these vortices is substantially attenuated, such that only a region of small spatial extent is evident. One can therefore conclude that increasing the radius of gyration, as indicated in the images at r_g/C = 1.2 and 2.1, results in attenuation of the region of high QC^2/V_{rg}^2 in not only the leading-edge vortex, but also the tip and root vortices.

The image at the largest value of Rossby number r_g/C = 5.1 in figure 3.3 indicates further degradation of the leading-edge vortex relative to that at r_g/C = 2.1. It is now defined primarily by the lowest (grey-yellow) level of QC^2/V_{rg}^2 = 3. Correspondingly,

the tip and root vortices are not significantly deflected towards the axis of rotation and the higher levels of QC^2/V_{rg}^2 = 8 and QC^2/V_{rg}^2 = 13 are absent over most of the interior of the tip and root vortices.

Figure 3.4 shows corresponding views looking towards the leading-edge of the plate. The same principal features as indicated in figure 3.3 are evident. That is, degradation of the highest level of QC^2/V_{rg}^2 = 13 within the components of the vortex system occurs for increasing values of Rossby number r_g/C. This view also indicates that, in addition to the less severe deflection of the root and tip vortices towards the radius of curvature, the tip vortex is at an increased height from the trailing-edge of the wing for the larger values of Rossby number r_g/C = 2.1 and 5.1 relative to r_g/C = 1.2.

Figures 3.5-3.7 show opaque (blue) iso-surfaces of downwash v/V_{rg} superposed on the iso-surfaces of QC^2/V_{rg}^2 given in figures 3.3 and 3.4. The schematic of figure 3.5 shows a side view of a sectional cut of the wing and the direction of vertical velocity that is associated with the negative (blue) downwash. The images in figures 3.5 through 3.7 indicate that the spatial extent of the negative (blue) iso-surface of downwash v/V_{rg} decreases substantially with increasing values of r_g/C. That is, for increasing values of r_g/C = 1.2, 2.1 and 5.1, the width of this v/V_{rg} iso-surface in the spanwise dimension z decreases markedly. This decreasing spatial extent is directly correlated to the attenuation of higher levels of QC^2/V_{rg}^2 = 8 and QC^2/V_{rg}^2 = 13 within the interiors of the leading-

edge, tip, and root vortices as the value of Rossby number is increased. Correspondingly, the leading-edge of the v/V_{rg} iso-surface moves downstream of the leading-edge of the wing. For all values of r_g/C, the v/V_{rg} iso-surface extends well downstream of the trailing-edge of the wing.

3.3.2 Multiple slices of flow structure along span of wing

Figures 3.8 through 3.11 indicate sectional cuts of the flow structure at six locations *A* through *F* along the span of the wing. In order to indicate the distinctions between features on adjacent sectional cuts, the span of the wing in these layouts is stretched by a factor of two. The root and tip of the wing correspond respectively to sectional cuts *A* and *F*.

Figure 3.8 shows contours of constant (black line) vorticity ω_z normalized with the chord *C* and the velocity V_{rg} of the wing at the radius of gyration. This dimensionless vorticity $\omega_z C/V_{rg}$ is shown on sectional cuts *A* through *F*. The black lines correspond to $\omega_z C/V_{rg} = \pm 4$ through $\omega_z C/V_{rg} = \pm 10$ with $\Delta\omega_z C/V_{rg} = 1$. At the lowest Rossby number $r_g/C = 1.2$, the vorticity contours remain relatively close to the surface of the wing for spanwise locations *A*-*D*. In contrast, at the highest Rossby number $r_g/C = 5.1$, the vorticity contours remain close to the surface of the wing only at spanwise location *A*, *i.e.*, near the root. At larger values of spanwise location corresponding to planes *B*

through *F*, the vorticity contours are substantially deflected away from the surface of the wing, which is expected for the limiting case of a wing undergoing purely rectilinear motion at high angle of attack α.

Figure 3.9 shows (color) contours of spanwise velocity w/V_{rg} superposed on contours of constant (black line) vorticity $\omega_z C/V_{rg}$. At the smallest value of Rossby number r_g/C = 1.2, the largest magnitude (red) flow from the root to the tip is coincident with the black line contours of $\omega_z C/V_{rg}$ located downstream of the trailing-edge**,** which represent the reoriented tip vortex in the wake region, evident in the volumetric iso-surfaces of the *Q*-criterion given in figures 3.3 through 3.7. At successively larger values of Rossby number r_g/C, the peak magnitudes of w/V_{rg} on each sectional cut decrease in accord with the decrease of the peak values of $\omega_z C/V_{rg}$. This trend corresponds to decreased deflection of the tip vortex across the wake, as shown by the iso-surfaces of QC^2/V_{rg}^2 in figure 3.3.

Figure 3.10 shows (color) contours of spanwise vorticity flux $\omega_z wC/V_{rg}^2$ superposed on contours of constant (black line) vorticity $\omega_z C/V_{rg}$. At the lowest Rossby number r_g/C = 1.2, the region of largest (dark blue) magnitude of $\omega_z wC/V_{rg}^2$ is coincident with the deflected tip vortex across the wake of the wing, evident from comparison with figure 3.3. At r_g/C = 2.1 and 5.1, the scale and magnitude of the blue

region of $\omega_z wC/V_{rg}^2$ decrease relative to the (dark blue) contours shown at r_g/C = 1.2, in accord with the decreased magnitude of the spanwise velocity w/V_{rg} indicated in figure 3.9. Regarding the patterns of spanwise vorticity flux $\omega_z wC/V_{rg}^2$ along the leading-edge in the outboard region of the wing, corresponding to sectional cuts *D* through *F*, positive (blue) values dominate for all values of Rossby number r_g/C = 1.2 through 5.1.

Figure 3.11 shows contours of constant downwash velocity v/V_{rg} superposed on contours of constant (black line) vorticity $\omega_z C/V_{rg}$. Large magnitude (dark red) downwash velocity is most prevalent at lower Rossby numbers r_g/C = 1.2 and 2.1, extending over the spanwise locations *A* through *D.* At spanwise locations *B, C,* and *D,* the region of large amplitude downwash extends from the (black line) vorticity $\omega_z C/V_{rg}$ concentration corresponding to the leading-edge vortex to the $\omega_z C/V_{rg}$ concentration of the deflected tip vortex. The peak magnitude of downwash v/V_{rg} is larger (dark red) at the lowest Rossby number r_g/C = 1.2 than at r_g/C = 2.1 (light red). At r_g/C = 5.1, the spatial extent of the (red-yellow) downwash regions is significantly decreased on each of the sectional cuts and, furthermore, the magnitude is further attenuated relative to the (darker red) values at r_g/C = 1.2 and 2.1. Moreover, at section *B*, the contours of elevated downwash velocity v/V_{rg} do not extend up to the leading-edge vortex at r_g/C = 5.1. Viewing together the contours of downwash velocity and the vorticity layers at the

leading-edge of the wing, at all radii of gyration r_g/C = 1.2, 2.1 and 5.1, it is evident that downwash velocity of larger magnitude and spatial extent is associated with enhanced retention of the leading-edge vorticity layer (cluster) closer to the surface of the wing.

In essence, the nature of the tip vortex deflected across the wake region of the wing, described in figures 3.3-3.7, is closely related to the sectional representations of the flow structure along the span of the wing. As the value of Rossby number increases, this deflected tip vortex experiences: a decrease in the degree of deflection towards the center of rotation; and a decrease in the level of spanwise-oriented vorticity within its interior. Correspondingly, an increase of Rossby number also yields increased deflection of the separated, leading-edge vorticity layer in a direction away from the surface of the wing; this deflection is correlated with a decrease in spatial extent and magnitude of the downwash velocity, as well as a decrease in magnitude of the spanwise velocity and vorticity flux in the trailing-edge region of the wing.

3.3.3 Flow structure at midspan of wing

Figure 3.12 shows sectional cuts of spanwise vorticity $\omega_z C/V_{rg}$ at the midspan of the wing. These patterns are shown as a function of two parameters: (i) the Rossby number r_g/C; and (ii) the distance of wing travel $r_g\Phi/C$. The images in the left column of figure 3.12 correspond to the travel distance $r_g\Phi/C$ = 0.7 of the wing. They show the early development of the flow structure after the onset of wing motion. At this value of

$r_g\Phi/C$ = 0.7, the sectional patterns of $\omega_z C/V_{rg}$ are generally similar over the range of Rossby number from r_g/C = 1.2 to 5.1. In particular, the concentration of negative (red-yellow) vorticity at the leading-edge of the wing, which represents the leading-edge vortex, has a similar scale and vorticity magnitude at all values of Rossby number. The concentration of positive (blue) vorticity, located downstream of the trailing-edge of the wing, is the starting vortex, which is shed after the onset of wing motion. Its peak vorticity magnitude $\omega_z C/V_{rg}$ decreases with increasing Rossby number r_g/C, whereas its distance from the trailing-edge is constant.

The images in the middle column of figure 3.12 represent the flow structure at a distance of wing travel $r_g\Phi/C$ = 1.8. At the lowest value of r_g/C = 1.2, the form of the vorticity concentration at the leading-edge is very similar to that at the lower value of $r_g\Phi/C$ = 0.7. At larger values of r_g/C = 2.1, 3.1 and 5.1, however, the length of the leading-edge vortex increases as it deflects away from the surface of the wing. Regarding the concentration of positive (blue) vorticity downstream of the trailing-edge of the wing, its peak value is smaller at larger values of r_g/C = 3.1 and 5.1, while its distance downstream of the trailing-edge is larger.

The images in the right column of figure 3.12 indicate the flow structure at a larger distance of wing travel $r_g\Phi/C$ = 5.5; they correspond to the volume representations given in the previous section. At the lowest Rossby number r_g/C = 1.2, the structure of

the leading-edge vortex resembles the structure at $r_g\Phi/C$ = 1.8 and 0.7. That is, a well-defined, attached leading-edge vortex persists regardless of travel distance $r_g\Phi/C$. At higher Rossby numbers r_g/C = 2.1, 3.1, and 5.1, the length of the leading-edge vortex increases as it deflects away from the surface of the wing. Moreover, at r_g/C = 3.1 and 5.1, the spatial extent of the region of highest (red) vorticity magnitude decreases, relative to the corresponding cases at r_g/C = 3.1 and 5.1 shown in the middle column of figure 3.12. In fact, at $r_g\Phi/C$ = 5.5 and r_g/C = 5.1, the form of the vorticity layer separating from the leading-edge closely resembles the separated shear layer along a wing at high angle of attack α undergoing rectilinear, translating motion (Ozen and Rockwell, 2011). Furthermore, the images in the right column of figure 3.12 indicate that the negative (blue) concentration of vorticity in the vicinity of the trailing-edge has a relatively high peak magnitude at r_g/C = 1.2, in comparison with the substantially attenuated magnitudes at larger values of r_g/C = 2.1, 3.1 and 5.1. The distance from the trailing-edge to the center of each of these respective concentrations is actually smaller than, or approximately equal to, the corresponding distances at the smaller value of travel distance r_g/C = 1.8, thereby indicating that they represent the cross-section of the tip vortex that is deflected across the wake, rather than vorticity that is shed from the trailing-edge as a starting vortex and convected away from the edge. This feature is evident in the three-dimensional representations of *Q*-criterion shown in figures 3.3 through 3.7, *i.e.*, the blue concentration of vorticity in the right column of figure 3.12 at

each respective Rossby number corresponds to a sectional slice of the iso-surface of QC^2/V_{rg}^2 that represents the reoriented tip vortex described in figures 3.3 through 3.7.

In essence, the overview of figure 3.12 indicates that when the Rossby number r_g/C is sufficiently small, that is, r_g/C = 1.2, the structure of the leading-edge vortex is preserved over the range of travel distance $r_g\Phi/C$ of the wing. Remarkably, this preservation of the leading-edge vortex is also associated with preservation of a high degree of concentration of vorticity $\omega_z C/V_{rg}$ of the positive (blue) vortical structure, in the vicinity of the trailing-edge. From the three-dimensional flow structure given in figures 3.3 through 3.7, it is clear that this positive concentration is the sectional cut of the tip vortex that is deflected across the wake. At higher values of r_g/C, however, the form and degree of concentration of vorticity in the leading-edge vortex continues to evolve with successively larger values of travel distance $r_g\Phi/C$ of the wing. Correspondingly, at larger values of r_g/C and $r_g\Phi/C$, the peak magnitude of the positive (blue) vorticity $\omega_z C/V_{rg}$ concentration in the region of the trailing-edge is, in general, substantially attenuated. As indicated in figures 3.3 and 3.4, large values of QC^2/V_{rg}^2, and thereby vorticity $\omega_z C/V_{rg}$ are attenuated in the interior region of the tip vortex at larger values of radius of gyration r_g/C.

Figure 3.13 shows (color) contours of spanwise vorticity flux $\omega_z wC/V_{rg}^2$ superimposed upon (black) contour lines of spanwise vorticity $\omega_z C/V_{rg}$ = ±6, ±8, ±10. This layout of images, which shows the effects of variation of Rossby number r_g/C and travel distance $r_g\Phi/C$ of the wing, is the same as for figure 3.12. At the smallest values of Rossby number r_g/C = 1.2 and travel distance $r_g\Phi/C$ = 0.7 of the wing in figure 3.13, negative (red) spanwise vorticity flux $\omega_z wC/V_{rg}^2$ is present within the leading-edge vortex and the starting vortex (compare figure 3.12). Combinations of larger values of Rossby number r_g/C and travel distance $r_g\Phi/C$ of the wing tend to promote the onset of positive (blue) spanwise vorticity flux $\omega_z wC/V_{rg}^2$ within the leading-edge vortex, and for the limiting case of r_g/C = 5.1 and $r_g\Phi/C$ = 5.5, neither positive (blue) nor negative (red) flux $\omega_z wC/V_{rg}^2$ is evident. This trend of the patterns of vorticity flux within the concentration of vorticity at the leading-edge is associated with an increase in length of the vorticity concentration and its deflection away from the surface of the wing (compare figure 3.12). Regarding the concentration of vorticity flux in the vicinity of the trailing-edge, the images shown in the left column ($r_g\Phi/C$ = 0.7) of figure 3.13 indicate a high level of negative (red) $\omega_z wC/V_{rg}^2$ at r_g/C = 1.2, and an attenuated negative level at r_g/C = 2.1, 3.1 and 5.1. All of these concentrations of vorticity flux are associated with the vortex shed during the onset of motion. As shown in the middle column ($r_g\Phi/C$ = 1.8)

and right column ($r_g\Phi/C$ = 5.5) of figure 3.13, the vorticity flux $\omega_z wC/V_{rg}^2$ associated with the vorticity concentration in the vicinity of the trailing-edge at a later stage of the flow development has a positive (blue) value, and represents the sectional cut of the tip vortex that is deflected across the wake. The scale and/or peak magnitude of $\omega_z wC/V_{rg}^2$ decreases with increasing value of Rossby number r_g/C.

Figure 3.14 shows patterns of vorticity flux $\omega_z wC/V_{rg}^2$ for the extreme cases of Rossby number r_g/C and rotation distance $r_g\Phi/C$ given in figure 3.13. As indicated in the left column of figure 3.13, shortly after the onset of motion ($r_g\Phi/C$ = 0.7) the stable leading-edge vortex at r_g/C = 1.2 involves large magnitude flux through its center. The images in the right column of figure 3.14 correspond to the larger travel distance $r_g\Phi/C$ = 5.5 of the wing. There is a relationship between the degree of preservation of the leading-edge vortex and, in the region of the trailing-edge, the magnitude and scale of the (blue) vorticity flux of the sectional cut of the deflected tip vortex across the wake (compare figure 3.12). At r_g/C = 1.2, the leading-edge vortex is generally preserved with significant magnitude of negative (red) vorticity flux $\omega_z wC/V_{rg}^2$; this vortex preservation coexists with the large magnitude positive (blue) $\omega_z wC/V_{rg}^2$ of the sectional cut of the tip vortex deflected across the wake. On the other hand, in the image at the lower right, for r_g/C = 5.1, the concentrated leading-edge vortex is substantially degraded and the

magnitude of the concentrated region of (blue) $\omega_z wC/V_{rg}^2$ in the region downstream of the trailing-edge is attenuated.

Figure 3.15 shows representations of the component of flow velocity u, which is the projection of the flow velocity V in the direction of the tangential velocity V_{rg} of the wing motion; contours of constant u/V_{rg} are indicated. The color dark blue represents u/V_{rg} = -1. This (dark blue) region corresponds to a region of highly separated flow involving negative (upstream-oriented) flow in this reference frame. Viewing the entire layout of images in figure 3.15, it is evident that when r_g/C and $r_g\Phi/C$ are sufficiently small, the region where the u component of velocity nears or exceeds the velocity of the wing at the radius of gyration (dark blue) has a minimum spatial extent. On the other hand, for the extreme case of large r_g/C = 5.1 and $r_g\Phi/C$ = 5.5, the (dark blue) region corresponding to u/V_{rg} = -1 has a very large spatial extent, thereby indicating a large region of separated flow. This observation is in accord with deflection of the vorticity layer from the leading-edge away from the surface of the wing.

3.3.4 Volumetric representations of flow structure at very large travel distance

The representations of the flow structure considered up to this point are for a rotating wing prior to completion of one full revolution. In this section, comparisons are made with the flow structure after multiple revolutions. Figures 3.16-3.18 show

comparisons of: (i) the flow structure for a travel distance $r_g\Phi/C$ = 5.5, which corresponds to values of angular rotation 270° and 61° for radii of gyration r_g/C = 1.2 and 5.1; and (ii) the flow structure at very large travel distance $r_g\Phi/C$ = 78.4, which corresponds to 3,870° degrees (10.75 revolutions) for r_g/C = 1.2 and 875° (2.5 revolutions) for r_g/C = 5.1. The images of figures 3.16-3.18 show the same level of the *Q*-criterion as in figure 3.3 for display of the QC^2/V_{rg}^2 iso-surfaces.

The top row of figure 3.16 indicates, at a Rossby number r_g/C = 1.2, very similar iso-surfaces for the lowest level of QC^2/V_{rg}^2 = 3 (grey-yellow) for both $r_g\Phi/C$ = 5.5 and $r_g\Phi/C$ = 78.4. At higher levels of QC^2/V_{rg}^2 = 8 (brown- orange) and 13 (orange), some degradation of the spatial extent of the iso-surfaces is evident at $r_g\Phi/C$ = 78.4 relative to $r_g\Phi/C$ = 5.5, particularly for the highest (orange) value of QC^2/V_{rg}^2 = 13. This detectable degradation occurs in both the leading-edge and tip vortices, but, in a broad sense, the structure of the vortex system remains intact. The bottom row of figure 3.16 indicates more extensive modification to the flow structure at a larger Rossby number r_g/C = 5.1 for $r_g\Phi/C$ = 78.4. In this regime, the defined region of the flow structure at the leading-edge, which is evident at $r_g\Phi/C$ = 5.5, shrinks in size at $r_g\Phi/C$ = 78.4 and is displaced downstream towards the midchord of the wing. The (grey-yellow) QC^2/V_{rg}^2 = *3* iso-

surface in the tip-region, which trails well into the wake of the wing at $r_g\Phi/C = 5.5$, is no longer evident at $r_g\Phi/C = 78.4$.

Figure 3.17 shows views looking towards the leading-edge of the plate. It further illustrates the changes of the flow structure seen in figure 3.16. At a Rossby number $r_g/C = 1.2$, the lowest level (grey-yellow) of $QC^2/V_{rg}^2 = 3$ indicates that the location of the reoriented tip vortex relative to the trailing-edge is similar at $r_g\Phi/C = 5.5$ and $r_g\Phi/C = 78.4$.

Figure 3.18 shows superposed, opaque (blue) iso-surfaces of downwash velocity with transparent iso-surfaces of the *Q*-criterion. The top row of figure 3.18 indicates persistence of a large region of high-level (blue) downward velocity v/V_{rg} at $r_g\Phi/C = 78.4$ for a Rossby number $r_g/C = 1.2$. Slight modification of this iso-surface is evident in the root region due to a minor degradation of the coherence of the root vortex at $r_g\Phi/C = 78.4$. In contrast, the bottom row of figure 3.18 indicates the disappearance of all regions of high-level downwash at $r_g\Phi/C = 78.4$ for a Rossby number $r_g/C = 5.1$.

3.4 CONCLUSIONS

The flow structure on a rotating wing is characterized in terms of three-dimensional and sectional images using a technique of particle image velocimetry. This structure is sensitive to the distance of the wing from the center of rotation, represented by the radius of gyration r_g or the Rossby number r_g/C, in which C is the wing chord. Moreover, it is also a function of the distance travelled $r_g\Phi/C$ along the arc of rotation of the wing, where Φ is the angle of rotation. To assess the effects of variations of Rossby number r_g/C, the flow structure is compared at given values of travel distance $r_g\Phi/C$.

Variation of the flow structure with Rossby number r_g/C is represented by volumetric, transparent iso-surfaces of the Q-criterion, where Q physically represents the difference between rotation $||\Omega||^2$ and strain $||S||^2$. Large, positive values of Q indicate regions where the vorticity (rotation) $||\Omega||^2$ dominates irrotational strain $||S||^2$. Nested, transparent iso-surfaces of QC^2/V_{rg}^2 therefore allow definition of the interior structure of the leading-edge, root, tip, and trailing-edge vortices as a function of Rossby number r_g/C. As the Rossby number increases, the influence of rotation on the flow structure decreases, yielding rapid degradation of coherent vortical structures. With increasing r_g/C, the highest levels of QC^2/V_{rg}^2 in the interior of the leading-edge vortex are attenuated, and the entire vortex is distorted and displaced away from the leading-edge.

Simultaneously, the highest levels of QC^2/V_{rg}^2 within the tip and root vortices are also attenuated, and they lose their ordered, coherent structure. These findings suggest that stability or retention of the leading-edge vortex is actually coupled with the interior structure of the tip and root vortices. This interpretation is in accord with the results of Carr *et al.* (2013), where increased tip vortex coherence was associated with increased leading-edge vortex coherence. Moreover, higher interior levels of QC^2/V_{rg}^2 are associated with increased coherence of the tip and root vortices. In essence, high levels of QC^2/V_{rg}^2 within the interior of the entire three-dimensional vortex system, which are observed at low Rossby number r_g/C, thereby indicate the strong relationship between the leading-edge vortex and the tip and root vortices.

A further consequence of wing rotation is deflection of the tip and root vortices towards the center of rotation. It is most severe at the lowest value of Rossby number r_g/C, where the deflected tip vortex extends across the wake in the region immediately downstream of the trailing-edge, thereby contributing significantly to the magnitude of downwash at upstream locations. For increasing values of r_g/C, however, the deflection of the trajectories of the root and tip vortices towards the center of rotation decreases, and at the highest value of r_g/C, only small radial deflection is evident.

The three-dimensional vortex system, involving the leading-edge, tip and root vortices, induces a region of large magnitude downwash, which is located between the tip and root vortices. The scale (spatial extent) of this downwash region is strongly

correlated with the magnitude of QC^2/V_{rg}^2 within the interior of the vortex system. At the lowest value of Rossby number r_g/C, the scale of the downwash region is largest and it extends upstream to the coherent leading-edge vortex. At successively larger values of Rossby number r_g/C, however, the scale of the region of large magnitude downwash successively decreases, and its leading-edge moves downstream of the leading-edge of the wing. Loss of identity of the stable leading-edge vortex, which occurs with increasing values of Rossby number r_g/C, is therefore directly linked to diminished spatial extent of the region of downwash of large magnitude.

These three-dimensional volume representations of the flow structure are complemented by sectional cuts along the span of the wing. The foregoing trends are accompanied by increased deflection of the leading-edge vorticity layer away from the surface of the wing with increasing values of Rossby number r_g/C. Simultaneously, the magnitude of spanwise velocity w/V_{rg} and vorticity flux $\omega_z wC/V_{rg}^2$ in the trailing region of the wing are attenuated, as is, the downwash v/V_{rg}. These effects are strongly correlated with the degree of deflection and strength of the tip vortex across the wake of the wing.

An overview of the combined effects of Rossby number r_g/C and travel distance $r_g\Phi/C$, which extends over relatively wide ranges of r_g/C and $r_g\Phi/C$, reveals several regimes of the sectional flow structure. At the lowest value of r_g/C, a stable (attached)

leading-edge vortex exists over the entire range of $r_g\Phi/C$. At larger values of r_g/C and $r_g\Phi/C$, patterns of vorticity indicate that the leading-edge vortex lifts away from the wing surface until, at the combination of the largest values of r_g/C and $r_g\Phi/C$, the flow structure approaches that expected on a purely translating wing, whereby the separated vorticity layer is displaced well away from the surface of the wing.

Rotation of the wing to very large angle Φ, *i.e.*, through a number of revolutions such that a very large value of travel distance $r_g\Phi/C$ is attained, reveals if the asymptotic state of the flow structure differs from the structure at smaller travel distance. At a low value of Rossby number r_g/C, the highly coherent three-dimensional flow structure remains essentially intact with only minor degeneration of the iso-surfaces of Q-criterion. On the other hand, increase of the value of r_g/C by a factor of five yields a severely degraded flow structure at very large travel distance $r_g\Phi/C$.

The results at all travel distances indicate the significant role of rotation in maintaining coherent vortical structures. When the rotational influence is greatest (low Rossby number), coherent vortical structures persist regardless of travel distance. When this rotational influence is reduced (higher Rossby number), vortical structures are initially less coherent than at low Rossby number, and these structures degrade rapidly with increasing travel distance.

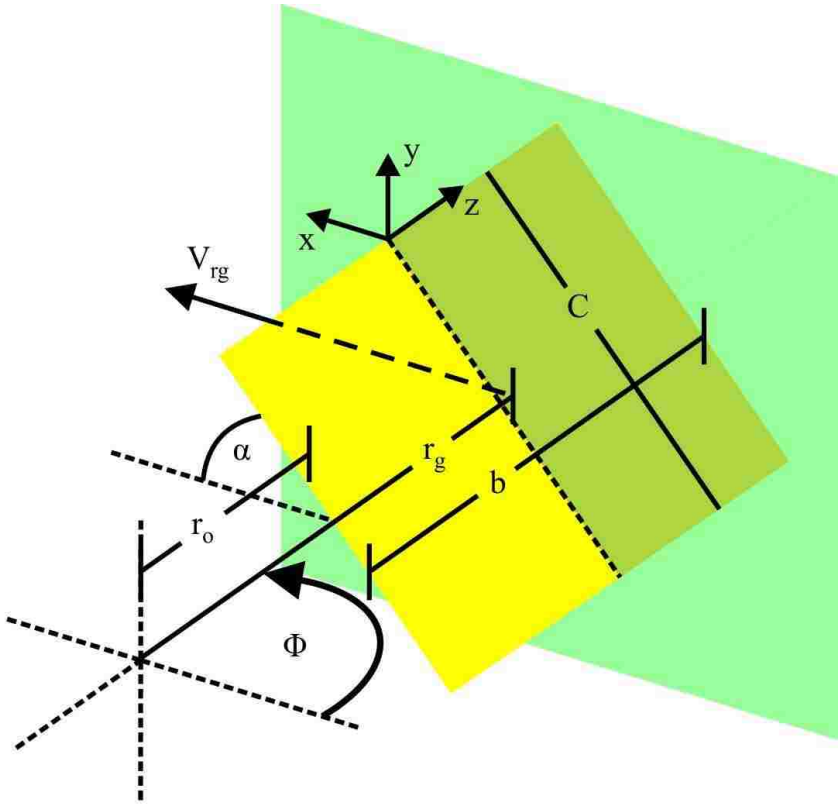

Figure 3.1. Schematic of rotating wing and relevant dimensions.

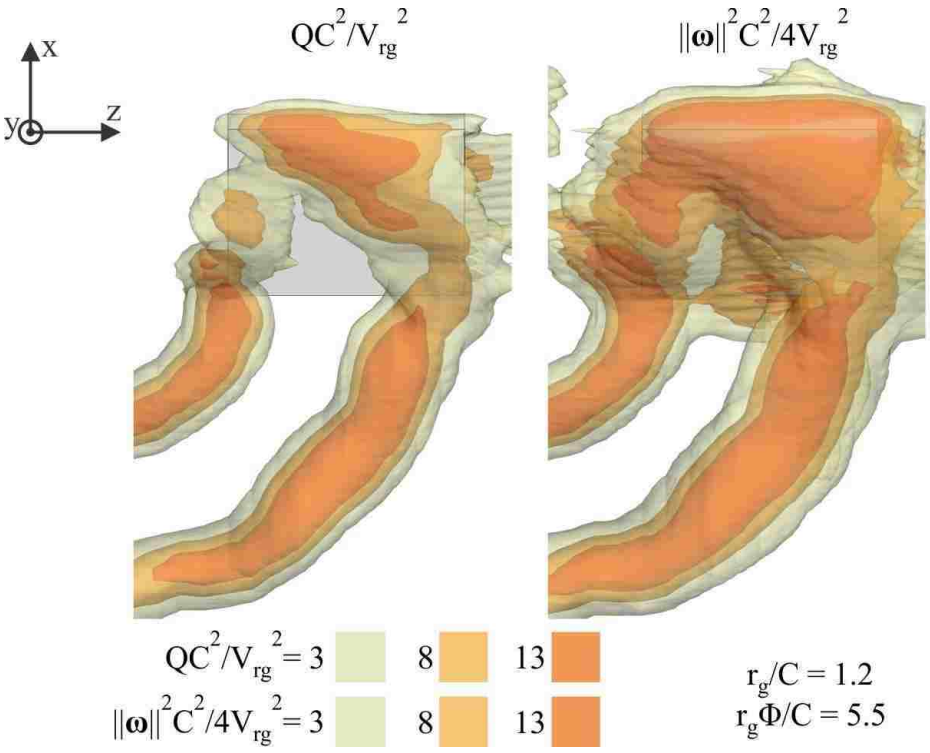

Figure 3.2. Transparent iso-surfaces of *Q*-criterion compared with transparent iso-surfaces of vorticity magnitude scaled to match *Q*-criterion; $r_g/C = 1.2$, $r_g\Phi/C = 5.5$.

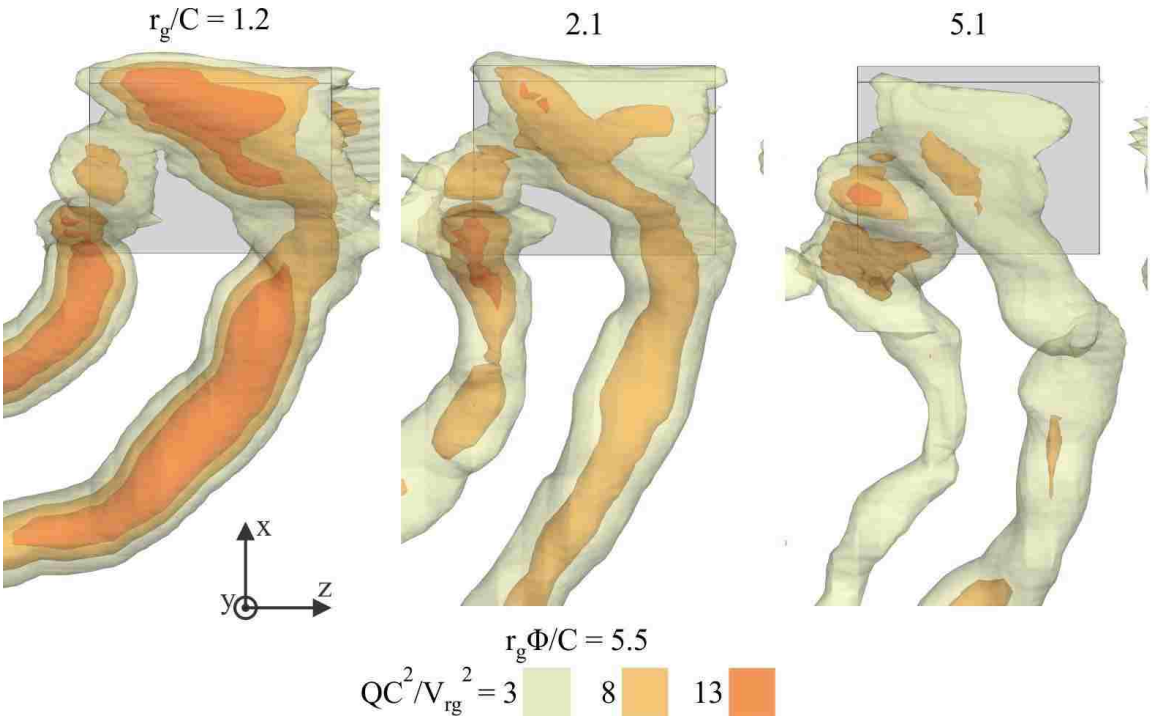

Figure 3.3. Transparent iso-surfaces of *Q*-criterion at different values of Rossby number r_g/C and $r_g\Phi/C$ = 5.5.

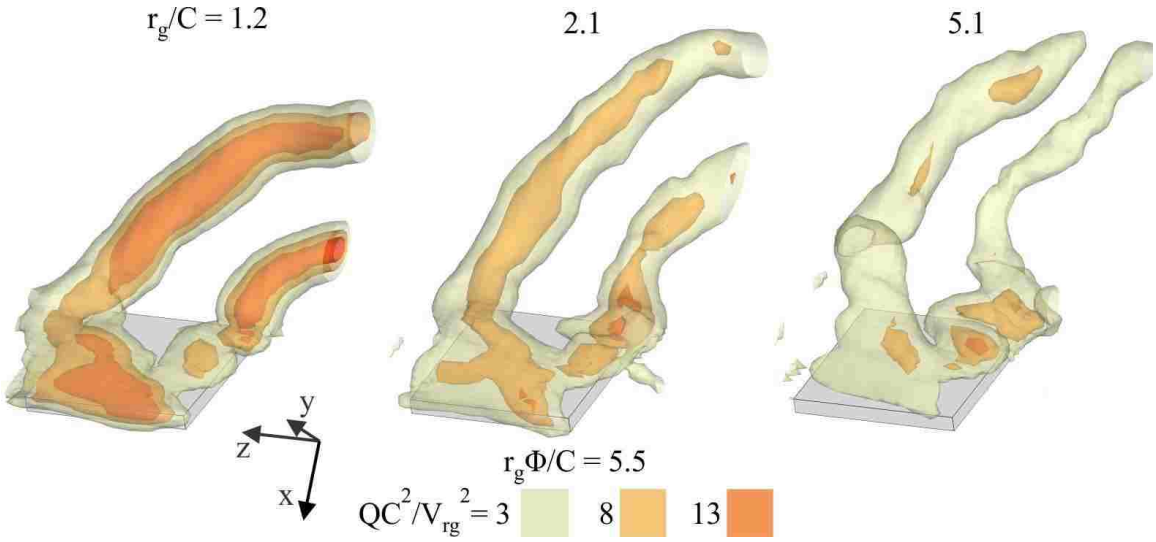

Figure 3.4. Transparent iso-surfaces of *Q*-criterion at different values of Rossby number r_g/C and $r_g\Phi/C = 5.5$.

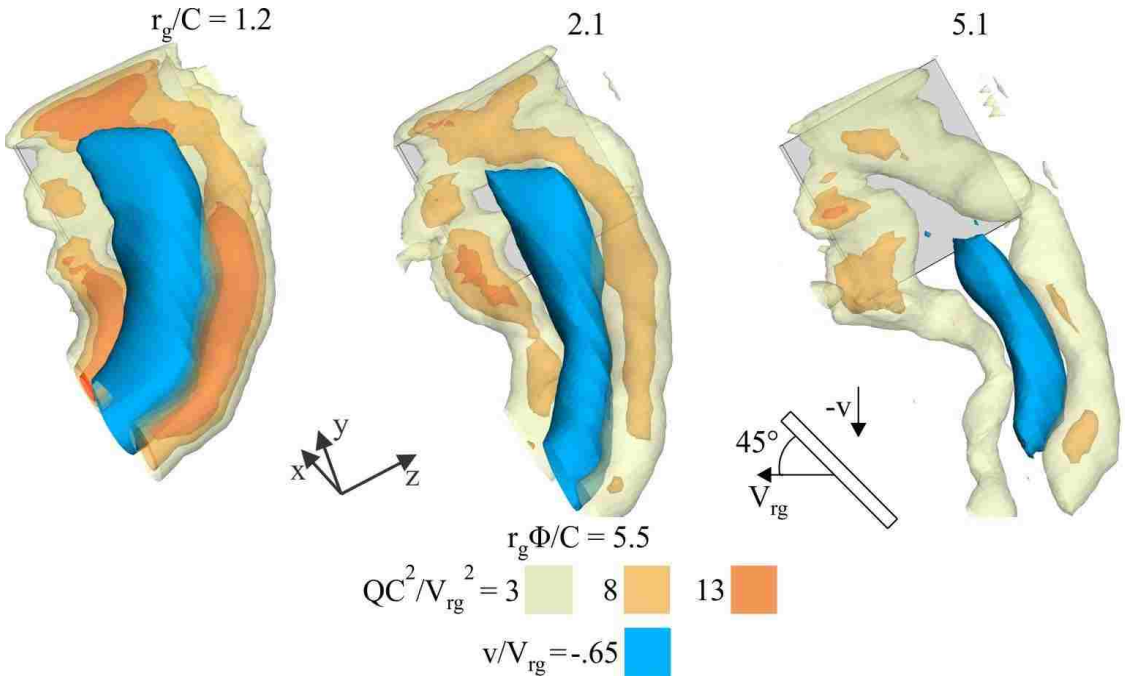

Figure 3.5. Transparent iso-surfaces of *Q*-criterion and opaque iso-surface of downwash (downward velocity) v/V_{rg} at different values of Rossby number r_g/C and $r_g\Phi/C$ = 5.5.

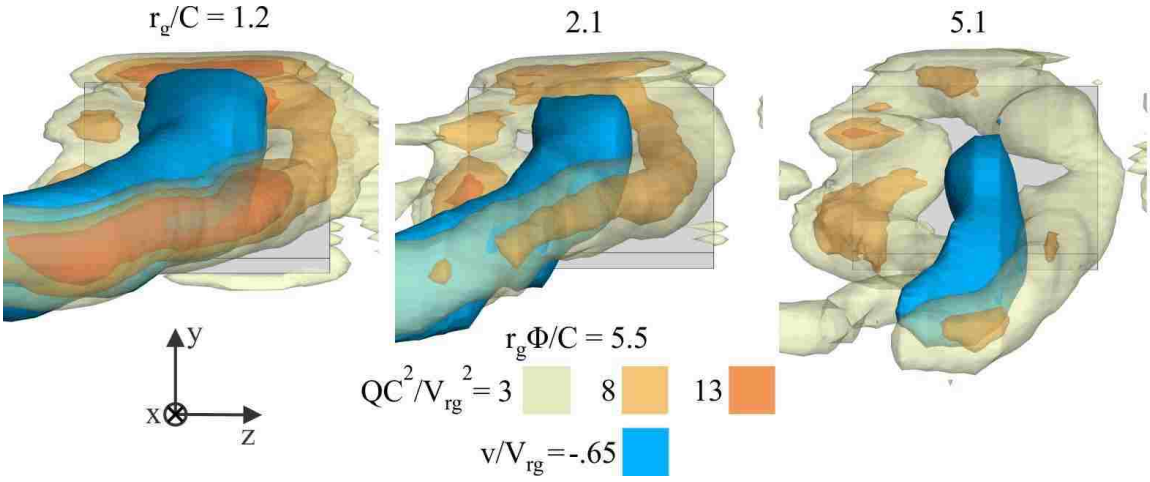

Figure 3.6. Transparent iso-surfaces of *Q*-criterion and opaque iso-surface of downwash (downward velocity) v/V_{rg} at different values of Rossby number r_g/C and $r_g\Phi/C$ = 5.5.

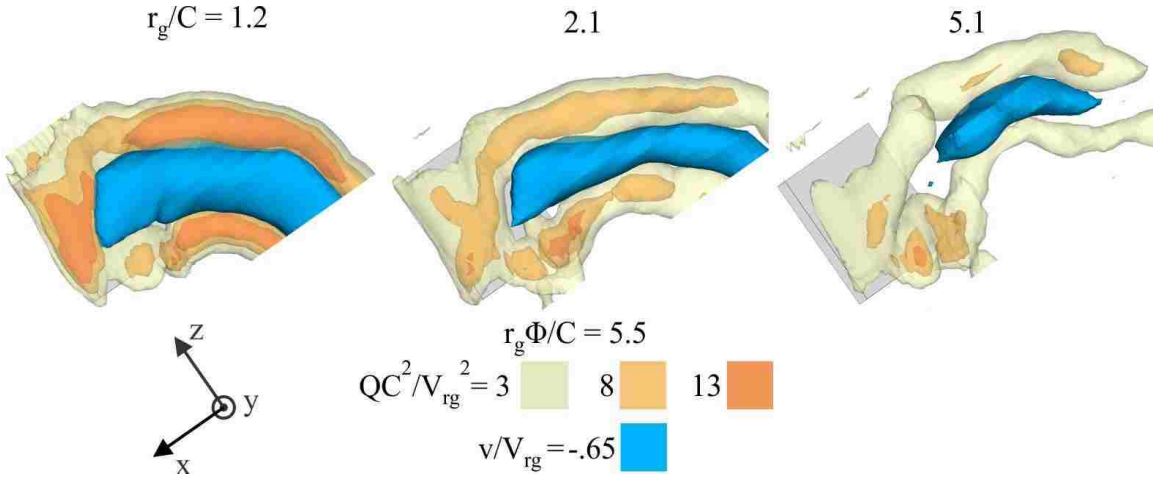

Figure 3.7. Transparent iso-surfaces of *Q*-criterion and opaque iso-surface of downwash (downward velocity) v/V_{rg} at different values of Rossby number r_g/C and $r_g\Phi/C$ = 5.5.

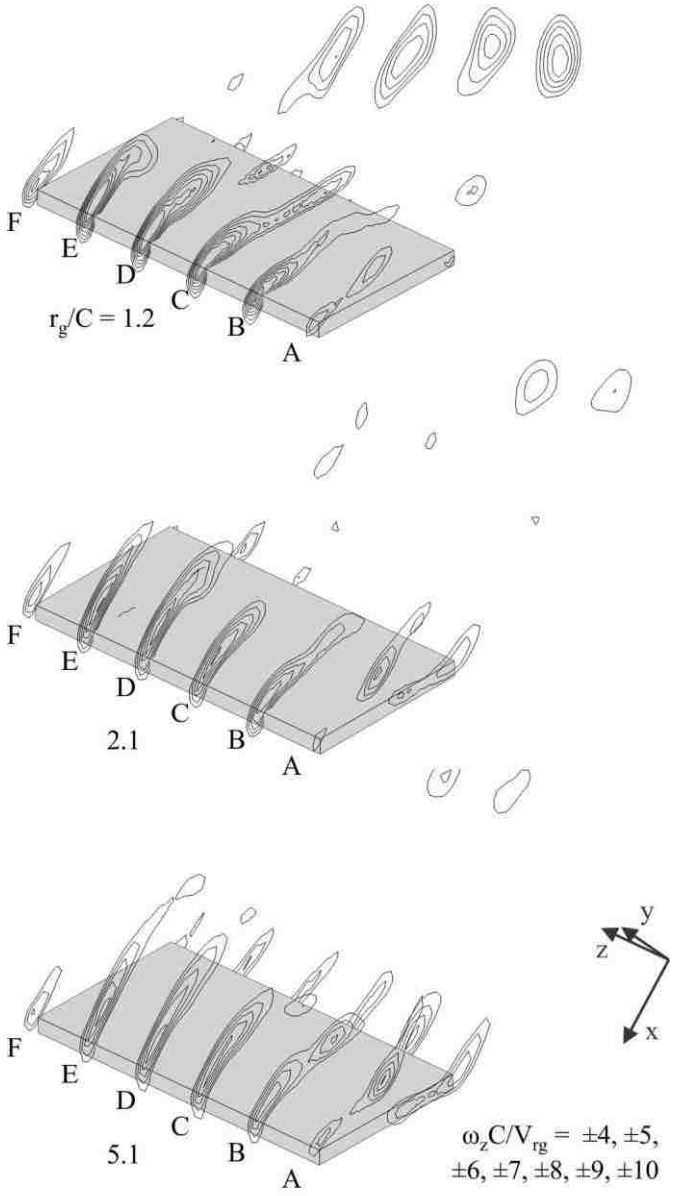

Figure 3.8. Sectional cuts of dimensionless spanwise $\omega_z C/V_{rg}$ in the range ±4 to ±10 at six spanwise locations for different values of Rossby number r_g/C. For all cases, the travel distance of the wing is $r_g \Phi/C$ = 5.5. The wing span is expanded to 200% of original dimension for visualization.

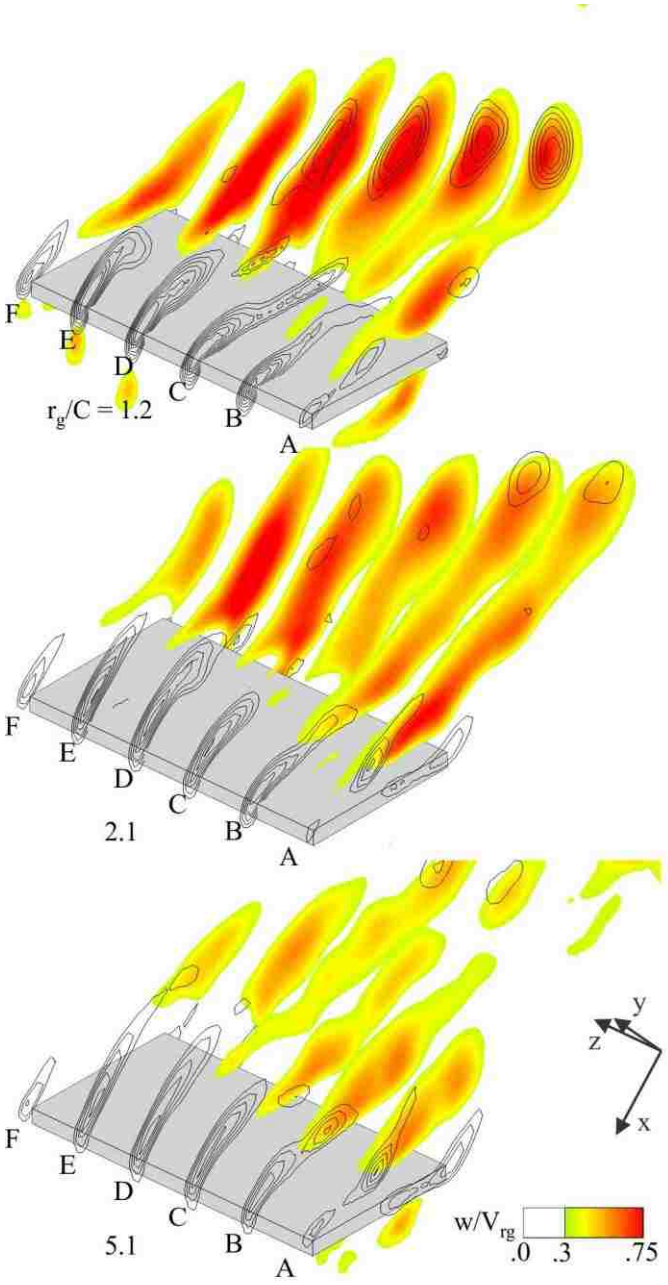

Figure 3.9. Sectional cuts of flow structure at six spanwise locations for different values of Rossby number r_g/C. Color contours of constant spanwise velocity are superposed on black line contours of constant spanwise vorticity. For all cases, the travel distance of the wing is $r_g\Phi/C$ = 5.5. The wing span is expanded to 200% of original dimension for visualization.

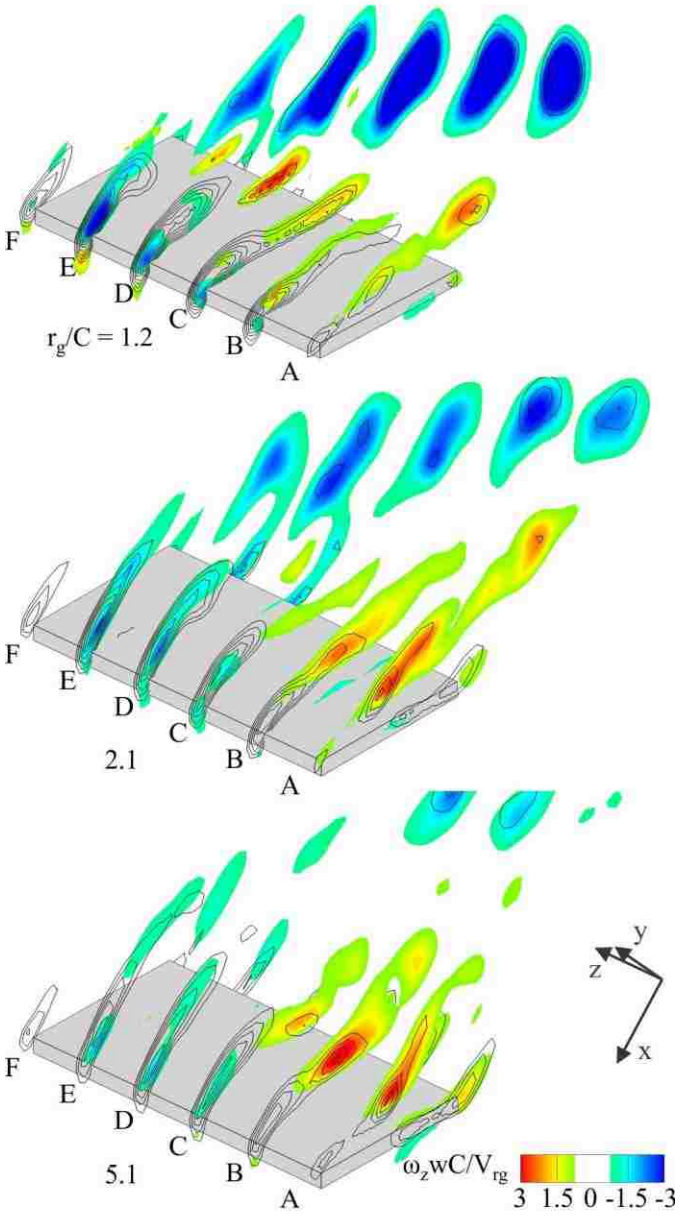

Figure 3.10. Sectional cuts of flow structure at six spanwise locations for different values of Rossby number r_g/C. Color contours of constant spanwise vorticity flux are superposed on black line contours of constant spanwise vorticity. For all cases, the travel distance of the wing is $r_g\Phi/C$ = 5.5. The wing span is expanded to 200% of original dimension for visualization.

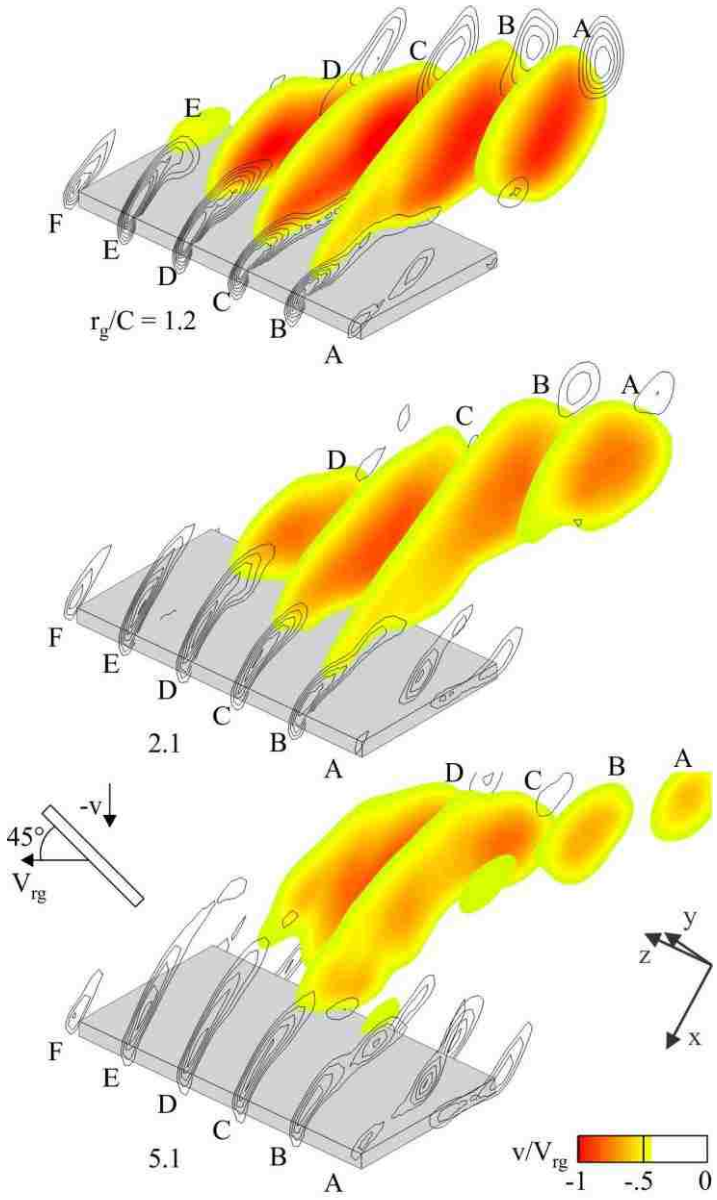

Figure 3.11. Sectional cuts of flow structure at six spanwise locations for different values of Rossby number r_g/C. Color contours of constant downward velocity component (downwash) are superposed on black line contours of constant spanwise vorticity. For all cases, the travel distance of the wing is $r_g\Phi/C$ = 5.5. The wing span is expanded to 200% of original dimension for visualization.

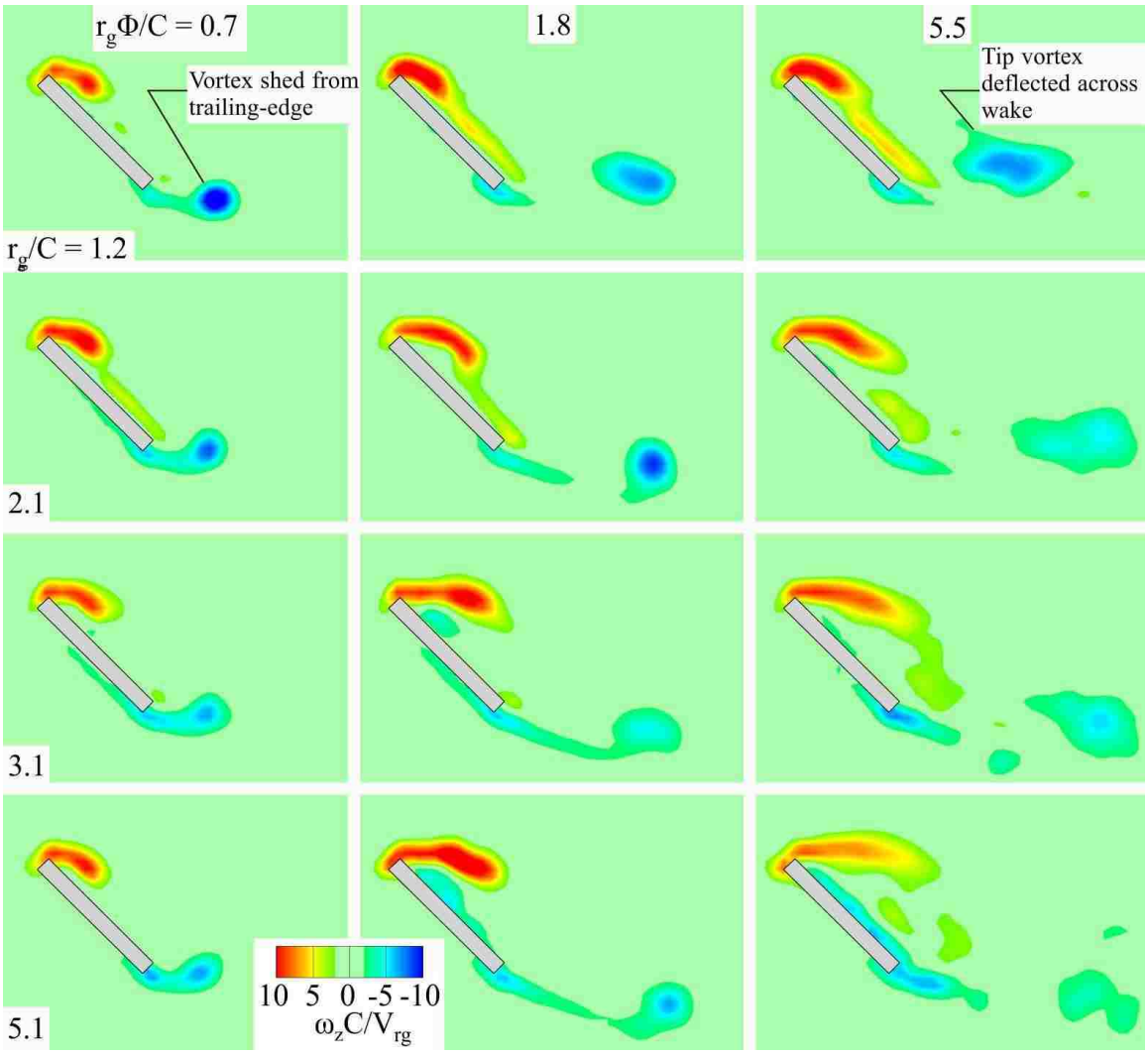

Figure 3.12. Sectional cuts at midspan of spanwise vorticity at different values of Rossby number r_g/C as indicated, and rotation distance $r_g\Phi/C$.

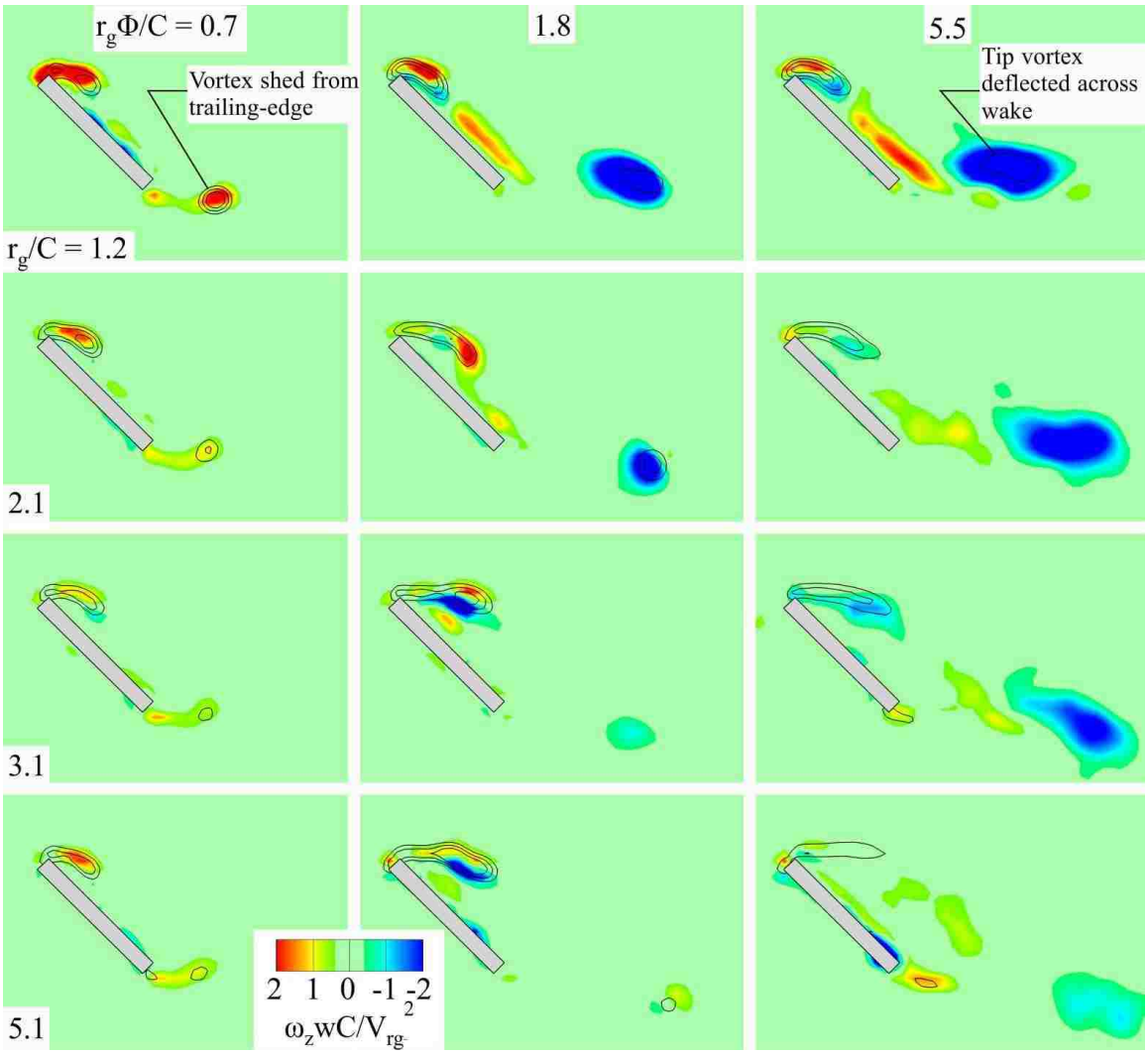

Figure 3.13. Sectional cuts at midspan of spanwise vorticity flux at different values of Rossby number r_g/C as indicated, and rotation distance $r_g\Phi/C$.

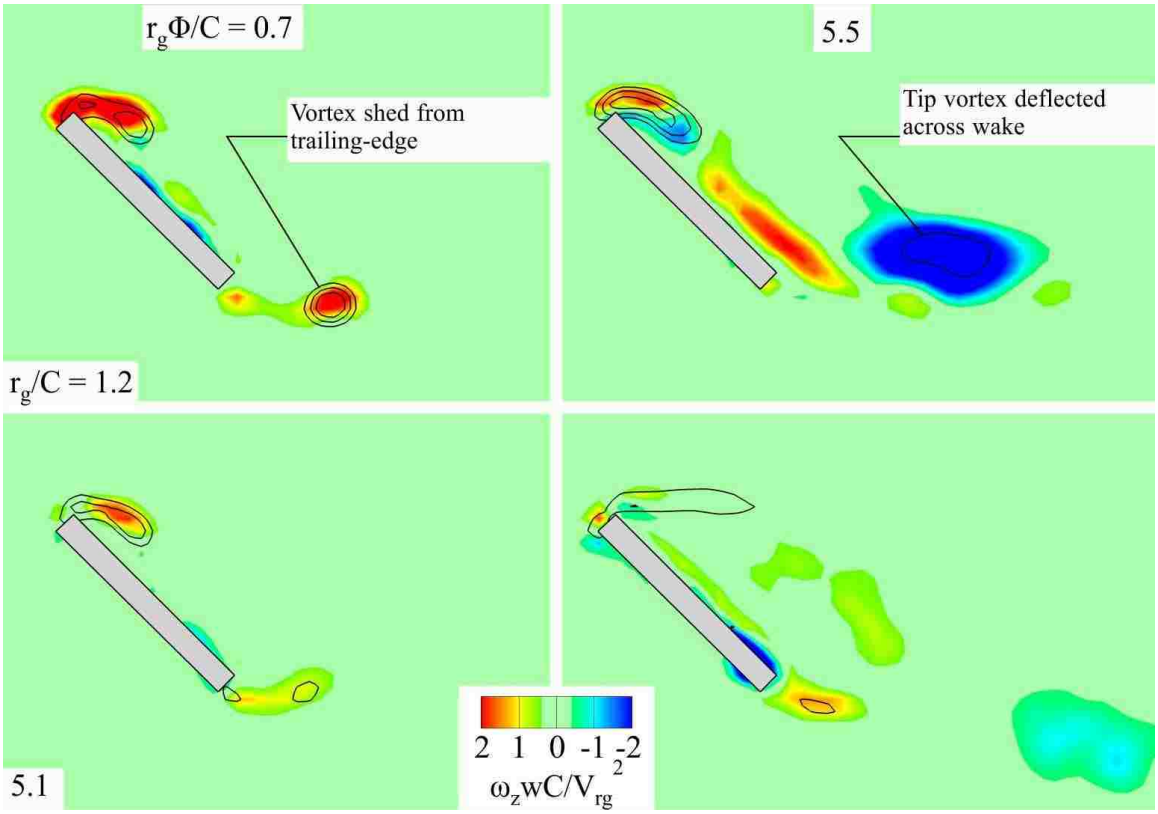

Figure 3.14. Sectional cuts at midspan of spanwise vorticity flux for extreme values of Rossby number r_g/C and rotation distance $r_g\Phi/C$.

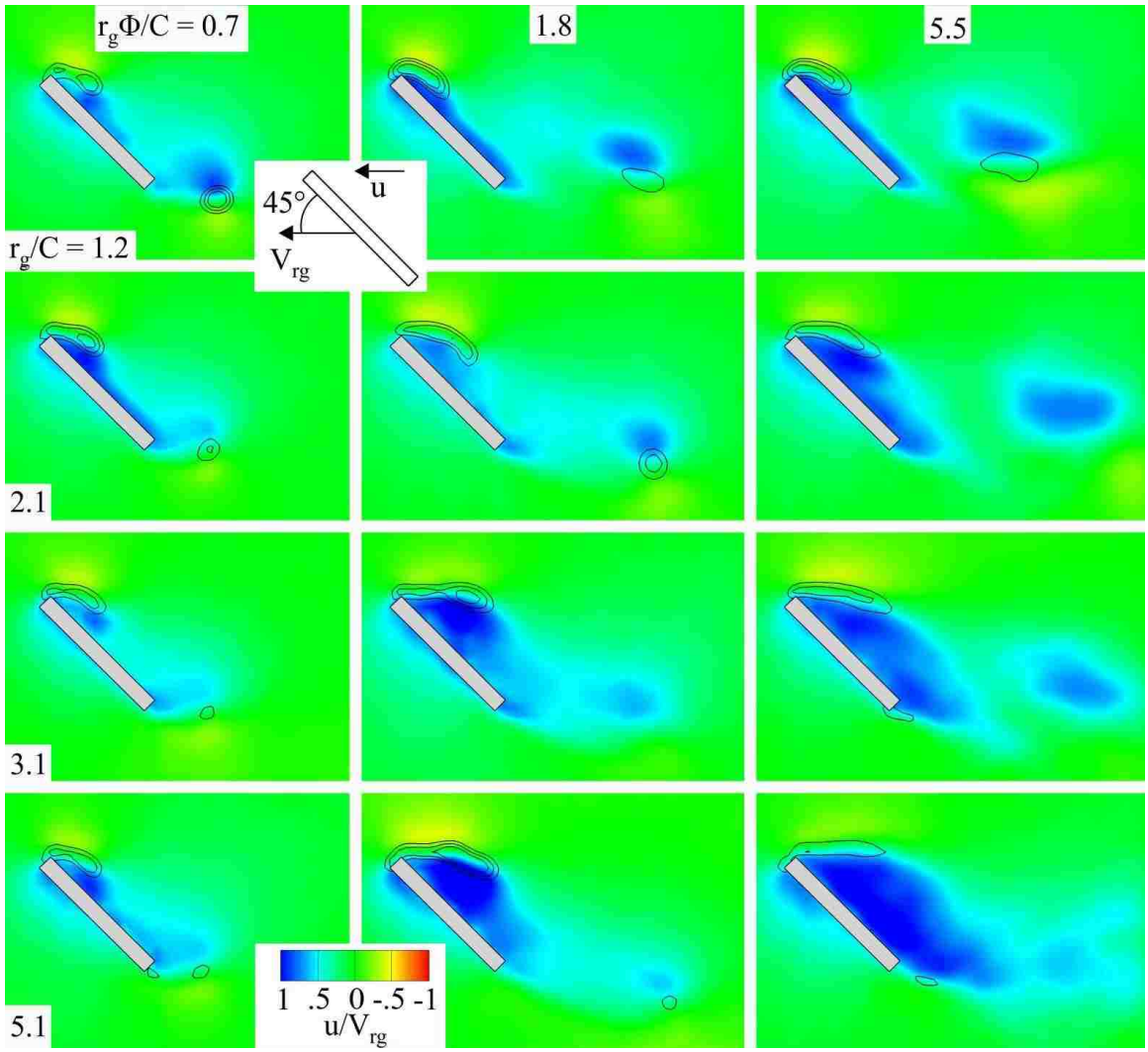

Figure 3.15. Sectional cuts at midspan of *u* velocity at different values of Rossby number r_g/C as indicated, and rotation distance $r_g\Phi/C$.

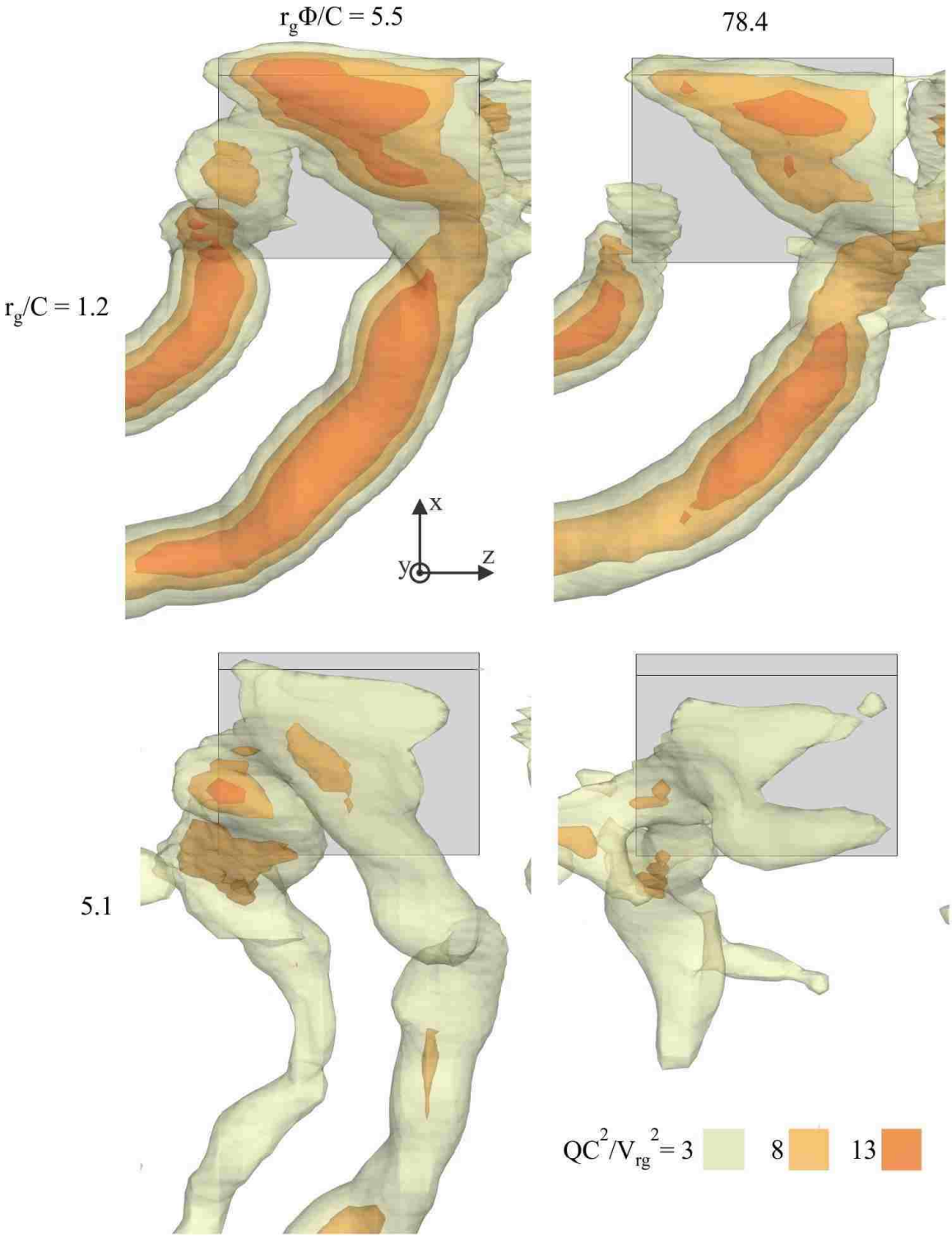

Figure 3.16. Transparent iso-surfaces of *Q*-criterion at different values of Rossby number r_g/C, and rotation distance $r_g\Phi/C$.

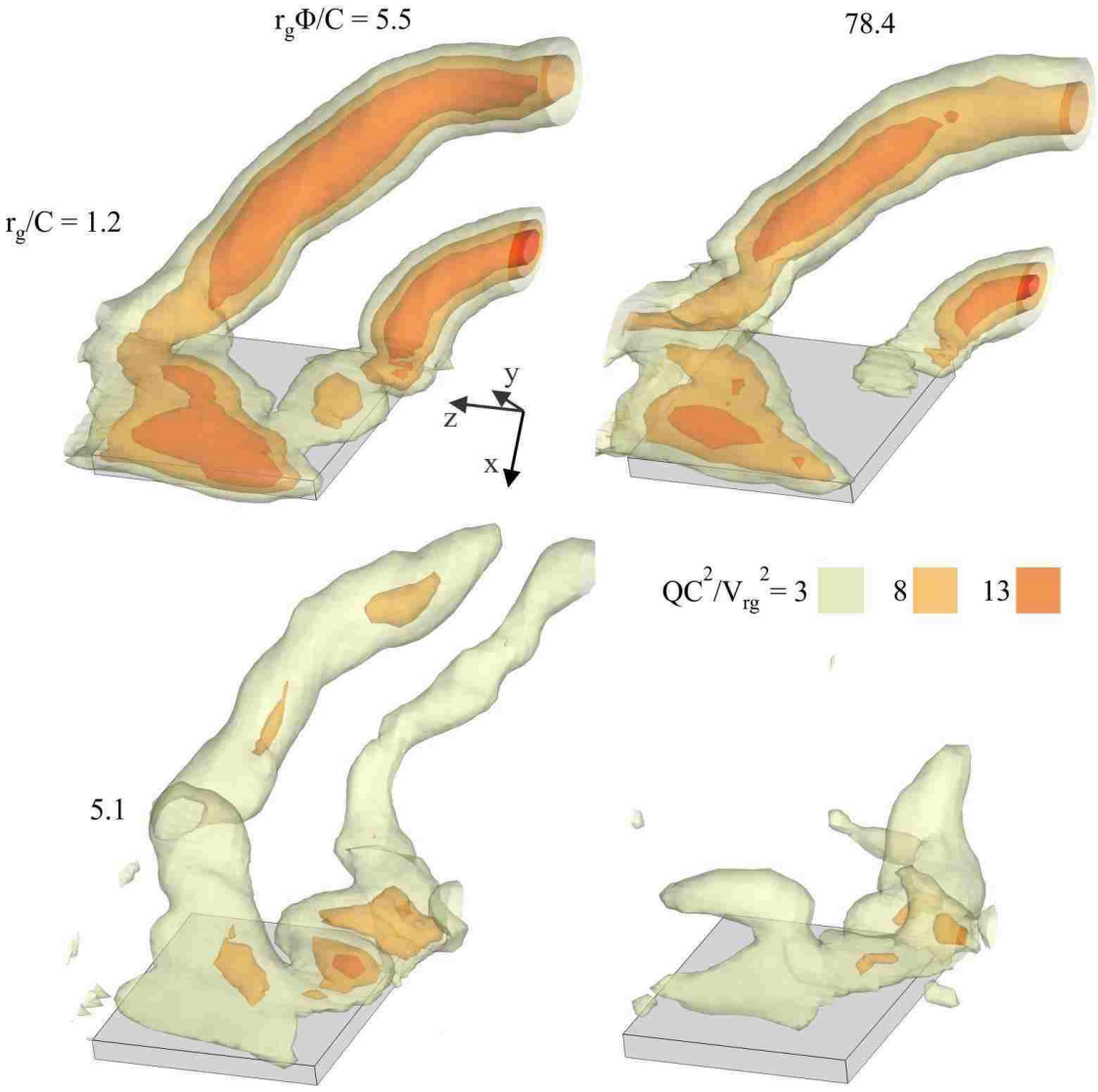

Figure 3.17. Transparent iso-surfaces of *Q*-criterion at different values of Rossby number r_g/C, and rotation distance $r_g\Phi/C$.

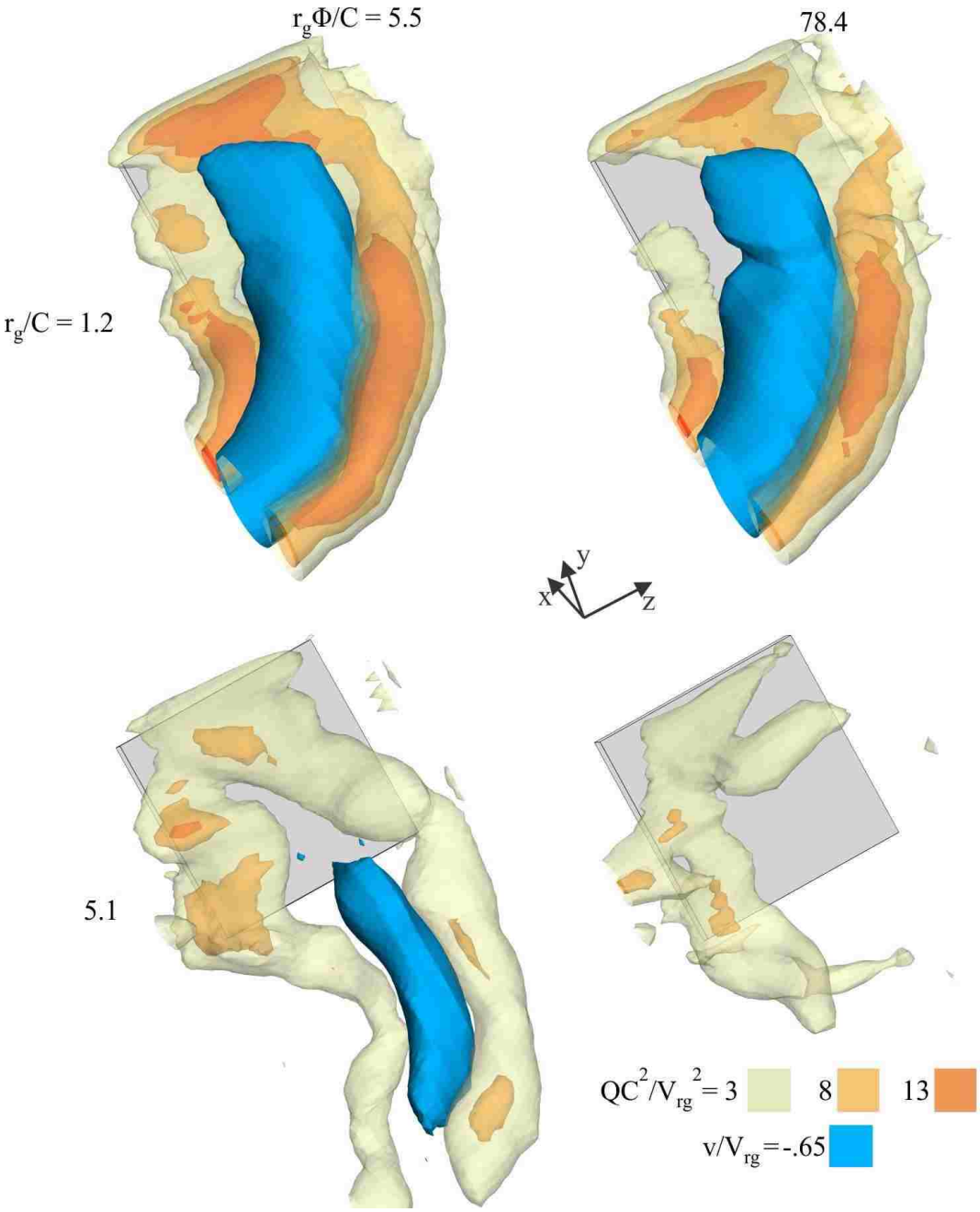

Figure 3.18. Transparent iso-surfaces of *Q*-criterion and opaque iso-surface of downwash (downward velocity) at different values of Rossby number r_g/C, and rotation distance $r_g\Phi/C$.

CHAPTER 4

FLOW STRUCTURE ON A WING OF MODERATE ASPECT RATIO

In this chapter, the stages of development of the flow structure along a wing having moderate aspect ratio (AR = 2) are characterized via particle image velocimetry. Volumetric and sectional representations of the flow patterns, in terms of vorticity, components of velocity, vorticity flux, and Q-criterion are determined at two radii of gyration r_g. This chapter is divided into subsections that provide an introduction to this part of the investigation, a description of the experimental systems specific to this chapter, an assessment of the quantitative flow visualization results, and concluding remarks.

4.1 BACKGROUND

In recent years, the development of the flow structure on rotating wings and rectilinearly translating wings at low Reynolds number *Re* and high angle of attack α has received substantial attention. Dickinson *et al.* (1999), Lentink and Dickinson (2009*b*), Garmann *et al.* (2013), Garmann, and Visbal (2013) each characterized the forces on wings undergoing these types of motions, and those investigations found an increase in lift and drag when a wing was rotated instead of rectilinearly translated. This increase in aerodynamic forces due to wing rotation has been associated with the impressive flight performance of small biological flyers, such as insects. The difference in aerodynamic loading on similar wings resulting from different classes of motion has motivated investigation into the development of the flow structure on these wings.

The transient flow structure on wings undergoing basic types of motions has been visualized qualitatively, using dye or bubble injection, as well as quantitatively, using particle image velocimetry or computational simulations. The investigations of Lentink and Dickinson (2009*b*), Kim and Gharib (2010), Jardin *et al.* (2012), Garmann *et al.* (2013), and Garmann and Visbal (2013) characterized the flow structure on a wing at low Reynolds number and high angle of attack that underwent both types of motion. In these studies, two classes of development of vortex structures have been observed: (i) stable leading-edge vortices; and (ii) arch vortices. These structures were respectively observed on wings undergoing rotation ($r_g/C = O(1)$), and rectilinear translation ($r_g/C = \infty$), *i.e.*,

wing rotation has been associated with a stable leading-edge vortex, and wing translation has been associated with an arch vortex.

Chapter 3 addressed the volumetric flow-structure on a rotating wing having low aspect ratio $AR = 1$; it was sensitive to the radius of gyration in the range $1.2 \leq r_g/C \leq 5.1$. However, the development of the flow structure along a wing having moderate aspect ratio at different radii of gyration r_g/C, which is more practically significant, has not been addressed. More specifically, the possibility of a radical change of the form of the three-dimensional vortical structure, due to only moderate alteration of the radius of gyration r_g/C, has not been pursued. Comparison of the basic forms of the vortical structure, on the basis of iso-Q, helicity, vorticity and downwash, has not been addressed. Such an assessment can lead to insight into the manner and duration of their evolution. This investigation addresses these issues through time-resolved, stereoscopic particle image velocimetry. The three-dimensional vortex systems are characterized via nested, transparent iso-surfaces of Q-criterion, iso-surfaces of Q-criterion colored with helical density, and iso-surfaces of downwash, as well as sectional slices of vorticity, downwash and tangential velocity.

4.2 EXPERIMENTAL SYSTEM AND TECHNIQUES

A large, free-surface water channel with test section dimensions 5435 mm x 613 mm was employed as the test facility. The water depth in this channel was maintained at

approximately 508 mm during experiments. All experiments were performed in quiescent fluid without inflow.

For the present experiments, an aspect ratio $AR = b/C = 2.0$ rectangular flat plate was used as a model wing. Figure 4.1 shows an isometric diagram of the wing and relevant dimensions. The wing had dimensions b = 55.2 mm and C = 25.4 mm. The thickness of the wing was t_w = 2.3 mm, corresponding to a thickness to chord ratio t_w/C = .09. The wing was supported at its midchord by a connecting rod of diameter 2.3 mm. This connecting rod was affixed to a vertical shaft of diameter 12.7 mm, which served as the rotation axis. The wing was located approximately 305 mm above the bottom surface of the test section.

A computer controlled stepper motor rotated the wing about a vertical axis as shown in figure 4.1. This motion involved rapid acceleration from rest to constant angular velocity. The flow around the wing was characterized as a function of wing travel distance $r_g\Phi/C$, where r_g is the radius of gyration and Φ is the angle of rotation of the wing, as shown in figure 4.1. The distance $r_g\Phi/C$ therefore corresponds to the length of the arc subtended by the radius of gyration of the wing. The motion was smoothed according to the function described by Eldredge *et al.* (2009). Smoothing was applied such that the profile of travel distance $r_g\Phi/C = f(t)$ at the radius of gyration of the wing was identical for all experiments. The wing reached constant tangential velocity at approximately $r_g\Phi/C$ = 0.5. The velocity at the radius of gyration during rotation at constant angular velocity was V_{rg} = 49 mm/s. This velocity yielded a Reynolds number

of $V_{rg}C/\nu$ = 1400, where ν is the kinematic viscosity of water. The angle of attack was α = 45° for all experiments. Two values of radius of gyration were investigated: r_g/C = 1.7 and r_g/C = 4.7. These values of r_g/C corresponded to root distances r_o = 16 mm and 92 mm.

Stereoscopic particle image velocimetry (SPIV) was employed to determine the sectional, quantitative flow structure along the rotating wing. The in-plane resolution (vector spacing) and magnification for the PIV calibration were respectively .05C and 7.1 pixels/mm.

Three-dimensional, phase-averaged volumes of the flow structure were constructed from averaged, three-dimensional velocity fields on sectional planes. Nine vector-fields were averaged at each section. The spacing of the sectional vector-fields was $\Delta z/C$ = 0.1, where Δz is the distance between adjacent planes. Each of the reconstructed volumes had the following minimum x, y and z dimensions: 4.8C x 6.7C x 2.9C. Chapter 2 gives an assessment of the uncertainty of the volumetric reconstruction technique employed in this investigation. Images were captured at an acquisition rate of 15 Hz to allow for temporal determination of the flow structure. This acquisition rate corresponded to a travel distance between volumetric reconstructions of $\Delta r_g \Phi/C$ = 0.13, *i.e.*, the temporal resolution of the experimental system allowed reconstruction of quantitative flow volumes at intervals of $\Delta r_g \Phi/C$ = 0.13. These volumetric reconstructions were then transformed from the lab-fixed frame of reference, inherent to PIV analysis, to a frame of reference in which the wing is stationary.

Figure 4.1 also shows the orientation of two coordinate systems relative to the rotating wing. The flow velocities described in this study correspond to the *xyz* coordinate system, *e.g.*, *u/Vrg*, which is the flow velocity in the direction of the *x*-axis. In this coordinate system, the *x* dimension is parallel to the tangential direction of wing rotation, the *y* dimension is orthogonal to both the tangential direction of wing rotation and the span of the wing, and the *z* dimension is parallel to the span of the wing. A second coordinate system, with spatial dimensions χ, η and ζ, is also provided for interpretation of different three-dimensional viewing perspectives. In this coordinate system, the χ and ζ dimensions are respectively parallel to the chord of the wing and the span of the wing, and the η dimension is orthogonal to the leeward and windward surfaces of the wing.

4.3 VOLUMETRIC FLOW STRUCTURE

4.3.1 Iso-surfaces of flow structure

Figures 4.2 through 4.6 show the effects of radius of gyration r_g/C, and travel distance $r_g\Phi/C$ on nested, transparent iso-surfaces of qC^2/V_{rg}^2. The equation for q is:

$$qC^2/V_{rg}^2 = 0.5[\ \Omega_{ij}\Omega_{ij} - S_{ij}S_{ij}\ ] = 0.5[\ ||\Omega||^2 - ||S||^2\ ] \qquad (3.1)$$

Nested, transparent iso-surfaces at values of qC^2/V_{rg}^2 = 2, 7, and 15 are represented respectively by gray-yellow, brown-orange and orange colors. These iso-surfaces therefore indicate regions of the flow where rotation $||\boldsymbol{\Omega}||^2$ dominates

irrotational strain $||S||^2$. Herein references to Q represent the non-dimensionalized Q-criterion, which is defined as $Q = qC^2/V_{rg}^2$.

Figure 4.2 shows the initial development of the flow structure at $r_g\Phi/C = 0.5$. Three perspective views of these iso-surfaces are shown in each figure: (from top) front; plan; and trimetric-views. A diagram of the wing, showing the orientation of each view relative to the $\chi\eta\zeta$ coordinate system, is indicated in the inset in the center of each row of images. The center of rotation (not shown) is located to the left of the wing. The flow structure at this early stage is similar for both values of radius of gyration r_g/C. The $Q = 2$ iso-surfaces indicate a vortex loop located adjacent to the leading-edge, tip, and trailing-edge of the wing. Higher level $Q = 7$ and 15 iso-surfaces are most prevalent in the leading-edge region for both radii of gyration. At $r_g/C = 1.7$, the iso-surfaces associated with elevated levels of Q-criterion $Q = 7$ and $Q = 15$ are more concentrated on the portion of the wing outboard of its midspan, and the $Q = 2$ iso-surface in the leading-edge region tends towards a conical shape. In contrast, the $Q = 2$ and 7 iso-surfaces are more evenly distributed along the leading-edge at $r_g/C = 4.7$. For both values of r_g/C, the Q-criterion iso-surfaces are located very close to the surface of the wing in the regions of the leading-edge and the tip of the wing. The tip-vortex at $r_g/C = 1.7$ contains a larger extent of the iso-surface of $Q = 7$ compared to the tip vortex at $r_g/C = 4.7$. Regarding the starting

vortex from the trailing-edge at r_g/C = 4.7, it contains a large surface of Q = 7; in contrast, the starting vortex at r_g/C = 1.7 is dominated by the lower level Q = 2 surface.

Figure 4.3 shows the flow structure at $r_g\Phi/C$ = 1.5, *i.e.*, after the wing has traveled 1.5 chord lengths. The higher level Q = 7 and 15 iso-surfaces have increased in spatial extent in the cores of both leading-edge vortices, and have begun to lift away from the wing surface at both radii of gyration. At r_g/C = 1.7, this lift-off occurs predominantly on the outboard portion of the wing, close to the wing tip. In fact, in the leading-edge region, the distance from the wing surface to the Q = 7 and 15 iso-surfaces is proportional to the distance along the span, *i.e.*, the interior of the leading-edge vortex is near the wing at its root, and farthest from the wing near the tip. On the other hand, at r_g/C = 4.7, the leading-edge vortex remains 'pinned' or close to the wing at the corners of the leading-edge. At both radii of gyration, the strength of the tip vortex has increased relative to its strength at $r_g\Phi/C$ = 0.5 (compare figure 4.2), as indicated by larger Q = 7 and Q = 15 iso-surfaces near the wing tip. At the smaller radius of gyration r_g/C = 1.7, the iso-surface corresponding to the highest level of Q = 15 within the tip vortex has a larger spatial extent compared to r_g/C = 4.7. This tip vortex extends into the wake, where it connects to the shed (starting) vortex at both r_g/C = 1.7 and 4.7.

Figure 4.4 shows further development of the flow structure at a larger travel distance $r_g\Phi/C$ = 2.0. At r_g/C = 1.7, the change in Q-criterion iso-surfaces between

figures 4.3 and 4.4 is minor. In contrast, the flow structure at r_g/C = 4.7 is substantially altered. Specifically, the leading-edge vortex continues to lift-off the surface of the wing, and takes the form of an arch-vortex. This observation of an arch vortex represents the first characterization of such a structure on a rotating wing. That is, as the radius of gyration becomes sufficiently large, the effects of centripetal acceleration and radial pressure gradient that promote formation of the attached, conical leading-edge vortex (Garmann and Visbal, 2013) give way to formation of an arch vortex. This vortical structure was originally computed for rectilinear plunging motion by Visbal (2011), and confirmed experimentally for rectilinear pitching to high angle of attack in presence of inflow by Yilmaz and Rockwell (2011). Visbal *et al.* (2013) further assessed the computational and experimental studies of the arch vortex on a plunging wing. Further investigations of the arch vortex involve computations for an impulsively started, rectilinearly translating wing at high angle of attack (Garmann *et al.* 2013), and a wing undergoing hover motion in a rectilinear mode (Garmann and Visbal, 2013). In figure 4.4, the Q = 7 and Q = 15 iso-surfaces form the legs of the arch vortex at r_g/C = 4.7. These legs appear to have evolved from the Q = 7 iso-surfaces that were pinned to the leading-edge corners of the wing at $r_g\Phi/C$ = 1.5 in figure 4.3. They have shifted toward the midspan of the wing, *i.e.*, they have pinched together relative to their location at $r_g\Phi/C$ = 1.5. For both values of r_g/C in figure 4.4, the Q = 7 and 15 iso-surfaces within the tip vortex are now evident in the region of the trailing-edge of the wing (see plan

view of figure 4.4), and, in the tip region located upstream of the trailing-edge of the wing, the flow structure is dominated by the lowest level of $Q = 2$.

The flow development from $r_g\Phi/C = 0.5$ to $r_g\Phi/C = 2.0$ at small radius of gyration, shown in figures 4.2 through 4.4, is similar to that computed on an impulsively started rotating wing (Garmann *et al.* 2013), and a reciprocating wing undergoing rotational motion (Garmann and Visbal, 2013). That is, when the radius of gyration is small, an attached leading-edge vortex forms quickly and persists as the wing rotates. At moderate radius of gyration, the flow structure closely resembles that computed on an impulsively started rotating wing (Garmann *et al.* 2013), and a reciprocating wing undergoing rectilinear motion (Garmann and Visbal, 2013). For those type of motion, an arch vortex forms on the wing, and the development of this structure is not as rapid.

Figure 4.5 shows further development of the flow structure at a travel distance of $r_g\Phi/C = 3.0$. The $Q = 7$ and $Q = 15$ iso-surfaces in the leading-edge vortex have moved downstream, and decreased in spatial extent, relative to $r_g\Phi/C = 2.0$. Along with these changes to the vortical structure of the leading-edge vortex, the tip vortex is now increasingly deflected toward the center of rotation at $r_g\Phi/C = 3.0$; at $r_g\Phi/C = 2.0$, it was approximately parallel to the tangential velocity of the wing. In figure 4.5, at $r_g/C = 4.7$, the legs of the arch-vortex continue to move together (pinch), thereby continuing the trend observed at smaller travel distances $r_g\Phi/C$. Simultaneously, the arch vortex also moves further away from the wing surface (as evident in the top row of the figure 4.5),

and in the downstream direction (evident in the middle row of figure 4.5). The iso-surfaces of Q associated with this structure no longer directly connect to the tip-vortex, even at the lowest value Q = 2. The higher value Q = 7 and 15 iso-surfaces within the arch vortex decrease in spatial extent and undergo distortion, indicating loss of coherence.

The effect of radius of gyration r_g/C on vortex formation up to this value of travel distance $r_g\Phi/C$ is as follows. When r_g/C is sufficiently small, a coherent leading-edge vortex forms on the wing, and this vortex reaches a developed state at a travel distance of $r_g\Phi/C$ = 1.5, *i.e.*, the vortical structure near the wing does not significantly change after $r_g\Phi/C$ = 1.5. In contrast, at a larger value of r_g/C = 4.7, the development of the flow structure leads to an arch vortex. Similar types of vortical structures were observed respectively on both impulsively started rotating and rectilinearly translating wings (Kim and Gharib 2010; Garmann *et al.* 2013), and rotating and rectilinearly translating wings in simulated hover motion (Jardin *et al.* 2012; Garmann and Visbal, 2013). In the studies of Garmann *et al.* (2013), and Garmann and Visbal (2013), the coherent leading-edge vortex was associated with significantly higher negative pressure on the leeward side of the wing than the arch vortex evident on the rectilinearly translating wings. Greater lift and drag forces accompanied the increased negative pressure beneath the leading-edge vortex on the rotating wing.

Figure 4.6 shows the flow structure after the wing has rotated through 5.5 chords of travel, *i.e.*, $r_g\Phi/C$ = 5.5. At r_g/C = 1.7, the Q = 2 iso-surface is similar to the Q = 2 iso-

surface observed at $r_g\Phi/C$ = 3.0, and the coherent leading-edge vortex and tip vortex continue to dominate the flow structure. The Q = 7 and 15 iso-surfaces have shifted upstream toward the leading-edge of the wing. The branched structure of the Q = 7 iso-surface indicates periodic shedding of high level vortical structures from the leading-edge, within the leading-edge vortex. The tip vortex no longer contains high level Q = 7 and 15 iso-surfaces, but this loss of coherence in the tip vortex does not appear to affect the coherence of the leading-edge vortex negatively. In comparison, the flow structure at r_g/C = 4.7 substantially changes from its form at $r_g\Phi/C$ = 3.0 (compare figure 4.5). At $r_g\Phi/C$ = 5.5 in figure 4.6, the arch vortex has been swept downstream and is no longer in the field of view. The region along the surface of the wing that was previously occupied by the arch vortex is largely devoid of highly level Q = 7 and 15 iso-surfaces. The low level Q = 2 iso-surfaces along the wing indicate a degree of recovery of a very weak leading-edge vortex that extends approximately from the root to the midspan of the wing, but it is much weaker than the vortex at r_g/C = 1.7. The iso-surfaces of Q-criterion at r_g/C = 4.7 also indicate loss of a coherent tip vortex.

Figure 4.7 indicates iso-surfaces of Q = 4.5 colored with helical density h, also known as helicity. The equation for h is:

$$h = \mathbf{V}\cdot\boldsymbol{\omega} = u\omega_x + v\omega_y + w\omega_z. \qquad (4.2)$$

Elevated magnitudes of h indicate regions where the velocity $\boldsymbol{V}$ and vorticity $\boldsymbol{\omega}$ are sufficiently large and tend to be aligned with each other. These regions are associated

with significant flow along the rotation axis of a vortex, which results in helical streamline patterns. Helicity h can also be interpreted as the flux of vorticity along the rotation axis of a vortex (Moffatt, 1969). Herein H represents the non-dimensionalized helical density, which is defined as $H = hC/V_{rg}^{2}$. A trimetric view perspective (bottom rows of figures 4.2 through 4.6) is employed for this figure. Four travel distances $r_g\Phi/C$ = 0.5, 1.5, 2.5, and 5.5 are represented.

The top row of figure 4.7 shows patterns of positive (blue), and negative (red) helicity shortly after the onset of wing motion, *i.e.,* at $r_g\Phi/C$ = 0.5. At this early stage of the flow development, similar patterns of helicity H are apparent for both radii of gyration r_g/C = 1.7 and 4.7. Large magnitude positive (blue) H occurs along the tip vortices, and negative (red) H along the leading-edge vortices. The larger scale tip vortex at r_g/C = 1.7 shows large magnitude (darker) positive H over a larger extent.

The second row of figure 4.7 shows the distribution of helical density H at $r_g\Phi/C$ = 1.5. The iso-surfaces of Q are similar at r_g/C = 1.7 and 4.7; they consist of a coherent vortex across the leading-edge and tip of the wing, which forms a loop with the starting, *i.e.*, trailing, vortex, that has less spatial extent. However, the distribution of H along these iso-surfaces is remarkably different. At r_g/C = 1.7, large magnitude, positive (blue) H is evident across both the leading-edge vortex and the tip vortex, and it extends along the tip vortex into the wake. This consistent positive (blue) H along the Q iso-surface

indicates unidirectional flux of vorticity along this three-dimensional vortical structure. At r_g/C = 4.7, however, the magnitude of H is smaller along the leading-edge vortex (lighter blue and red colors), and the sign of H alternates between negative (red) and positive (blue). This pattern indicates lack of a unidirectional vorticity flux along the iso-surface.

The third row in figure 4.7 indicates the further development of patterns of H at $r_g\Phi/C$ = 2.5. At r_g/C = 1.7, the Q iso-surface and distribution of H along the iso-surface are generally similar to those at $r_g\Phi/C$ = 1.5. The primary difference appears in the junction between the leading-edge and tip vortices. In this region, the Q iso-surface is not as compact and organized as at $r_g\Phi/C$ = 1.5. In comparison with this general preservation of the forms of Q and H at r_g/C = 1.7, the corresponding patterns at r_g/C = 4.7 change significantly from $r_g\Phi/C$ = 1.5 to 2.5. The Q iso-surface now indicates a well-defined arch vortex, as shown in figures 4.3 and 4.4. The magnitude of H on the arch vortex iso-surface is further reduced from the levels apparent at $r_g\Phi/$C = 1.5. Along with the reduction (lighter color) of the level of H in the arch vortex, the magnitude of H along the tip vortex is also reduced.

The bottom row of images in figure 4.7 corresponds to $r_g\Phi/C$ = 5.5, that is, well after the onset of wing motion. The flow structure at the smaller radius of gyration r_g/C = 1.7 has changed significantly, relative to the structure at $r_g\Phi/C$ = 2.5. In particular, the

iso-Q surface that represents the tip vortex is less organized and has a smaller spatial extent. Additionally, a region of Q-criterion with large magnitude negative (red) H has formed near the junction between the trailing-edge and tip of the wing. Remarkably, the overall form of the leading-edge vortex shows only minor alterations, that is, the iso-Q surface representing the leading-edge vortex is largely unchanged from $r_g\Phi/C$ = 2.5 to 5.5. The level of H along that iso-surface is, however, no longer uniformly positive (blue). At r_g/C = 4.7, the change in the iso-Q surface and helicity H is more dramatic. The arch vortex, evident at $r_g\Phi/C$ = 2.5, is absent at $r_g\Phi/C$ = 5.5. It has been replaced by a smaller, coherent leading-edge vortex that terminates near the midspan of the wing. This small leading-edge vortex is not associated with significant helicity.

Figure 4.8 shows (opaque) iso-surfaces of elevated downward velocity or downwash v/V_{rg} = 0.65, superposed on the (transparent) iso-Q surfaces shown in figures 4.2 through 4.6. A plan view perspective (middle row of figures 4.2 through 4.6) is employed for this figure. The four travel distances displayed in figure 4.7, $r_g\Phi/C$ = 0.5, 1.5, 2.5, and 5.5, are represented in figure 4.8.

The first row of figure 4.8 corresponds to a travel distance of $r_g\Phi/C$ = 0.5. At this travel distance, the Q = 2 iso-surfaces at both radii of gyration have significant spatial extent, but the v/V_{rg} iso-surfaces do not. The formation of a small region of elevated downwash at r_g/C = 1.7 is adjacent to the Q = 15 iso-surface at that radius of gyration.

This observation indicates that coherent vortex formation occurs before significant downwash is established on the leeward side of the wing.

Images of the downwash and the *Q*-criterion iso-surfaces at $r_g\Phi/C$ = 1.5 are represented in the second row of figure 4.8. At this travel distance, the spatial extent of the elevated downwash region is much larger than at $r_g\Phi/C$ = 0.5 for both radii of gyration. At r_g/C = 1.7, the (opaque) downwash iso-surface has formed downstream of the coherent leading-edge vortex, and inboard of the coherent tip vortex. This iso-surface continues downstream along the tip vortex, past the trailing-edge of the wing and into the wake (out of the image). At r_g/C = 4.7, the downwash v/V_{rg} iso-surface has a different shape and smaller spatial extent than at r_g/C = 1.7. At this radius of gyration, the majority of the v/V_{rg} iso-surface is immediately behind the *Q* iso-surfaces that represent the forming arch vortex. Near the tip of the wing, the coherent tip vortex induces an additional downwash region, which extends approximately 0.25*C* past the trailing-edge.

The third row of images in figure 4.8 corresponds to $r_g\Phi/C$ = 2.5. At r_g/C = 1.7, the overall structure of the *Q* iso-surfaces is similar to that at $r_g\Phi/C$ = 1.5. The most significant change occurs in the tip region, where the tip vortex appears to become less organized at $r_g\Phi/C$ = 2.5. The spatial extent of the v/V_{rg} iso-surface increases from $r_g\Phi/C$ = 1.5 to 2.5. At r_g/C = 4.7, the *Q*-criterion iso-surfaces indicate movement of the arch vortex toward the trailing-edge of the wing. This movement forces the v/V_{rg} iso-

surface downstream as well. The spatial extent of the downwash region near the root of the wing also increases, possibly due to induction from the left side of the arch vortex and the root vortex.

The bottom row of figure 4.8 corresponds to a travel distance of $r_g\Phi/C$ = 5.5. At r_g/C = 1.7, there is an increase in the spatial extent of the Q iso-surfaces in the leading-edge and tip regions. This increase in spatial extent is accompanied by a shift of the downwash iso-surface toward the root of the wing, in accord with the larger Q-criterion iso-surface in the tip region. Overall, the iso-Q surfaces at r_g/C = 1.7 are similar at $r_g\Phi/C$ = 2.5 and 5.5. At r_g/C = 4.7, the changes to both Q-criterion and v/V_{rg} iso-surfaces between $r_g\Phi/C$ = 2.5 and 5.5 are more pronounced. The Q iso-surfaces indicate that the arch vortex is no longer present at $r_g\Phi/C$ = 5.5. Higher-level Q iso-surfaces are no longer present, and, along with this change, the large v/V_{rg} iso-surface seen at $r_g\Phi/C$ = 2.5 is also absent. Instead, there is a significantly smaller region of elevated downwash between the Q = 2 iso-surfaces that represent the root vortex and the leading-edge vortical structure.

4.3.2 Multiple sectional patterns along span

Figures 4.9 through 4.11 indicate sectional cuts of the flow structure at eight spanwise locations A through F along the wing. In order to indicate the distinctions

between features on adjacent sectional cuts, the span of the wing is stretched by a factor of 1.5 in these layouts. A diagram showing the orientation of each view relative to the $\chi\eta\zeta$ coordinate system is indicated at the top of each figure.

Figure 4.9 shows contours of constant (black line) vorticity $\omega_z C/V_{rg}$. The black contour lines correspond to vorticity values $\omega_z C/V_{rg} = \pm 4$ through ± 10 with $\Delta\omega_z C/V_{rg} = 1$. At the smaller radius of gyration $r_g/C = 1.7$, and the shortest travel distance shown $r_g\Phi/C = 1.0$, the density of the vorticity contour lines along the leading-edge increases with spanwise location. In contrast, at $r_g/C = 4.7$ the contour lines at spanwise locations *C*, *D*, and *E* tend to have a similar form, *i.e.*, the shape of the vorticity contours does not change as much across the span of the wing at $r_g/C = 4.7$ as it does at sections *C*, *D*, and *E* for $r_g/C = 1.7$. The vorticity concentrations located downstream of the trailing-edge, which correspond to the starting vortex that is shed from the trailing-edge, have distributions along the span that are similar to the patterns of vorticity concentrations along the leading-edge at both $r_g/C = 1.7$ and 4.7; they have larger circumference near the tip at $r_g/C = 1.7$ and are more uniform along the span at $r_g/C = 4.7$.

At $r_g\Phi/C = 2.0$ the overall form of the distribution of patterns of vorticity along the span of the wing at the smaller radius of gyration $r_g/C = 1.7$ is similar to the spanwise distribution at $r_g\Phi/C = 1.0$. That is, the scale of the vorticity concentration formed in the

separated shear layer increases along the span of the wing, from section *B* to section *E*. At spanwise locations *E* and *F*, the concentration of vorticity contours on the leading-edge resembles a separated shear layer. At r_g/C = 4.7, the arch vortex formation, observed in iso-surfaces of the *Q*-criterion (Compare figure 4.4), is manifested in large-scale concentrations of vorticity at sections *C*, *D*, and *E*. This arch vortex appears to be approximately symmetric around spanwise location *D*, which corresponds to z/b = 0.57, or just outboard of the midspan of the wing.

The third row of figure 4.9 corresponds to a travel distance $r_g\Phi/C$ = 3.0. At the smaller radius of gyration r_g/C = 1.7, the sectional patterns of vorticity at spanwise location *F* and, to a lesser extent, spanwise location *E*, resemble a separated shear layer. At r_g/C = 4.7, the patterns of vorticity concentration near the leading-edge resemble a separated shear layer at spanwise locations *C* through *F*. At locations *D* and *E*, large-scale vorticity concentrations, associated with formation of the arch vortex, are still apparent downstream of the separated shear layer along the leading-edge.

The bottom row of figure 4.9 represents the flow structure at the largest travel distance $r_g\Phi/C$ = 5.5. At r_g/C = 1.7, the leading-edge vortex is located close to the wing at spanwise locations inboard of the midspan, and a structure resembling a separated shear layer has formed at spanwise locations outboard of the midspan. At r_g/C = 4.7, the contours of constant vorticity take the form of narrow, extended layers formed from the

leading-edge of the wing at spanwise locations *B* through *F*. These types of layers are representative of fully separated flow at high angle of attack.

Figure 4.10 shows (color) contours of downwash velocity v/V_{rg} superposed on contours of constant (black line) vorticity $\omega_z C/V_{rg}$. These red-yellow contours indicate dominance of downwash for all cases shown, *i.e.*, there is no upwash velocity with a magnitude above the cut-off threshold ($v/V_{rg} \geq 0.4$). Generally speaking, for all values of travel distance $r_g\Phi/C$, larger scale regions of large (red) magnitude downwash v/V_{rg} occur for the small radius of gyration $r_g/C = 1.7$, relative to moderate radius of gyration $r_g/C = 4.7$. This observation is correlated with persistence of ordered concentrations of vorticity $\omega_z C/V_{rg}$ in the shear layer from the leading-edge of the wing at $r_g/C = 1.7$, relative to the patterns observed at $r_g/C = 4.7$.

For the smallest travel distance $r_g\Phi/C = 1.0$, and radius of gyration $r_g/C = 1.7$, the contours of downwash velocity v/V_{rg} extend from the downstream edge of each concentration of vorticity. These contours indicate that the largest scales of large (red) magnitude of v/V_{rg} occur at spanwise locations beyond the midspan of the wing (spanwise locations *D*-*F*). At spanwise locations *E* and *F*, the elevated contours of v/V_{rg} extend from the vorticity concentration of the separated shear layer to the vorticity concentration that represents the starting vortex shed from the trailing-edge. At larger

travel distance $r_g\Phi/C$ = 2.0, the spatial extent of the large (red) magnitude downwash v/V_{rg} increases and shifts inboard. That is, the contours of large v/V_{rg} become more extensive and move away from the outboard spanwise location *F*, and toward the wing root *i.e.*, spanwise locations *C* to *E*. These regions of pronounced v/V_{rg} at sections *C* to *E* persist for larger values of travel distance $r_g\Phi/C$ = 3.0 and 5.5. Taking an overview of the sectional patterns of v/V_{rg} for all values of travel distance $r_g\Phi/C$ in the left column of figure 4.10, a dramatic transformation occurs from the startup patterns at small travel distance $r_g\Phi/C$ = 1.0, to the patterns that persist from $r_g\Phi/C$ = 2.0 to the largest travel distance $r_g\Phi/C$ = 5.5. This preservation of large contours of downwash from $r_g\Phi/C$ = 2.0 to $r_g\Phi/C$ = 5.5 is in accord with similar preservation of *Q*-criterion (see figures 4.4 to 4.6), and helicity (see figure 4.7).

The right column of figure 4.10 shows the patterns of downwash v/V_{rg} at the larger value of radius of gyration r_g/C = 4.7. Considering, first of all, the small travel distance $r_g\Phi/C$ = 1.0, the downwash contours are similar in magnitude and spatial extent at spanwise locations *B* to *E*. At all spanwise locations, the regions of elevated downwash are located at the downstream edges of the patterns of vorticity concentration, formed from the leading-edge of the wing. These contours, however, do not extend to the respective vorticity concentrations that represent the starting vortex, formed from the trailing-edge of the wing, as they do at spanwise locations *D* and *E* for r_g/C = 1.7. As the

wing rotates at constant velocity to larger values of travel distance $r_g\Phi/C$, larger scale regions of downwash form. In comparison with the images at smaller radius of gyration r_g/C = 1.7 in the left column, these regions have lower (lighter red) levels of peak downwash at most spanwise locations. Furthermore, at the travel distance $r_g\Phi/C$ = 2.0, the moderately high (light red) levels of downwash velocity v/V_{rg} are located at the downstream edges of the vorticity concentrations $\omega_z C/V_{rg}$ that represent the arch vortex at spanwise locations *C* to *E* (compare the iso-*Q* surfaces of figure 4). At $r_g\Phi/C$ = 3.0, the locations of the indicated contours of v/V_{rg} relative to the positions of the vorticity concentrations $\omega_z C/V_{rg}$ remain the same as at smaller travel distances $r_g\Phi/C$ = 1.0 and 2.0. At $r_g\Phi/C$ = 5.5, the arch vortex has been swept downstream of the trailing-edge (compare figure 4.6), and significant concentrations of vorticity associated with the separated shear layer from the leading-edge are no longer evident. Instead, elongated regions of low-level vorticity occur at spanwise locations *B* through *F,* along the span of the wing. Correspondingly, regions of moderately large (red-yellow) downwash occur well downstream of the leading-edge of the wing.

Figure 4.11 shows sectional cuts of the flow structure at the spanwise location *D* designated in figures 4.9, 4.10 and 4.12. These images show the velocity vectors in a reference frame equivalent to flow past a stationary wing, superposed with (color) contours of velocity u/V_{rg} in the direction of rotation, and contours of constant (blue line)

spanwise vorticity $\omega_z C/V_{rg}$. The magnitude of the velocity at infinite distance from the wing, approaching the wing from the left (not evident in these images), is equal to the velocity V_{rg} of the wing at its radius of gyration. As indicated in the color band in the inset of figure 4.11, these color contours represent a range of velocity from u/V_{rg} = -0.6 to 0.15, with a white band that represents u/V_{rg} = 0. The (red) contour $u/V_{rg} > 0$ indicates regions where the flow has positive tangential flow velocity relative to the wing in a wing-fixed reference frame. The left column of images represents the small radius of gyration r_g/C = 1.7, while the right column shows images corresponding to the moderate radius of gyration r_g/C = 4.7.

Considering, first, the images at r_g/C = 1.7 (left column) for all three values of travel distance $r_g\Phi/C$ = 1.5, 3.0 and 5.5, the velocity vectors near the wing have substantial magnitude and are oriented in the downstream direction, as indicated by the green contours, with the exception of a very small region of mildly positive u/V_{rg} (orange-red) at the smallest value of travel distance $r_g\Phi/C$ = 1.5. These patterns of velocity vectors, along with the lack of any significant upstream flow along the wing, indicate the absence of substantial regions of flow separation or stall. The (blue) vorticity lines indicate that the leading-edge vortex remains close to the leeward surface of the wing at all values of travel distance. In other words, there is a correlation between: (i)

preservation of the coherent vorticity concentration in the separating shear layer that remains close to the surface of the wing; and (ii) the absence of a region of stalled flow.

In contrast, the corresponding patterns at r_g/C = 4.7 (right column) show respectively small-scale and large-scale regions of upstream oriented (red) velocity at travel distances $r_g\Phi/C$ = 1.5 and 3.0. These regions are associated with the swirl induced by the vorticity concentration in the separated shear layer, indicated by the (blue) contour lines of vorticity. This vorticity concentration is the sectional cut of the arch vortex, indicated in the three-dimensional representations of figures 4.3 and 4.5. However, at the largest travel distance of $r_g\Phi/C$ = 5.5, the magnitude of the velocity vectors has decreased dramatically; only a low-level (blue) layer of vorticity is evident because the aforementioned vorticity concentration has been swept downstream (compare with the three-dimensional image of figure 4.6). The overall flow pattern at $r_g\Phi/C$ = 5.5 is characteristic of a highly separated or stalled flow.

The images of figure 4.11 serve as a guide for interpretation of the sectional patterns in figure 4.12, which shows (color) contours of velocity u/V_{rg} in the direction of rotation superposed on contours of constant (black line) vorticity $\omega_z C/V_{rg}$, as described and interpreted in figure 4.11. The contours of u/V_{rg} in figure 4.12 are similar to the contours of u/V_{rg} in figure 4.11.

At small radius of gyration r_g/C = 1.7 in figure 4.12 (left column), the contours of u/V_{rg} at sections *D* and *E* show (red) regions where the velocity component is upstream $u/V_{rg} > 0$. Overall, at small radius of gyration, the scale of regions where the flow is upstream $u/V_{rg} > 0$ is minimal.

At larger radius of gyration r_g/C = 4.7, (red) regions where the flow is upstream $u/V_{rg} > 0$ are more prevalent. At $r_g\Phi/C$ = 1.5, these regions initially form at spanwise locations *C-E,* between the surface of the wing and the vorticity concentrations that represent the arch vortex. Each of these regions of upstream flow is induced by the vorticity concentration in the separated shear layer, as observed in figure 4.11. At $r_g\Phi/C$ = 3.0, large (red) regions of significant upstream flow u/V_{rg} = 0.15 exist beneath the vorticity contours associated with the arch vortex, at spanwise locations *D* and *E*. At $r_g\Phi/C$ = 5.5, a (red) region of $u/V_{rg} > 0$ at spanwise locations *D* and *E* exists in presence of low level distributed vorticity. This overall pattern corresponds to highly separated or stalled flow, as addressed in figure 4.11.

When considered together, figures 4.10 through 4.12 provide the following insight. The formation of a stable leading-edge vortex at small radius of gyration, evident in iso-surfaces of the *Q*-criterion and patterns of spanwise vorticity on sectional planes, is associated with increased downwash velocity on the leeward side of the wing. This flow structure is not associated with significant regions of upstream oriented velocity

component ($u/V_{rg} > 0$) in a wing-fixed reference frame. In contrast, the formation of an arch vortex does not promote substantial downwash or flow attachment on the leeward side of the wing. Instead, large regions of upstream oriented swirl flow $u/V_{rg} > 0$ are induced by the vorticity concentration. Eventually, fully separated or stalled flow, involving large-scale regions of upstream oriented flow having low velocity magnitude, occurs when the arch vortex is swept away from the wing.

4.4 CONCLUSIONS

The development of the three-dimensional vortex structure on a wing of moderate aspect ratio ($AR = 2$) undergoing pure rotation (rotation at constant angular velocity and fixed angle of attack α) is characterized via volumetric reconstruction of results obtained from phase-averaged stereoscopic particle image velocimetry. This characterization is carried out at small and moderate values of radius of gyration, $r_g/C = 1.7$ and 4.7, for a range of travel distances from $r_g\Phi/C = 0.5$ to $r_g\Phi/C = 5.5$. The evolution of the vortex structure is fundamentally different at these radii of gyration, and gives rise to distinctive classes of vortices, namely a conical leading-edge vortex and an arch vortex.

Vortical structures on the wing are represented by volumetric, transparent iso-surfaces of the Q-criterion. These iso-surfaces indicate regions of the flow where rotation $||\boldsymbol{\Omega}||^2$ dominates irrotational strain $||S||^2$. At small radius of gyration ($r_g/C = 1.7$), a coherent leading-edge vortex forms on the leeward surface of the wing; it is associated

with a tip vortex that remains coherent downstream of the trailing-edge and extends well into the wake of the wing. This overall flow structure is preserved to the maximum travel distance characterized herein. On the other hand, at moderate radius of gyration (r_g/C = 4.7), an arch vortex forms on the leeward surface of the wing; it eventually loses its coherence and is swept downstream. During the initial stage of development of both the conical leading-edge vortex and the arch vortex, the patterns and the time of onset of high levels of *Q*-criterion within the components of the three-dimensional vortex, that is, the leading-edge vortex, the tip vortex and the trailing vortex, show significant differences and foretell the fundamentally different forms of the vortex structure.

The *Q*-criterion iso-surfaces, which are employed to characterize the basic forms of the vortex structure described in the foregoing, have been employed with the helicity $h = \boldsymbol{V}^*\boldsymbol{\omega}$ to provide further insight into the evolution of the vortex structure. Helicity may be interpreted as the magnitude of vorticity flux along the axis of the vortex. It is demonstrated that, at small radius of gyration, for the case of the three-dimensional vortex system associated with the conical, attached leading-edge vortex, a large magnitude of positive helicity is maintained along the axis of the vortex system as it develops along the wing. Correspondingly, the coherence of the three-dimensional vortex system is preserved. In contrast, at moderate radius of gyration, for which the arch vortex develops, the peak magnitude of helicity is attenuated, and, more importantly, the sign of the helicity alternates across the span of the arch vortex, indicating non-unidirectional vorticity flux along the axis of the vortex. The arch vortex rapidly degenerates as it is swept downstream.

Further distinction of the evolution of the attached conical leading-edge vortex and the arch vortex is evident in patterns of downwash velocity v/V_{rg}. At small radius of gyration, the persistence of coherent vortical structures containing high magnitude Q-criterion near the leading-edge of the wing results in a large downwash region at all travel distances greater than $r_g\Phi/C$ = 0.5. In comparison, the magnitude and spatial extent of the downwash are substantially diminished at moderate radius of gyration for larger travel distance, and, correspondingly, large magnitude iso-surfaces of the Q-criterion do not persist.

The volumetric representations of the three-dimensional flow structure described in the foregoing are complemented by sectional patterns along the span of the wing. The initial development of the flow structure, shortly after onset of the wing motion, is as follows. For the small radius of gyration, the patterns of spanwise vorticity on sectional planes are asymmetric with respect to the midspan of the wing; larger concentrations of vorticity occur near the tip of the wing. For moderate radius of gyration, however, the patterns of spanwise vorticity are nearly symmetric. Well after the onset of wing motion, the patterns of spanwise vorticity on sectional planes depend strongly on the radius of gyration, and show fundamentally different forms. For small radius of gyration, the vorticity concentrations tend to remain close to the surface of the wing. For moderate radius of gyration, however, such concentrations are deflected away from the surface of the wing, and at sufficiently large travel distance, vorticity concentrations give way to low level layers of distributed vorticity in the shear layer, accompanied by a large region

of low velocity between the vorticity layer and the surface of the wing, *i.e.*, a fully separated flow.

The magnitude and spatial extent of sectional patterns of downwash and tangential velocity are closely related to the aforementioned sectional patterns of vorticity contours. When the vorticity concentration remains close to the surface of the wing, as is the case at small radius of gyration, large magnitude downwash extends downstream from the edges of the vorticity contours. Moreover, the tangential velocity beneath the vorticity concentration is oriented in the downstream direction. On the other hand, when the vorticity contours take an elongated form and are deflected substantially away from the surface of the wing, the magnitude and extent of the sectional downwash is greatly diminished, and the flow travels upstream in the region below the shear layer emanating from the leading-edge of the wing. In turn, these features of the downwash and tangential velocity are intimately related to formation and development of both the conical leading-edge vortex and the arch vortex.

The results presented herein indicate that, for a wing having sufficiently large aspect ratio, an increase of the radius of gyration, from a small to a moderate value, produces a dramatic change in the vortex structure, *i.e.*, from an attached conical leading-edge vortex to an arch vortex. In essence, this means that the strong rotational effects that occur at small radius of gyration, namely the centripetal force and the radial pressure gradient, as assessed for a rotating wing by Lentink and Dickinson (2009*a* & *b*) and Garmann *et al.* (2013), are attenuated with increasing radius of gyration, such that the arch vortex, which heretofore has been observed only on wings in rectilinear motion,

becomes dominant. This formation of the arch vortex occurs over a larger travel distance than the relatively rapid onset of the attached leading-edge vortex, and it eventually loses its coherence as it is swept downstream. The arch vortex characterized herein closely resembles the flow structure on a rectilinearly translating wing at similar angle of attack. Visbal (2011) first defined the arch vortex on a wing undergoing unsteady rectilinear motion, namely heaving, and subsequent computational studies have characterized the arch vortex on wings undergoing unsteady hover (Garmann and Visbal, 2013), and steady translation after an impulsive start (Garmann *et al.* 2013). These computations are complemented and confirmed by the three-dimensional experimental imaging of Yilmaz and Rockwell (2011), and Visbal *et al.* (2013).

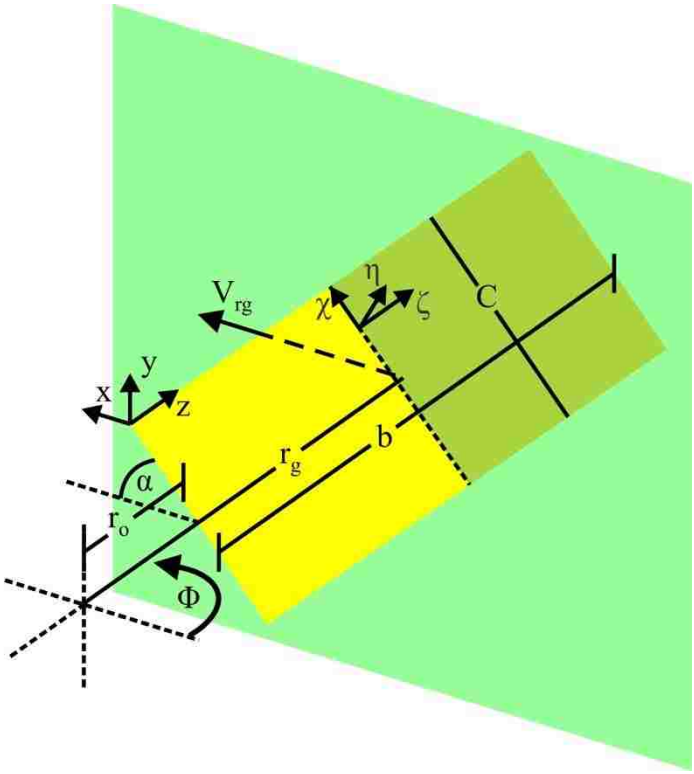

Figure 4.1. Schematic of rotating wing and relevant dimensions.

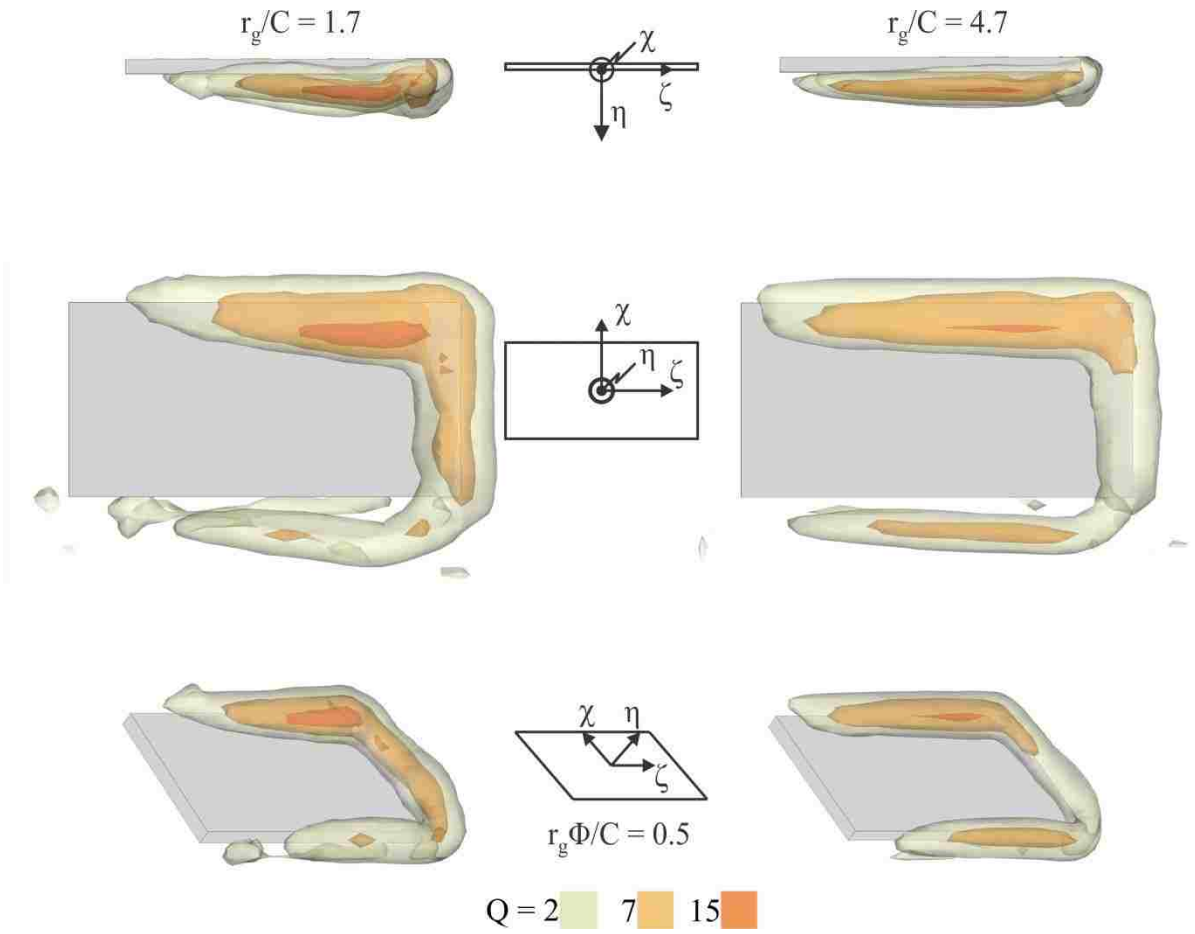

Figure 4.2. Transparent iso-surfaces of *Q*-criterion at different values of Rossby number r_g/C. Rotation distance $r_g\Phi/C = 0.5$.

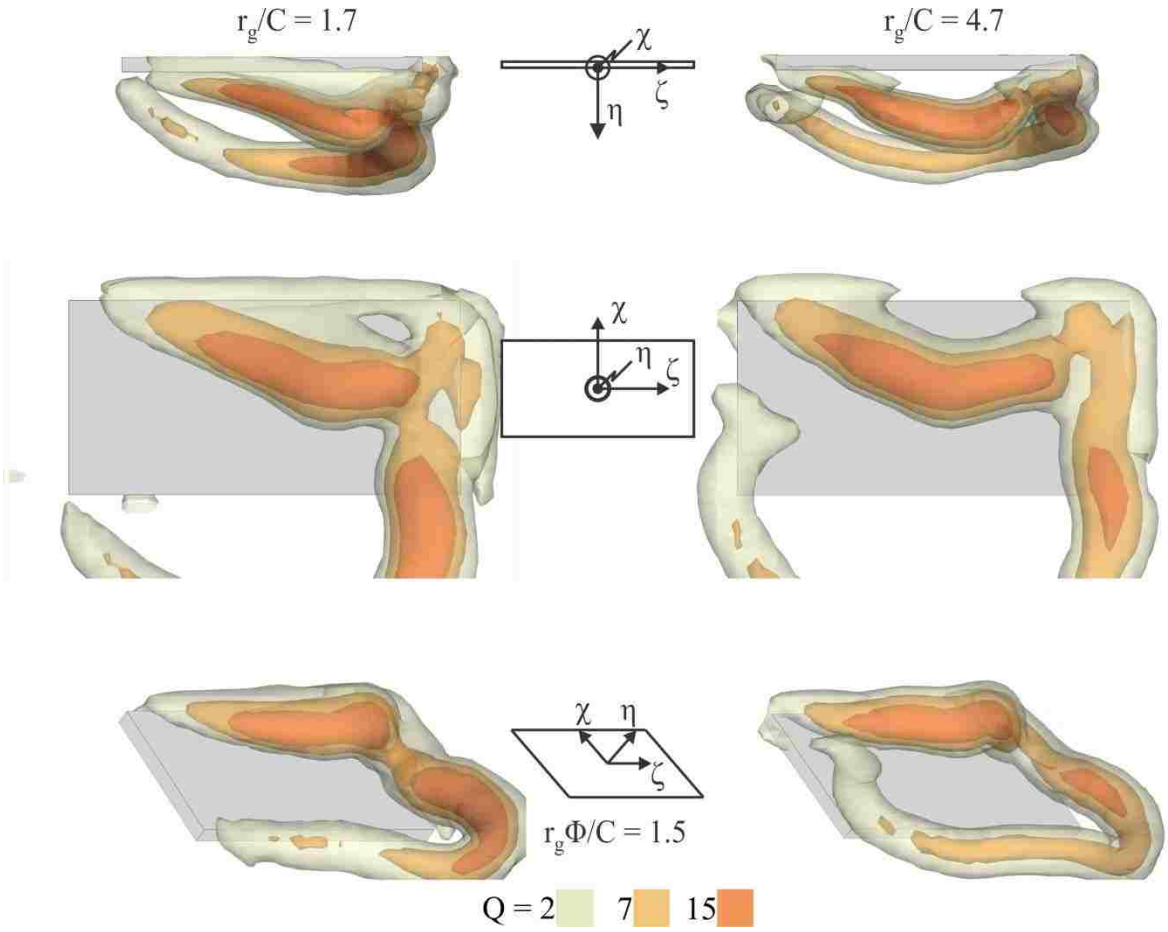

Figure 4.3. Transparent iso-surfaces of *Q*-criterion at different values of Rossby number r_g/C. Rotation distance $r_g\Phi/C$ = 1.5.

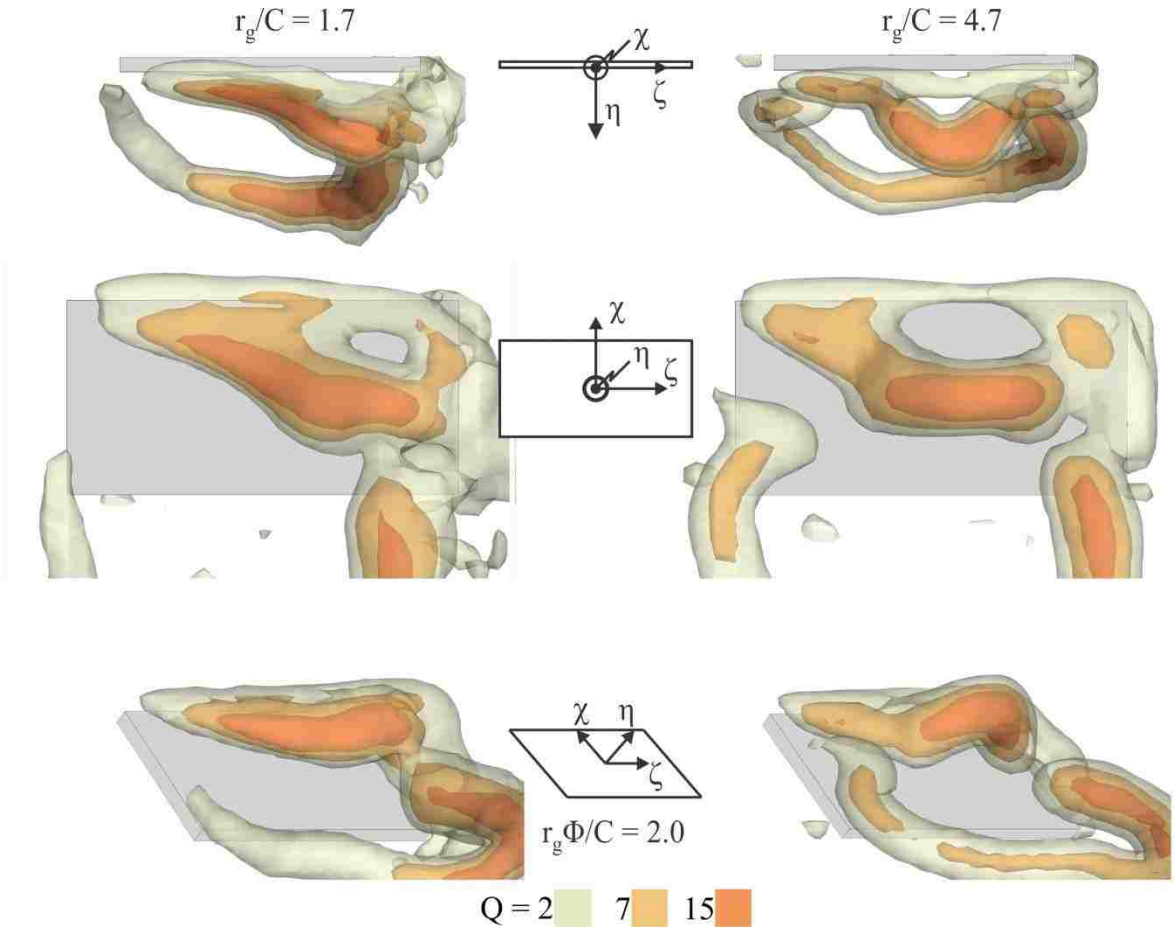

Figure 4.4. Transparent iso-surfaces of *Q*-criterion at different values of Rossby number r_g/C. Rotation distance $r_g\Phi/C = 2.0$.

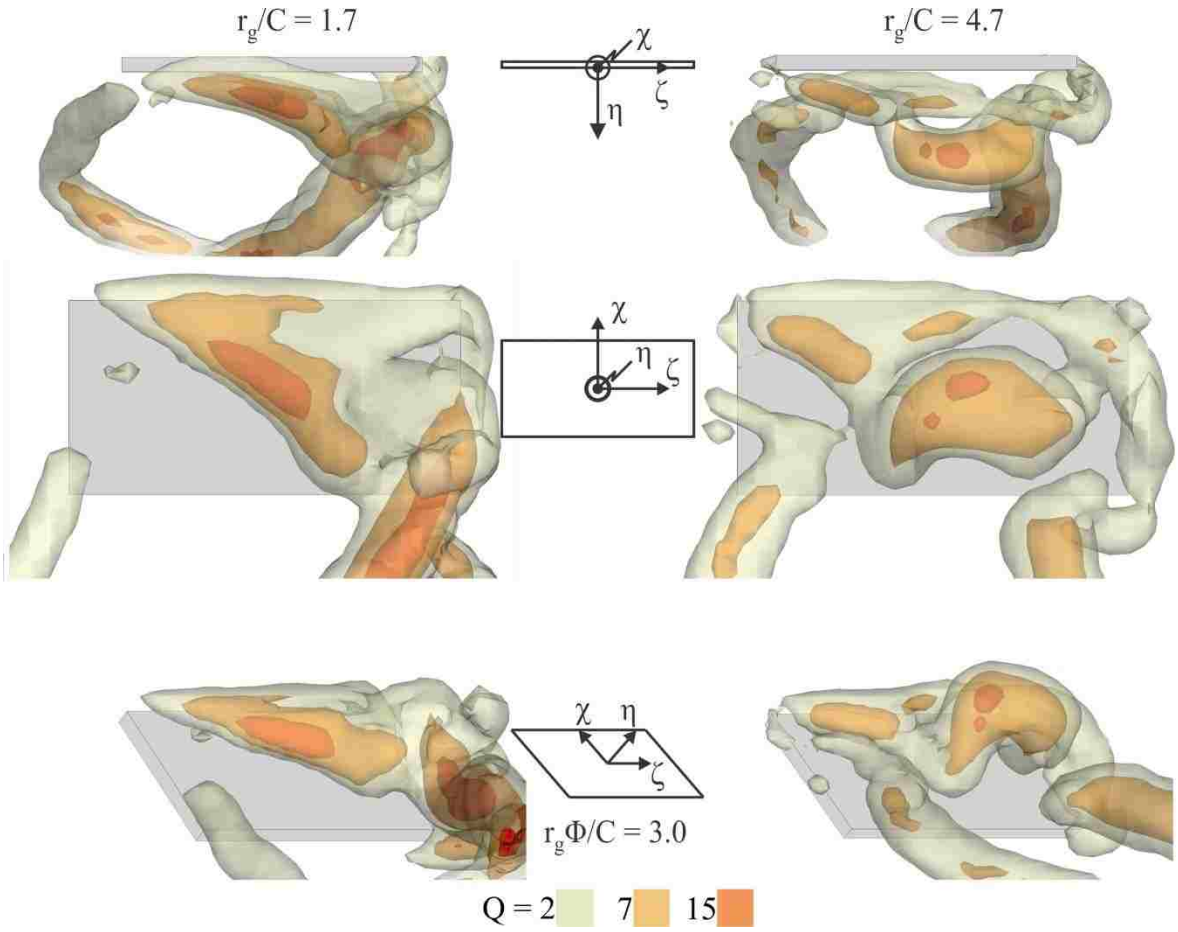

Figure 4.5. Transparent iso-surfaces of *Q*-criterion at different values of Rossby number r_g/C. Rotation distance $r_g\Phi/C = 3.0$.

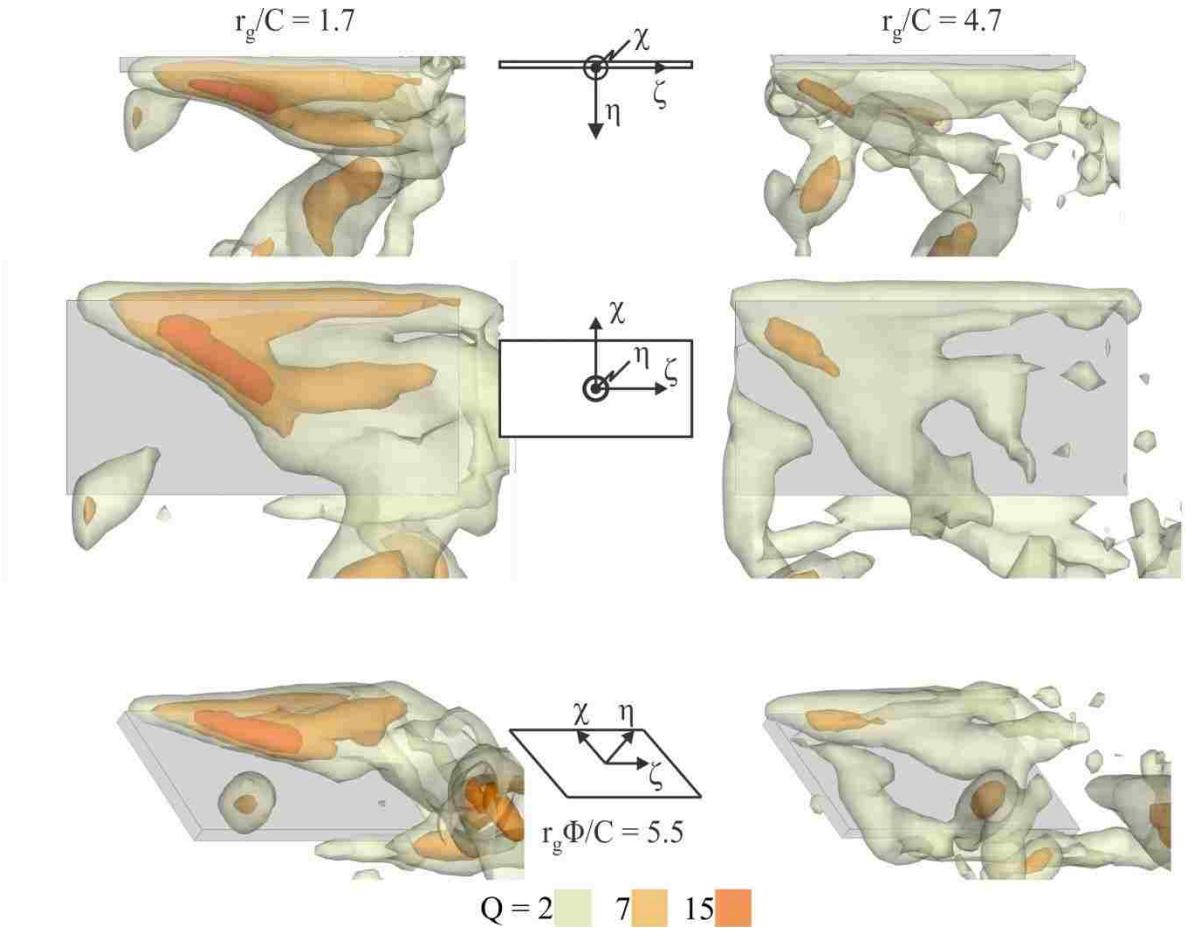

Figure 4.6. Transparent iso-surfaces of *Q*-criterion at different values of Rossby number r_g/C. Rotation distance $r_g\Phi/C = 5.5$.

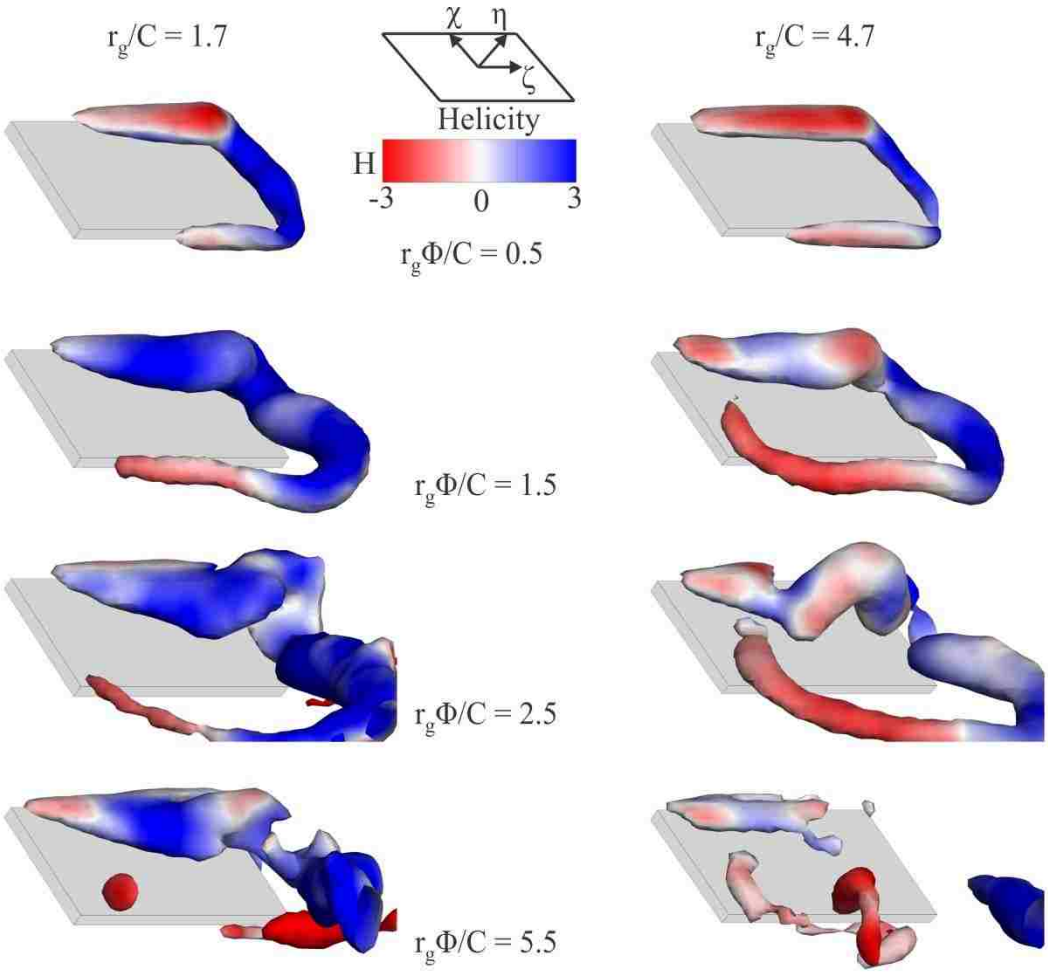

Figure 4.7. Iso-surfaces of *Q*-criterion $Q = 4.5$ colored with helical density H at different values of Rossby number r_g/C and rotation distance $r_g\Phi/C$.

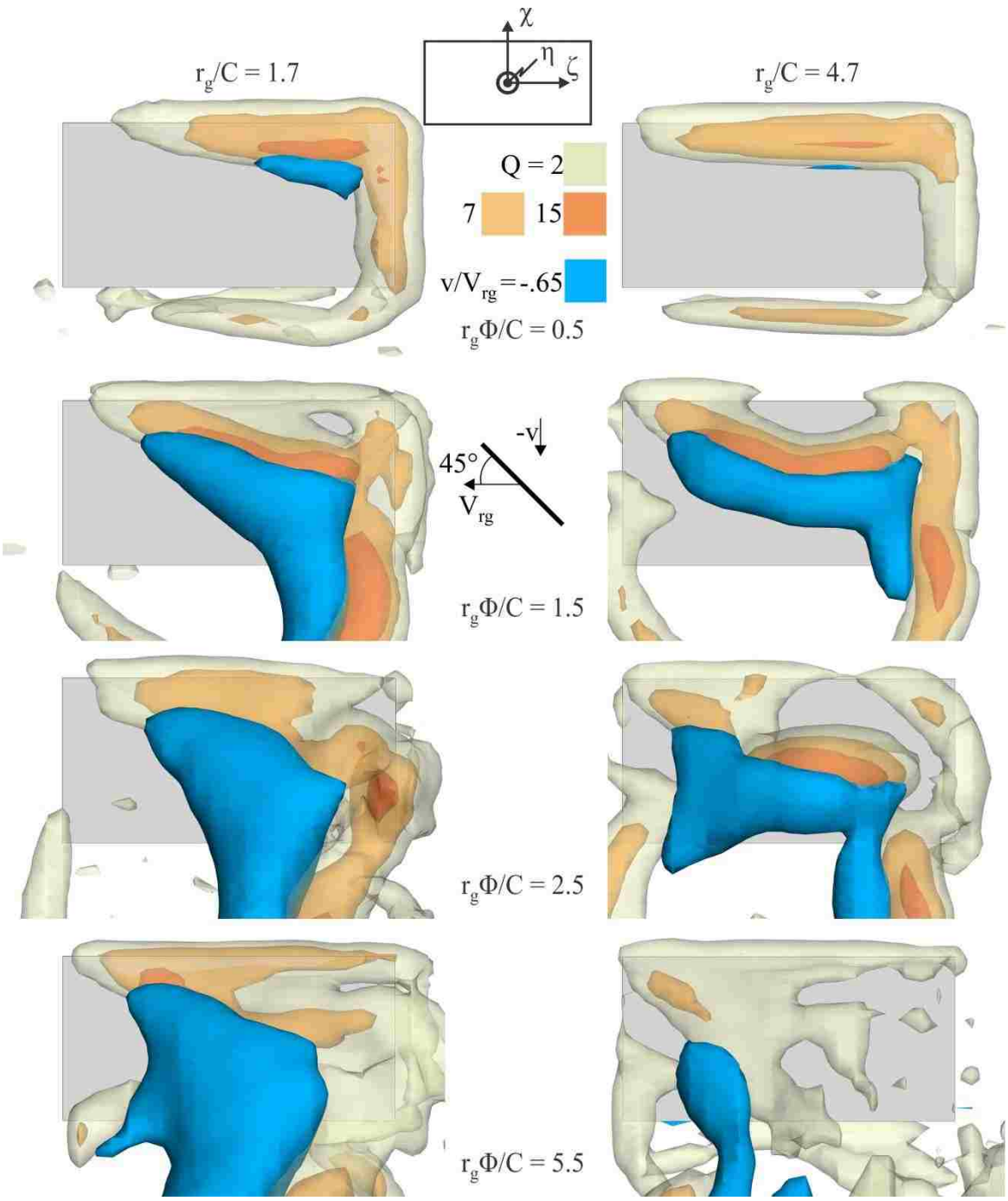

Figure 4.8. Transparent iso-surfaces of *Q*-criterion and opaque iso-surfaces of downwash at different values of Rossby number r_g/C and rotation distance $r_g\Phi/C$.

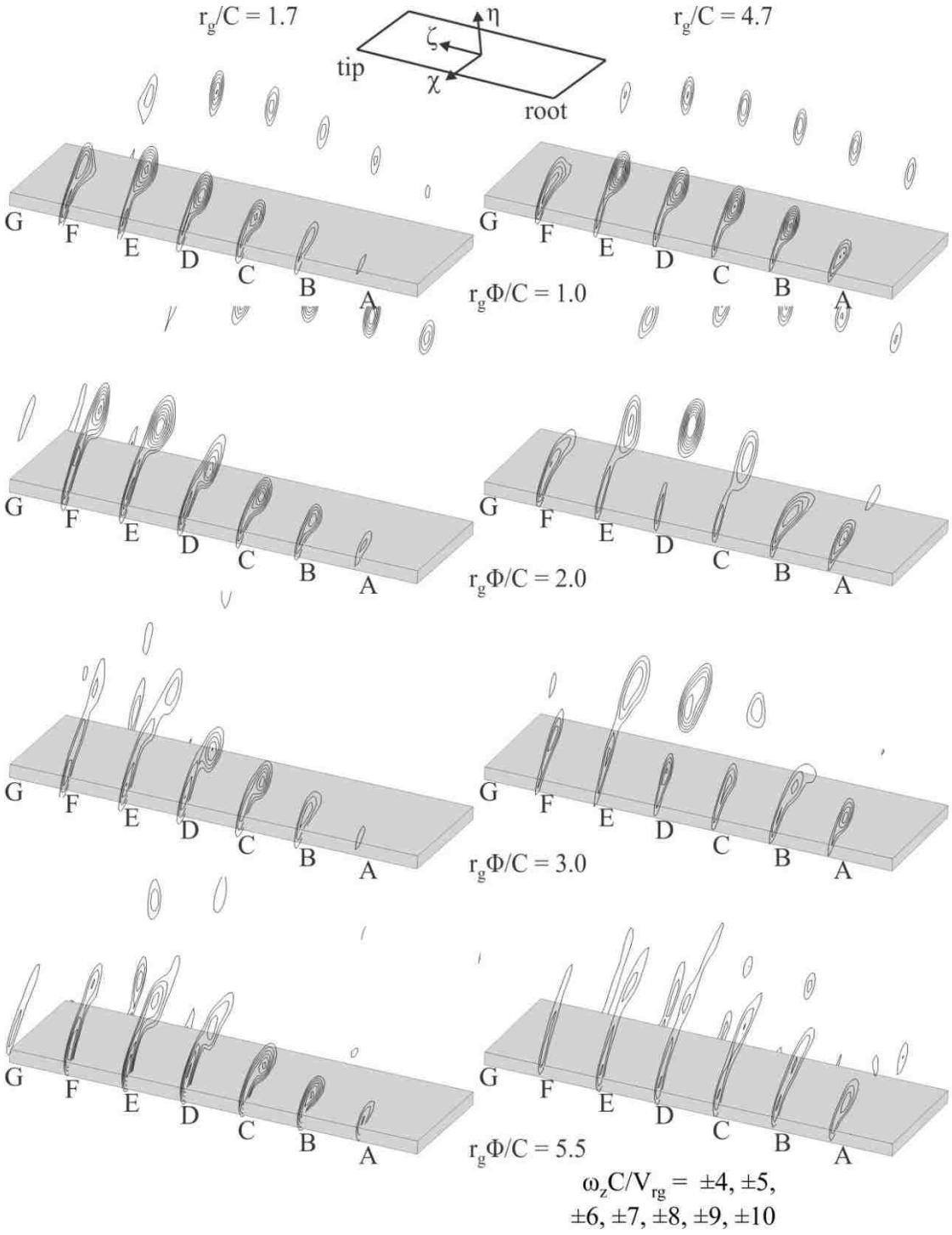

Figure 4.9. Sectional cuts of dimensionless spanwise vorticity $\omega_z C/V_{rg}$ at seven spanwise locations for different values of Rossby number r_g/C and travel distance $r_g\Phi/C$. The wing span is expanded to 150% of original dimension for visualization.

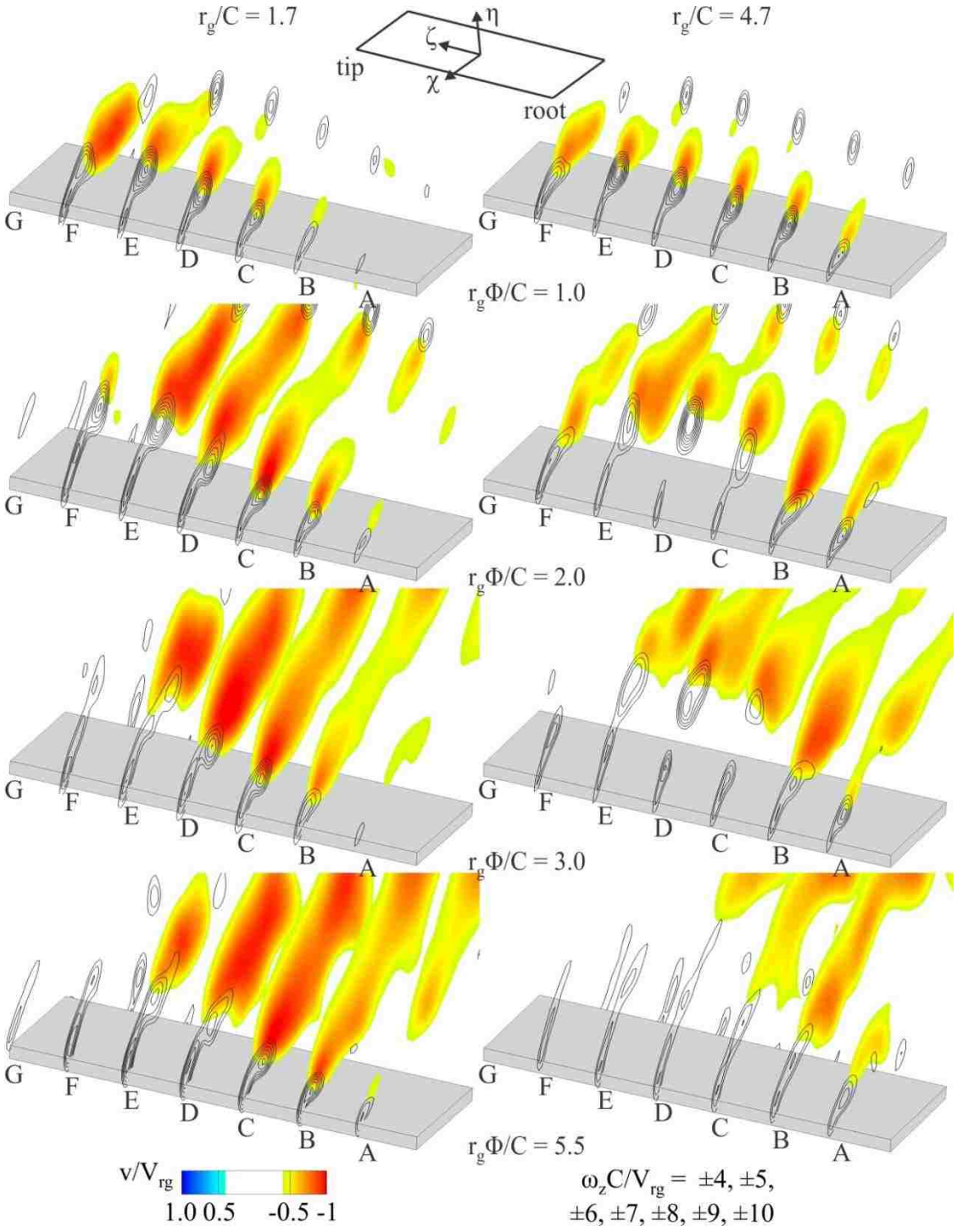

Figure 4.10. Sectional cuts of flow structure at seven spanwise locations for different values of Rossby number r_g/C and travel distance $r_g\Phi/C$. Contours of constant values of downward velocity component (downwash) are superposed on contours of constant spanwise vorticity. The wing span is expanded to 150% of original dimension for visualization.

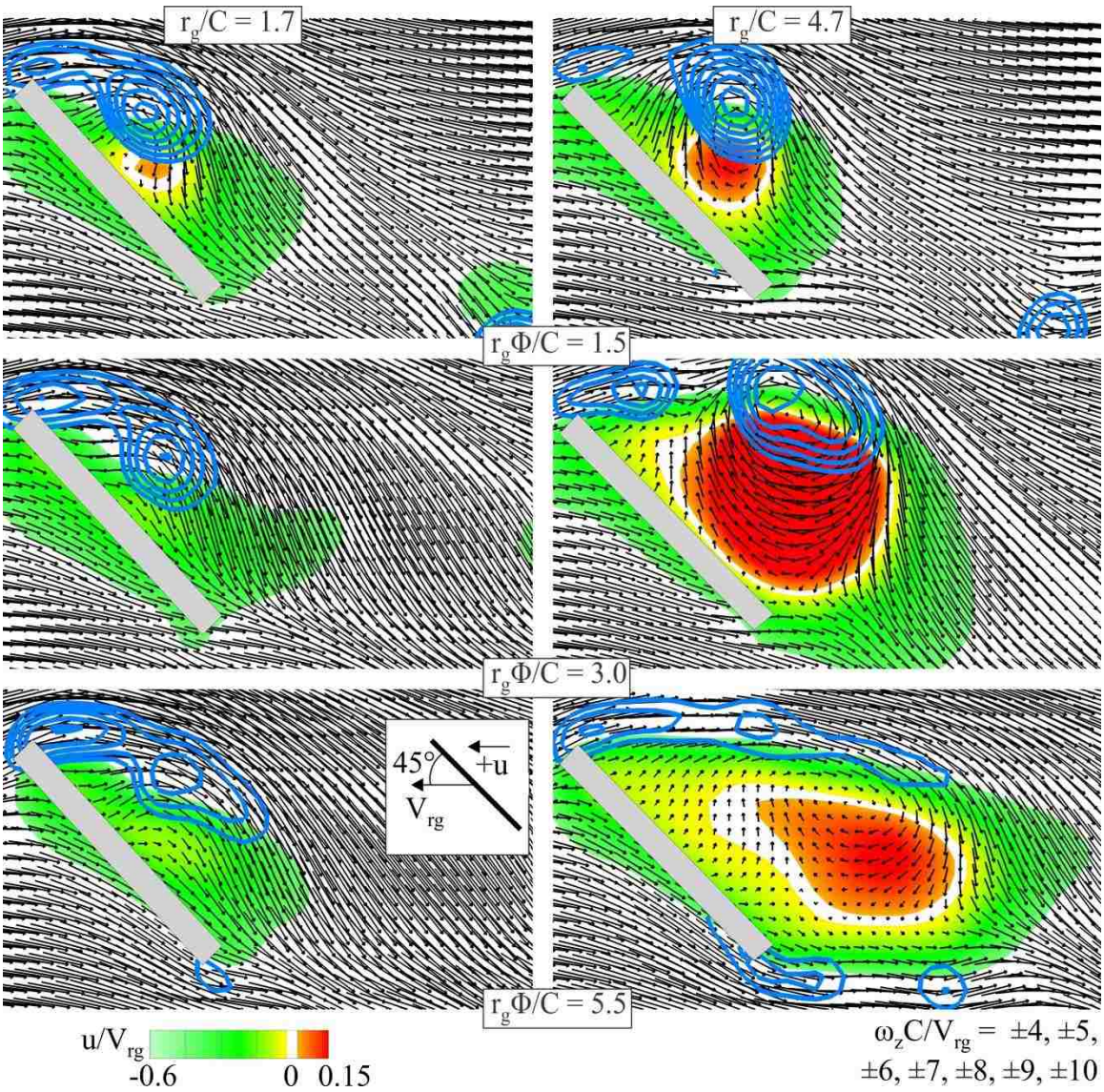

Figure 4.11. Sectional cuts of flow structure at spanwise location z/b = 0.57 (spanwise location D in figures 4.9, 4.10, and 4.12) for different values of Rossby number r_g/C and travel distance $r_g\Phi/C$. Contours of constant values of tangential velocity component u (see schematic) are superposed on velocity vectors V and contours of constant spanwise vorticity.

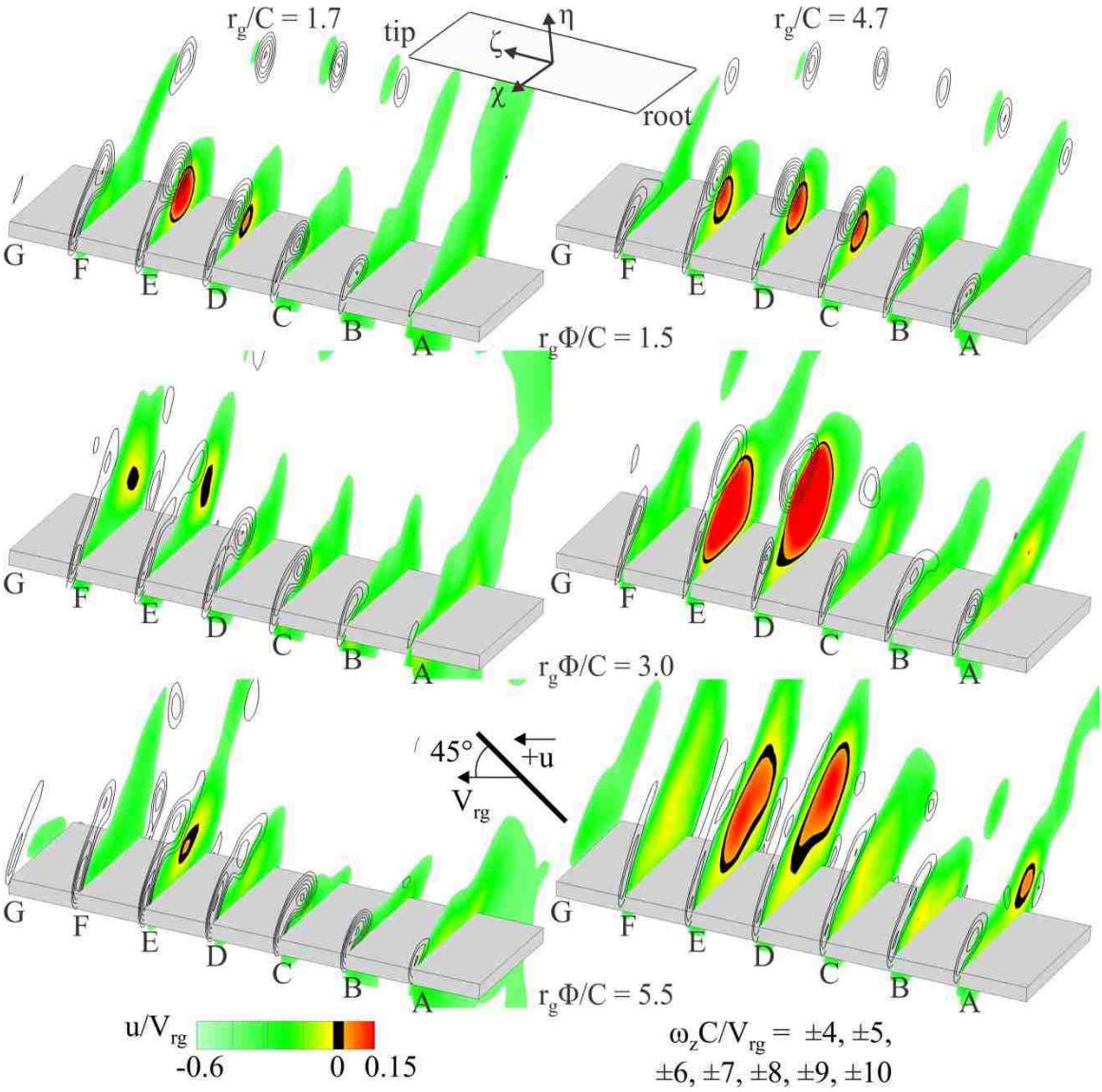

Figure 4.12. Sectional cuts of flow structure at seven spanwise locations for different values of Rossby number r_g/C and travel distance $r_g\Phi/C$. Contours of constant values of tangential velocity component are superposed on contours of constant spanwise vorticity. The wing span is expanded to 150% of original dimension for visualization.

CHAPTER 5

CONCLUSIONS AND RECOMMENDATIONS

5.1 CONCLUSIONS

This investigation provides new insight into the flow structure associated with bio-inspired, low Reynolds number flight through experimental determination of the unsteady flow velocities in the fluid surrounding a purely rotating wing, that is, a wing rotating at constant angular velocity Φ, and angle of attack α, after an initial acceleration from rest in quiescent fluid. Specifically, this investigation characterizes the transformation of the flow structure due to change of the radius of gyration r_g, from very low values to moderate values. Increasing r_g reduces the influence of rotation on the flow structure. To simulate the desired wing motion, a computer controlled, rotating wing model was designed and implemented; it precisely followed the prescribed wing kinematics. Stereoscopic particle image velocimetry (SPIV) was employed to determine the velocity field around this rotating wing model. This SPIV technique yielded sectional representations of the flow field, which were phase-averaged and reconstructed into volumetric representations. Chapters 3 and 4 respectively provide conclusions specific to a low aspect ratio wing AR = 1, and a moderate aspect ratio wing AR = 2. In the

following, overall conclusions are presented regarding the effect of radius of gyration, and recommendations are proposed for future research and design considerations for micro air vehicles (MAVs).

This investigation addresses the volumetric flow structure for several radii of gyration, and the transformation of this structure due to changes of radius of gyration r_g and increasing distance travelled by the wing $r_g\Phi/C$. This approach leads to characterization of the transient development of flow structure at different radii of gyration. Post processing of the volumetric representations of flow velocities allows quantitative determination of several derived quantities, including vorticity, vorticity flux, helical density, and *Q*-criterion. These quantities are used to define the flow physics resulting from the wing motion.

When the radius of gyration is minimized, highly coherent vortical structures are observed after moderate travel distance, *i.e.*, well after the onset of motion of the wing. These coherent structures include leading-edge, root, and tip vortices. The leading-edge vortex is conical in shape, with increasing diameter from the root of the wing to the tip of the wing, where it joins with the tip vortex. Both the root and tip vortices are severely deflected toward the radius of gyration as they extend into the wake of the wing. Other organized flow features are also observed when the radius of gyration is minimized, including significant spanwise vorticity flux or helicity throughout the vortex system, and significant downward velocity (downwash) in the region bounded by the vortex system. In addition, the volume of stalled fluid is minimal at small radius of gyration. That is,

there are insignificant regions of the flow that are either (i) moving at approximately the tangential velocity of the wing in a lab-fixed reference frame, or (ii) moving at approximately zero tangential velocity in a wing-fixed reference frame,

When the radius of gyration r_g is increased to larger values, the coherent vortical structures observed at small values of degrade or lose intensity. This degradation affects the entire vortex system, including the leading-edge vortex, root vortex, and tip vortex; that is, all of these vortical structures lose strength and become less organized when the radius of gyration is increased. This loss of vortex organization is associated with reductions of the magnitude and spatial extent of regions of downwash velocity, spanwise vorticity flux and helicity. Moreover, deflection of the root and tip vortices towards the radius of gyration decreases, and the spatial extent of stalled fluid increases.

Radius of gyration also significantly influences the early temporal development of flow structures on a rotating wing. On an AR = 1 wing, a stable leading-edge vortex is observed at the midspan for all travel distances when r_g is minimized. When the radius of gyration is minimized on an AR = 2 wing, a leading-edge vortex quickly develops, and this vortex persists in a similar form as the wing continues to rotate. In contrast, when radius of gyration is increased to moderate values, the development of the flow structure is less rapid and does not lead to a coherent leading-edge vortex on either aspect ratio wing. In particular, on the larger aspect ratio AR = 2 wing, the formation and shedding of an arch vortex, which has previously been characterized only on wings undergoing translational motion, is observed at moderate radius of gyration. This vortex is similar in

size and strength to the leading-edge vortex, but it is not stable, *i.e.*, it does not persist as the wing continues to rotate. Instead, the arch vortex is swept away from the wing and is replaced by less organized vortical structures.

Minimization of the radius of gyration also maintains a stable leading-edge vortex at very large travel distance on a low aspect ratio $AR = 1$ wing. At the largest radius of gyration investigated herein, the volumetric flow structure is marginally coherent at moderate travel distance; rotation to extremely large travel distance yields loss of organized vortical structures. In contrast, at small radius of gyration, the organized vortical structures, observed at moderate travel distance, are largely preserved at very large travel distance.

This investigation demonstrates that the radius of gyration of a rotating wing critically influences the formation and stability of the coherent vortex system, which involves the leading-edge, tip and root vortices. When the radius of gyration is minimized, coherent vortical structures form rapidly and persist at all travel distances. In contrast, when the radius of gyration is increased to moderate values, coherent vortical structures that form on the wing do not stabilize. Instead, they degrade as the wing rotates. These results indicate the important influence of rotation on stability of the flow structure, and therefore lift production, in biological flight. A stable, attached leading-edge vortex, which other investigators have demonstrated is a key factor in lift production in biological flight, can be maintained on a purely rotating wing at sufficiently low radius of gyration, well after the onset of motion.

5.2 RECOMMENDATIONS

This study has identified r_g as a parameter that is critical to bio-inspired flight. Moderate changes in the radius of gyration have been shown to significantly affect the formation of vortical structures on a rotating wing, and minimization of this parameter positively affects stability of the leading-edge vortex. The different vortical structures observed herein have been linked by other investigators to significantly changes in lift force. In particular, it has been demonstrated that a coherent leading-edge vortex is essential for bio-inspired flight, which requires production of lift at high angle of attack. Knowledge of the role of r_g on leading-edge vortex formation and stability has several repercussions for future investigations in this field. First, the strong influence of this parameter on the flow structure invites further research. Secondly, the current results highlight the importance of r_g as a design parameter for MAVs.

Increase of the radius of gyration to a moderate value causes the flow structure on a rotating wing to resemble the flow structure on a translating wing. Other investigators have characterized the difference in lift forces on rotating and translating wings. Further research that compares the lift forces on the wing at, small, moderate, and infinite radius of gyration, while simultaneously determining the lift forces through direct measurement, will be useful in fully understanding the importance of the radius of gyration on the lift forces.

The effect of radius of gyration in accord with other effects important to bio-inspired flight will also be important in fully understanding the role of this parameter in

lift production on biological flyers. These flyers use a wide range of wing geometries to generate lift. Herein, only purely rotating, rectangular planform wings were considered. Characterization of the effects of these different wing geometries on the flow structure will therefore be worthwhile. Wing flexibility should also be investigated, as it could substantially alter the effective planform of the wing, and stabilize or destabilize the vortical structures that are important to lift production.

It will also be necessary to characterize the flow field under varying conditions, such as inflow or different types of motion of the wing, in order to determine the robustness of the stable leading-edge vortex. In the quiescent fluid experiments employed for this investigation, small radius of gyration was sufficient to ensure coherence of the flow structure. Variations of the inflow, including gusts, and classes of wing motion, including heaving motion, should be investigated to assess the stability of the coherent vortical structures, especially the leading-edge vortex. Such results could determine the practicality of using constantly rotating wings for lift generation on MAVs.

Practical, engineering-related issues should also be addressed. In spite of the additional research that will be necessary to completely characterize the stability of the leading-edge vortex, as well as the other components of the three-dimensional vortex system, the current knowledge of parameters related to bio-inspired flight offers a good foundation to guide the design of micro air vehicles (MAVs). Leading-edge vortex stability at low radius of gyration has proved to be a key component in biological flight. Radius of gyration should therefore be considered in the selection of wing aspect ratio, as well as in the design of drive systems. For instance, large, obstructive motor drive

systems may force the wing away from the rotation axis and increase radius of gyration. This situation should be avoided. Since, when the radius of gyration is sufficiently small, the leading-edge vortex is stable well after the onset of motion, MAV design should incorporate wings undergoing constant rotation, rather than complicated, reciprocatory wing motions employed on recent bio-mimetic aircraft. These reciprocatory designs are very difficult to optimize and manufacture, and they carry significantly larger power requirements to generate oscillatory motion. It will be more advantageous to design MAVs with sufficiently small radius of gyration that operate at constant rotational velocity, similar to a conventional propeller, so that the advantage of lift performance associated with a coherent leading-edge vortex can be exploited, while the design complexity is minimized.

It will also be necessary to investigate the flow structure and associated aerodynamic performance of MAV vehicles in situ. Research of this nature will allow determination of optimum wing geometry and configuration for a given MAV design, to ensure the stability of the leading-edge vortex. These designs may incorporate propeller-like wings with multiple blades, as well as several lift sources at a number of locations along the MAV geometry. The interaction of flow structures from each of these sources will affect overall aircraft performance; the conditions for optimization of these configurations should be addressed.

REFERENCES

Adrian, R. J. 1984 "Scattering particle characteristics and their effect on pulsed laser measurements of fluid flow: speckle velocimetry vs particle image velocimetry". *Applied optics* **23**.11: 1690-1691.

Adrian, R. J. & Westerweel, J. 2011 *Particle image velocimetry*. Cambridge: Cambridge University Press.

Ansari, S.A., Phillips, N., Stabler, G., Wilkins, P.C., Zbikowski, R. & Knowles, K. 2009 "Experimental investigation of some aspects of insect-like flapping flight aerodynamics for application to micro air vehicles". *Experiments in Fluids* **46**, 777-798.

Aono, H., Liang, F. & Liu, H. 2008 "Near- and far-field aerodynamics in insect hovering flight: an integrated computational study". *Journal of Experimental Biology* **211**, 239-257.

Birch, J.M. & Dickinson, M.H. 2001 "Spanwise flow and the attachment of the leading-edge vortex on insect wings". *Nature* **412**, 729-733.

Birch, J.M., Dickson, W.B. & Dickinson, M.H. 2004 "Force production and flow structure of the leading-edge vortex on flapping wings at high and low Reynolds numbers". *Journal of Experimental Biology* **207**, 1063-1072.

Bomphrey, R.J., Lawson N.J., Taylor G.K. & Thomas A.L.R. 2006 Application of digital particle image velocimetry to insect aerodynamics: measurement of the leading-edge vortex and near wake of a Hawkmoth. *Experiments in Fluids* **40**, 546-554.

Bross, M., Ozen, C. A. & Rockwell, D. 2013 "Flow structure on a rotating wing: effect of steady incident flow". *Physics of Fluids* **25**, 081901.

Bross, M. & Rockwell, D. 2014 "Flow structure on a simultaneously pitching and rotating wing". *Journal of Fluid Mechanics* **756**, 354-383.

Carr, Z. R., Chen, C. & Ringuette, M. J. 2013 "Finite-span rotating wings: three-dimensional vortex formation and variations with aspect ratio". Experiments in Fluids **54**, 1444.

Dickinson, M.H. & Götz, K.G. 1992 “Unsteady aerodynamic performance of model wings at low Reynolds numbers”. *Journal of Experimental Biology* **174**, 45-64.

Dickinson, M.H., Lehmann, F.O. & Sane S.P. 1999 “Wing rotation and the aerodynamic basis of insect flight”. *Science* **284**, 1954-1960.

Eldredge, J.D., Wang, C.J. & Ol, M. 2009 “A computational study of a canonical pitch-up, pitch-down wing maneuver”. In *39th AIAA Fluid Dynamics Conference*. San Antonio, Texas.

Ellington, C.P. 1984 “The aerodynamics of hovering insect flight, *I – VI*”. *Philosphical Transactions of the Royal Society of London, B* **305**, 1-181. 191

Ellington, C.P., van den Berg, C., Willmott, A.P. & Thomas, A.L.R. 1996 “Leading-edge vortices in insect flight”. *Nature* **384**, 626-630.

Garmann, D. J., Visbal, M. R. & Orkwis, P. D. 2013 “Three-dimensional flow structure and aerodynamic loading on revolving wing”. *Physics of Fluids* **25**, 034101.

Garmann, D. J. & Visbal, M. R. 2013 “A numerical study of hovering wings undergoing revolving or translating motions”. *AIAA Paper*, 2013-3052.

Garmann, D. J. & Visbal, M. R. 2014 “Dynamics of revolving wings for various aspect ratios”. *Journal of Fluid Mechanics* **748**, 932–956.

Harbig, R. R., Sheridan, J. & Thompson, M. C. 2013 “Reynolds number and aspect ratio effects on the leading-edge vortex for rotating insect wing planforms”. *Journal of Fluid Mechanics* **717**, 166–192.

Hart, D.P. 1998*a* “High-speed PIV analysis using compressed image correlation”. *Journal of Fluids Engineering* **120**, 463-470.

Hart, D.P. 1998*b* “The elimination of correlation errors in PIV processing”. In *9th International Symposium on Applications of Laser Techniques to Fluid Mechanics*. Lisbon, Portugal.

Hill, M. J. M. 1894 “On a spherical vortex”, *Philosophical Transactions of the Royal Society of London* **185**, pp. 213-245.

Hubel, T. Y. & Tropea, C. 2009 “Experimental investigation of a flapping wing model”. *Experiments in Fluids* **46**, 945–961.

Hunt, J.C.R., Wray, A.A. & Moin, P. 1988 “Eddies, stream, and convergence zones in turbulent flows”. In *Center for Turbulence Research Report*, pp. 193-208. Stanford, USA: Center for Turbulence Research.

Jardin, T., Farcy, A. & David, L. 2012 “Three-dimensional effects in hovering flapping flight”. *Journal of Fluid Mechanics* **702**, 102–125.

Jones, A.R. & Babinsky, H. 2011 “Reynolds number effects on leading-edge vortex development on a waving wing”. *Experiments in Fluids* **51**, 197-210. 192

Keennon, M., Klingebiel, K., Won, H. & Andriukov, A. 2012 “Development of the Nano Hummingbird: A Tailless Flapping Wing Micro Air Vehicle”. *AIAA Paper*, 2012-0588.

Kim, D. & Gharib, M. 2010 “Experimental study of three-dimensional vortex structures in translating and rotating plates”. *Experiments in Fluids* **49**, 329-339.

Kweon, J. & Choi, H. 2010 “Sectional lift coefficient of a flapping wing in hovering motion”. *Physics of Fluids* **22**, 071703.

Lawson, N. J. & Wu, J. 1997 “Three-dimensional particle image velocimetry: experimental error analysis of a digital angular stereoscopic system”. *Measurement Science and Technology* **8**, 1455-1464.

Lentink, D. & Dickinson, M.H. 2009*a* “Biofluiddynamic scaling of flapping, spinning and translating fins and wings”. *Journal of Experimental Biology* **212**, 2691-2704.

Lentink, D. & Dickinson, M.H. 2009*b* “Rotational accelerations stabilize leading-edge vortices on revolving fly wings”. *Journal of Experimental Biology* **212**, 2705-2719.

Liu, H., Ellington, C.P., Kawachi, K., van den Berg, C., Willmott, A.P. 1998 “A computational fluid dynamic study of hawkmoth hovering”. *Journal of Experimental Biology* **201**, 461-477.

Lu, Y. & Shen, G.X. 2008 “Three-dimensional flow structures and evolution of the leading-edge vortices on a flapping wing”. *Journal of Experimental Biology* **211**, 1221-1230.

Luo, G. & Sun, M. 2005 “The effects of corrugation and wing planform on the aerodynamic force production of sweeping model insect wings”. *Acta Mechanica Sinica* **21**, 531-541.

Mayo, D. B. & Jones, A. R. 2013 “Evolution and breakdown of a leading-edge vortex on a rotating wing”. *AIAA Paper* 2013-0843.

Moffatt, H. 1969 “The degree of knottedness of tangled vortex lines”. *Journal of Fluid Mechanics* **35**, 17–129.

"Nano Hummingbird." AV Human Power. AeroVironment, 2014. Web. 31 Oct. 2014.

Ozen, C. A. 2012 *Unsteady flow structure on rotating and flapping wings*. PhD dissertation, Lehigh University. Ann Arbor: ProQuest/UMI. (Publication No. 3542677.)

Ozen, C. A. & Rockwell, D. 2011 “Flow structure on a rotating plate”. Experiments in Fluids **52**, 207–223.

Ozen, C. A. & Rockwell, D. 2012 “Three-dimensional vortex structure on a rotating wing”. *Journal of Fluid Mechanics* **748**, 932–956.

Pines, D. J. & Bohorquez, F. 2006 “Challenges facing future micro-air-vehicle development”. *Journal of Aircraft* **43**, 290–305.

Poelma, C., Dickson, W.B. & Dickinson, M.H. 2006 “Time-resolved reconstruction of the full velocity field around a dynamically-scaled flapping wing”. *Experiments in Fluids* **41**, 213-225.

Prasad, A.K. 2000 “Stereoscopic particle image velocimetry”. *Experiments in Fluids* **29**, 103-116.

Sane, S.P. 2003 “The aerodynamics of insect flight”. *Journal of Experimental Biology* **206**, 4191-4208.

Sane, S. P. & Dickinson, M. H. 2001 “The control of flight force by a flapping wing: lift and drag production”. *Journal of Experimental Biology* **204**, 2607–2626.

Schlueter, K., Jones, A. R., Granlund, K. & Ol, M. 2014 “Effect of root cutout on force coefficients of rotating wings”. *AIAA Journal* **52** (6), 1322–1325.

Shyy, W., Aono, H., Chimakurthi, S.K., Trizila, P., Kang, C.K., Cesnik, C.E.S. & Liu, H. 2010 “Recent progress in flapping wing aerodynamics and aeroelasticity”. *Progress in Aerospace Sciences* **46**, 284-327.

Sun, M. & Tang, J. 2001 “Unsteady aerodynamic force generation by a model fruit fly wing in flapping motion”. *Journal of Experimental Biology* **205**, 55-70.

Taira, K. & Colonius, T. 2009 “Three-dimensional flows around low-aspect-ratio flat-plate wings at low Reynolds numbers”. *Journal of Fluid Mechanics* **623**, 187-207.

Usherwood, J.R. & Ellington, C.P. 2002*a* "The aerodynamics of revolving wings, *I. Model hawkmoth wings*". *Journal of Experimental Biology* **205**, 1547-1576.

Usherwood, J.R. & Ellington, C.P. 2002*b* "The aerodynamics of revolving wings, *II. Propeller force coefficients from mayfly to quail*". *Journal of Experimental Biology* **205**, 1547-1576.

Visbal, M. R. 2011 "Three-dimensional flow structure on a heaving low-aspect-ratio wing", *AIAA Paper*, 2011-219.

Visbal, M. R., Yilmaz, T. O. & Rockwell, D. 2013 "Three dimensional vortex formation on a heaving low-aspect-ratio wing: Computations and experiments". *Journal of Fluids and Structures* **38**, 58-76.

Wang, Z.J. 2005 "Dissecting insect flight". *Annual Review of Fluid Mechanics* **37**, 183-210.

Willmott, A. P. & Ellington, C. P. 1997*a* "The mechanics of flight in the hawkmoth manduca sexta. *I*. Kinematics of hovering and forward flight". *Journal of Experimental Biology* **200**, 2705–2722.

Willmott, A. P. & Ellington, C. P. 1997*b* "The mechanics of flight in the hawkmoth manduca sexta. *II*. Aerodynamic consequences of kinematic and morphological variation". *Journal of Experimental Biology* **200**, 2723–2745.

Wojcik, C. J. & Buchholz, J. H. J. 2014 "Vorticity transport in the leading-edge vortex on a rotating blade". *Journal of Fluid Mechanics* **743**, 249–261.

Yilmaz, T. O. 2012 *Investigation of three-dimensional flow structure on maneuvering finite-span wings.* PhD dissertation, Lehigh University. Ann Arbor: ProQuest/UMI. (Publication No. 3493765.)

Yilmaz, T.O. & Rockwell, D. 2011 "Flow structure on finite-span wings due to pitch-up motion". *Journal of Fluid Mechanics* **691**, 518-545.

APPENDIX A

ADDITIONAL IMAGES OF THE FLOW STRUCTURE ON A WING AT DIFFERENT RADII OF GYRATION

In chapters 3 and 4, the flow along a wing is characterized for wings having low aspect ratio (AR = 1), and moderate aspect ratio (AR = 2). In addition to the experimental results presented therein, several other volumetric reconstructions and representations of the flow structure were determined. This appendix supplements chapters 3 and 4 with several figures that were not included in those results. It is divided into sections that respectively compare flow patterns for different values of Reynolds number, rotation angle, Cartesian versus cylindrical coordinates, and aspect ratio. Herein the symbols Q, H, and ω respectively refer to the normalized values of Q-criterion qC^2/V_{rg}^2, helical density hC/V_{rg}^2, and vorticity $\omega C/ V_{rg}$.

A.1 Effect of Reynolds number on flow structure

Figure A.1 shows sectional cuts of spanwise vorticity ω_z at the midspan of the wing. These patterns are shown as a function of Reynolds number $Re_{rg} = V_{rg}C/\nu$, in the range $1400 \leq Re_{rg} \leq 5000$. In this range, there are minor changes to the vorticity patterns. Specifically, the reoriented tip vortex appears to be slightly affected by this parameter, *i.e.*, there are minor variations in the vorticity contours representing the reoriented tip vortex in this range of Reynolds number.

A.2 Flow structure at same value of rotation angle Φ

Figures A.2 through A.5 show iso-surfaces and expanded sectional slices of the flow structure on an $AR = 1$ wing similar to the representations employed in figures 3.3 through 3.11. In these figures, however, rotation angle Φ is held constant at 270°, instead of comparisons at the same value of travel distance $r_g\Phi/C$ based on the radius of gyration r_g, which are employed in chapter 3. When the rotation angle is instead employed to characterize the development of the flow structure, the difference in flow structure at $r_g/C = 1.2$ and 5.1 is more extreme. For instance, in figure A.2, the vortical structures are much less organized at larger Rossby number. No coherent root or tip vortices are apparent, and the leading-edge vortex has extremely low levels of Q. In addition, in figure A.5 the region of elevated downwash vanishes at $r_g/C = 5.1$.

Figure A.6 shows sectional cuts of spanwise vorticity ω_z at the midspan of the wing. These patterns are shown as a function of two parameters: (i) the Rossby number r_g/C; and (ii) the angle of rotation Φ. Taking an overview of figure A.9, Φ = 90° is generally a sufficient large rotation angle for stabilization of the flow structure, *i.e.*, the flow structure at Φ = 90° closely resembles the structure later at Φ = 270°. Generally, when the rotation angle is used to characterize flow structure, the effects of radius of gyration on the flow structure development around an AR = 1 wing are more pronounced than when the travel distance $r_g\Phi/C$ is used, as in chapter 3.

The flow structure development on an AR = 2 wing as a function of rotation angle Φ is shown in figures A.7 through A.10, using the views employed in chapter 4. Nested iso-surfaces of the Q-criterion are superposed with opaque iso-surfaces of downward velocity (downwash). Initially, at Φ = 15° (figure A.7), much larger vortical structures form at moderate radius of gyration. This is a result of the much larger volume through which the wing has translated at moderate radius of gyration. As the rotation angle increases (figures A.8 and A.9), the flow structures at low radius of gyration become larger, and remain organized, while the flow structures at moderate radius of gyration break down, and become less coherent. At Φ = 270° (figure A.10), the flow structure at moderate radius of gyration is very low level, and is not associated with significant downwash, while at low radius of gyration the flow structure is still organized, it contains elevated levels of iso-Q, and the organized flow structure is associated with a significant region of elevated downwash.

A.3 Streamlines

Figures A.11 through A.14 show the effects of radius of gyration r_g/C, and travel distance $r_g\Phi/C$ on streamlines that originate on the leeward surface of a rotating $AR = 2$ wing. These lines are placed on a rectangular grid, with $0.1C$ spacing between adjacent streamlines, yielding a total of 231 lines. Plan, end, and trimetric views are shown. Initially, at $r_g\Phi/C = 1.0$ (figure A.11), the streamlines closely follow the travel path of the wing. This is especially apparent in the end view (top row), where the streamlines are nearly uniformly distributed along the span, and there is minor swirling very near the surface of the wing.

As the wing continues to rotate at $r_g\Phi/C = 2.0$ (figure A.12), the streamlines highlight different flow features. At low radius of gyration, a significant number of the streamlines outboard of the midspan roll up into the tip vortex. It is also evident that streamlines near the leading-edge are entrained into this tip vortex, after traveling through the leading-edge vortex. At moderate radius of gyration, streamlines are instead entrained into the arch vortex. The density of streamlines in this arch vortex is higher than in any other region of the flow.

At larger travel distances $r_g\Phi/C = 3.0$ (figure A.13), and $r_g\Phi/C = 5.5$ (figure A.14), the streamline pattern at low radius of gyration is similar to the pattern seen at $r_g\Phi/C = 2.0$ (figure A.12). In contrast, the streamlines at moderate radius of gyration, and a travel distance $r_g\Phi/C = 3.0$, show the breakdown of the arch vortex. The streamlines in

this vortex are less concentrated than in the previous figure, and the vortex has shifted toward the tip of the wing. At $r_g\Phi/C$ = 5.5, the arch vortex is no longer evident; it has been replaced by a large region of swirling streamlines. In contrast, at low radius of gyration, the leading-edge/tip vortex system remains.

A.4 Comparison of vorticity components in Cartesian and cylindrical coordinates

Figures A.16 through A.20 compare the components of vorticity on rotating *AR* = 1 and *AR* = 2 wings when represented in Cartesian (*xyz)*, and cylindrical (*rθz*) coordinates. A plan-view schematic of these coordinate systems in relation to the rotating wing is shown in figure A.15. For all figures, each component of vorticity is represented with ω_i = ||4|| iso-surfaces, where ω_i is the indicated component of vorticity: *x, z, r, θ*. Orange iso-surfaces are associated with positive vorticity ω_i = +4, and blue iso-surfaces are associated with negative vorticity ω_i = -4.

Figure A.16 shows plan views of an *AR* = 1 wing at the extreme radii of gyration investigated herein, and at a travel distance of $r_g\Phi/C$ = 5.5. It is clear from this figure that the cylindrical coordinate system separates vorticity representing the leading-edge and trailing-edge vortices into radial vorticity ω_r, and vorticity representing root and tip vortices into azimuthal vorticity ω_θ. In contrast, when the vorticity is represented in

Cartesian coordinates, the tip vortex at low radius of gyration is a mixture of spanwise vorticity ω_z (blue), and tangential vorticity ω_x (orange).

Figures A.17 through A.20 show plan views of an AR = 2 wing at two radii of gyration for several travel distances. This sequence therefore shows the development of vorticity in Cartesian and cylindrical coordinates. The same layout and iso-surfaces employed in figure A.16 are again used in figures A.17 through A.20. The effect of cylindrical coordinates is to isolate the root and tip vortices as azimuthal vorticity ω_θ. Another feature highlighted with these vorticity representations is the legs of the arch vortex at moderate radius of gyration. When the vorticity components are separated, these legs are represented with iso-surfaces of both azimuthal vorticity ω_θ, and tangential vorticity ω_x, near the surface of the wing and below the arch vortex, which is represented with radial vorticity ω_r, and spanwise vorticity ω_z at travel distance $r_g\Phi/C$ = 2.0 (figure A.17).

A.5 Flow structure for different aspect ratio *AR* wings

Figures A.21 through A.25 show comparisons of the flow structure at different radii of gyration for wings of aspect ratio AR = 1, 2, and 5. The travel distance for these images is $r_g\Phi/C$ = 5.5. In figures A.21 through A.23, nested, transparent iso-surfaces of Q-criterion are shown. In these figures, it is clear that the most coherent vortical

structures occur on the AR = 1 wing. The Q = 7 and Q = 15 iso-surfaces are largest on that wing. However, the leading-edge vortical structures on the AR = 2 wing are also highly organized at low radius of gyration. In contrast to the images of AR = 1 and 2 wings, the overall flow structures on the AR = 5 wing are significantly different. Low level Q-criterion persists near the leading-edge across the span of that wing. In addition, a highly coherent vortex, with a cylindrical shape, branches off of the leading-edge vorticity near the root-leading-edge corner of the wing, and this vortex extends diagonally towards the trailing-edge and across the wing planform. It eventually reaches the trailing-edge of the wing (see figure A.21). When the vortex crosses the trailing-edge, it rapidly breaks down. Outboard of this vortex breakdown, there are significantly more low level Q-criterion iso-surfaces near the trailing-edge of the wing than there are inboard of the vortex breakdown.

Figure A.24 shows iso-surfaces of Q-criterion (Q = 4.5) colored with helical density H in a lab-fixed reference frame. When the aspect ratio or the radius of gyration is minimized, large magnitude (blue) helical density is evident throughout the tip vortex, and vortical structures are generally more organized. When these parameters are not minimized, less coherent vortical structures exist, with lower magnitude helical density on their surfaces.

Figure A.25 shows nested, transparent iso-surfaces of Q-criterion superposed with opaque iso-surfaces of downward velocity v/V_{rg} (downwash). The downwash iso-surface on the AR = 5 wing is significantly different from the downwash iso-surfaces on wings of lower aspect ratio. For this wing, a large downwash iso-surface exists, despite the lack of

an organized root or tip vortex, which was a feature associated with significant downwash velocity on the lower aspect ratio wings. The relative size of the downwash, compared to the total planform area of the wing, is, however, significantly less for the *AR* = 5 wing than the *AR* = 1 and *AR* = 2 wing at low radius of gyration, *i.e.*, the lower aspect ratio wings generate significantly more downwash per unit of planform area.

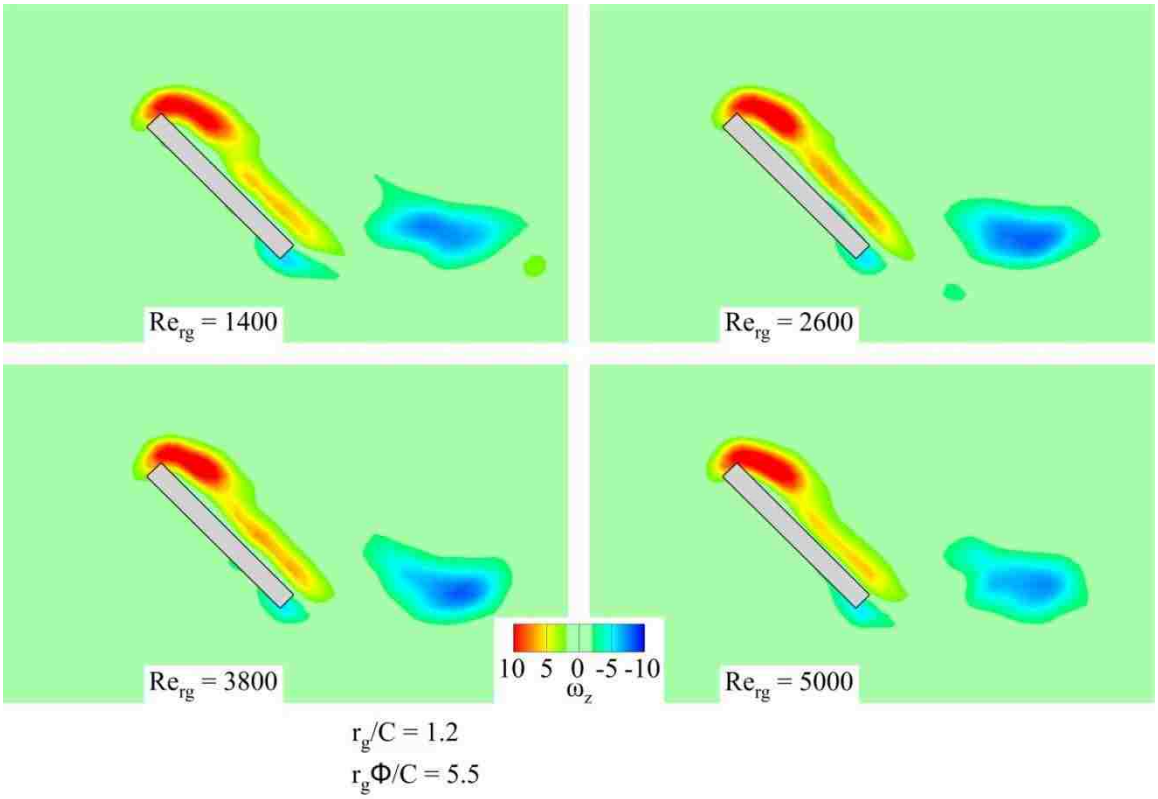

Figure A.1. Sectional cuts of spanwise vorticity at midspan for different values of Reynolds number Re_{rg} based on velocity at the radius of gyration.

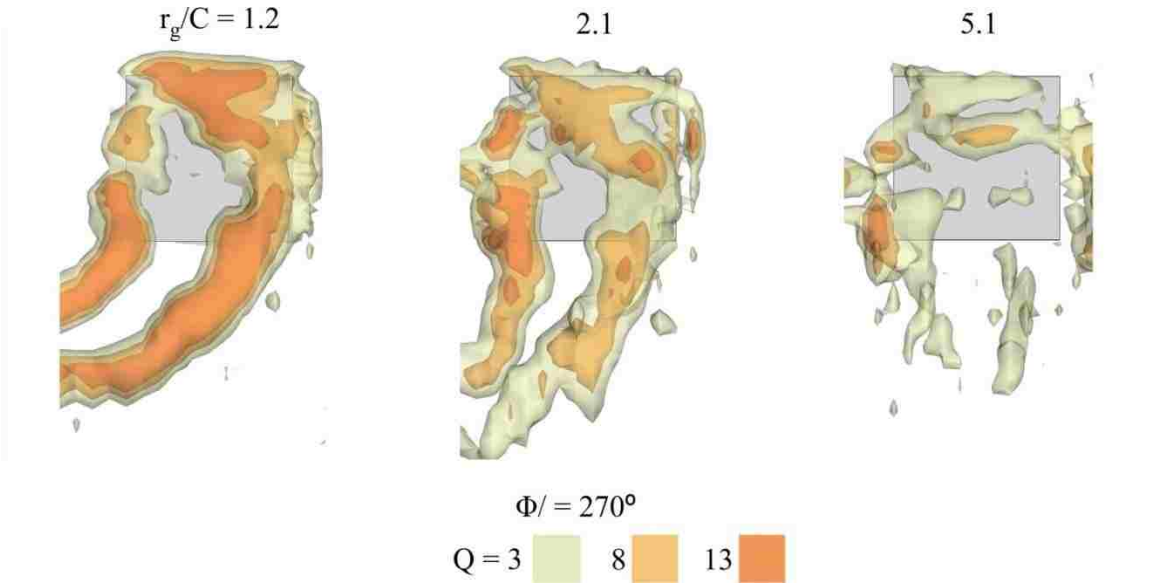

Figure A.2. Plan view of Transparent iso-surfaces of *Q*-criterion at different values of Rossby number r_g/C at $\Phi = 270°$.

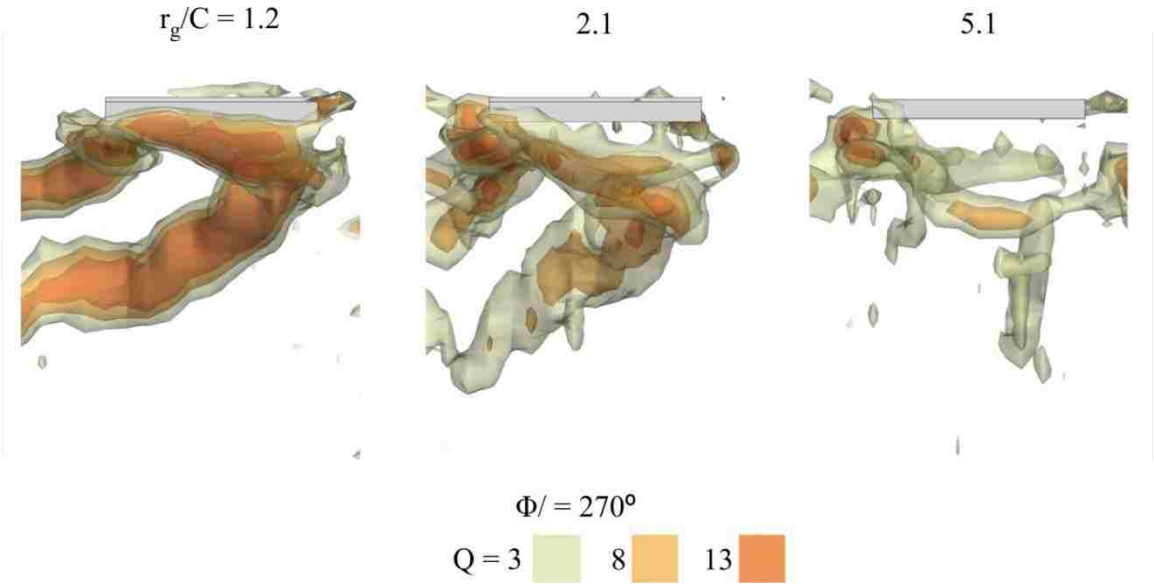

Figure A.3. End view of transparent iso-surfaces of *Q*-criterion at different values of Rossby number r_g/C and $\Phi = 270°$.

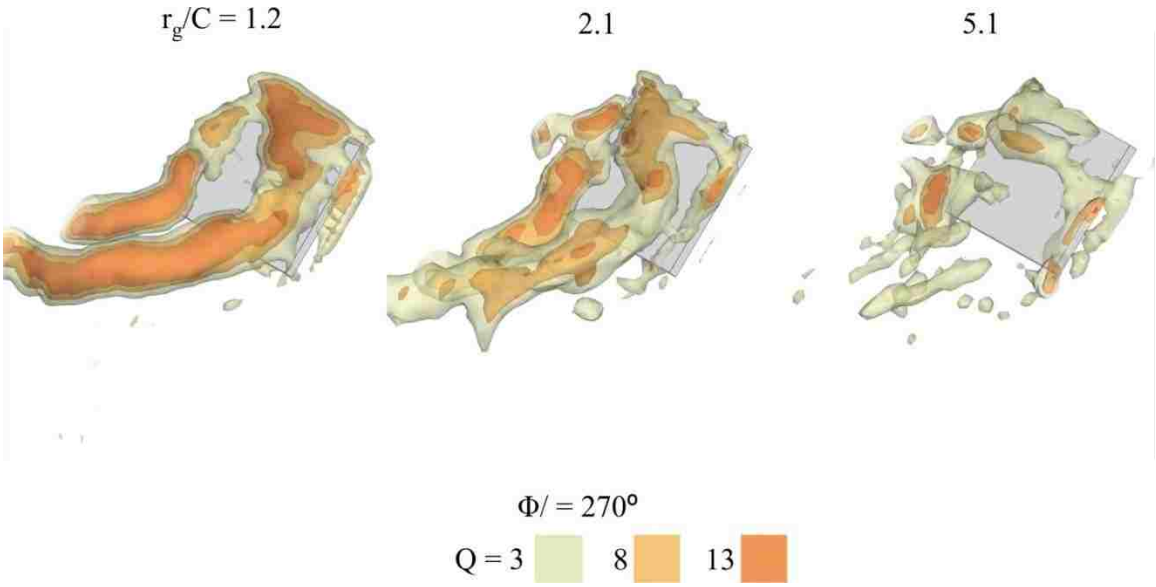

Figure A.4. Trimetric view of transparent iso-surfaces of *Q*-criterion at different values of Rossby number r_g/C and $\Phi = 270°$.

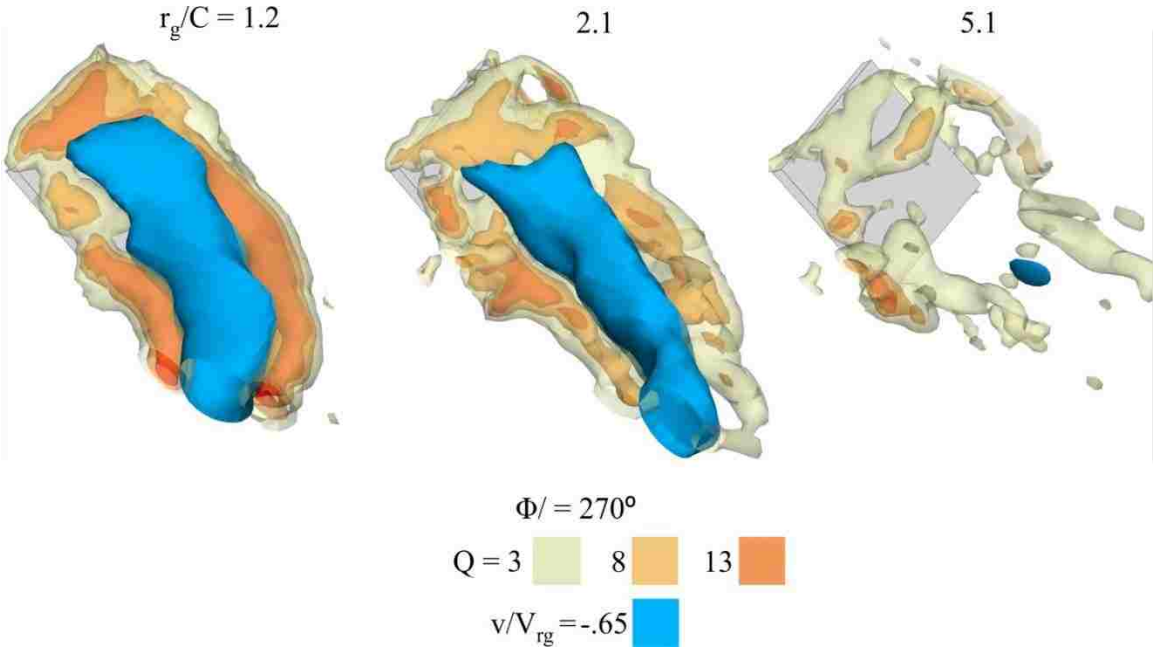

Figure A.5. Trimetric view of transparent iso-surfaces of *Q*-criterion and opaque iso-surfaces of downwash (downward velocity) v/V_{rg} at different values of Rossby number r_g/C and $\Phi = 270°$.

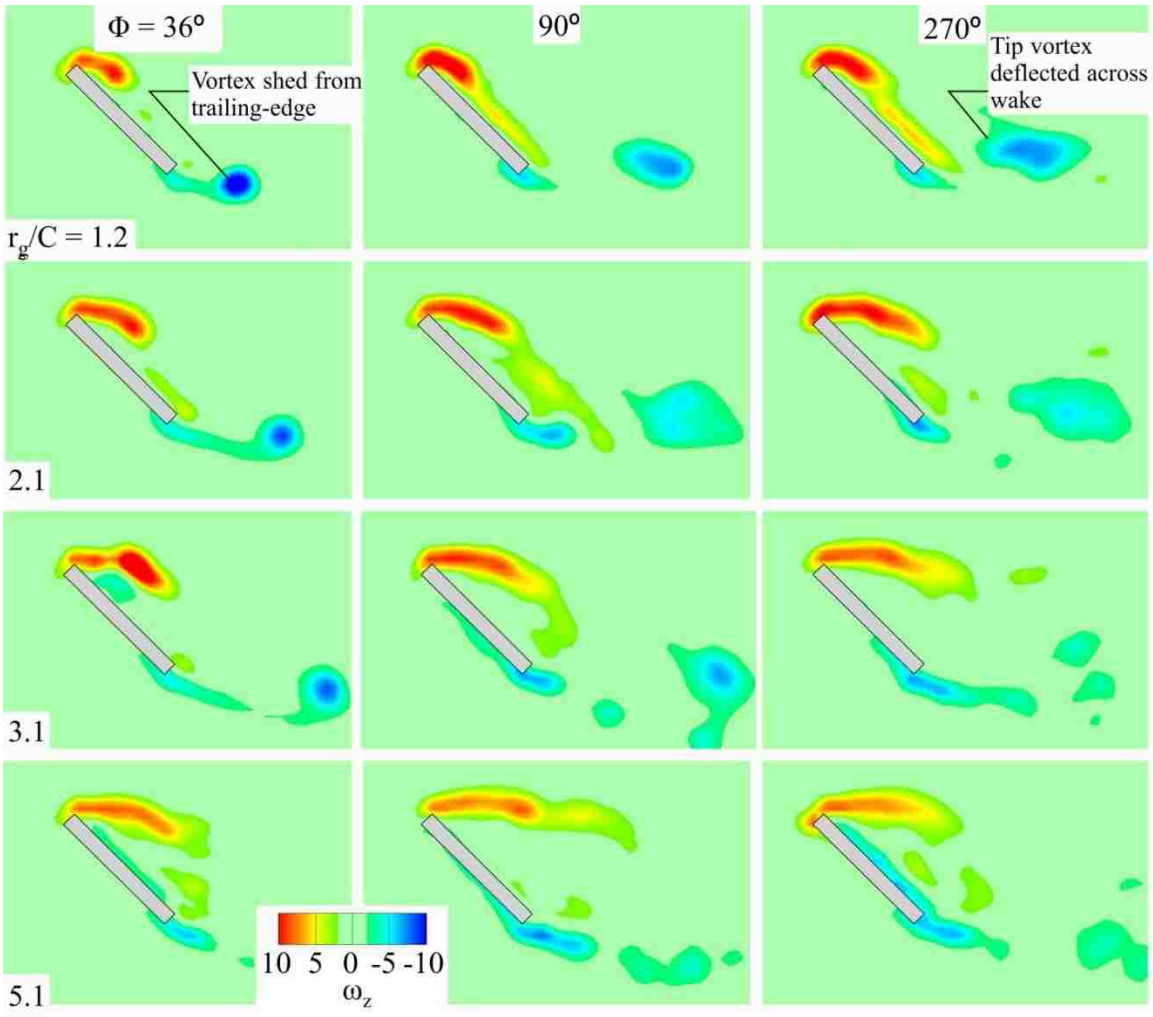

Figure A.6. Sectional cuts at midspan of spanwise vorticity at different values of Rossby number r_g/C as indicated, and rotation angle Φ.

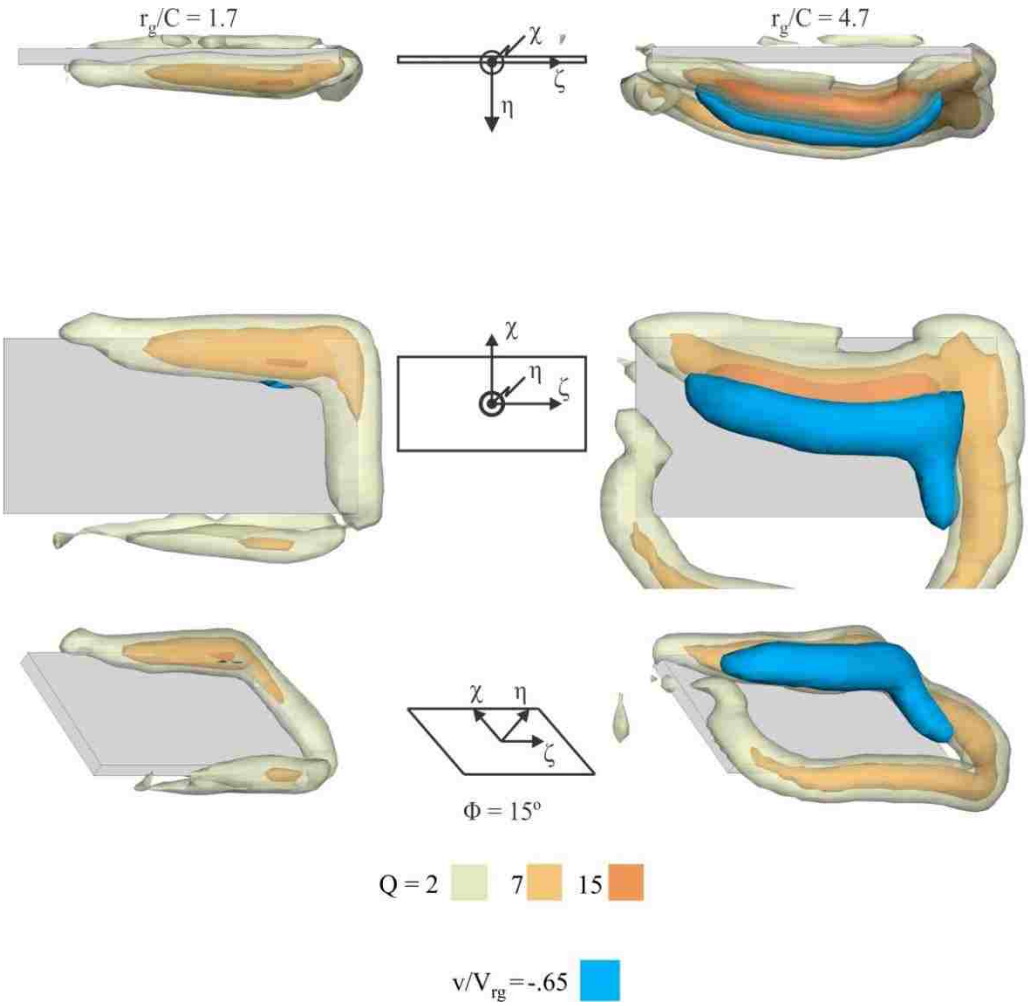

Figure A.7. Transparent iso-surfaces of *Q*-criterion and opaque iso-surfaces of downwash at different values of Rossby number r_g/C. Rotation angle Φ = 15°.

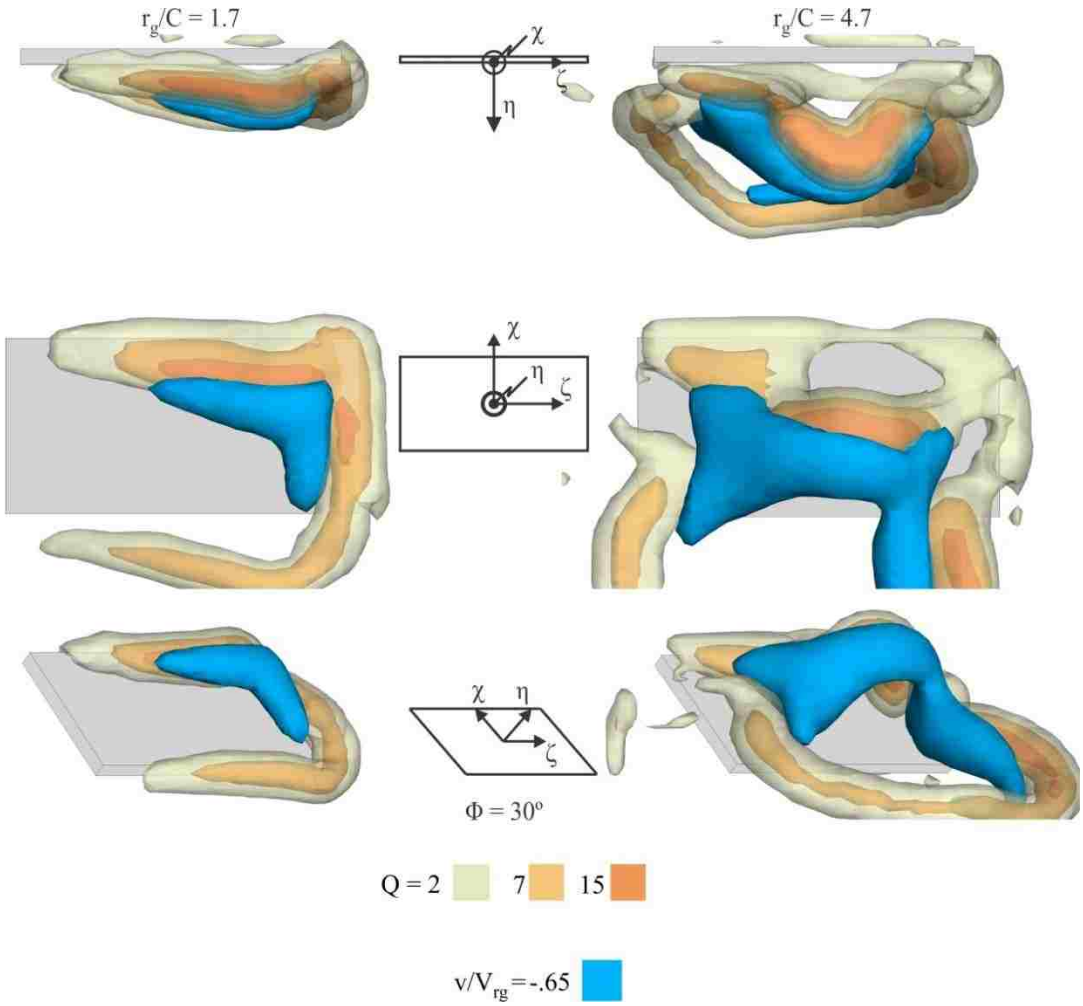

Figure A.8. Transparent iso-surfaces of *Q*-criterion and opaque iso-surfaces of downwash at different values of Rossby number r_g/C. Rotation angle $\Phi = 30°$.

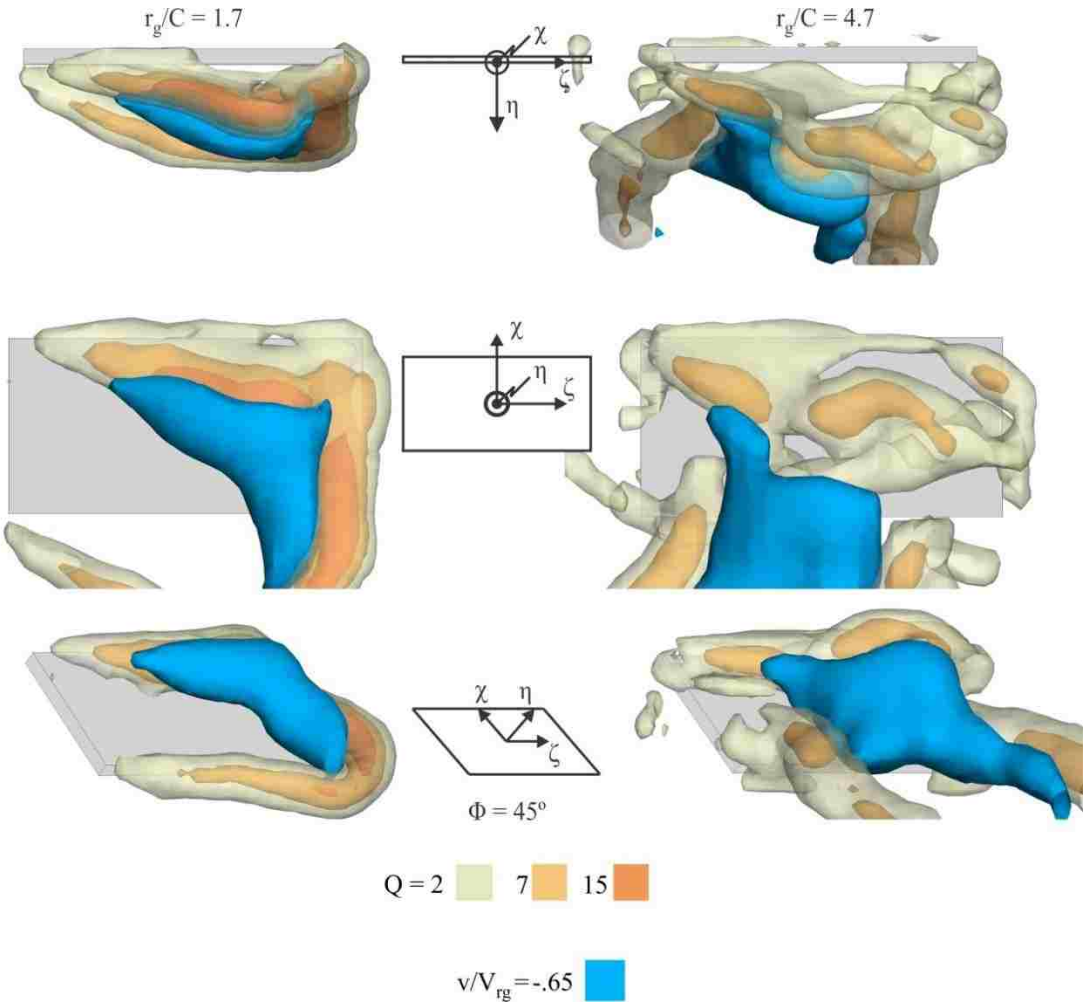

Figure A.9. Transparent iso-surfaces of *Q*-criterion and opaque iso-surfaces of downwash at different values of Rossby number r_g/C. Rotation angle $\Phi = 45°$.

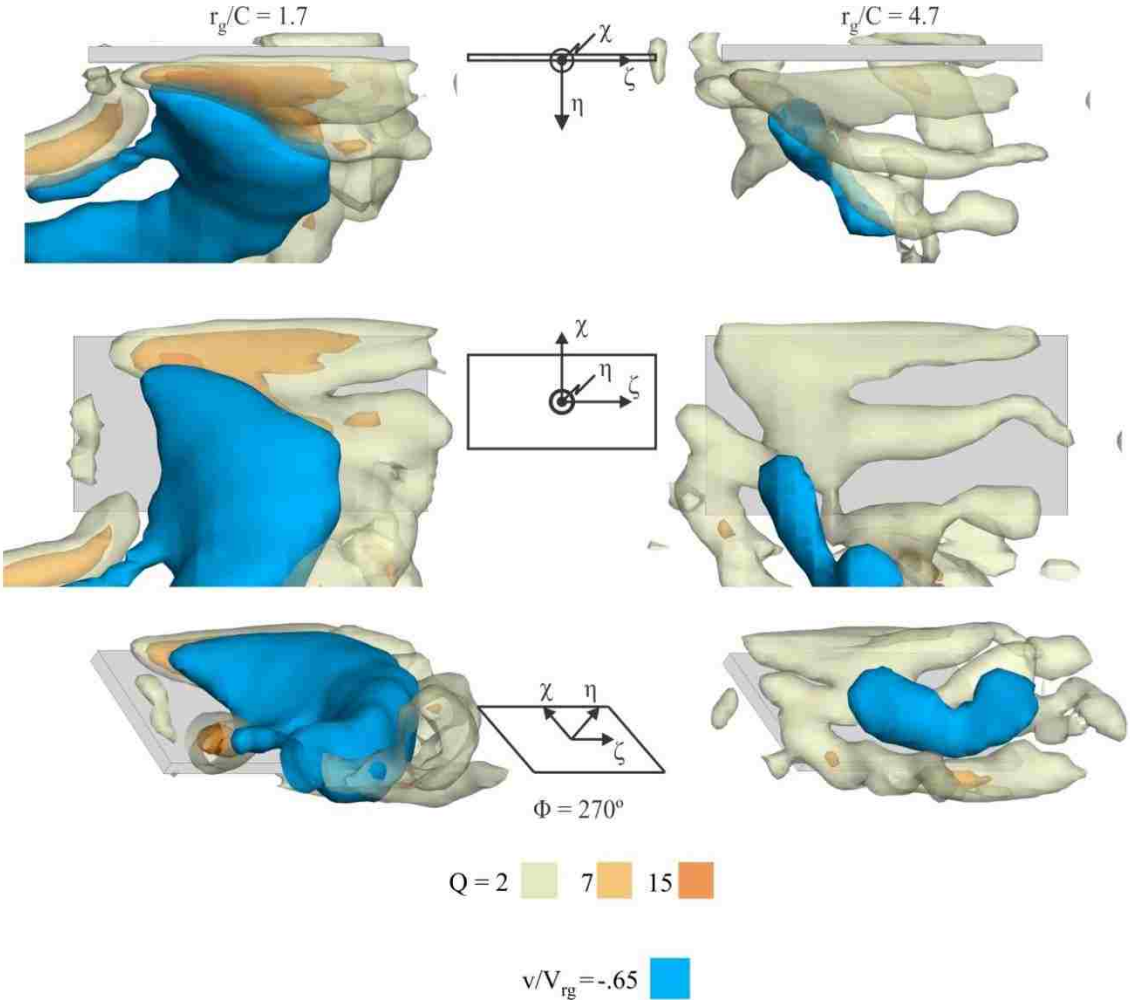

Figure A.10. Transparent iso-surfaces of *Q*-criterion and opaque iso-surfaces of downwash at different values of Rossby number r_g/C. Rotation angle Φ = 270°.

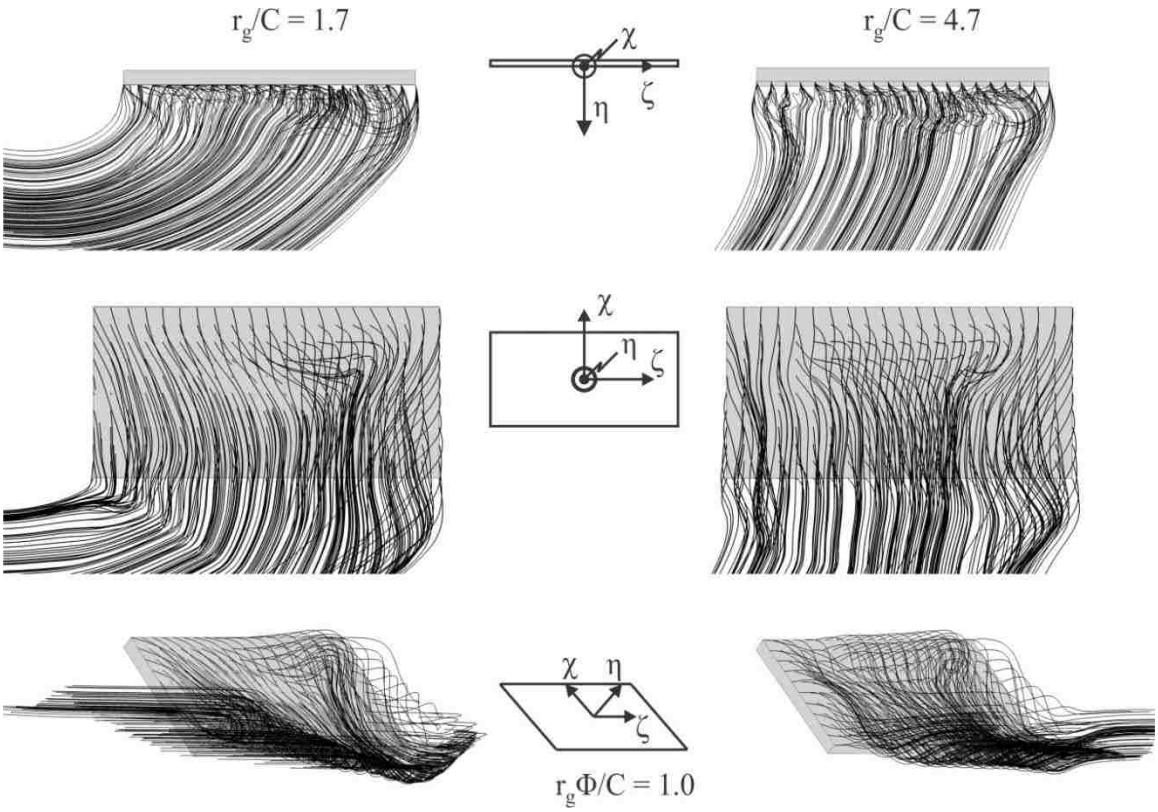

Figure A.11. Streamlines originating from a 0.1*C* rectangular grid on the leeward surface of a rotating wing for different values of Rossby number r_g/C. Rotation distance $r_g\Phi/C$ = 1.0.

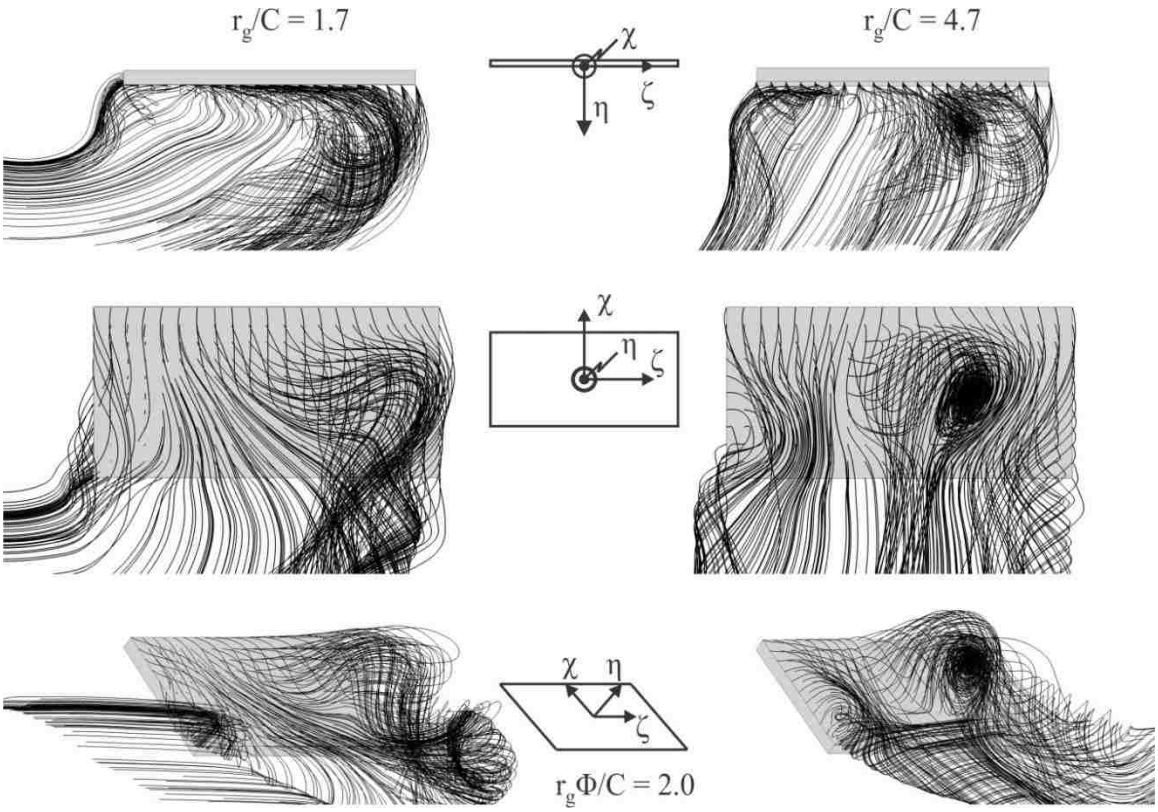

Figure A.12. Streamlines originating from a 0.1*C* rectangular grid on the leeward surface of a rotating wing for different values of Rossby number r_g/C. Rotation distance $r_g\Phi/C$ = 2.0.

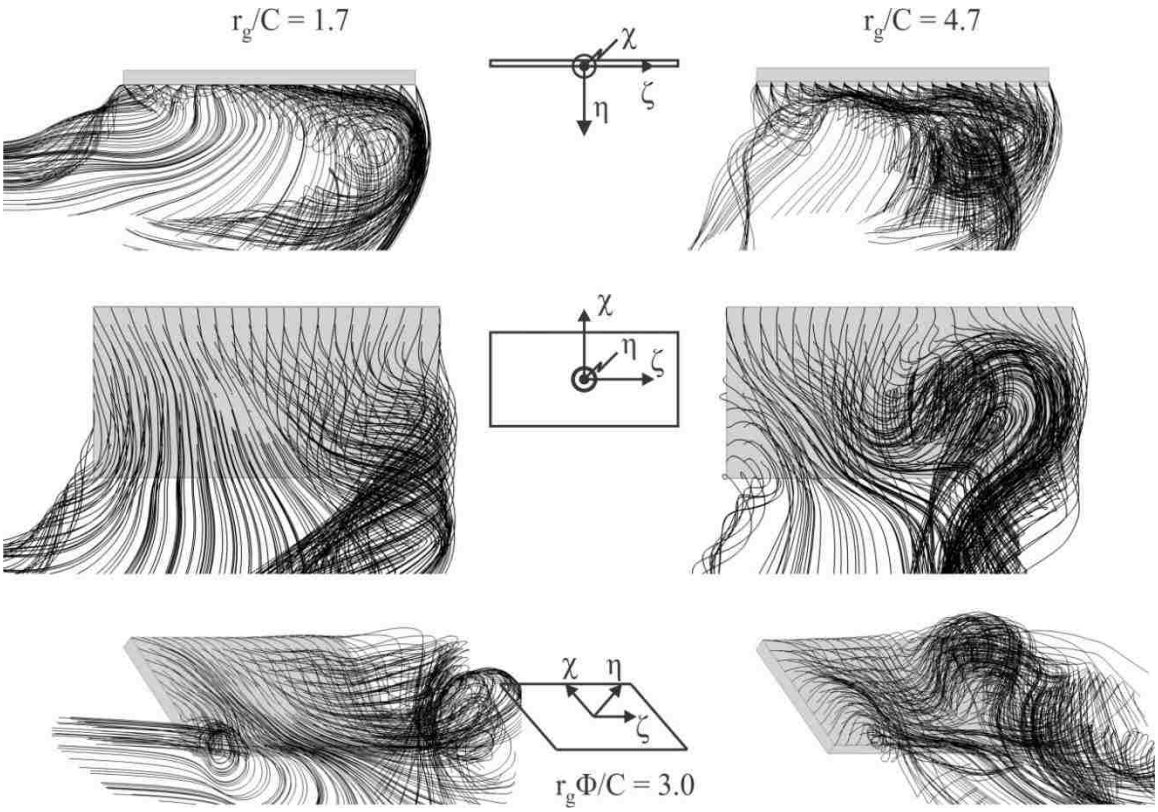

Figure A.13. Streamlines originating from a 0.1*C* rectangular grid on the leeward surface of a rotating wing for different values of Rossby number r_g/C. Rotation distance $r_g\Phi/C$ = 3.0.

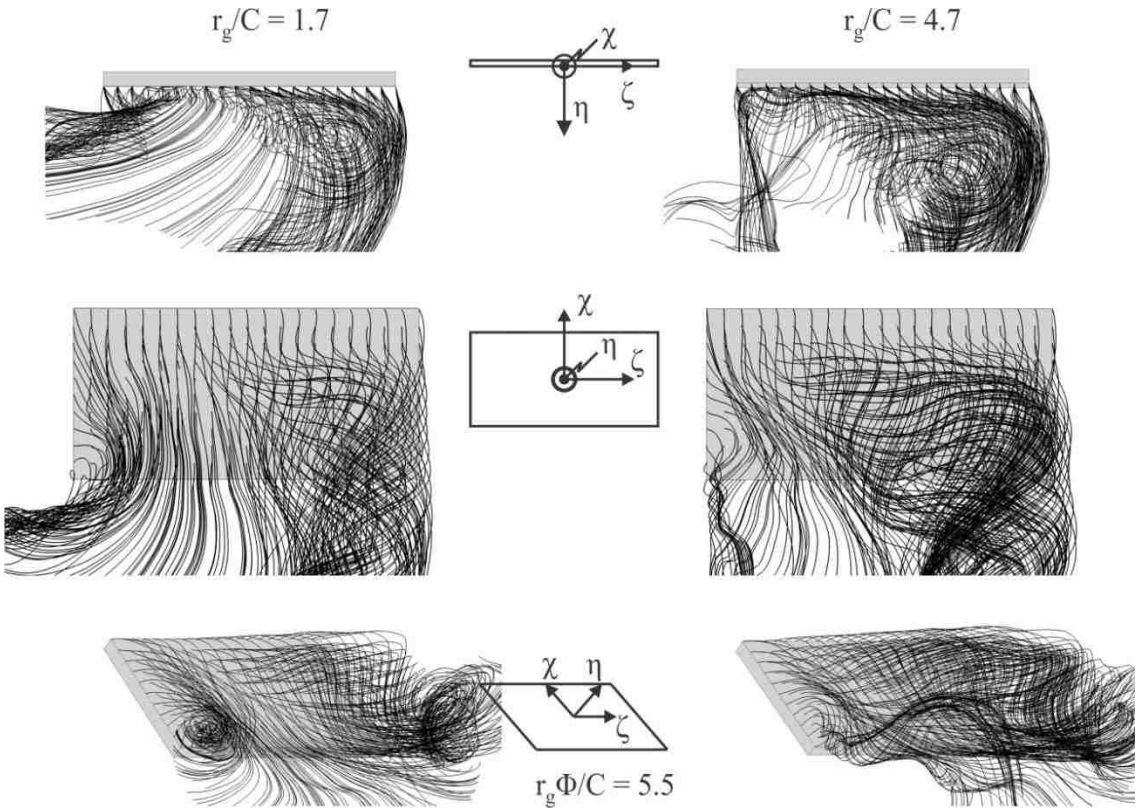

Figure A.14. Streamlines originating from a 0.1*C* rectangular grid on the leeward surface of a rotating wing for different values of Rossby number r_g/C. Rotation distance $r_g\Phi/C$ = 5.5.

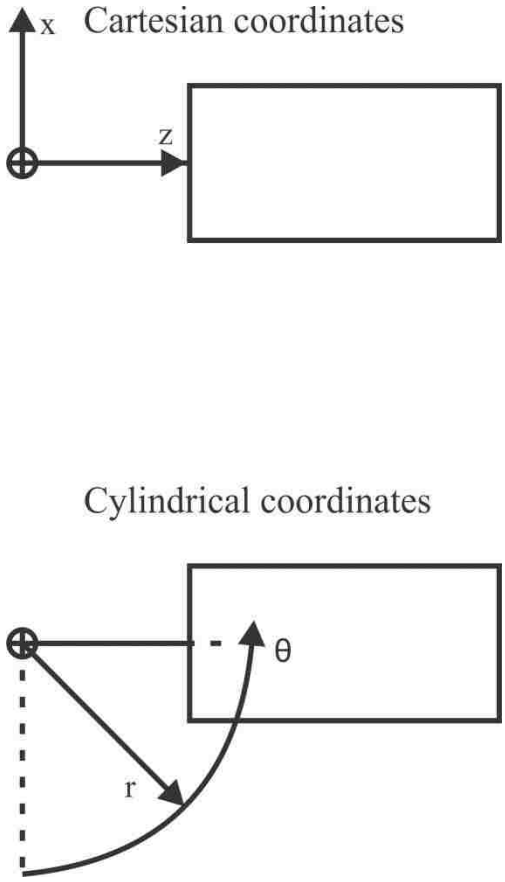

Figure A.15. Schematic of Cartesian and cylindrical coordinate systems used to represent components of vorticity in figures A.16 through A.20.

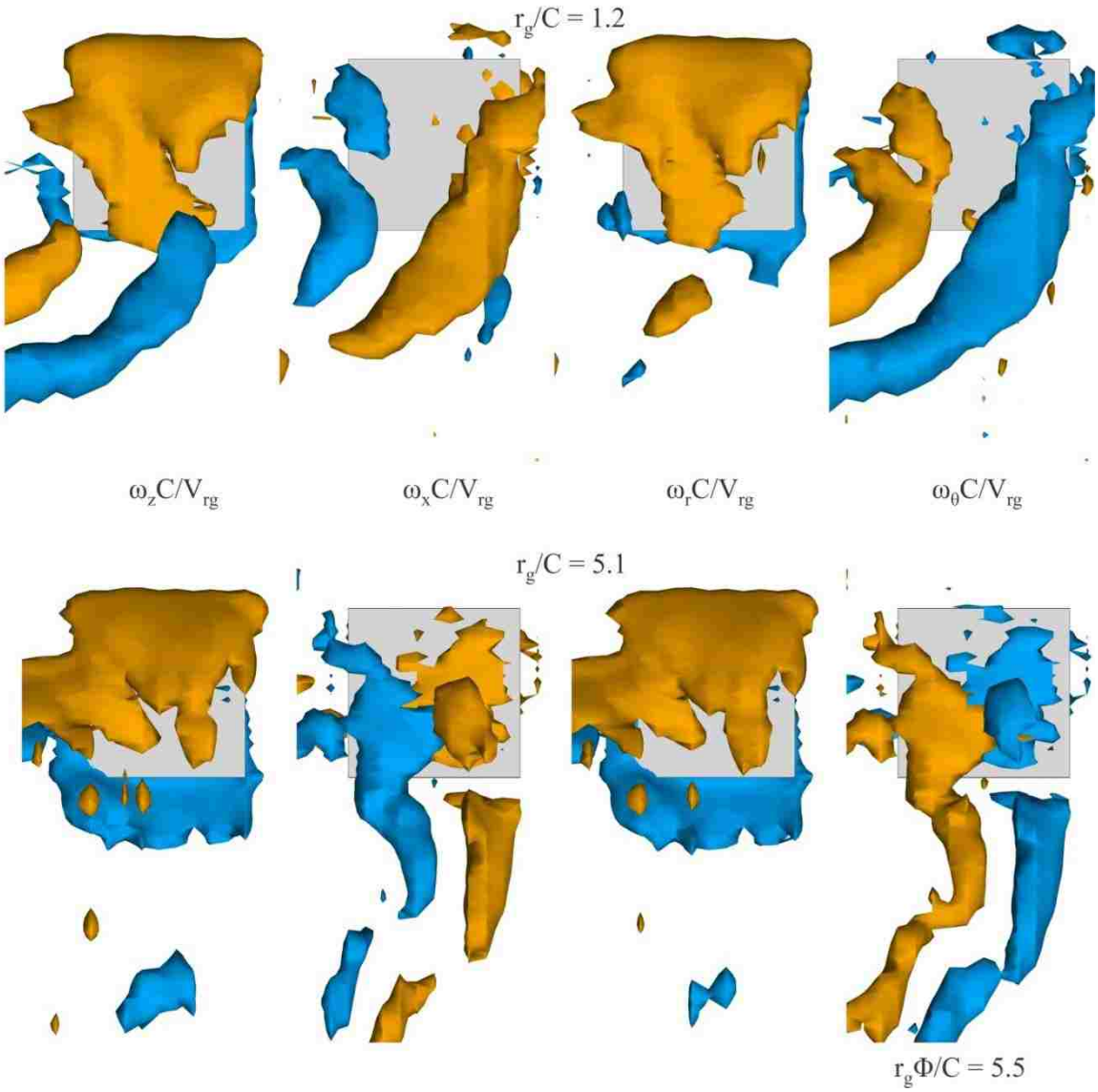

Figure A.16. Plan view of iso-surfaces of components of vorticity in rectangular and cylindrical coordinates at different values of Rossby number r_g/C. All iso-surfaces have a magnitude of $\|\omega_i\| = 4$. Orange iso-surfaces indicate positive vorticity and blue iso-surfaces indicate negative vorticity. $AR = 1$. Rotation distance $r_g\Phi/C = 5.5$.

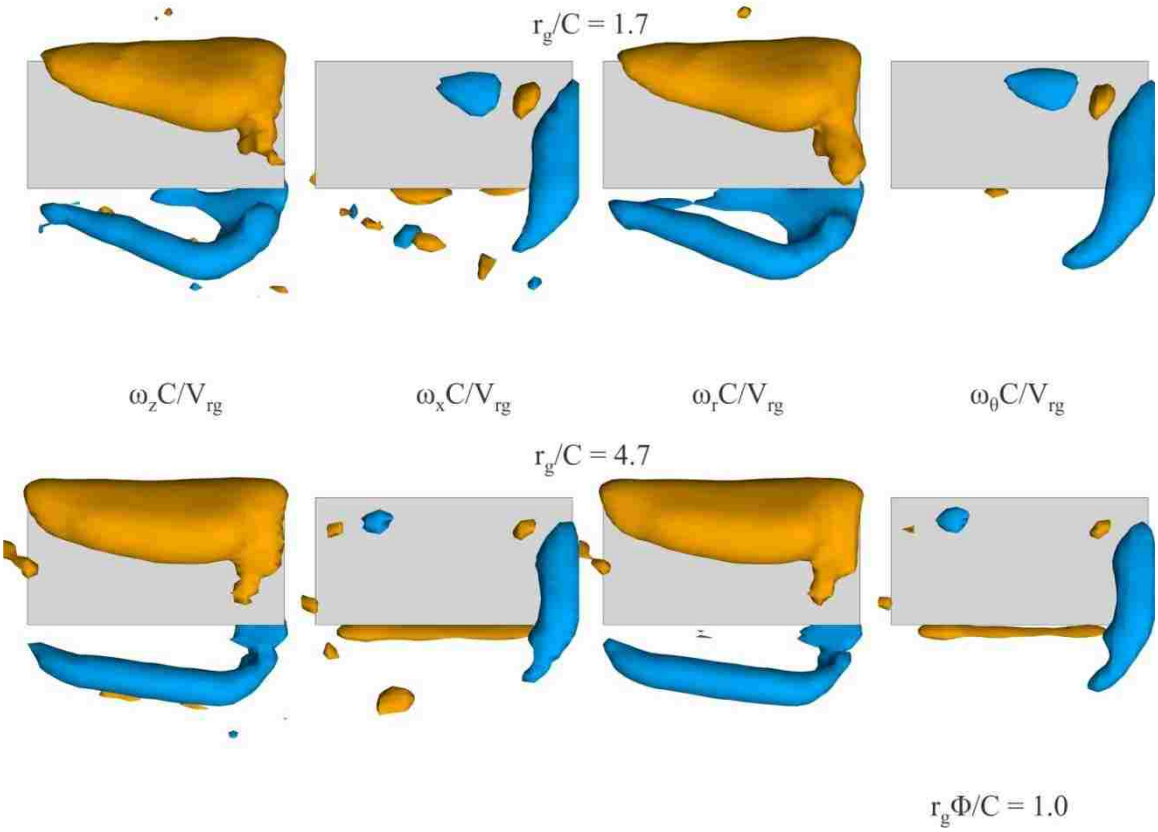

Figure A.17. Plan view of iso-surfaces of components of vorticity in rectangular and cylindrical coordinates at different values of Rossby number r_g/C. All iso-surfaces have a magnitude of $||\omega_i||$ = 4. Orange iso-surfaces indicate positive vorticity and blue iso-surfaces indicate negative vorticity. AR = 2. Rotation distance $r_g\Phi/C$ = 1.0.

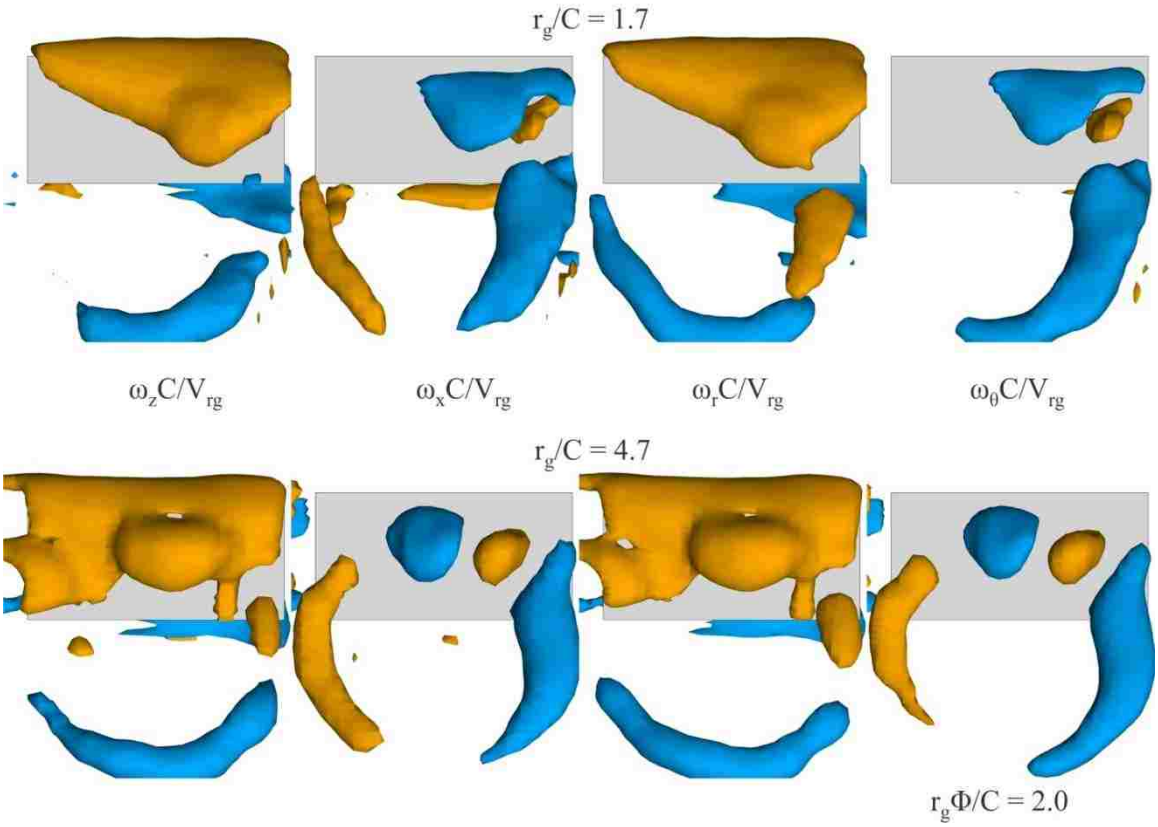

Figure A.18. Plan view of iso-surfaces of components of vorticity in rectangular and cylindrical coordinates at different values of Rossby number r_g/C. All iso-surfaces have a magnitude of $||\omega_i||$ = 4. Orange iso-surfaces indicate positive vorticity and blue iso-surfaces indicate negative vorticity. AR = 2. Rotation distance $r_g\Phi/C$ = 2.0.

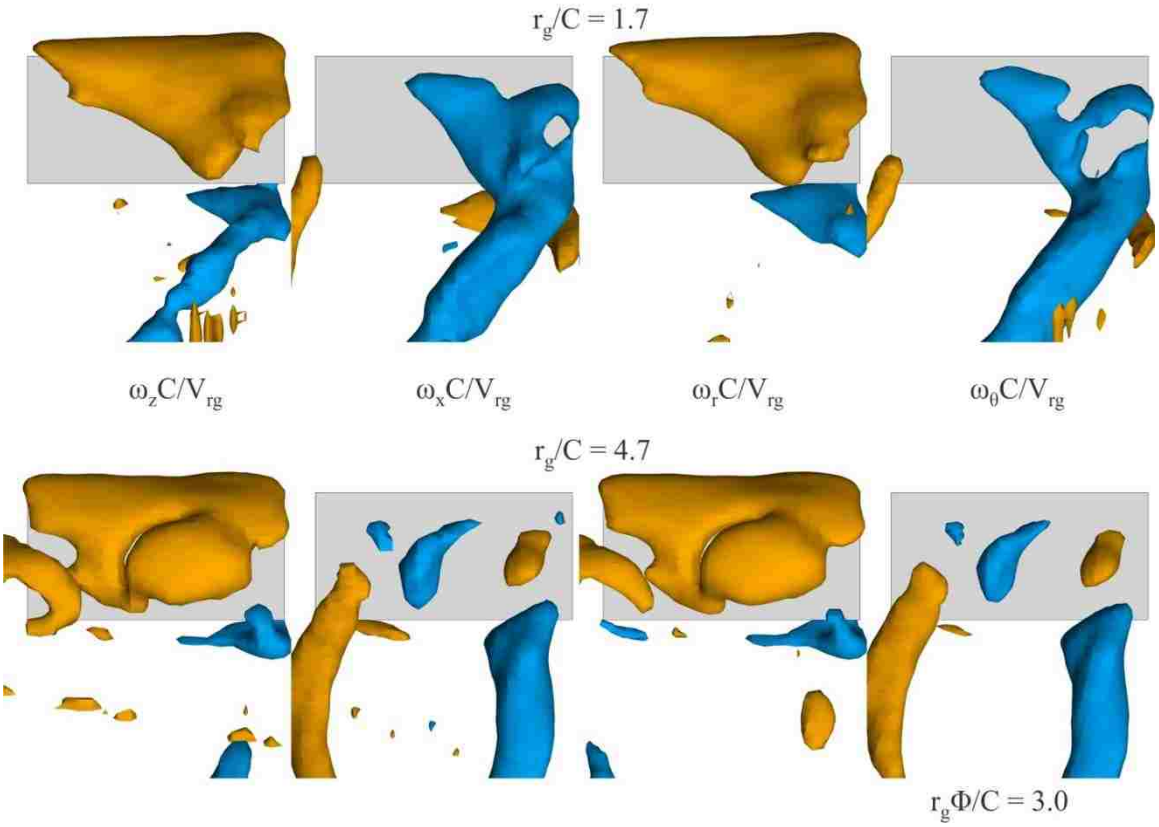

Figure A.19. Plan view of iso-surfaces of components of vorticity in rectangular and cylindrical coordinates at different values of Rossby number r_g/C. All iso-surfaces have a magnitude of $\|\omega_i\| = 4$. Orange iso-surfaces indicate positive vorticity and blue iso-surfaces indicate negative vorticity. $AR = 2$. Rotation distance $r_g\Phi/C = 3.0$.

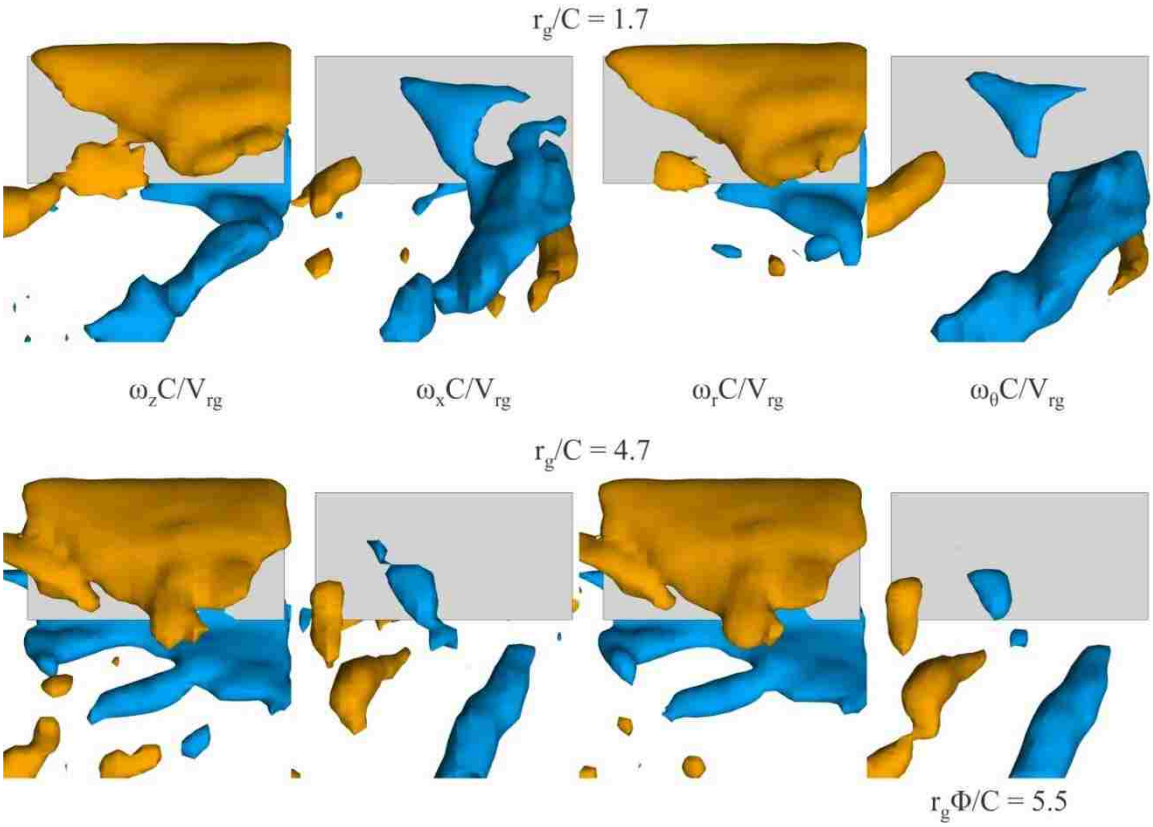

Figure A.20. Plan view of iso-surfaces of components of vorticity in rectangular and cylindrical coordinates at different values of Rossby number r_g/C. All iso-surfaces have a magnitude of $||\omega_i||$ = 4. Orange iso-surfaces indicate positive vorticity and blue iso-surfaces indicate negative vorticity. AR = 2. Rotation distance $r_g\Phi/C$ = 5.5.

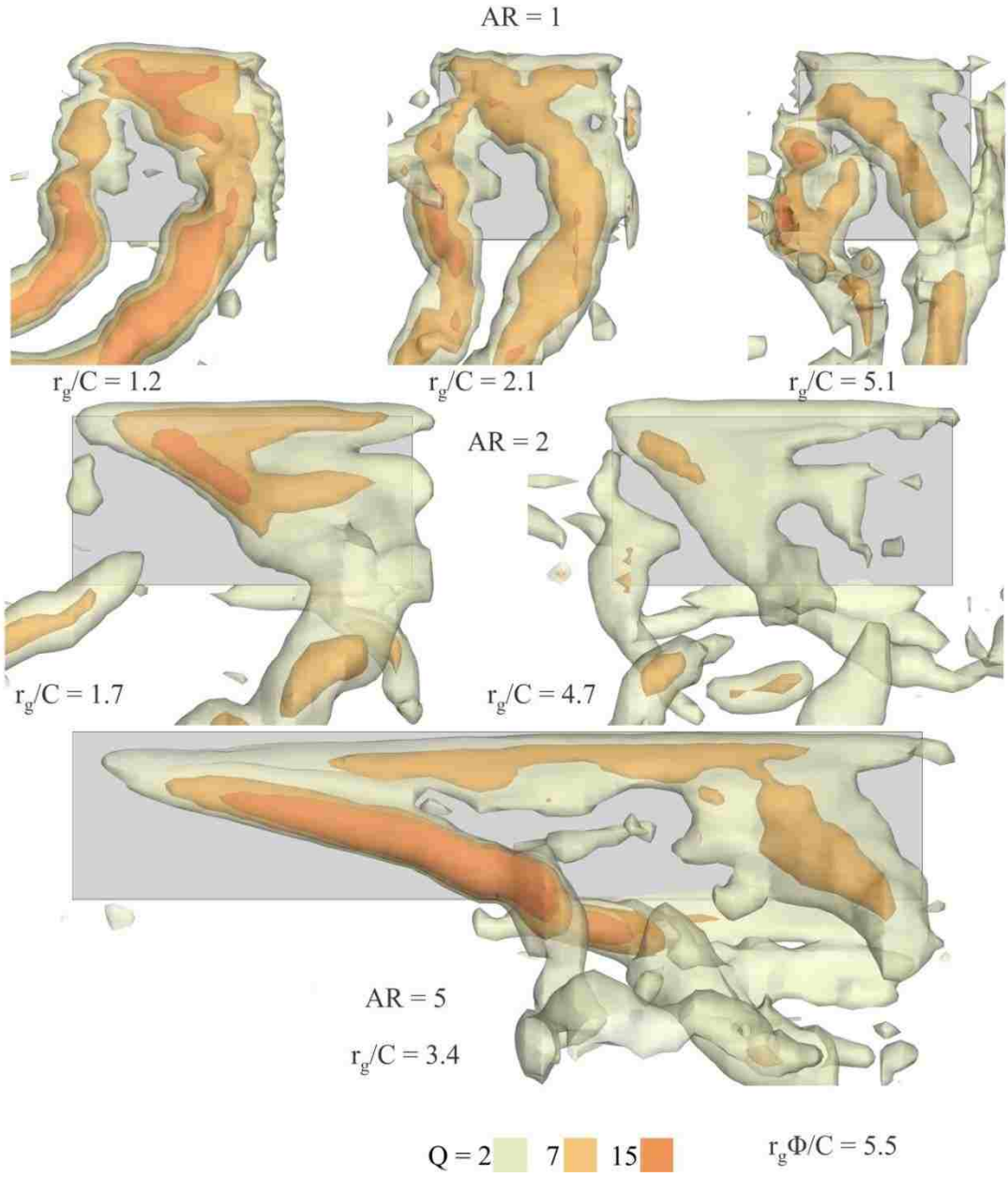

Figure A.21. Plan view of transparent iso-surfaces of *Q*-criterion at different values of Rossby number r_g/C and aspect ratio $AR = b/C$. Rotation distance $r_g\Phi/C = 5.5$. Lab-fixed reference frame.

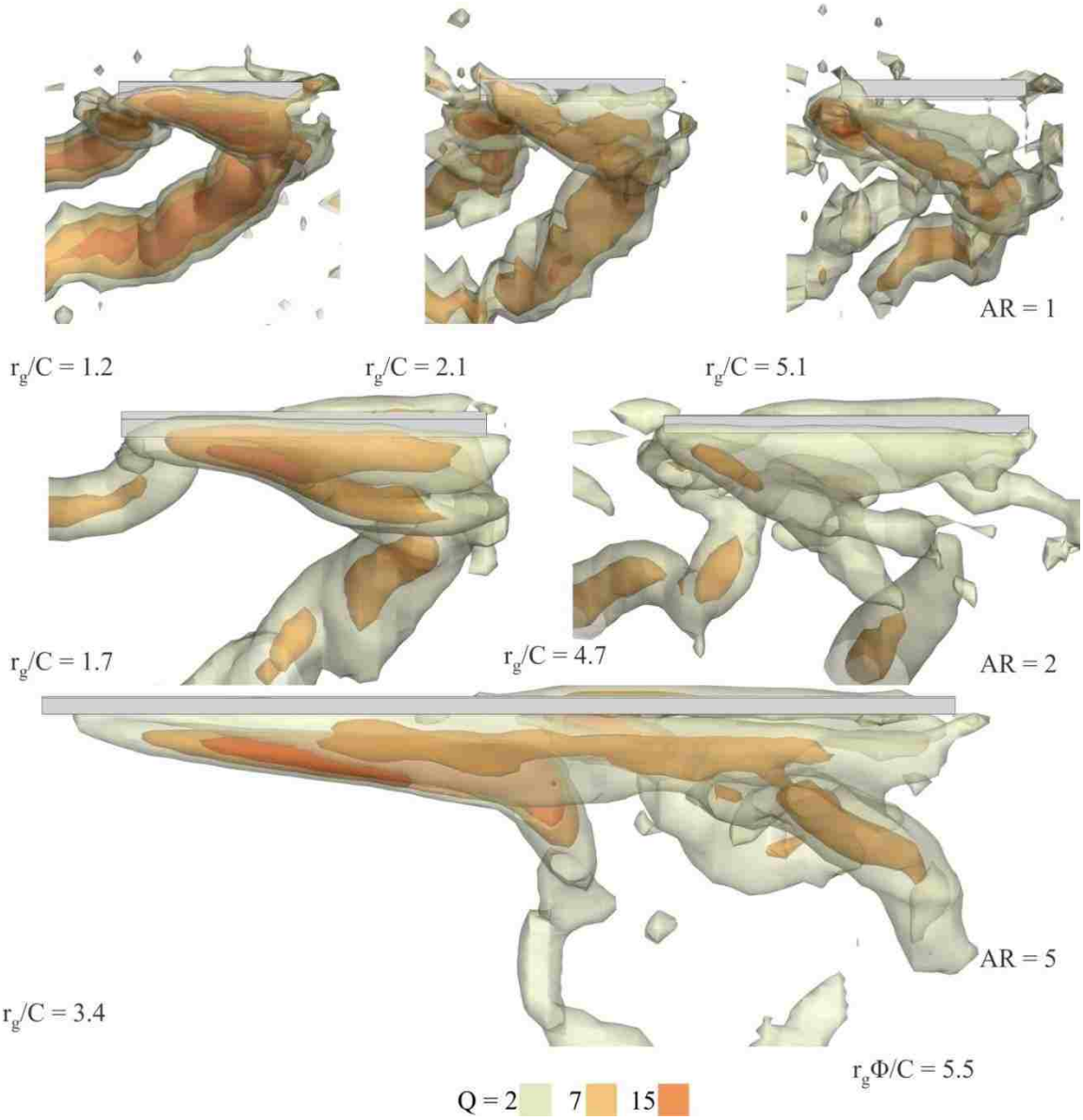

Figure A.22. End view of transparent iso-surfaces of *Q*-criterion at different values of Rossby number r_g/C and aspect ratio $AR = b/C$. Rotation distance $r_g\Phi/C = 5.5$. Lab-fixed reference frame.

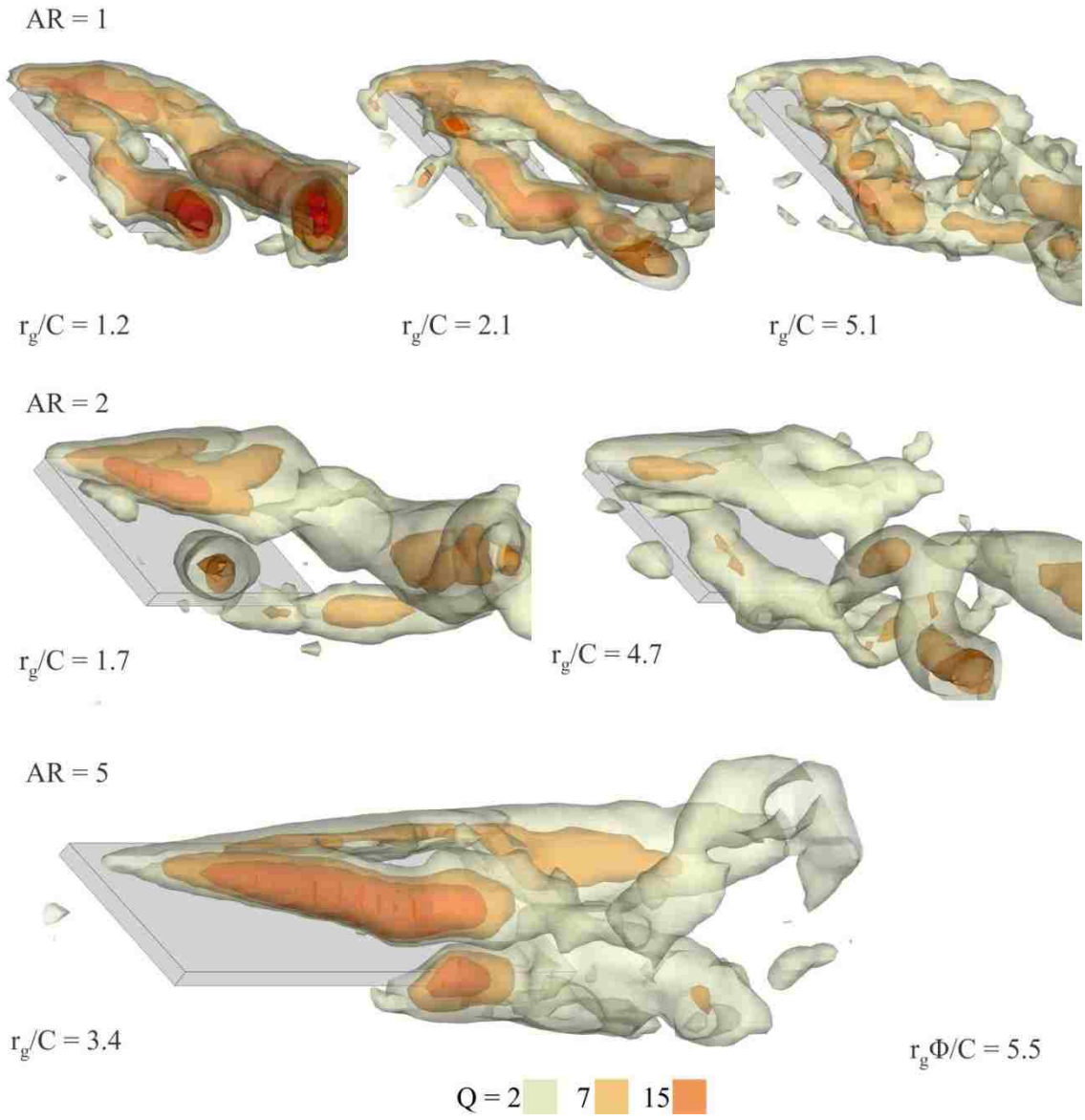

Figure A.23. Trimetric view of transparent iso-surfaces of *Q*-criterion at different values of Rossby number r_g/C and aspect ratio $AR = b/C$. Rotation distance $r_g\Phi/C = 5.5$. Lab-fixed reference frame.

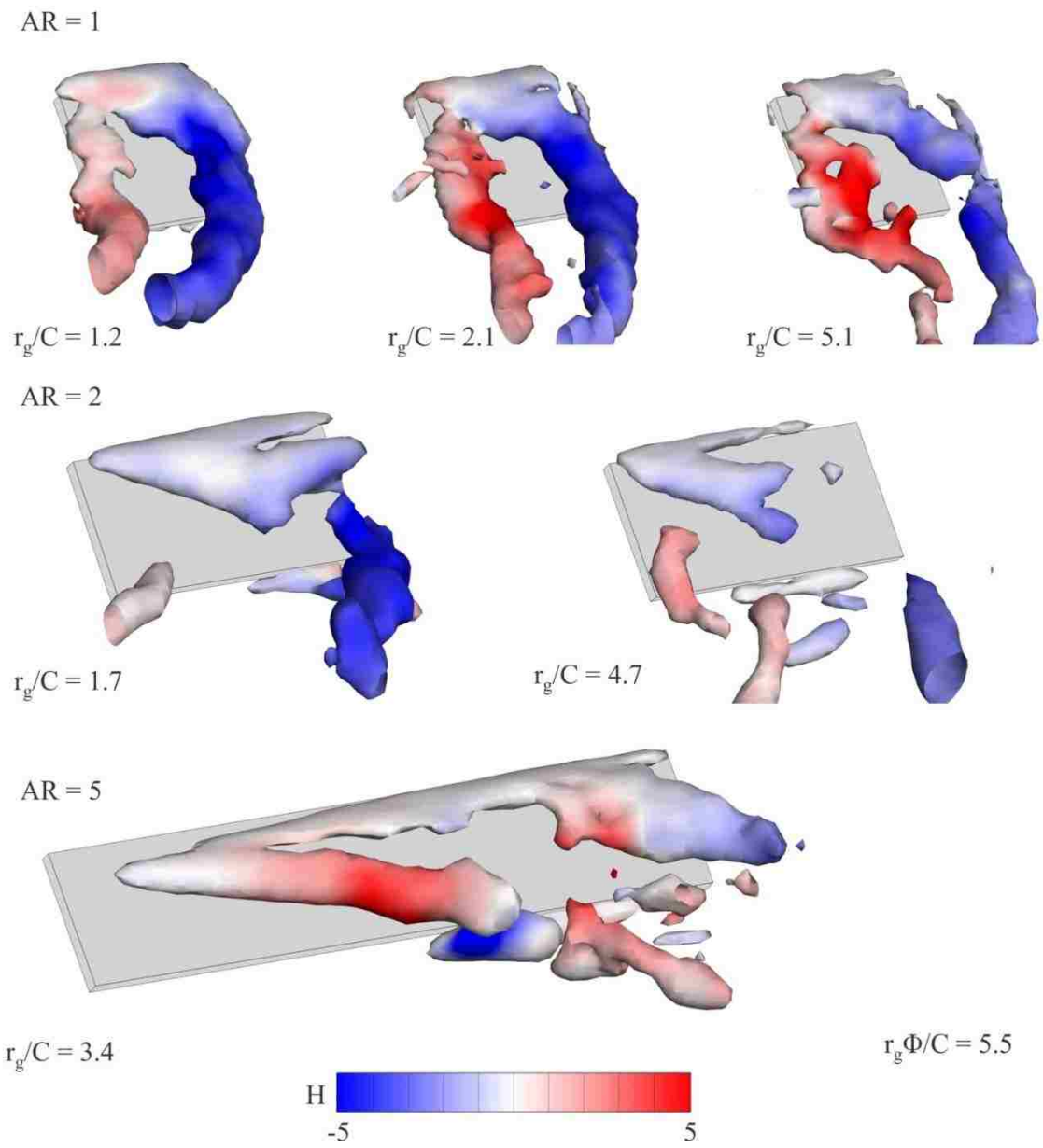

Figure A.24. Trimetric view of iso-surfaces of *Q*-criterion $Q = 4.5$ colored with helical density H at different values of Rossby number r_g/C and aspect ratio $AR = b/C$. Rotation distance $r_g\Phi/C = 5.5$. Lab-fixed reference frame.

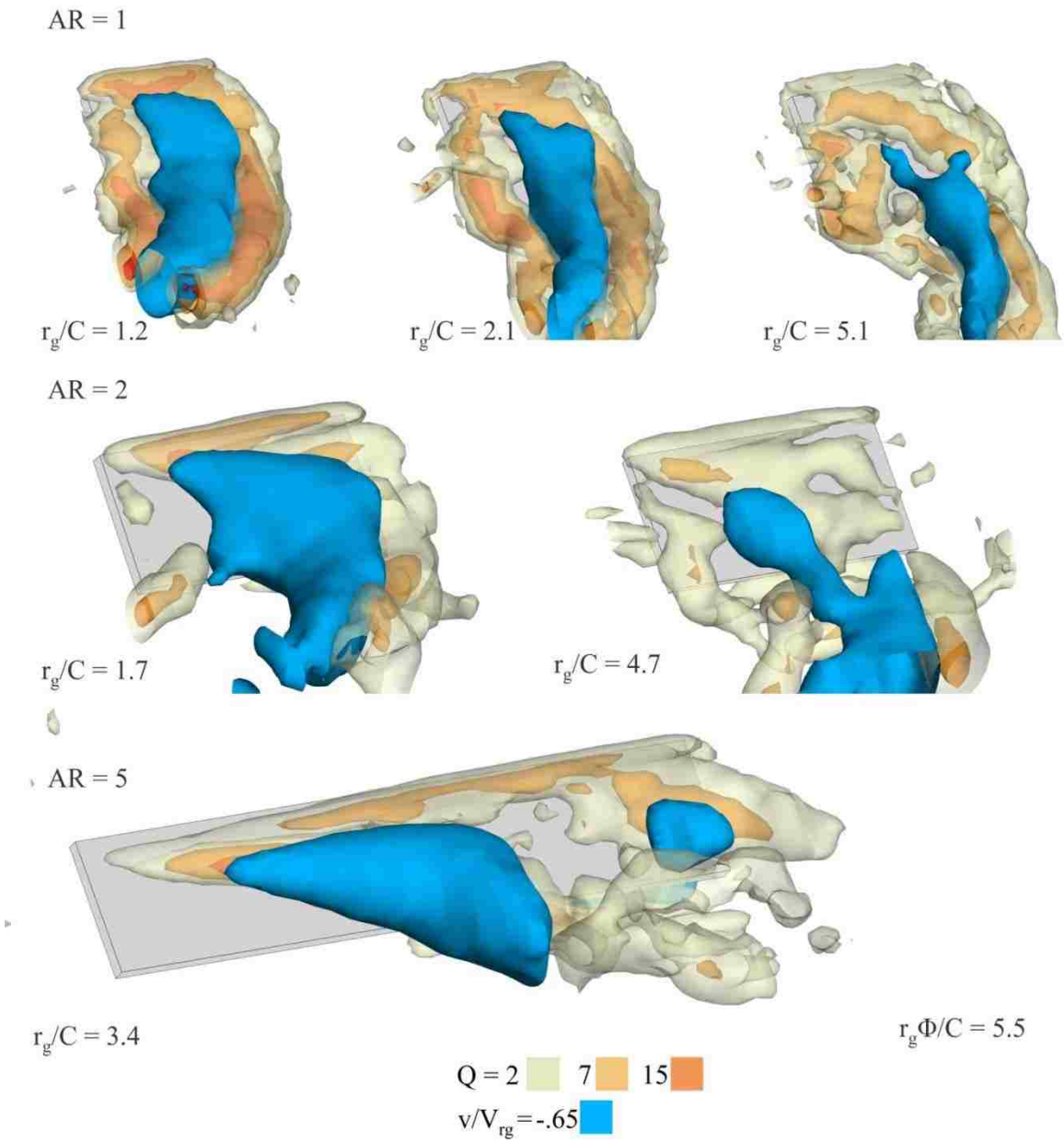

Figure A.25. Trimetric view of transparent iso-surfaces of *Q*-criterion and opaque iso-surfaces of downwash at different values of Rossby number r_g/C and aspect ratio $AR = b/C$. Rotation distance $r_g\Phi/C = 5.5$. Lab-fixed reference frame.

VITA

The author was born on April 2nd, 1987 in Princeton, New Jersey, USA, to parents Patricia Wolfinger and Raymond Wolfinger. He graduated cum laude from Ramapo College of New Jersey, with a Bachelor of Science in Physics, in May, 2010. The author was married in September of 2011 to Kaitlyn Millsaps. He then received a Master of Science in Mechanical Engineering, from Lehigh University, in May, 2012, under advisement of Professor Donald Rockwell. He is currently continuing his research with Professor Rockwell, and working toward a PhD in Mechanical Engineering.

To date, the author's work in fluid mechanics has been published in two journal articles, and presented at two technical conferences. The first journal article, "Shallow flow past a cavity: Coupling with a standing gravity wave", was published in *Physics of Fluids*, in October, 2012. The second journal article, "Flow structure on a rotating wing: effect of radius of gyration", was published in the *Journal of Fluid Mechanics*, in September, 2014.